2014

Nanostructured ICP-CNT Electrodes for Capacitive Deionisation and Water Clean Up

Mohammed Suliman Almoiqli
University of Wollongong

Australian Research Council Centre of Excellence for Electromaterials Science, The Intelligent Polymer Research Institute, Department of Chemistry.

Nanostructured ICP-CNT Electrodes for Capacitive Deionisation and Water Clean Up

by

Mohammed Suliman ALMOIQLI

This thesis is presented as part of the requirement for the

Award of the Degree of

DOCTOR OF PHILOSOPHY

of the

University of Wollongong

March, 2014

This work is dedicated to my parents, Mr. Suliman ALMOIQLI and Mrs. Safiah ALMARWANI and my lovely wife Mrs. Elaf ALBALAWI and my two beautiful sons, Joseph and Omar and all my family for their love and support

DECLARATION

I, Mohammed Suliman ALMOIQLI, declare that this thesis submitted in fulfilment of the requirements for the award of ***Doctors of Philosophy***, in the ***School of Chemistry***, University of Wollongong, is wholly my own work unless otherwise referenced or acknowledged. The document has not been submitted for qualifications at any other academic institution.

Mohammed ALMOIQLI

March, 2014

ABSTRACT

The development of electrodes and flow-through cells in a CDI system are considered in this thesis. Novel 3D nanostructured electrodes and improved designs of flow-through cells in a CDI system are described. The main objectives were: (1) to develop a fundamental knowledge and understanding of reticulated vitreous carbon (RVC), conducting polymers such as Poly(3,4-ethylenedioxythiophene) (PEDOT), single-walled carbon nanotubes (SWCNT) and graphene; (2) to use a RVC electrode structure to build 3D PEDOT microstructure electrodes, 3D nanoweb structure SWCNT and 3D nanoweb hierarchical graphene/SWCNT composite electrodes; (3) to explore possible applications of these electrodes in a CDI system; and (4) to study the effect of increasing the amount of materials in terms of unit geometric volume and geometric area on the electrosorption capacity.

PEDOT/RVC composite electrodes with varying amounts of PEDOT loadings were considered for application as novel 3D microstructure electrodes in Chapter 3. PEDOT was successfully deposited by electropolymerization on RVC and used for the first time as materials and electrodes in CDI technology. The aim of this chapter was achieved as demonstrated by the improved performance of the CDI electrode in terms of unit geometric volume and geometric area. The electrosorption capacity in terms of unit geometric volume and geometric area of electrodes increase with increasing amounts of PEDOT in the electrode, and the highest electrosorption capacity obtained was 0.37 mg/cm^3 or 0.12 mg/cm^2 or 6.52 mg/g of PEDOT in the PEDOT-120/RVC electrode (240 mg coated 4.2 cm^3 RVC electrode) at 75 mg/L NaCl solution, at 0.8 V electrode voltage, and 80 ml/min flow-rate. This result is a

better desalting performance than carbon materials, and the adsorption/ regeneration of PEDOT/RVC electrodes was facile with high efficiency achieved. The water production by $1m^3$ of PEDOT-120min/RVC electrode from 75 mg/L NaCl feed solution was 129,176 L/day to produce water less than 1 mg/L NaCl concentration. It has been shown that the capacitance of PEDOT-120min/RVC electrode compared to a bare RVC electrode had increased by a factor of 2230, and the electrochemical properties were ideal.

The successful use of 3D PEDOT/RVC in a CDI system led to the use of a RVC electrode again in Chapter 4 to build huge 3D functionalized SWCNT (a-SWCNT) nanoweb structures by filling the RVC pores using a dip coating method. A unique 3D electrode was constructed and explored as a novel CDI electrode. The electrical voltage of 1.5 V and flow-rate of 50 ml/min were the optimum conditions and they were the key factors that affected the NaCl ion removal performance at the sites of acid treated SWCNT (a-SWCNT). The maximum electrosorption capacity result for 23.58%wt of a-SWCNT/RVC composite electrode (50mg a-SWCNT coated 2.16 cm^3 RVC electrode) was 3.23 mg/g of a-SWCNT or 0.08 mg/cm^3 at 75 mg/L feed concentration. After that, an improved CDI system was designed to accept solution flowing through the electrodes and its effect on desalination cycle time was studied. It is clear that for one desalination cycle, 42 minutes was required for the flow-between (FB) electrodes configuration and 18 minutes for the flow-through (FT) electrodes configuration. This encouraged efforts to design a new CDI cell with a flow-through electrode system. The electrosorption capacity of all electrodes in new cell was increased and the time required for one desalination cycle decreased as well. For example, the electrosorption capacity for 3.63 %wt a-SWCNT was

increased from 8.39 mg/g to 10.40 mg/g and the time of one desalination cycle decreased from 30 min to 10 min using flow feed between (FB) electrodes and flow feed through (FT) electrodes, respectively. This means that electrosorption capacity increased 23.96% and the time required for one desalination cycle decreased around three times. In addition, the effect of distance between electrodes, the electrosorption dynamic and isotherm were studied using new cell. The ion removal characteristics were affected by various distances between electrodes. As the distance increased, the ion removal amount was not affected, but the adsorption time required increased when the distance was increased in all cases. The energy output of the CDI system was affected by an increase in the space between electrodes. It was found that NaCl adsorption obeyed pseudo first -order kinetics rather than pseudo second-order kinetics and that NaCl ions were not adsorbed onto the a-SWCNT surface via chemical interaction. Furthermore, the electrosorption for this electrode obeys both the Langmuir isotherm and the Freundlich isotherm models. This phenomenon suggests that monolayer adsorption was the primary adsorption mechanism during the electrosorption process. The maximum electrosorption capacity result for 23.58 %wt a-SWCNT electrode was 8.89 mg/g at 500 mg/L feed concentration, as compared with a theoretical maximum value of 13.08 mg/g calculated using the Langmuir isotherm model.

The goals of Chapter 5 are to increase the electrosorption capacity of 3D a-SWCNT/RVC electrodes from Chapter 4 and reduce the duration of electrosorption–desorption cycles of Chapter 4 by improving the ease of ions adsorption to and ions desorption from the electrode surfaces. This was achieved by use of composite microwave irradiated graphene oxide (mwGO) with a-SWCNT. The a-SWCNT

materials were contained sandwiched between the graphene sheets to build a 3D highly porous architecture inside the electrodes and increase the electrodes conductivity as well as afford rapid ions diffusion. The results led to a conclusion that the best performing electrode, with a specific capacitance of 179.39 F/g was the 9-CNT/mwGO/RVC (ie a-SWCNT:mwGO ratio was 9:1) electrode, which represents a 29 % increase in specific capacitance compared with the a-SWCNT/RVC electrode. This 9-CNT/mwGO/RVC electrode also had very high CV curve stability, maintaining 99% current stability after 200 cycles. Moreover, the time saving of one electrosorption–desorption cycle with the 9-CNT/mwGO/RVC electrode was 27.78 %; compared with the CNT/RVC electrode which required 18 min. In addition, the electrosorption removal of NaCl by the 9-CNT/mwGO/RVC electrode in terms of mass of the electrode (3.82 mg/g) increased 18.27 % compared with that of the CNT/RVC electrode (3.23 mg/g) using 1.5V applied voltage and 50 ml/min flow-rate as the optimum conditions. The full desalination process to produce water of less than 1 mg/L NaCl concentration in the CDI system using 9-CNT/mwGO/RVC composite electrode increased desalinated water production by 67.78% per day compared with the same CDI system using a-SWCNT/RVC composite electrode. The maximum water produced per day is 29,958 L using $1m^3$ of 9-CNT/mwGO/RVC electrode and the maximum electrosorption capacity result for the same electrode was 10.84 mg/g at 500 mg/L feed concentration, as compared with a theoretical maximum value of 16.59 mg/g calculated using the Langmuir isotherm model. Also, the performance of electrodes adsorptions was evaluated by dynamics study and it was shown to follow the Pseudo-first-order model.

ACKNOWLEDGMENTS

I would like to express my gratitude to Allah (God) for providing me the blessings to complete this work. I have to thank Allah again for giving me this opportunity to continue my study and work with one of the leading scientists in the fields of Electromaterials and Nanotechnology, “Professor Gordon G. Wallace", and with one of the intelligent researchers, "Dr. Jun Chen". I also would like to ask Him for blessing that this project would be one of the tools to help people in drinking water treatment.

This work could not have been completed without support of many people. I would like to deeply thank my supervisor Professor Gordon G. Wallace and Dr. Jun Chen for their excellent support and encouragement through all stages of my thesis. I truly appreciate the time they have spent on my work as well as encouragement throughout my time in IPRI.

Huge thanks to everybody in IPRI and AIIM who are still here or have left for new adventures. My appreciation to Associate Professor Chee Too for reading and commenting on my thesis. Thanks to Associate Professor Peter Innis and Dr Patricia Hayes for their great guidance in Raman studies. Thanks to Dr Stephen Beirne for his help in flow-through cell design and 3D printing. Thanks to Tony Romeo for his assistance with SEM measurements. Thanks to Mr. Mark Romano and Mr. Dennis Antiohos for their generous help in Graphene oxide synthesis, characterization and discussion.

I gratefully acknowledge King Abdulaziz City for Science and Technology (KACST), University of Wollongong and Australian Research Council for their scholarships and financial support for my PhD.

I would like to thank my parents Suliman and Safiah, all my sisters Amal, Hanadia, Haind, Mona and Rem, my grandmother Saleha, my two beautiful sons Joseph and Omar and my lovely wife Elaf. Thanks for your prayers for me, unconditional and endless love and support in all my life.

ABBREVATIONS

A	Area of electrode
ACN	Acetonitrile
Ag/AgCl	Silver/silver chloride reference electrode
AFM	Atomic force microscopy
BW	Brackish water
C	Carbon
C_h	Chiral vector
C_{sp}	Specific capacitance
CDI	Capacitive deionization
cm	Centimetre
cm^{-1}	**W**avenumber
CNT (s)	Carbon nanotube (s)
CPs	Conducting polymers
CV	Cyclic voltammogram
CVD	Chemical vapour deposition
D	Separation between the plates
d	Distance
DMF	N, N-Dimethylformamide
V	Direct voltages
E	Young's modulus
ED	Electrodialysis
EDR	Electrodialysis reversal
F	Faraday's constant

GO	Graphene oxide
GPa	Gigapascal
HiPCO	High-pressure carbon monoxide
ICPs	Intrinsically Conducting Polymers
I-V	Current-Voltage
L	Length/ Liter
MWNT(s)	Multi walled carbon nanotube (s)
mV	Millivolt
M.wt	**M**olecular weight
mwGO	Microwave irradiated graphene oxide
n	Power law index
nm	Nanometre
NMP	N-Methyl-2-pyrrolidone
NF	**N**anofiltration
PANi	Polyaniline
PEDOT	Poly(3,4-ethylenedioxythiophene)
PET	Polyethylene terephthalate
PPy	Polypyrrole
PSS	Polystyrene sulfonate
PTh	Polythiophene
Q	Charge
RGO	Reduced graphene oxide
RO	Reverse osmosis
$\boldsymbol{R_T}$	Total resistance
RVC	Reticulated vitreous carbon

S	Siemens
SEM	Scanning electron microscope
SWNT(s)	Single walled carbon nanotube (s)
SW	Seawater
TDS	Total dissolved solid
TGA	Thermal gravimetric analyser
UV-vis	Ultraviolet-visible
XRD	X-ray diffraction
XRS	X-ray photoelectron spectroscopy
Z	Geometric volume
$\boldsymbol{\sigma}$	Conductivity
$\boldsymbol{\varepsilon}$	Extinction coefficient
$\boldsymbol{\eta}$	Viscosity
λ	Wavelength
μ	Micro
^{o}C	Degree Celsius temperature

TABLE OF CONTENTS

DECLARATION ii

Abstract iii

ACKNOWLEDGMENTS vii

ABBREVATIONS viii

TABLE OF CONTENTS xi

LIST OF FIGURES xxiii

LIST OF TABLES xxxiv

1 Introduction and Literature Review 1

1.1 Background and Motivation 2

1.2 Water 4

1.2.1 Water resources 4

1.2.2 Basic Purification technologies 5

1.2.2.1 Membrane Technologies 6

1.2.2.2 Chemical approaches 7

1.2.2.3 Thermal Technologies 8

1.2.2.4 Disadvantages of basic purification technologies. 9

1.2.3 Purification technologies under research and development 9

1.3 Capacitive Deionization technology 11

1.3.1 Background 11

1.3.2 Theory of capacitive deionization 14

1.3.3 Capacitive deionization cell 15

1.3.4 Electrode evaluations 16

1.4 Electrode materials 16

1.4.1 Reticulated vitreous carbon 18

1.4.2 Intrinsically Conducting Polymers 20

1.4.2.1 Poly (3,4-ethylenedioxythiophene), “PEDOT” 21

1.4.3 Carbon nanotubes 25

1.4.3.1 Properties of carbon nanotubes 27

1.4.3.2 Applications of carbon nanotubes in water purification 28

1.4.4 Graphene oxide 29

1.4.4.1 Synthesis of graphene oxide (GO). 31

1.4.4.2 Application of reduced graphene oxide in capacitive deionization (CDI). 33

1.5 Aims of thesis 37

2 Experimental techniques 38

2.1 Introduction 39

2.2 Methods of synthesis and preparation of materials 40

2.2.1 Reagents and materials 40

2.2.2 Electropolymerization method 41

2.2.3 Functionalization of carbon nanotubes. 43

2.2.4 Dispersion of carbon nanotubes in solvent 44

2.2.5 Synthesis of graphene oxide (GO). 45

2.2.6 Reduction of graphene oxide. 45

2.2.7 Sonication 46

2.3 Characterization techniques 47

2.3.1 Cyclic voltammetry 47

2.3.2 UV-Visible spectroscopy 50

2.3.3 X-ray photoelectron spectroscopy (XPS) 52

2.3.4 Microscopy 53

2.3.5 Scanning Electron Microscopy (SEM) 53

2.3.6 Raman spectroscopy 55

2.3.7 Thermogravimetric analysis (TGA) 56

2.3.8 X-ray diffraction (XRD) 57

2.4 Capacitive deionization 59

2.4.1 CDI system components 59

2.4.2 Design and fabrication a flow-through cell 60

2.4.3 Measurement of amount of ion removal from the NaCl aqueous solution 61

2.4.4 Electrode evaluation in the capacitive deionization 62

2.4.5 Electrosorption dynamics 64

2.4.6 Electrosorpitive isotherm 66

3 : Novel three-dimensional PEDOT/RVC electrode structure for capacitive deionization. 67

3.1 Introduction 68

3.1.1 Aims of the work in this chapter 70

3.2 Experimental 71

3.2.1 Chemicals and materials 71

3.2.2 Methods 71

3.2.2.1 Pre-treatment of the RVC electrode 71

3.2.2.2 Electrochemical polymerization of PEDOT on RVC electrode 72

3.2.2.3 Physical characterisation 72

3.2.2.4 Electrochemical characterisation 73

3.2.2.5 Measurement of amount of ion removal from the NaCl aqueous solution 73

3.3 Results and discussions 74

3.3.1 PEDOT deposited on RVC electrode 74

3.3.1.1 Cyclic voltammetry 74

3.3.1.2 Polymerization Mechanism of PEDOT 75

3.3.1.3 Effect of applied constant potential on PEDOT electrosynthesis .. 76

3.3.1.4 Electrodeposition of different amounts of PEDOT on RVC electrodes 78

3.3.2 PEDOT surface properties 81

3.3.3 Thermogravimetric analysis 85

3.3.4 Raman spectroscopy 86

3.3.5 Electrochemical characterizations 88

3.3.5.1 Comparison between RVC before and after PEDOT coating. 88

3.3.5.2 Effect of increasing scan rate on the electrode capacitance 90

3.3.5.3 Capacitance 91

3.3.5.4 Cycling stability of PEDOT/RVC electrodes 96

3.3.6 Construction of a capacitive deionization cell 97

3.3.6.1 CDI flow-through open cell fabrication 97

3.3.7 Effect of working conditions on ion removal efficiency..... 99

3.3.7.1 Effect of applied voltage on ions removal 99

3.3.7.2 Effect of flow-rate on ions removal 101

3.3.8 Effect of PEDOT loading of PEDOT/RVC electrode on ions removal 103

3.3.9 Electrosorption performance of PEDOT coated RVC electrode 104

3.3.10 CDI stability 108

3.3.11 Effect of NaCl concentration on electrosorption capacity 109

3.3.12 Water production by CDI system 110

3.4 Conclusion 113

4 Novel SWCNT loaded porous RVC electrodes for capacitive deionization. 114

4.1 Introduction 115

4.1.1 Aims of the work in this chapter 117

4.2 Experimental 118

4.2.1 Chemicals and Materials 118

4.2.2 Methods 118

4.2.2.1 Functionalization of carbon nanotubes 118

4.2.2.2 Dispersion of a-SWCNT 119

4.2.2.3 Pre-treatment of the RVC electrode 119

4.2.2.4 a-SWCNT dip coated RVC Electrode 119

4.2.2.5 Electrochemical characterisation 120

4.2.2.6 Physical characterisation 121

4.2.2.7 Measurement of amount of ion removal from the NaCl aqueous solution 121

4.2.2.8 Construction of a capacitive deionization cell 121

4.3 Results and discussions 122

4.3.1 Characterisation of SWCNT after functionalization 122

4.3.1.1 Raman spectroscopy 122

4.3.1.2 Visible spectrophotometry 124

4.3.2 Dispersion of a-SWCNT in DMF 126

4.3.3 Optimization of RVC electrodes coated with a-SWCNT 128

4.3.4 Optimization of the loading level of a-SWCNT on RVC electrode 130

4.3.5 Scanning Electron Microscopy of a-SWCNT 131

4.3.6 Electrochemical behaviour evaluation using cyclic voltammetry 132

4.3.6.1 The capacitance of RVC electrode before and after loading with a-SWCNT 133

4.3.6.2. Effect of increasing scan rate on the electrode capacitance 134

4.3.6.2 Cycling stability of a-SWCNT/RVC electrodes 140

4.3.7 Effect of working conditions on ion removal efficiency..... 141

4.3.7.1 Effect of applied voltage 142

4.3.7.2 Effect of flow-rateon electrosorption 143

4.3.8 Effect of a-SWCNT loading on electrosorption..... 145

4.3.9 Effect of CDI cell configuration on ions removal efficiency..... 149

4.3.10 New design for flow-through cell 152

4.3.11 Effect of flow-rate and voltage on ions removal efficiency..... 153

4.3.12 Effect of distance between the electrodes on efficiency of electrosorption..... 155

4.3.13 Adsorption/ desorption performance of a-SWCNT loaded RVC electrodes..... 157

4.3.14 Comparison between new cell (flow feed through electrode) and old cell (flow feed between electrode) 160

4.3.15 CDI cycling stability 162

4.3.16 Electrosorption dynamics..... 163

4.3.17 Electrosorption isotherms 167

4.3.18 Comparison of present work with previous published research studies 170

4.4 Conclusions 173

5 Performance enhancement of capacitive deionization (CDI) system by modified 3D SWCNT/RVC electrodes using microwave irradiated graphene oxide (mw GO). . 175

5.1 Introduction 176

5.1.1 Aims of the work in this chapter 178

5.2 Experimental 179

5.2.1 Chemicals and Materials 179

5.2.2 Methods 180

5.2.2.1 Functionalization of carbon nanotubes 180

5.2.2.2 Synthesis of graphene oxide (GO) 180

5.2.2.3 Exfoliation and reduction of graphene oxide using microwave irradiation 180

5.2.2.4 Dispersion of microwave irradiated graphene oxide (mwGO) and acid treated Single-Walled Carbon Nanotubes (a-SWCNT) 181

5.2.2.5 Preparation of a-SWCNT/mwGO composite coating solution.... 181

5.2.2.6 Pre-treatment of the RVC electrode 182

5.2.2.7 a-SWCNT, mwGO, and a-SWCNT/mw GO composite dip coated RVC electrodes 183

5.2.2.8 Electrochemical characterisation..... 185

5.2.2.9 Physical characterisation 186

5.2.2.10 Measurement of amount of ion removal from the NaCl aqueous solution 187

5.2.2.11 Construction of a capacitive deionization cell 187

5.3 Results and discussion..... 188

5.3.1 Characterisation of a-SWCNT after functionalization..... 188

5.3.2 Dispersion of a-SWCNT in DMF 188

5.3.3 Chemical conversion of graphite to graphene oxide..... 188

5.3.3.1 Surface chemistry of graphene oxide (GO)..... 189

5.3.3.1.1 Energy-dispersive X-ray spectroscopy..... 189

5.3.3.1.2 Fourier-Transform Infrared spectroscopy (FTIR) 192

5.3.4 Microwave assisted exfoliation and reduction of graphene oxide 192

5.3.4.1 Surface chemistry of graphene oxide (GO) after microwave irradiation. 195

5.3.4.1.1 Raman spectra..... 195

5.3.4.1.2 X-ray photoelectron spectroscopy (XPS) spectra 197

5.3.4.1.3 Thermogravimetric analysis (TGA) 198

5.3.4.2 Dispersion of mwGO in DMF 199

5.3.5 Electrodes surface morphology 203

5.3.6 Electrochemical behaviour of electrodes studied using cyclic voltammetry 208

5.3.6.1 Capacitive behaviours of mwGO/RVC, CNT/RVC, and various CNT/mwGO/RVC composite electrodes. 208

5.3.6.2 The effect of increasing loading level on capacitive behaviours. 211

5.3.6.3 Effect of increasing scan rate on the electrode capacitance 214

5.3.7 Adsorption performance of 9-CNT/mwGO coated RVC electrode. 219

5.3.7.1 Optimization of conditions for ion removal efficiency 221

5.3.8 Capacitive deionization (CDI) system 222

5.3.8.1 Adsorption/ desorption performance of various ratios of CNT/mwGO loaded RVC electrodes. 222

5.3.8.2 Electrosorption dynamics 227

5.3.8.3 CDI cycling stability 231

5.3.8.4 Electrosorption isotherm 232

5.3.8.5 Water production by CDI system 236

5.4 Conclusion 239

6 Conclusions and Recommendation 241

6.1 Summary and conclusion 242

6.2 Recommendations 248

6.3 References 250

LIST OF FIGURES

Figure 1.1: (a) Distribution of earth's water [2], and (b) worldwide water resources per capita and level of rainfall as a function of each continent. (c) The type of water usage by sector for developing and high-income countries [6]. 5

Figure 1.2: Timeline of scientific developments of CDI, indicating milestones since the inception of CDI in 1960 [42]. 13

Figure 1.3: (a) Electrosorption of ions on application of a potential and (b) desorption of ions on removal of potential. 15

Figure 1.4: Schematic of the inlet and outlet fittings, electrode contact screws and mounting bolts are omitted. The two aerogels are separated by a polymer mesh and are supported by titanium electrodes on the backside to decrease contact resistance. A rubber gasket is seated in a separate channel outside the test section [53]. 16

Figure 1.5: Various carbon materials used for CDI; (a) Graphene-like carbon flake, (b) multi-walled carbon nanotubes, (c) electrospun fibres, (d) activated carbon cloth, (e) carbon aerogels, and (f) ordered mesoporous carbon [42]. 17

Figure 1.6: Schematic model of the structure of reticulated vitreous carbon [87]..... 20

Figure 1.7: The chemical structure of conducting polymers: polypyrrole, polyaniline and polythiophene, where n indicates the number of repeat units [100]. 21

Figure 1.8: Molecular structure of (a) PEDOT-ClO_4 and (b) PEDOT-PSS polymers [102, 103]. 22

Figure 1.9: The scanning electron micrographs of PEDOT electrode prepared by galvanostatic method at a fixed current of (a) 0.5 and (d) 2 mA cm^{-2}; prepared potentiostatically at (b) 0.90 and (e) 1.2 V; and prepared by cyclic voltammetry with sweep rate of 10 mV/s in the potential range of (c) 0–0.9 and (f) 0–1.2 V vs. SCE [105]. 23

Figure 1.10: Schematic diagram of (a) single-walled carbon nanotube (SWCNT) and multi-walled carbon nanotube (MWCNT), and (b) how a graphene sheet is rolled to form a CNT [143, 144]. 27

Figure 1.11: Scheme showing a graphene, graphite, graphene oxide (GO) and reduce graphene oxide (RGO) structures. 31

Figure 1.12: (a and b) scanning electron microscopy (SEM) image, (c) Raman spectra and (d) XRD spectra of GO and mw rGO powder before and after microwave irradiation [198]. 33

Figure 1.13:(a) Illustration of the CNT/rGO composite preparation process and (b) the CDI performance of graphene and the CNT/rGO composite using a 780 mg/L NaCl solution [212]. 36

Figure 2.1: Three-electrode system for electropolymerization. 42

Figure 2.2: Refluxing method using diluted 6 M HNO_3 for 6 hours. 44

Figure 2.3: Schematic ultrasonic probe used in experiments. 46

Figure 2.4: Cyclic voltammogram curve of 1 mM $[Fe(CN)_6]^{4-}/[Fe(CN)_6]^{3-}$ in 1 M NaCl; scan started from negative to positive potential. 48

Figure 2.5: Schematic diagram of basic principle of UV/Visible spectroscopy system. 51

Figure 2.6: Schematic diagram of basic components of an XPS system. 52

Figure 2.7: (a) Photo image of Leica DM 6000 Microscope, and (b) the Leica smart touchscreen function buttons located behind the focus knobs controls. 53

Figure 2.8: Schematic diagram of a Scanning Electron Microscope (SEM). 54

Figure 2.9: Basic principle of a Raman spectroscopy system [254]. 55

Figure 2.10: (a) thermogravimetric analyser (TA Instruments Q500) and (b) a platinum sample pan which was used to hold the samples inside the furnace... 57

Figure 2.11: Basic principle of the X-ray diffraction (XRD) technique. 59

Figure 2.12: Photographs of pump tubing, peristaltic pump for recirculating the salt solution into the system, an on-line flow-through cell, an on-line conductivity sensor, conductivity meter, and (RS232G port) adapter. 60

Figure 2.13: Photograph of a Connex 350 3D printer, by (Objet). 61

Figure 2.14 : Calibration curve linearity for ionic conductivity *vs* NaCl concentration. 62

Figure 2.15: The electrosorption of Na^+ onto GNFs electrode at (a) different bias potentials, (b) different flow-rates [33]. 63

Figure 3.1: Cyclic voltammetry of RVC electrode in a solution containing 0.01 M EDOT and 0.1 M $LiClO_4$ in acetonitrile, using a three-electrode system; RVC electrode and Ag/AgCl (3M NaCl) were used as counter electrode (CE) and reference electrode (RE), respectively. 75

Figure 3.2: Scheme of oxidative polymerization mechanism of PEDOT. 76

Figure 3.3: Chronoamperometric curves at various constant potential applied to coat RVC electrodes by PEDOT in a solution containing 0.01 M EDOT and 0.1 M $LiClO_4$ in acetonitrile, using a three-electrode system; RVC electrode and Ag/AgCl (3M NaCl) were used as counter electrode (CE) and reference electrode (RE), respectively. 78

Figure 3.4: Combination chronoamperogram at 1.3 V constant potential obtained at RVC electrodes (4.2 cm^3) in a solution containing 0.01 M EDOT and 0.1 M $LiClO_4$ in acetonitrile, using a three-electrode system; RVC electrode and Ag/AgCl (3M NaCl) were used as counter electrode (CE) and reference electrode (RE), respectively. 80

Figure 3.5: SEM of PEDOT coated RVC electrode for 10 min electropolymerization at 1.3V. Top surface (a,b,c) and cross-section (d).....82

Figure 3.6: SEM of PEDOT coated RVC electrode for 120 min electropolymerization at 1.3V, showing the top surface.....83

Figure 3.7: The top surface and cross-section of PEDOT coated RVC strut for 10 min polymerization (a,b), for 20 min polymerization (c,d), for 50 min polymerization (e,f), for 70 min polymerization (g,h) and for 120 min polymerization (i,j), respectively. 84

Figure 3.8: TGA curves of pure RVC electrode and various PEDOT/RVC composite electrodes.....86

Figure 3.9: Raman spectra of PEDOT-ClO_4 grown by chronoamperometry at 1.3 V in acetonitrile containing 0.01 M EDOT and 0.1 M $LiClO_4$.....88

Figure 3.10: (a) Cyclic voltammograms of 1 cm^3 bare RVC and same size of PEDOT-120min/RVC composite electrode in 1M NaCl using a scan rate of 5 mV/s and Ag/AgCl reference electrode. (b) Effect of increasing polymerization time of PEDOT on the specific capacitance of PEDOT/RVC electrodes.....89

Figure 3.11: Cyclic voltammograms of PEDOT-120min/RVC electrode at: (a) 5 to 50 mV/s scan rates and (b) 50 to 200 mV/s scan rates in a three-electrode systems in 1 M NaCl solution. 91

Figure 3.12: (a) The specific capacitance (F/g) of PEDOT/RVC electrodes at various scan rates. (b) Cyclic voltammograms of PEDOT/RVC electrodes using current per gram of PEDOT and current per geometric volume of electrode at 5 mV/s scan rate. (c) The specific capacitance of PEDOT/RVC electrodes in terms of F/g and F/cm^3 at 5 mV/s scan rate. Electrolyte: 1 M NaCl solution. Potential range: between -0.2 to 0.8 V vs Ag/AgCl using a three-electrode system. 94

Figure 3.13: The electrochemical cycling stability of PEDOT-120min/RVC electrode in 1 M NaCl solution recorded in the potential range between -0.2 to 1.0 V vs Ag/AgCl using a three-electrode system at 5 mV/s scan rate for 200 cycles. ...96

Figure 3.14: Schematic diagram of a capacitive deionization (CDI) cell. 98

Figure 3.15: (a) Effect of applied voltage on electrosorption at a PEDOT-20min/RVC composite electrode using a 35 ml/min flow-rate and 75 mg/L NaCl feed solution. (b) Plot of electrosorption capacity as a function of electrical voltage. 101

Figure 3.16: Effect of flow-rate on the electrosorption behaviour of PEDOT-20min/RVC composite electrode. Applied voltage: 0.8 V. Concentration of NaCl feed solution: 75 mg/L. 102

Figure 3.17: Effect of PEDOT loading of PEDOT/RVC electrode on ions removal efficiency using a CDI system. Applied voltage: 0.8 V. NaCl feed solution concentration: 75 mg/L. Flow-rate: 80 ml/min. 104

Figure 3.18: Effect of PEDOT loading of PEDOT/RVC electrodes on electrosorption as reported in terms of mass of PEDOT, and geometric volume of the PEDOT/RVC electrode. 106

Figure 3.19: Multiple electrosorption–desorption and current response cycles for PEDOT-120min/RVC electrode upon polarization and depolarization at 0.8 V and 0.0 V, respectively. NaCl feed solution concentration: 75 mg/L. 109

Figure 3.20: Electrosorption capacity of PEDOT-120min/RVC composite electrode at varous concentrations of NaCl feed solution. Applied voltage: 0.8V. Flow-rate: 80 ml/min. 110

Figure 3.21: (a) Calibration curve of electrosorption vs concentration of NaCl feed solution. (b) Concentration of feed solution vs desalination cycles number for full desalination process to produce water of less than 1 mg/L NaCl concentration. 112

Figure 4.1: Schematic diagram of (a) flow-between and (b) flow-through electrodes systems in a CDI cell..... 117

Figure 4.2: The full process of dip coating RVC in a-SWCNT solution. 120

Figure 4.3: Raman spectra of single-walled carbon nanotubes before and after treatment by 6M HNO_3 for 6 hours at 120 °C..... 124

Figure 4.4: The Visible absorption spectra of dispersions containing 0.2%w/v pristine SWCNT and a-SWCNT which were measured after a 20- Fold dilution. 125

Figure 4.5: Effect of increasing sonication time on: (a) the Visible absorption spectrum of a dispersion containing 0.2% w/v a-SWCNT which was measured after a 20-fold dilution, where inset photo images are of 0.2% w/v containing a-SWCNT before sonication and after 30 minutes sonication and optical microscope image after 5 min and 30 min sonication time; and (b) Absorbance at 660 nm. (c) Effect of increasing sonication time on sonication energy. Arrows in (a) indicate the direction of increase in sonication time. 127

Figure 4.6: (a,b,c) Photo images and (d,e,f) SEM micrographs of 60, 45 and 30 ppi RVC samples, respectively. (g) The specific capacitance of a-SWCNT coated RVC electrodes of various porosities in 1 M NaCl solution calculated from cyclic voltammograms recorded in a voltage range between -0.2 to 1.0 V using a three-electrode system vs Ag/AgCl at 5mV/s scan rate. 129

Figure 4.7: a-SWCNT loading of RVC as a function of number of dip coatings in a-SWCNT dispersion. Insets: images of RVC electrode before coating and after being completely filled (23.58 %wt a-SWCNT coated RVC electrode). 130

Figure 4.8: Scanning electron microscopy (SEM) images (a, and b) top surface, (c) cross-section and (d and e) 45° view of 23.58%wt a-SWCNT loading. 132

Figure 4.9: (a) Comparison cyclic voltammograms of 1 cm^3 bare RVC electrode and same size of 23.58 %wt a- SWCNT coated RVC electrode in 1 M NaCl scanned at 20 mV/s, and using a RVC counter electrode and Ag/AgCl reference electrode in a three-electrode system and (b) Effect of a- SWCNT loading of a-SWCNT/RVC composite electrodes on specific capacitance. 134

Figure 4.10: (a) Cyclic voltammograms of 3.63 %wt a-SWCNT coated RVC electrode, and (b) specific capacitance of various a-SWCNT coated RVC electrodes at various scan rates in 1 M NaCl solution in the voltage range between -0.2 to 1.0 V vs Ag/AgCl using a three-electrode system. Cyclic voltammograms of a-SWCNT coated RVC electrodes at 20 mV/s, in terms of (c) current per gram of a-SWCNT, and (d) current per geometric volume of electrode. (e) Capacitance of the electrodes per gram of a-SWCNT and per geometric volume of the electrode. 138

Figure 4.11: The electrochemical cycling stability of a-SWCNT coated RVC electrodes, with different a-SWCNT loadings, in 1 M NaCl solution recorded after 200 cycles in the voltage range between -0.2 to 1.0 V vs Ag/AgCl using a three-electrode system at 20 mV/s scan rate. 141

Figure 4.12: (a) Conductivity variations of NaCl solution with applied voltage and operating time. (b) The electrosorption as a function of applied voltage. 143

Figure 4.13: Variations of the conductivity of NaCl solution with various applied flow-rates and operating time. (a) 3.63 %wt, (b) 12.50 %wt, (c) 17.43 %wt and 23.58%wt a-SWCNT coated RVC electrodes. 145

Figure 4.14: (a) Adsorption and release behaviour and (b) the electrosorption capacity in terms of mass of a-SWCNT and in terms of geometric volume of composite electrode of various loadings of a-SWCNT on RVC electrode using the CDI system. 148

Figure 4.15: Schematic diagram of flow-between and flow-through electrodes in CDI cell. 150

Figure 4.16: Comparison of the NaCl adsorption and release behaviour of 23.58 %wt of a-SWCNT coated RVC electrode when configured for flow-between and flow-through system in a CDI cell. 151

Figure 4.17 : Schematic of a flow-through cell (a) and cross-section of flow distributor chamber (b). 153

Figure 4.18: Conductivity variations of NaCl solution with various flow-rates, as a function of operating time. 154

Figure 4.19: The effect of distance between electrodes (5 mm, 15 mm and 25 mm) on the current and conductivity behaviour of 23.58 %wt a-SWCNT coated RVC electrode at 1.5 Volt and 50 ml/min flow-rate. 157

Figure 4.20: (a) Adsorption and release behaviour, and (b) the electrosorption capacity in terms of mass of a-SWCNT and the geometric volume of electrode of various a-SWCNT coated RVC electrode coatings of a-SWCNT (wt%): 3.63%, 12.50%, 17.43% and 23.58%. 159

Figure 4.21: Multiple electrosorption–desorption cycles of 75 ppm NaCl solution for 23.58 %wt a-SWCNT coated RVC electrode. Polarization and depolarization was performed at 1.5 V and 0.0 V, respectively. 163

Figure 4.22: The (a) electrosorption, (b) intraparticle diffusion, (c) adsorption kinetics pseudo-first-order, and (d) adsorption kinetics pseudo-second-order, of NaCl onto23.58 %wt a-SWCNT coated RVC electrode at 1.5 V and 50 mL/min flow-rate. 166

Figure 4.23: The electrosorption isotherm for 23.58 %wt a-SWCNT coated RVC electrode at 1.5 V and 50 ml/min NaCl flow-rate. 169

Figure 5.1: Schematic diagram of the preparation process of composite a-SWCNT/mw GO coating solution. 182

Figure 5.2: Schematic diagram of the preparation process of ratio 9:1 composite a-SWCNT/mw GO coated RVC electrode. 185

Figure 5.3: (a and b) Energy-dispersive X-ray (EDX) spectra, (c) the X-ray diffraction (XRD) patterns of the graphite flakes powder and graphene oxide (GO) film respectively, and (d) Fourier-Transform Infrared (FT-IR) spectrum

for graphene oxide film. Inset shows scanning electron microscopy (SEM) and optical images of the (a) graphite flakes powder and (b) the GO film. 191

Figure 5.4: (a and b) Scanning electron microscopy (SEM) images of GO and mwGO, respectively, (c) the X-ray diffraction (XRD) patterns of GO and mwGO and (d and e) Energy-dispersive X-ray (EDX) spectrum of graphene oxide (GO) film and microwave irradiated graphene oxide. Inset shows optical images of the (d) GO film and (e) mwGO. 194

Figure 5.5: Raman spectroscopy of flake graphite, graphene oxide and microwave reduced graphene oxide..... 196

Figure 5.6: X-ray photoelectron spectroscopy (XPS): comparison of the C1s spectra for (a) graphene oxide (GO) and (b) microwave irradiated graphene oxide (mwGO). 198

Figure 5.7: Thermogravimetric analysis (TGA) of natural graphite flakes, graphene oxide (GO), and microwave irradiated graphene oxide. 199

Figure 5.8: Effect of increasing sonication time on: (a) the Visible absorption spectrum of a dispersion containing 0.1% w/v mwGO which was measured after a 5-fold dilution, where inset photo images are of 0.1% w/v containing mwGO before sonication and after 35 minutes sonication, and (b) Absorbance at 660 nm *vs* sonication time. Arrows in (a) indicate the direction of increase in sonication time. (c) Effect of increasing sonication energy on absorbance at 660 nm for 0.1 % w/v mwGO dispersions. 202

Figure 5.9: Scanning electron microscopy (SEM) images (a) top surface, (b) 45^0 view, (c,d,e) cross-section of 9-CNT/mwGO/RVC electrode; (f) top surface, (g) 35^0 view, (h) cross-section of 8-CNT/mwGO/RVC electrode; (i) top surface, (j) 45^0 view of 7-CNT/mwGO/RVC electrode; and (k) top surface, (l) 45^0 view of mwGO electrode. 207

Figure 5.10: Comparison cyclic voltammograms and (inset) specific capacitance for mwGO/RVC, CNT/RVC, 7-CNT/mwGO/RVC, 8-CNT/mwGO/RVC and 9-

CNT/mwGO/RVC electrodes in 1 M NaCl solution recorded in the voltage range between -0.2 to 1.0 V vs Ag/AgCl in a three-electrode system at 5 mV/s scan rate. 210

Figure 5.11: Cyclic voltammograms of 9-CNT/mwGO composite coated RVC electrodes in 1 M NaCl solution recorded in the voltage range between -0.2 to 1.0 V vs Ag/AgCl using a three-electrode system at 5 mV/s, in terms of (a) current per gram of composite, and (b) current per geometric volume of electrode. (c) Capacitance of the electrodes per gram of composite and per geometric volume of the electrode. 214

Figure 5.12: (a) Cyclic voltammograms and (b) specific capacitance at various scan rates, and (c) the cyclic voltammograms stability scanned at 20 mV/s using 9-CNT/mwGO/RVC electrode in 1 M NaCl solution recorded in the voltage range between -0.2 to 1.0 V vs Ag/AgCl in a three-electrode system. 217

Figure 5.13: (a) Adsorption behaviour, and (b) the electrosorption capacity in terms of mass of composite material loading and the geometric volume of electrode of various 9-CNT/mwGO/RVC electrodes. Loadings (mg): 10, 30 and 50. 220

Figure 5.14: Conductivity variations of NaCl solution with various (a) applied voltages and (b) applied flow-rates, with respect to operating time; using the 9-CNT/mwGO/RVC electrode loaded with 50 mg composite material..... 222

Figure 5.15: (a) Adsorption and release behaviour, and (b) the electrosorption capacity in terms of mass of CNT/mwGO and the geometric volume of electrode of various ratios 10, 9, 8 and 7 CNT in CNT/mwGO/RVC electrodes. 226

Figure 5.16: (a, b, c, d) Electrosorption and (e, f, g, h) pseudo-first-order adsorption kinetics of NaCl electrosorption onto CNT/RVC, 9-CNT/mwGO/RVC, 8-CNT/mwGO/RVC and 7-CNT/mwGO/RVC electrodes, respectively, at 1.5 V and 50 mL/min flow-rate. Results have been derived from Figure 5.15 (a) (adsorption process). 230

Figure 5.17: Multiple electrosorption–desorption cycles of 75 ppm NaCl solution for 9-CNT/mwGO/RVC electrode upon polarization and depolarization at 1.5 V and 0 V, respectively. 232

Figure 5.18: The electrosorption isotherms for 9-CNT/mwGO/RVC and CNT/RVC electrodes at 1.5 V and 50 ml/min flow-rate using different initial concentrations of NaCl solutions.. 235

Figure 5.19: (a) Calibration curve of electrosorption vs concentration of NaCl feed solution. (b) Concentration of feed solution vs desalination cycles number for full desalination process to produce water of less than 1 mg/L NaCl concentration. 238

LIST OF TABLES

Table 1.1: Characteristics and Applications of Pressure-Driven Membrane Processes [12, 14, 20]. 7

Table 1.2: A brief overview of types of various thermal technologies. 8

Table 3.1: Charge consumed during polymerization, polymerization time and mass of PEDOT coating on RVC electrode calculated by Equation 3.1. 81

Table 3.2: Calculated Raman band wavenumbers and vibrational assignments of PEDOT. 87

Table 3.3: Specific capacitance of PEDOT/RVC electrodes measured in various units at various scan rates. 95

Table 3.4: Electrosorption performance of PEDOT/RVC composite electrodes with different PEDOT loadings. 107

Table 4.1 : Single-walled carbon nanotube (SWCNT) diameter and ratio of D to G bands before and after acid treatment 124

Table 4.2: RVC (2.16 cm^3) electrodes before and after a-SWCNT coating. 130

Table 4.3: Specific capacitance of various a-SWCNT coated RVC electrodes by F/g of a-SWCNT, F/area of electrode and F/ volume of electrode, in 1 M NaCl solution at various scan rates. 139

Table 4.4: Electrosorption capacity of various a-SWCNT coated RVC electrodes. 148

Table 4.5: The current of the CDI system for different inter-electrode distances used 1.5V applied voltage. 156

Table 4.6: Electrosorption capacity of various a-SWCNT coated RVC electrodes. 159

Table 4.7: Electrosorption capacities and the time of one desalination cycle of various a-SWCNT coated RVC electrodes obtained by comparing the performance between flow feed between (FB) electrodes and flow feed through (FT) electrodes with NaCl feed solution (75 mg/L)..... 161

Table 4.8: Comparison between the adsorption rate constant, qe, estimated and Correlation Coefficients associated with pseudo-first-order and pseudo-second-order Rate Equations and Intraparticle Diffusion. 165

Table 4.9: Determined parameters of regression coefficients R^2, K_L and K_F of Langmuir and Freundlich isotherms for NaCl electrosorption by using a-SWCNT (23.58 %wt) coated RVC electrode as electrosorption electrode. 169

Table 4.10: Comparison of electrosorption capacity of various carbon electrodes and electrodes developed in this thesis. 172

Table 5.1: Details of carbon materials coated on RVC (2.16 cm^3) electrodes..... 184

Table 5.2: Specific capacitance of various electrodes in terms of F/g of material, F/area of electrode and F/ volume of electrode, in 1 M NaCl solution at various scan rates. 218

Table 5.3: Electrosorption of NaCl by CNT/mwGO/RVC electrodes with various ratios of CNT, time of one desalination cycle. 225

Table 5.4: Comparison between the adsorption rate constant (k_1) and correlation coefficients of pseudo-first-order kinetics, and the estimated theoretical and experimental (q_e) of maximum electrosorption with pseudo-first-order model. 229

Table 5.5: Determined parameters of regression coefficients R^2, K_L and K_F of Langmuir and Freundlich isotherms for NaCl electrosorption by using the 9-CNT/mwGO/RVC electrode. 235

Table 6.1: Comparison of capacity, electrosorption capacity, estimate the maximum electrosorption amount (q_m) and the adsorption rate constant (k_1) of electrodes developed in this thesis. 247


UNIVERSITY OF
WOLLONGONG

1 INTRODUCTION AND LITERATURE REVIEW

1.1 Background and Motivation

The shortage of freshwater resources has become an important factor restricting social development. In addition, more than 80 countries face severe water shortage problems and 5 to10 million people die because of waterborne diseases. Therefore, sea water, brackish water desalination and wastewater reclamation and reuse are particularly important to address the shortage of freshwater resources. These can be a panacea for the growing freshwater crisis that threatens to engulf a population of 5 billion people, over 50 nations, by 2050. However, the energy guzzling nature of current desalination technologies (2 -20 kWhr/m^3) has resulted in very limited relief, characterized by a meagre 0.3% contribution to the annual water use because the costs involved are $4-$9/kgal for desalinated water as compared with $1-$3/kgal paid by urban users today.

Capacitive Deionization (CDI) technology has become a new desalination technology developed in recent years, which has advantages that include energy saving, no secondary pollution, simple operation, showing a broad prospect, a low-pressure and non-membrane desalination technology that employs the basic electrochemical principle of adsorbing ions in a capacitive fashion to high surface-area electrodes such that the outgoing stream becomes devoid of the ions that were present in the incoming stream. Although the power efficiency of CDI is nearly an order-of-magnitude (0.1 kWhr/m^3) superior to the existing processes, it is plagued by the problem of low water recovery ratio. Recently, a capacitive deionization process with permeating flow discharge to drastically reduce the problem of low water recovery ratio while still maintaining the sizeable power consumption advantage was proposed.

Development and evaluation results indicated that the CDI industrial modules could be manufactured cost effectively on a large scale and that such units have the potential to be very competitive with existing technologies with regards to overall operational and maintenance costs. Therefore, CDI technology can be viewed as a potential alternative to membrane technologies in the future. Regardless of the benefits to the potable water industry, CDI has the potential to incur a dramatic step reduction in the operational costs of desalination plants, which will make desalination a more viable alternative technology for large scale agriculture and industrial uses.

In this thesis, water production was increased by use of a modified flow-through cell in a CDI system that enhances the electrosorption performance of electrodes in terms of geometric volume. This modified flow-through cell was fabricated to change the direction of solution flow from between electrodes to directing flow through the electrodes. Increase in the electrosorption capacity of the electrode in terms of geometric volume was achieved by building 3D electrode structures to reduce the resistance of solution flow through the electrodes, increase the stability of electrodes towards high flow rate pressure, increase the possibility of ions to reach all electrode surfaces in a short time for electrosorption, and shorten the time of ions desorption from the electrode surface. Moreover the electrosorption capacity was increased by using new materials that have good conductivity and surface area with high porosity such as Poly(3,4-ethylenedioxythiophene) (PEDOT). In this thesis, traditional materials such as single-walled carbon nanotubes (SWCNT) and composite SWCNT/reduced graphene oxide were also used in a CDI system but in this instance they were used as 3D electrodes.

1.2 Water

1.2.1 Water resources

Water is essential to all of the critical processes required to sustain human life and it is necessary for biological, environmental and industrial prosperity lifestyle [1, 2]. Natural water like most other natural resources is unequally distributed in the earth [3]. Unfortunately, only about 3% of all water sources are potable (Figure 1.1 (a)), this causes that about 25% of the world's population do not have access to satisfactory quantities and quality of freshwater. In addition, more than 80 countries face severe water shortage problems [2, 4] and 5 to10 million people die because of waterborne diseases [5]. Nowadays, there are many reasons that lead to a shortage of drinking water. Figure 1.1 (b and c) show that the vast majority of people are living in continents which have the least amount of drinking water, and much of the water in developing countries is being used for agriculture [6]. Also, because of water pollution, the amount of available water is rapidly reducing [5]. These reasons and others will mean that two thirds of the world population will face severe water shortage problems in 2050 [5]. It is interesting to note that according to the UNESCO Centre for Membrane Science and Technology [7], in the past decade, Australia's capital cities have relied on surface waters to meet the demand for potable water and a significant percentage of water supplies has been used in industrial processes. However, these cities are experiencing the highest population growth and coupled with the greatest decline in average run-off. For instance, the population growth in the Gold Coast and Brisbane, and Sydney are 66% and 33% respectively, and the change in run-off is between -9 to -5 % and -4 to 0 %, respectively.

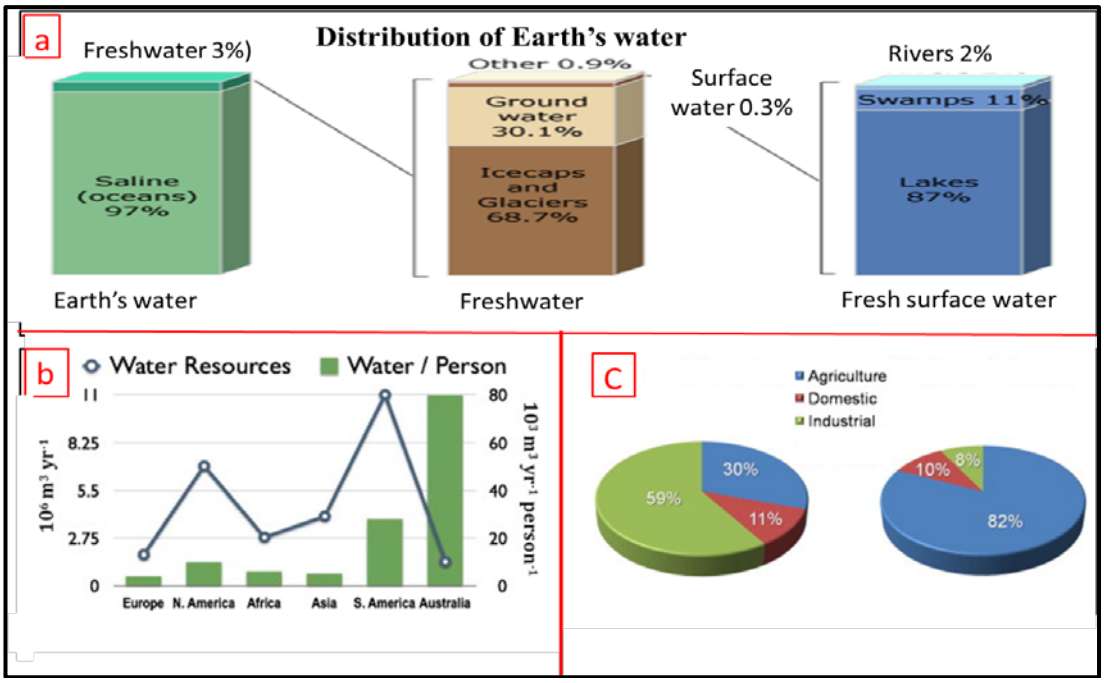

Figure 1.1: (a) Distribution of earth's water [2], and (b) worldwide water resources per capita and level of rainfall as a function of each continent. (c) The type of water usage by sector for developing and high-income countries [6].

1.2.2 Basic Purification technologies

In many cases the usable lifetime of this precious resource, water, could be extended by using an appropriate water treatment process. Desalination, which can be considered as one of the most promising water supply techniques, has been practised regularly for over 50 years and is a well-established means of water supply in many countries [8-10]. It is feasible technically and economically to produce large quantities of water of excellent quality [9]. In 1992, this has resulted in the building of more than 7500 desalination plants operated worldwide to turn 4.8 billion cubic meters of salt water into fresh water annually [11]. These plants used three basic categories of water purification technologies that are used for desalination. As such the use of membrane technologies, distillation processes (thermal technologies), and chemical approaches, such as ion exchange, has attracted considerable attention [12].

1.2.2.1 Membrane Technologies

A membrane is a thin film of porous material that allows water molecules to pass through it [13], but concurrently prevents the passage of larger and undesirable molecules such as viruses, bacteria, metals, and salts [13]. In general, membrane treatment processes use either pressure-driven or electrical-driven technologies. Pressure-driven membrane technologies include reverse osmosis (RO), nanofiltration (NF), ultrafiltration, and microfiltration [13-15]. The latter three techniques work similarly to reverse osmosis, except that less pressure is needed because of their use of larger membrane pore sizes [14, 15]. RO is the major technology used to produce pure water[16]. It is a physical procedure that uses the osmosis phenomenon [10, 17], a pressure greater than the osmotic pressure is applied on saltwater to reverse the flow, which results in pure water passing through the synthetic membrane pores separated from the salt. In Australia, desalination plants in operation or under construction use reverse osmosis membranes to produce drinking water [7]. Table 1.1 shows the Characteristics and Applications of Pressure-Driven Membrane Processes. In addition, Electrical-driven membrane technologies that are effective for salt removal include electrodialysis (ED) and electrodialysis reversal (EDR). Electrodialysis utilizes electromotive force applied to electrodes adjacent to both sides of a membrane to separate dissolved minerals in water [18, 19]. The separation of minerals occurs in a cell pair which consists of an anion transfer membrane, a cation transfer membrane, and two spacers [18, 19]. Electrodialysis reversal is a similar process to ED, except that the cation and anion reverse to routinely alternate current flow [18]. EDR has a higher recovery rate (up to 94%) because of the feedwater circulation within the system and alternating polarity [12].

Table 1.1: Characteristics and Applications of Pressure-Driven Membrane Processes [12, 14, 20].

Membrane Process	Applied Pressure (psi)	Minimum Particle Size Removed	Application (type, average removal efficiency %)
Microfiltration	4-70	0.1-3 µm	Particle/turbidity (>99%). Bacteria/protozoa (>99.99 %). TOC (<20%) with (UF) just. Virus / (partial credit only) with (UF) just.
Ultrafiltration	4-70	0.01-0.1 µm	
Nanofiltration	70-140	200-400 Daltons	Turbidity (>99%). Color (>98%). TOC (DBP control) (>95%). Hardness (softening) (>90%). Organic contaminant up 500 daltons (0-100%). Sulfate (>97%). Virus (>95%.
Reverse Osmosis	140-700	50-200 Daltons	Salinity (desalination) (>99%). Color (>97%). Radionuclide (not including radon) (>97%). Nitrate (85 to 95%). Pesticide/SOC (0-100%). Virus (>95%). As, Cd, Cr, Pb, F (40 to >98%).

1.2.2.2 Chemical approaches

Ion exchange technology was developed as early as in the 1970's and it is often used for water softening among other applications [16]. This technique can best be described as the interchange of ions between a solid phase (chemical resins such as zeolites) and a liquid phase (feedwater) surrounding the solid [12]. Ion

exchange using synthetic resins is the method of choice in many water treatment processes for removing inorganic contaminants in water and wastewater. The process, ion exchange, can be used in combination with reverse osmosis processes such as blending water treated by ion exchange with RO produced water to increase water production [12]. The main advantages of ion exchange over chemical precipitation are recovery of metal value, selectivity, less sludge volume produced and the meeting of strict discharge specifications [21].

1.2.2.3 Thermal Technologies

Thermal technologies are based on the concept of using evaporation and distillation processes [12]. Table 1.2 shows a brief overview of types of various thermal technologies which are applied to desalination of seawater (SW) and brackish water (BW).

Table 1.2: A brief overview of types of various thermal technologies.

Thermal technologies	**Brief Description**	**Feed-water**
Solar Distillation(SD)	This technique uses solar radiation as the source of heat energy. Water is evaporated, thus separating water vapour from dissolved substances, and is then condensed as pure water [22].	SW/BW
Multistage-Flash (MSF)	The MSF process entails two stages; ie heat rejection and heat recovery [3, 23].	SW
Multiple Effect Evaporation (MEE)	In the MEE process, the cool saltwater is sprayed over the top of hot tubes, then evaporates and the vapour is collected as potable water [24].	SW
Thermal Vapour Compression (TVC)	In the TVC process, **a** steam jet ejector is used to compress the vapour for the tubes in the first stage. A condenser is responsible for condensing the vapour to the final product [25].	SW

1.2.2.4 Disadvantages of basic purification technologies.

These technologies have some disadvantages related to using membranes and may include: a short design life, membrane cleaning using chemical treatment, need of high-pressure pump, high membrane replacement costs, low resistance to chlorine, and lack of resistance to fouling [26]. All RO and NF membrane systems have need of scaling control and it is achieved by either addition of acid or antiscalent to feedwater [12]. Also, it is very difficult to maintain the membrane and membrane technologies in the electrodialysis method as it uses expensive ion-exchange membrane and needs high voltage at a high concentration [5]. Most of the existing industrial scale desalination facilities get their energy from the combustion of fossil fuels, and thus in effect exchange potable water for CO_2, which causes global warming and eventually contributes to the demise of fresh water [11].

1.2.3 Purification technologies under research and development

In order to overcome these disadvantages, it is imperative to continue research into methods that will provide low-cost desalination, are environmentally friendly and that create greater economic and political stability in many regions of the world. As a consequence, scientists were demanded to focus their research on producing huge amounts of pure water in a highly efficient and environmentally benign manner. Electrodeionization, Membrane Distillation, Freeze Separation, Rapid Spray Evaporation, Vacuum Distillation and Capacitive Deionization are processes of water purification technologies that can be applied in the future to desalination.

- Electrodeionization, also known as continuous deionization [27], is a combination of ion exchange and electrodialysis [27]. It is a process that removes ionizable species from liquids using electrically active media and an electrical potential to effect ion transport [28].
- Membrane Distillation, which is a thermally driven process, is an emerging technology for separations [29]. In this way, liquid feed must be in direct contact with one side of the membrane where a temperature difference occurs on opposing sides and does not go through inside the dry pores of the membranes. Differences in vapour pressure drive the system and only vapour passes through the membrane [12, 29, 30].
- Freeze Separation is where freezing of saltwater forms pure water ice crystals, which have to be separated from brine and then melted to get potable water [12, 31].
- Rapid Spray Evaporation is where saltwater is sprayed through nozzles at high velocity. As it exits, it is vaporized whereas salt is not, thus producing potable water [12, 32].
- Freezing with Hydrates is the process of forming hydrates by cooling the saltwater vapour and separating it from the brine. Hydrates are decomposed to form potable water [12].
- Capacitive Deionization (CDI) is a process that utilizes the electrochemical double layer which is formed at the electrodes and electrolyte solution interfaces on the application of a direct current. The CDI system will be explained in a separate section because it is the main water purification technology considered in this thesis.

1.3 Capacitive Deionization technology

1.3.1 Background

Capacitive deionization (CDI) technology, which is also called electrosorption [33], is an electrochemical desalination tool [11, 34-37]. It provides a simple and robust approach to the removal of trace ions from solution [36, 38-40]. It generally follows the electric double layer theory [11]. Oren, A. [41] and Porada, et al. [42] gave an historical overview of the CDI system, and Figure 1.2 summarizes the CDI development until 2012. In the mid-1960s and the early 1970s, the concept of ion sorption and flow-through system was introduced by Caudle et al., who used porous carbon electrodes made of activated carbon powder. Later, Johnson et al. studied CDI as a reversible process with parallel combined parametric studies with investigations of the theoretical basis of CDI and of various electrode materials. These intensive studies were eventually discontinued for more than 17 years because of the instability of the electrodes, particularly the anode. During that period, the cost and efficiency of a CDI system was evaluated and they found that efficient and low-cost desalination based on CDI technology could indeed be achieved, provided that sufficiently stable high-surface area electrodes were used. Following this work, Johnson and Newman published a comprehensive theoretical analysis of ion adsorption on porous electrodes. The pioneering works of the groups of Caudle and Johnson triggered an enormous amount of work with a fundamental orientation aimed at reaching an understanding of the basic factors governing CDI. This research was accompanied by studies directed at developing novel electrode materials for efficient CDI and small devices for desalination. In more than half a century, it has been demonstrated that CDI technology has the potential to be such an energy

efficient desalination method because it is operated at low direct voltages (DV) between 0.8 to 1.6 voltage without high-pressure pumps and thermal heaters [11, 35-37, 43, 44]. The estimated maximum energy required for CDI desalination of brackish water (2000 mg/L) is 0.4 Wh/ gallon while the estimated maximum energy required for RO desalination of the same feed solution is 7.7 Wh/ gallon. The CDI process also exhibits several advantages such as a simple, modular design and no additional chemicals requirement for regeneration of the electrosorbent [34-37]. Therefore, the time of cleaning and maintenance in a CDI system is expected to decrease [34]. Recently, capacitive deionization (CDI) has been suggested to lower water treatment costs ($0.40/1000 gallon) while the average cost of the 22 brackish water treatment plants were $1.28/1000 gallon, alleviate fouling problems and prevent environmental pollution without any disadvantages [35-37, 43]. This technique might be important for future applications for water purification [43].

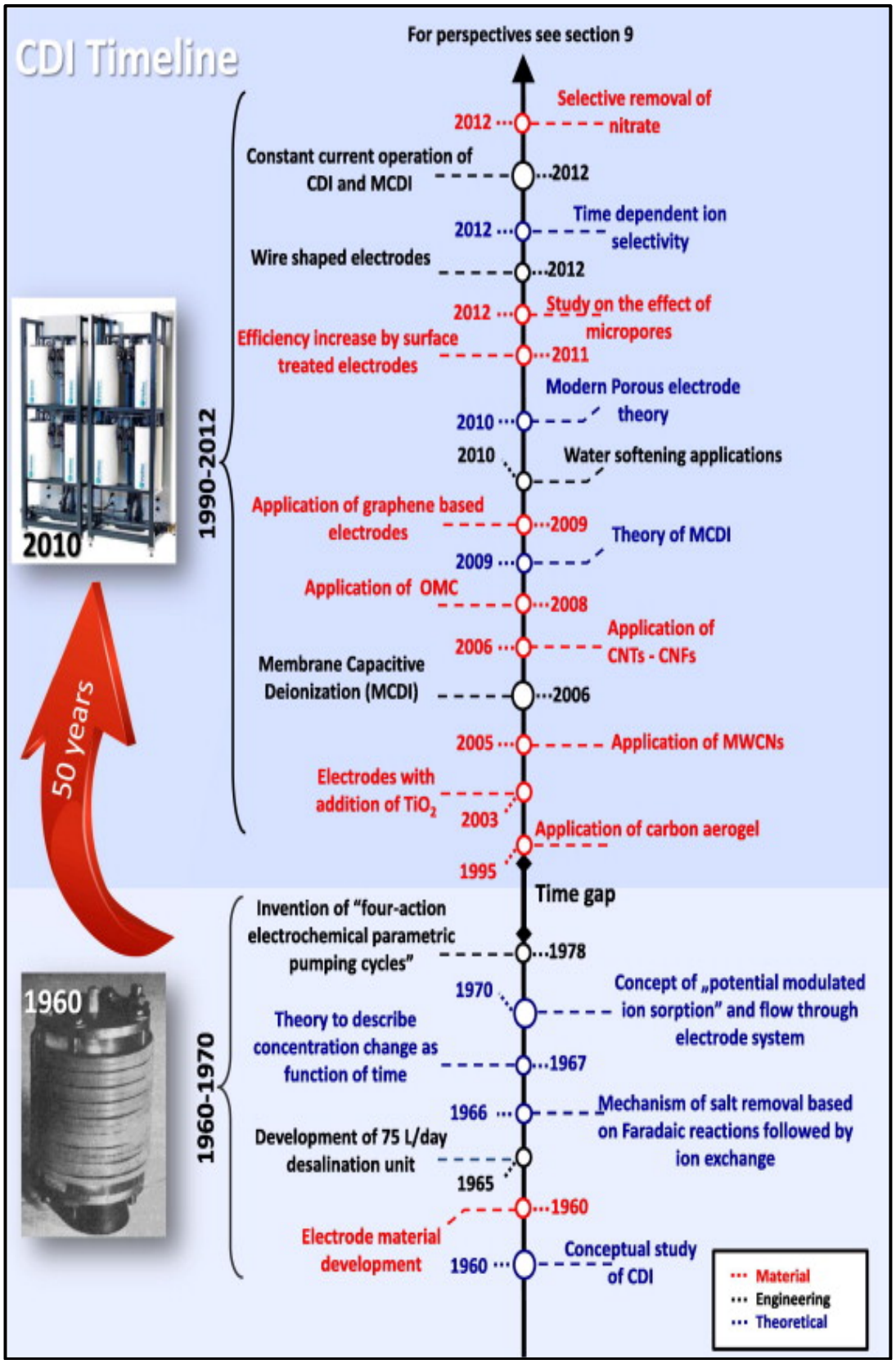

Figure 1.2: Timeline of scientific developments of CDI, indicating milestones since the inception of CDI in 1960 [42].

1.3.2 Theory of capacitive deionization

Electrochemical double layer capacitance is the phenomenon involved in the clean-up of water by a CDI system. The electrochemical double layer is formed at the electrodes and electrolyte solution interfaces on the application of a direct current. The chemical potential of negative ions and positive ions is different in polarized electrodes and electrolyte. This leads to the ions moving to the electrodes which have opposite polarity to form the first layer by electrostatic adsorption. The second layer contains less reverse charge as compared to the total charge of the first layer [11, 45]. The pores of electrodes are utilized to store ions, and fresh water is obtained when voltage is applied, as Figure 1.3 (a) shows [11, 45]. The number of ions that are moved and adsorbed to the electrode surface gradually decreases during the operation cycle [43, 45], because electrodes are saturated with salts or impurities[34]. Electrodes are regenerated by eliminating the electric field, as Figure 1.3 (b) shows. This leads to the adsorbed ions being desorbed from the surface of the electrodes. In addition to the electrostatic attractive force, Faradaic reactions between the dissolved impurities and the electrodes also contribute to the separation mechanisms of the electrodes [34]. In a classic parallel plate capacitor, charge separation is electrostatic. Capacitance scales directly with the area of the plates and the inverse distance of separation as shown in Equation (1.1).

$$C = \varepsilon_r \varepsilon_0 \frac{A}{D} \qquad \textbf{(Eq 1.1)}$$

where C is the capacitance in farads (F); A is the area of each plate in a traditional capacitor (usually metal) in square metres (m^2); ε_r is the relative static permittivity (sometimes called the dielectric constant) of the material between the plates, (vacuum =1 F/m), ε_0 is the permittivity of free space (8.854×10^{-12} F/m) and D is the separation between the plates in metres (m).

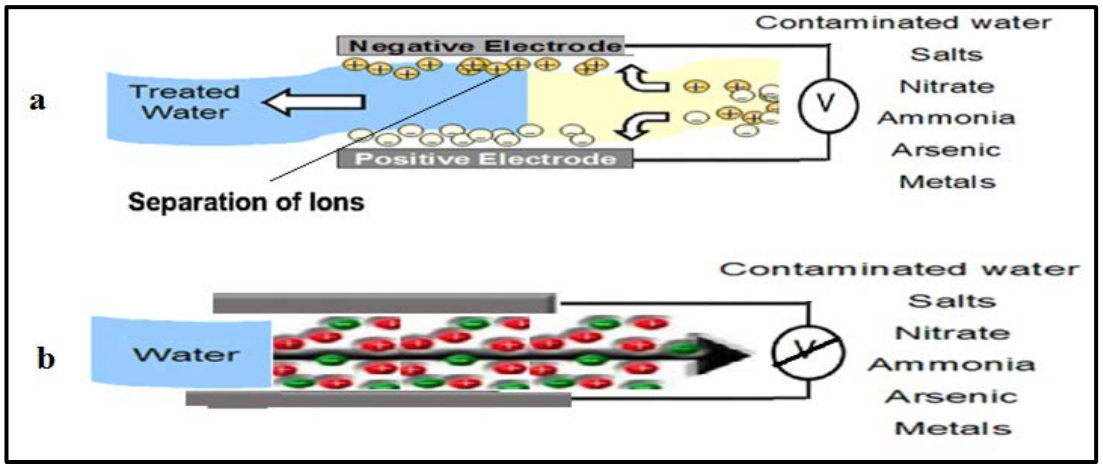

Figure 1.3: (a) Electrosorption of ions on application of a potential and (b) desorption of ions on removal of potential.

1.3.3 Capacitive deionization cell

A CDI cell consists of two electrodes that are placed face to face at both sides of a spacer which allows for aqueous solution to stream through it. These electrodes can be called anode and cathode and can be made out of any material, not necessarily only metals [11]. Membrane is used as a separator between the two electrodes in a CDI cell to prevent an electrical short and to maintain a constant distance [5]. Also a CDI cell includes: conductivity probes in the inlet and outlet lines which are used to measure solution conductivity [11], a voltmeter and an ammeter which are used to measure the electrical data required to determine energy consumption [11]. Moreover, the cell has two current collectors [35]. The graphite foils are used as inert current collectors on the back side of the electrodes [35, 36]. Aqueous solution is pumped in by a peristaltic pump from the bottom and drained off the top of the unit [35, 36]. The CDI unit, as illustrated in Figure 1.4, has been identified as a potential mass desalination alternative under laboratory conditions by the Lawrence Livermore National Laboratories[11], and it usually is modified by researchers to suit their applications [5, 11, 34-39, 41, 43, 44, 46-52].

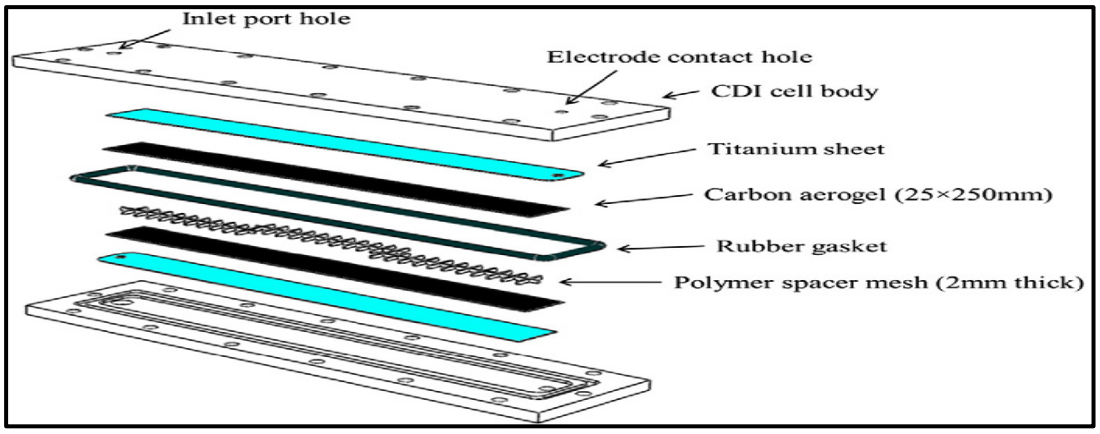

Figure 1.4: Schematic of the inlet and outlet fittings, electrode contact screws and mounting bolts are omitted. The two aerogels are separated by a polymer mesh and are supported by titanium electrodes on the backside to decrease contact resistance. A rubber gasket is seated in a separate channel outside the test section [53].

1.3.4 Electrode evaluations

There are two kinds of testing; one of them to evaluate the capacitive behaviour of the electrode materials and the other to evaluate the electrosorption capacity in a capacitive deionization unit. The capacitive behaviour of a capacitive electrode material is studied by ac impedance spectroscopy and cyclic voltammetry (CV) [33]. Other characterizations include: optical absorption spectra by Raman, Visible, Fourier Transform Infrared (FT-IR), and X-ray photoelectron studies (XPS) [54]. In addition, electrode surface morphology can be studied by scanning electron microscopy (SEM) and atomic force microscopy (AFM) [55]. The electrosorption capacity of electrodes are discussed in more detail in Chapter 2 (2.4.4).

1.4 Electrode materials

There are six major requirements for the materials of electrodes used in a capacitive deionization (CDI) unit. They are: good polarizability, low electrical resistance, high surface area and capacitance, no participation in faradaic reactions at

the applied voltage, high porosity and conductivity [52]. This means that the correct choice of electrode material is the most critical issue for the success of capacitive deionization processes [41]. There are a number of different porous carbon materials that can be applied as electrodes in capacitive deionization (CDI); such as carbon felt [56], carbon aerogels [57] , carbon cloth [36] and titania modified carbon cloth [38, 39]. More recently carbon nanotube structures [40, 58], carbon nanfibre [33] and inherently conducting polymers such as Polypyrrole [54] have been investigated for this purpose. Figure 1.5 provides a selection of various carbon materials used for CDI applications. These materials have been deemed a good electrodes for CDI because of their easy accessibility, low cost, resistance to acidic and basic environments, low density, diverse porous structure, and other properties [59].

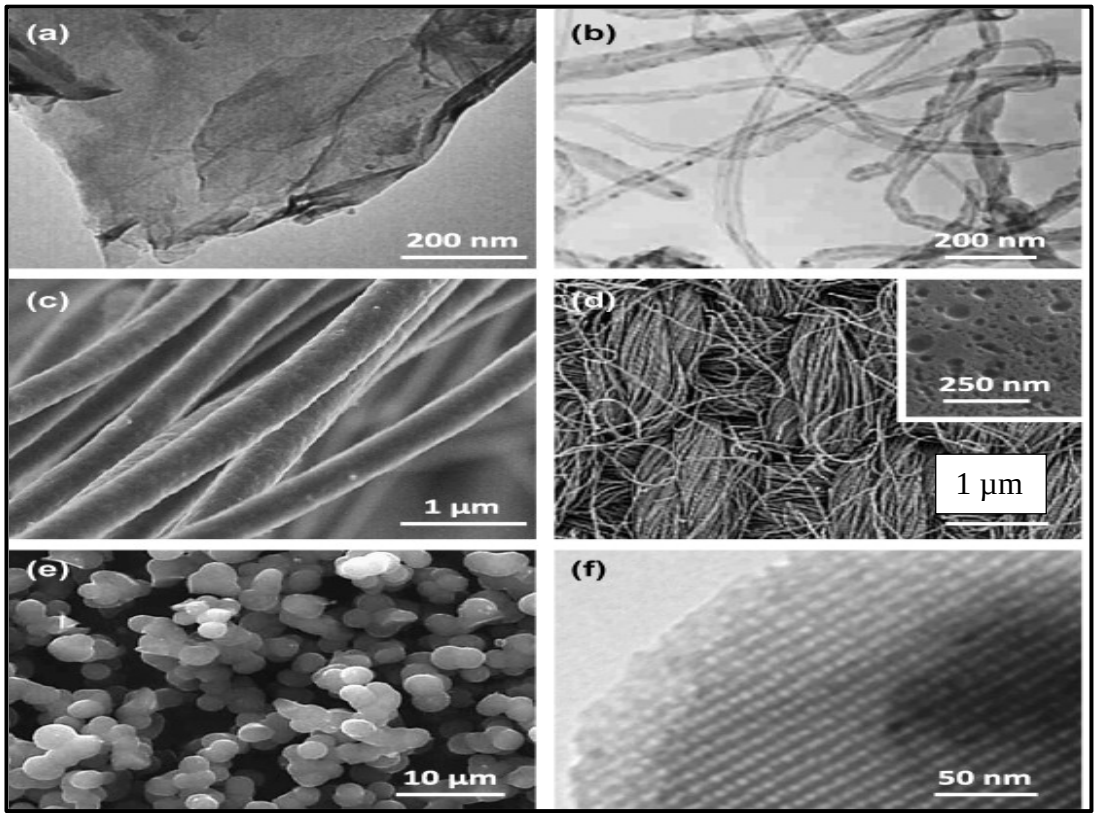

Figure 1.5: Various carbon materials used for CDI; (a) Graphene-like carbon flake, (b) multi-walled carbon nanotubes, (c) electrospun fibres, (d) activated carbon cloth, (e) carbon aerogels, and (f) ordered mesoporous carbon [42].

1.4.1 Reticulated vitreous carbon

In all the scientific chapters in this thesis, reticulated vitreous carbon (RVC) was used as substrates for active materials. The RVC electrode, which initially was designed as an acoustic isolator [60], was first developed in the mid to late 1960s as a thermally insulating, micro-porous glassy carbon electrode material [61]. It is described as a tridimensional (3D) porous structure having a honeycomb or foamy structure (Figure 1.6). Friedrich et al. [62] presented an illustrated review of RVC as an electrode material, encompassing characteristics such as a very high area: volume ratio depending on porosity grade, a low density, a low thermal expansion, a high corrosion resistance, high thermal and high electrical conductivities that are very attractive for electrochemical applications [63, 64]. Furthermore, RVC can easily be surface modified with various materials [65, 66] including conducting polymers [67-71]. In the last decades, these characteristics led to the publication of more than 200 papers on different important electrochemical applications and many other applications [72]. Examples of these applications that used RVC include those as bony prostheses [73], heart valves [74], molecular sieves [75], absorption electrode [76], cathode material in order to recover Co^{2+} ions [77], cation exchangers for the adsorption of Ca^{2+} ions from aqueous solutions[67]. It was applied in many primary and secondary battery systems [72, 78, 79], as porous cathode for the production of hydrogen gas from flowing alkaline solution [80] and viable field emission electron source [81]. Furthermore, the low density and high electrical conductivity of RVC electrodes are very attractive for electrochemical applications as three-dimensional electrodes [10]. The structure of RVC lends itself to easy surface modification with various materials [65, 66]. Also, the electrochemical deposition of conducting

polymers on carbon substrates has been studied with the goal of improving the mechanical properties of these polymers so as to use them as electrodes in different applications: batteries, sensors, capacitors or electro-chromic displays [67-71, 82-85]. Primary applications of RVC electrodes include: filters, chemical absorbers, molecular sieves, membranes, catalysts and catalyst supports, chemical hardware, mechanical seals, bearings, electrical devices, dental and surgical prosthetic devices and other implants, thermal insulators, lightweight structural elements and structural matrices for composites [86].

Despite, 3D RVC electrode does not has a significant surface area comparison with several other carbon materials such as activated carbon (AC), activated carbon nanofibre web (ACF) [265], carbon nanotubes (CNT) [321], composite carbon nanotubes with carbon nanofibre (CNT/CNF) [322], reduced graphite oxide (rGO) [320], and carbon aerogels (CA) [50] that have been studied as 3D CDI electrode materials, it will be the best 3D electrode can be working as 3D templates for all materials which will be used in this thesis. This because that the RVC electrode has an amazing properties cannot be available in others 3D electrodes such as reduce the resistance of solution flow through the electrode, increase the stability of composite electrode towards high flow-rate pressure, increase the possibility of ions to reach all electrode surfaces in a short time for electrosorption, and shorten the time of ions release from the electrode surface.

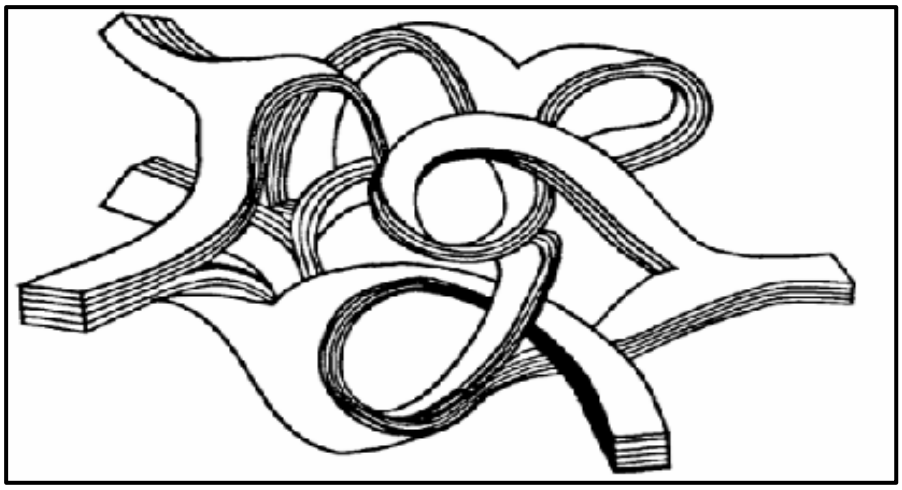

Figure 1.6: Schematic model of the structure of reticulated vitreous carbon [87].

1.4.2 Intrinsically Conducting Polymers

Intrinsically Conducting Polymers (ICPs) are organic polymers that are light weight, corrosion resistant, easily processed, and conduct electricity. In the late 1970s, Alan Heeger, Alan MacDiarmid and Hideki Shirakawa performed studies that led them to discover that polyacetylene films which are prepared by polymerizing the acetylene in the presence of a Ziegler catalyst are conductive. During this method a redox reaction occurs between the conjugated system and the doping agent [88, 89]. This discovery received tremendous interest among material scientists. Therefore in 2000, these three brilliant scientists were jointly awarded the Nobel Prize in Chemistry for the discovery of conducting polymers [90-93]. Polyaniline (PANi), polypyrrole (PPy) and polythiophene (PTh) (Figure 1.7) are further examples of polymeric conductors [94, 95]. It is interesting to note that these polymers in their neutral state are insulators and that the introduction of electron acceptors/donors by a process known as ‘doping’ causes them to revert to the conducting state [91, 92]. They have received extensive attention in recent years due to their excellent

electrical conductivity, chemical or electrochemical redox reversibility and good environmental stability [54, 96, 97]. They can display properties which were previously only thought to exist as metallic properties such as: magnetic, optical and, the vital one, electrical properties [98]. They can be distinguished by the presence of alternating double and single bonded sp^2 hybridized atoms. Many studies have shown that, due to this conjugation process, the molecule is able to form a planar conformation. This conformation allows the electrons in the π molecular orbitals to overlap which plays a crucial role in the formation of the conductive properties [94, 99].

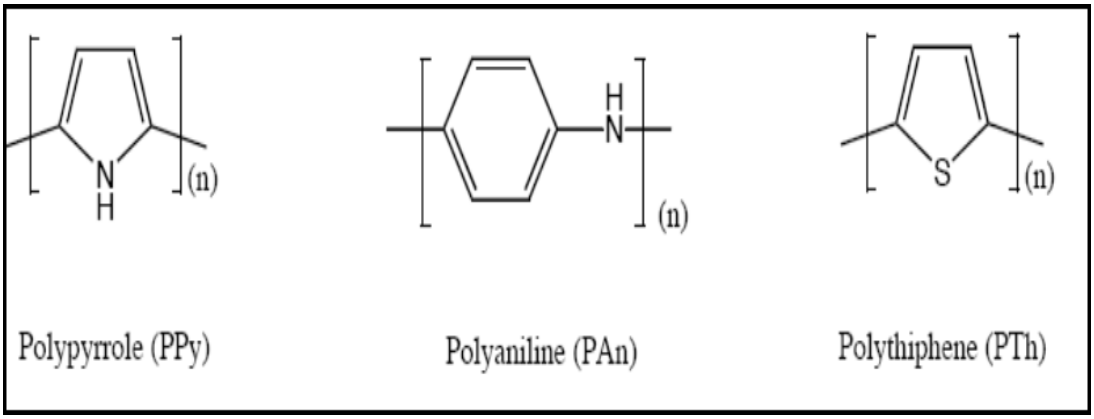

Figure 1.7: The chemical structure of conducting polymers: polypyrrole, polyaniline and polythiophene, where n indicates the number of repeat units [100].

1.4.2.1 Poly (3,4-ethylenedioxythiophene), "PEDOT".

During the last 15 years ICPs have transitioned from being laboratory materials to mature industrial products. Polythiophenes (Pth) are one prominent class of ICPs presently in the market and Poly(3,4-ethylenedioxythiophene) , which is abbreviated to PEDOT or PEDT, invented in the second half of the 1988s by Bayer in Germany, is one of the polythiophene derivatives and has the backbone structure

shown in Figure 1.8 [101]. It was prepared using standard oxidative chemical or electrochemical polymerization methods based on oxidising 3,4-ethylenedioxylthiophene (EDOT) monomer in the presence of polystyrene sulfonic acid (PSS) or perchlorate (ClO_4) as a dopant (Figure 1.8) [102, 103]. Previous studies have shown that the doping ion used in the fabrication of PEDOT-based sensors has an important effect on the analytical performance of the sensors [104]. Patra et al. investigated the effect of electrochemical routes on morphology and microstructure of PEDOT [105]. When PEDOT films were prepared at low current, low potentials and low potential ranges, the PEDOT surface morphology was essentially globular, whereas the morphology became porous at higher current densities and higher potentials of preparation. However, in the case of potentiodynamic preparation the morphology turns out to be rod-like and fibrous as shown in Figure 1.9.

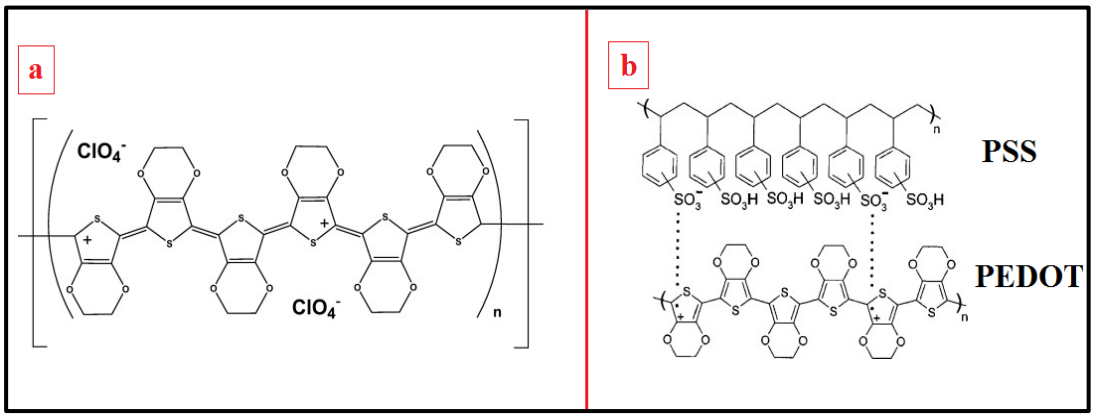

Figure 1.8: Molecular structure of (a) PEDOT-ClO_4 and (b) PEDOT-PSS polymers [102, 103].

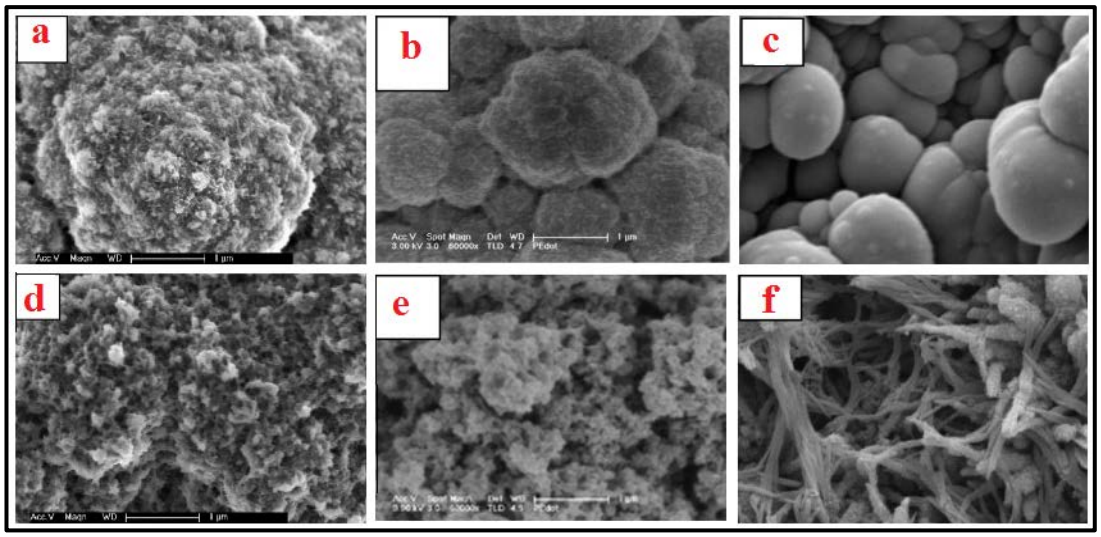

Figure 1.9: The scanning electron micrographs of PEDOT electrode prepared by galvanostatic method at a fixed current of (a) 0.5 and (d) 2 mA cm^{-2}; prepared potentiostatically at (b) 0.90 and (e) 1.2 V; and prepared by cyclic voltammetry with sweep rate of 10 mV/s in the potential range of (c) 0–0.9 and (f) 0–1.2 V vs. SCE [105].

PEDOT is probably the best conducting polymer available in terms of: remarkably high conductivity (300 S/cm [106, 107]) that does not change appreciably when heated at 100^0C for up to 1000 hours, low cost, suitable morphology, fast doping/undoping mechanism, superior thermal and electrochemical stability, charge capacity, low interface impedance, biocompatibility. In addition, it has low elastic modulus (between 1 to 2.7 GPa) [108], easy processability, high stability in the oxidized state and relative insensitivity to pH changes, high visible light transmissivity (band gaps ranging from 1.4 to 2.5 eV), and can be stored under ambient conditions without affecting its stability [109-113].

In addition, a high specific capacity from PEDOT was obtained, 691 mAh/g [114], which was higher than other conducting polymers, such as polyaniline (PAni) , polypyrrole (PPy), Polypropylene (PPP), polythiophene (PTh) and polydithieno

(3,2- b;2',3'-d)thiophene (PDTT) [106, 114, 115] and its specific capacitance in 1 M $LiClO_4$ solutions using three-electrode systems at the scan rate of 5 mV/s was about 110 F/g [116]. Furthermore, PEDOT is one of the conducting polymers that are commercially produced on a large-scale and sold for many potential applications in the domain of composite materials, solid electrolyte capacitors, tissue engineering, ink-jet printing, light emitting diodes, actuator, antistatic coatings, organic solar cells, supercapacitors which includes electrochemical double layer capacitors (EDLCs) and redox or pseudo-capacitors, electronic, electro-optic devices and organic field-effect transistors [102, 109, 117-120].

PEDOT has been regarded as a promising pseudo-capacitive material due to its fast charge–discharge kinetics and stores charge not only in the electrical double layer but also throughout the body of the polymer by rapid faradaic charge transfer. However, the redox reaction in pseudo-capacitors is a slower process compared with the double layer process in EDLCs and, hence, the pseudo-capacitor has lower charge/discharge performance than an EDLC capacitor. [121, 122]. Thus, the use of PEDOT for redox supercapacitors has several advantages comparing with metal oxide systems and EDLC. Therefore, many researchers have studied PEDOT as an electrode material for supercapacitors having high energy and power density [112, 123-125]. It should be noted that PEDOT, reported in the PEDOT/carbon composite electrodes for supercapacitors, was synthesized in-situ on carbon materials by electrochemical or chemical-polymerization from EDOT [126]. The electrochemical deposition of conducting polymers on carbon substrates has been studied with the goal of improving the mechanical properties of these polymers [82-84]. It is worth mentioning that several researchers have shown that the combination of rod-like

manganese oxide (MnO) with PEDOT, can further increase the specific capacitance values of MnO from 185 to 285 F/g using a potential scan rate of 20 mV/s in Na_2SO_4 and improve cycling retention [127].

PEDOT has been studied extensively in recent years for a bioactive coating for the electrode sites of chronic neural implants and other biostimulation devices, [128] and for electrochromic devices and electrodes [129]. PEDOT easily forms thin films with a high transparency in excess of 80% and it is generally used with PSS [101, 130]. PEDOT was also used to modify insulating substrates which leads to the formation of flexible and transparent devices that are of great interest for many applications such as plastic electronics, sensors, photovoltaic systems and molecular electronics [131]. In this thesis, PEDOT will be electrodeposited on RVC foam for use as electrodes in a capacitive deionization system. These electrodes will be further optimized by tuning the experimental parameters, such as film growth rate, film thickness, film capacitance, and electrosorption and desorption conditions in NaCl salt solution.

1.4.3 Carbon nanotubes

Carbon nanotubes (CNTs) were accidentally discovered in 1991 by a Japanese scientist, Iijima, using an arc-discharge process [132]. He observed during his experiment by using high-resolution transmission electron microscopy that graphite nanotubes were being deposited on the cathode of the arc discharge apparatus as several layers of cylindrical carbon structures which were identified as multi-walled carbon nanotubes (MWCNTs). In early 1993, single-walled carbon

nanotubes (SWCNTs) were independently discovered by scientists at IBM Almaden Research Center in USA and at NEC in Japan. They found that transition metals co-vaporized with carbon catalyse, cobalt was used at IBM and iron at NEC, the formation of SWCNT with a narrow range of diameters of around 1 nm [133, 134]. The graphene sheets rolled up into a cylindrical shape is made up of planar parallel sheets of carbon atoms arranged in hexagonal aromatic rings, which are covalently bound by sp^2 hybridisation [135]. Individual CNT can be either conducting or semiconducting as a result of the orientation of the graphene sheets in the CNT structure, depending on its chiral vector ($\mathbf{C_h}$), where n and m are two integers [136]. Figure 1.10 (b) shows three different orientations: zigzag nanotube when $m = 0$; an armchair nanotube results when $n = m$; and chiral nanotubes arise when $n \neq m \neq 0$ [137]. The length and direction of the chiral vector will clearly influence the diameter of nanotubes and hence influence their properties including conductivity and density [138]. The diameter of the SWCNTs and MWCNTs (Figure 1.10 (a)) are between 0.7 - 2 nm and 10 - 300 nm, respectively, and the length can approach the macroscale [139]. Moreover, CNTs have many impressive characteristics such as high electrical conductivity, mechanical strength, optical transparency and thermal stability [136, 140]. These properties have attracted great attention, produced significant activities, and opened a new window in many areas of science and engineering [136, 137, 141, 142].

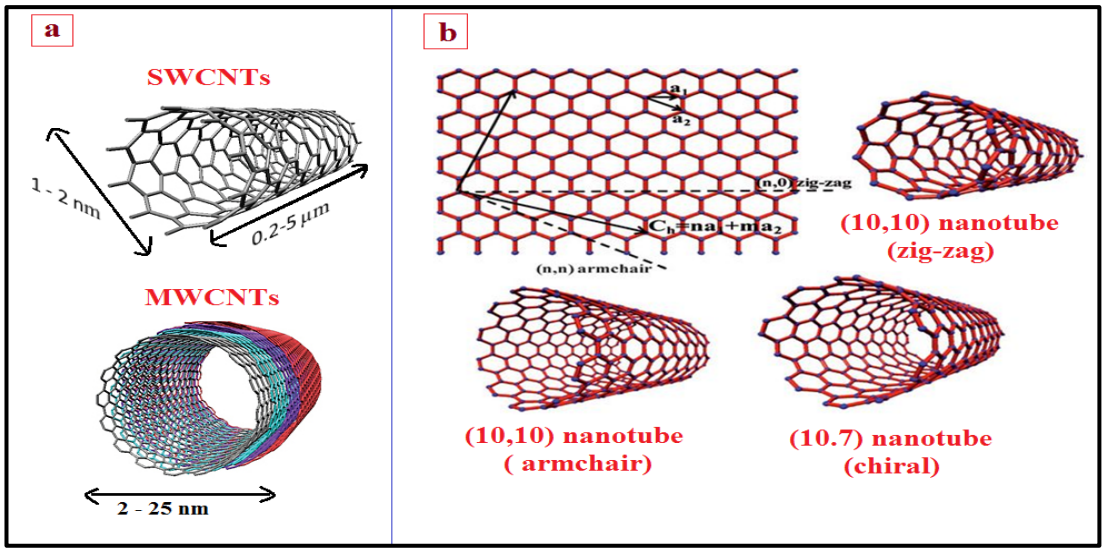

Figure 1.10: Schematic diagram of (a) single-walled carbon nanotube (SWCNT) and multi-walled carbon nanotube (MWCNT), and (b) how a graphene sheet is rolled to form a CNT [143, 144].

1.4.3.1 Properties of carbon nanotubes

Several physical properties of CNTs are of particular importance for capacitive deionization application, i.e. electrical conductivity, thermal conductivity, surface area and mechanical strength. The impressive properties of CNTs have extended their implications for science well into the 21st century. CNTs are one of the strongest materials in the world with elastic modulus reaching to 1 terapascal (TPa) and strength between 50 to 100 gigapascal (GPa) [145]. These extraordinary mechanical properties make them theoretically at least 100 times stronger and 5 times lighter than an equivalent weight of the strongest steel [146]. The mechanical properties of CNTs were affected by the diameter of CNTs and the temperature at synthesis [146, 147]. For example, when the diameter of CNTs are increased from 3 to 20 nm, the elastic modulus is dramatically decreased from 1 TPa to 100 (GPa) and at low temperature, brittle CNTs were produced [148, 149]. CNTs have also

demonstrated high thermal conductivity compared to other high thermally conductive materials such as copper [150]. Kwon et al. predicted that the thermal conductivity can reach up to 6600 W/mK [151]. Recent measurements attained about 3000 W/mK for MWCNTs [152] and above 2000 W/mK for SWCNTs [153, 154]. As described in Section (1.3.2.), CNT shells can be either metallic or semiconducting in nature, depending on their chirality and their conformation. Durkop et al. and Yao et al. have reported that, CNTs have carrier mobility of 10^5 cm^2/Vs and current carrying capacity of current density capabilities of 1×10^9 A/cm^2 [155, 156]. The CNTs could replace copper wire for electricity transport because its electrical conductivity is higher than copper [142]. Furthermore, the electrical resistivity of CNTs can reach to 10^{-6} Ωm [136]. In addition, it is possible to increase the electrical conductivity of CNTs from 300 S/m to 1600 S/m by incorporating CNTs into conductive polymers (CPs) such as polypyrrole (PPy) [157].

1.4.3.2 Applications of carbon nanotubes in water purification

The above characteristics make CNTs an ideal case for real world applications including electrical field emission, conductive and mechanically reinforced plastics, energy storage, field effect transistors, flexible transparent electrodes, solar cells, medical applications, water desalination and capacitive deionization [136, 140, 143, 146, 158-165]. The application of CNTs membranes has impact in the area of water technology development with their ultra-high water flux and low biofouling potential. CNT membranes are believed to lack various problems encountered when using conventional membrane separation processes that require a large amount of energy and meticulous maintenance [164, 165]. In

addition, CNTs were used as electrodes in CDI systems. Experimental data fit well with the Langmuir model, and the deduced maximum desalination capacity was 40 mg/g [166]. It was improved by compositing it with polyaniline (PAni). The composite electrodes showed a higher ion electrosorption capacity than those made from SWCNTs alone, and the composite electrodes can be easily regenerated, indicating excellent recyclability [163]. CNTs materials also were composited with graphene to increase performance of the CDI system as reported by Zhang et al. [167]. The composite electrodes exhibit excellent desalination behaviour, which is attributed to the improved electrical conductivity and higher accessible surface area, which are quite beneficial for the electrosorption of ions onto the electrodes.

1.4.4 Graphene oxide

Graphene is the name given to a single atomic layer of sp^2 carbon atoms tightly packed into a two-dimensional (2D) honeycomb lattice, and is a basic building block for graphitic materials [168, 169] as shown in Figure 1.11. The theory behind graphene was first introduced by theoretical physicist Philip Wallace in 1947 [170] and was then further explored by Hanns-Peter Boehm, who described single layer carbon foils in 1962 [171]. Graphene sheets are estimated to have microscopic corrugations with a lateral dimension of about 8 to 10 nm and a height displacement of about 0.7 to 1 nm [172, 173]. Common methods used to produce pristine graphene, such as by Geim, Novoselov et al., include using Scotch tape to peel off a single or a few layers of graphene sheets from bulk graphite [174]. Alternatively, one of the most efficient methods for producing graphene-like structures in high

quantities and low cost is the chemical reduction of graphene oxide (GO) [175], whereas chemical vapour deposition (CVD) is used to produce thin and continuous graphene films of larger size [176]. Graphene has recently been attracting tremendous attention within the scientific community owing to its unique properties such as large theoretical specific surface area (2630 m^2/g), high intrinsic mobility (200,000 cm^2/vs) [177, 178], high Young's modulus (1 TPa) [179] and thermal conductivity (~ 5000 W/mK), [180] and its optical transmittance (97.7%) and good electrical conductivity [181, 182]. Various applications for graphene have been reported; such as for catalytic electrodes in fuel cells [183], transparent electrodes in solar cells [184], supercapacitors [185] as well as electrodes in sensors [186] and transistors [187].

Graphene oxide (GO) is a single-atomic-layered material made by oxidizing graphite crystals which is available in large quantities at inexpensive prices. Structurally, the graphene oxide is similar to a graphene sheet with its base having oxygen-containing groups (Figure 1.11). Since these groups have a high affinity to water molecules, it is hydrophilic and can be easily dissolved in water and other solvents [188]. Graphene Oxide, which is a poor conductor, is formed by oxidizing crystalline graphite with a mixture of sodium nitrate, sulfuric acid, and potassium permanganate [189]. The oxidation method is also known as the Hummers method [190]. It has been reported that reducing GO films provides an alternative approach to obtaining highly conductive reduced graphene oxide (RGO) films. Thermal annealing and hydrazine vapour reduction of GO are the two most commonly used methods to directly obtain the most graphene properties [189, 191].

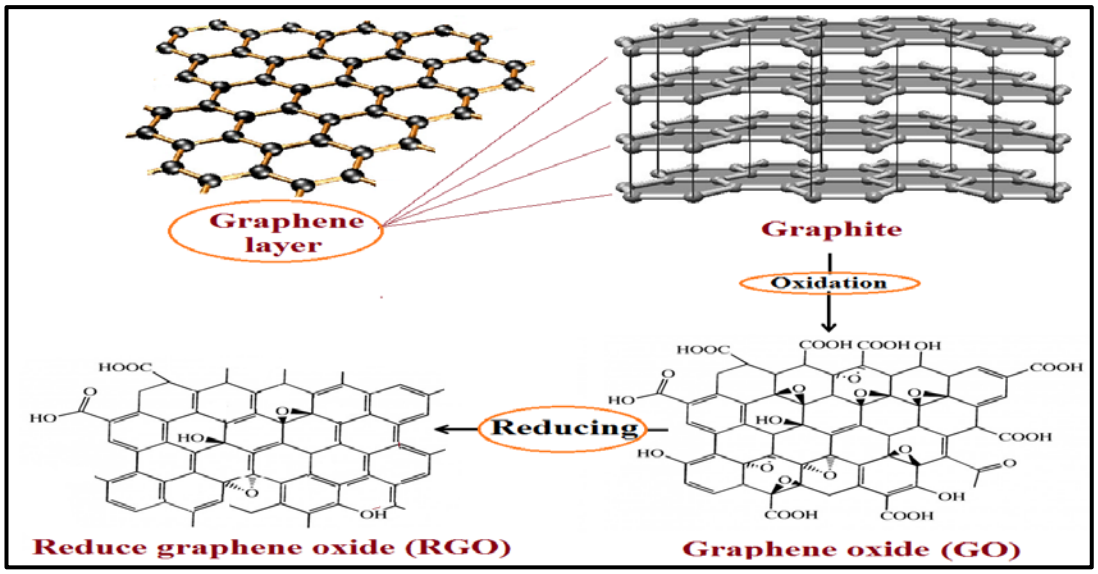

Figure 1.11: Scheme showing a graphene, graphite, graphene oxide (GO) and reduce graphene oxide (RGO) structures.

1.4.4.1 Synthesis of graphene oxide (GO).

The most common approach to graphite exfoliation is the use of strong oxidizing agents to produce graphene oxide. The first production of graphene oxide was demonstrated by Oxford chemist Brodie in 1859 who added a portion of potassium chlorate ($KClO_3$) to a slurry of graphite in fuming nitric acid (HNO_3) [192]. Later in 1898, Staudenmaier improved Brodie's technique by using concentrated sulphuric acid (H_2SO_4) as well as fuming nitric acid and adding the potassium chlorate in at intervals during the course of reaction [193]. This small change in the procedure made the production of highly oxidized GO during roughly a week. In the 1950s, Hummers reported the method most commonly used today with minor modifications for GO production that could be done in roughly 2 h and at lower temperatures [190]. In this approach, the graphite is oxidized by treatment with a mixture of potassium permanganate ($KMnO_4$) and sodium nitrate ($NaNO_3$) in concentrated H_2SO_4. Hydrogen peroxide (H_2O_2) is then added to decompose excess

permanganate ions which can act as contaminants in the form of manganese ions Mn^{4+} [194, 195]. It should be noted that all previous procedures presented hazards due to the formation of toxic NO_2, N_2O_4 and / or ClO_2 gas which the latter can combust in air. Luo et al. demonstrated that pre-exfoliation of graphite via microwave heating helped to remove intercalated species and improved oxygen absorption in subsequent Hummers processing [196]. In 2010, Marcano et al [197] described an alternative approach to producing graphene oxide that has significant advantages over the Hummers's method; with improved efficiency of the oxidation process and no toxic gas produced during the chemical reactions. The protocol for running this reaction consisted of the exclusion of the use of sodium nitrate ($NaNO_3$), increasing the amount of potassium permanganate ($KMnO_4$) used and performing the reaction in a 9:1 mixture of H_2SO_4/H_3PO_4. In our laboratory in the Intelligent Polymer Research Institute (IPRI) ,University of Wollongong, Antiohos et al. used microwave irradiation for a few seconds to exfoliate the GO which modified the method by Marcano [198]. This small added step after the procedure significantly altered the structure resulting in a highly porous interconnected network with minimal re-stacking of the graphene. The XRD confirms the exfoliation of the GO due to the significant decrease of the sharp peak at $2\theta = 10.2°$; while XPS spectra confirms that reduction of the GO is apparent due to the much sharper C-C at 284.4 eV peak with the relative abundance of C and O increasing to 92.22% and 7.53% respectively. The G/D band ratio of the Raman spectra also increased from 0.8 to 0.9 signifying that the conductivity of microwave irradiated GO has been increased. Figure 1.12 shows the scanning electron microscopy (SEM) images (a and b), Raman

spectra (c), and XRD spectra (d) of GO and mw rGO powder before and after microwave irradiation.

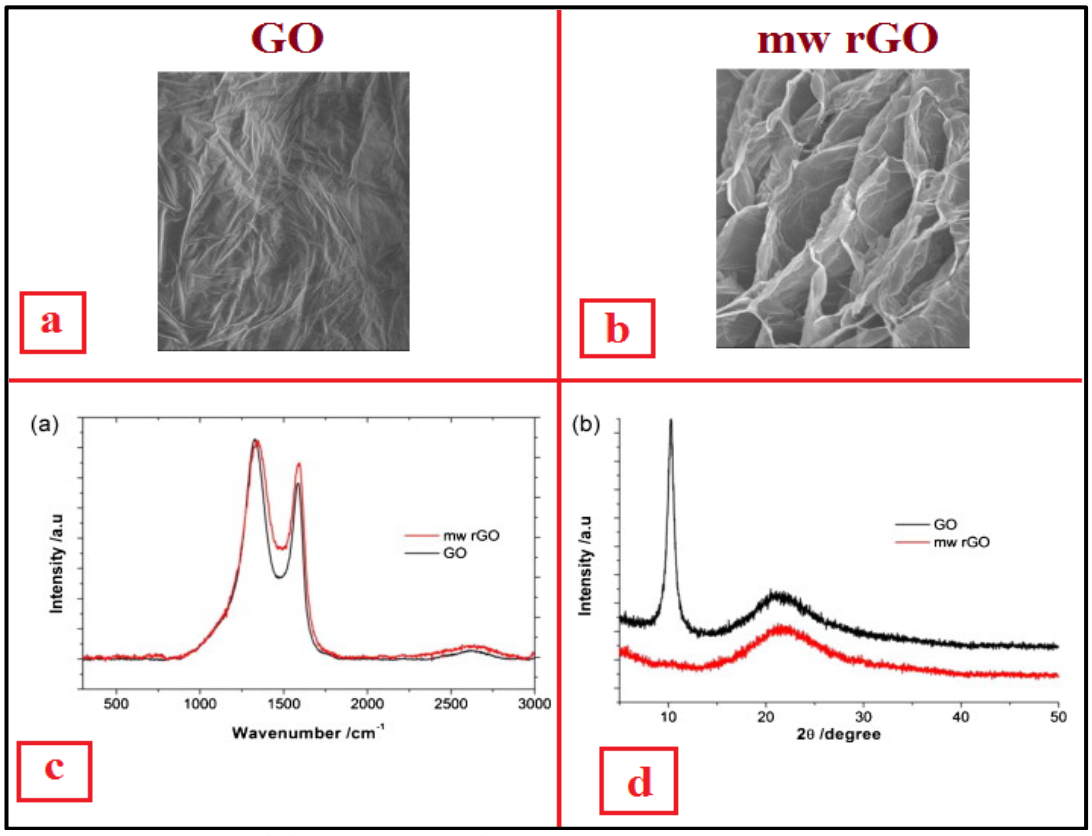

Figure 1.12: (a and b) scanning electron microscopy (SEM) image, (c) Raman spectra and (d) XRD spectra of GO and mw rGO powder before and after microwave irradiation [198].

1.4.4.2 Application of reduced graphene oxide in capacitive deionization (CDI).

Graphene as a newly found carbon material has become one of the most attractive subjects due to several breakthroughs in fundamental research and some promising practical applications [166, 194, 199-205]. It has a huge theoretical specific area of 2600 m^2/g [206] besides an excellent electrical conductivity as high as 7200 S/m at room temperature [207]. In addition, the interlayer spacing in a

graphene oxide electrode (more than 0.625 nm) allows the hydrated Na^+ ion, which has a radius of 0.358 nm, to enter into the electrodes [197]. These intriguing properties enable graphene to be used as a feasible electrode material for capacitive deionization (CDI). Li, et al. have pioneered the application of graphene as an electrosorption electrode for capacitive deionisation (CDI) for the first time in 2009 [208]. The graphene was fabricated by a modified Hummers method followed by a hydrazine reduction process, and was employed as the electrode for an electrosorption application. Batch-mode electrosorption experiments with good repeatability in NaCl solutions were conducted. It was found that higher ion removal is achieved with a higher applied voltage 2.0 V with the volume flow-rate of 40 ml/min. The results show that the graphene exhibits a high specific electrosorption capacity of 1.85 mg/g using 22.5 mg/L and of 22.04 mg/g using 490 mg/L. In 2010, graphene-like nanoflakes (GNFs) with relatively high specific surface area (222.01 m/g) have been prepared and used as electrodes for capacitive deionization (CDI) [209]. The GNFs were also synthesized by a modified Hummers' method using hydrazine for reduction. The results showed that the specific electrosorption capacity of the GNFs was higher than that of previously reported data using graphene under the same experimental conditions. In 2012, Li, et al. have used reduced graphene oxide (rGO) nanoflakes to enhance the specific capacitance of activated carbon (AC) [210]. It was synthesized using 20 wt% graphene by a facile chemical method. The best electrochemical performance of this composite electrode gave a specific capacitance of 181 F/g which is much higher than the AC electrode 67 F/g. The electrosorption capacity of the composite electrode became nearly twice as large as that of the AC electrode, indicating that rGO can serve as a flexible bridge to form a

‘‘plane-to-point’’ conducting network, which is beneficial for decreasing the aggregation of AC particles, and improves the electron transfer within the composite electrode. It is also higher than that for rGO nanoflakes electrode, indicating that the introduction of rGO is beneficial to enhancing the electrosorption of AC. Furthermore, Li, et al. have used rGO nanoflakes to enhance the specific capacitance of carbon nanotubes (CNTs) [211]. It was synthesized using 10 wt% graphene by a facile chemical method. The best electrochemical performance of this composite electrode gave a specific capacitance of 311 F/g which is much higher than the CNTs electrode (202 F/g) in 1M NaCl solution at a scan rate of 10 mV/s. The electrosorption capacity of composite and CNTs electrodes using 25mg/L NaCl solution were nearly the same; 0.88 and 0.87 mg/g, respectively. The conditions used were 1.6 V and 25 ml/min volume flow-rate but the time of electrode saturation in a single adsorption cycle decreased to half in the composite electrode compared with the CNTs electrode which took around 1 hour. In 2013, Wimalasiri and Zou made graphene electrodes for CDI, using a modified Hummers method as outlined by Marcano et al., and then 9 wt% of SWCNT was combined with GO nanosheets as shown in Figure 1.13 (a), not only to increase the interlayer distance, but to contribute to the overall surface area and conductivity of the active material [212]. The specific surface area of graphene and the CNTs/rGO composite was 362 and 391 m^2/g, respectively, and the mean pore diameter of graphene increased from 4.38 nm to 5.0 nm of the CNTs/rGO composite. Moreover, the specific capacitance of the CNTs/GO composite increased to 220 F/g at 5 mV/s scan rate from 140 F/g for graphene electrode in 1M NaCl solution. Furthermore, the electrosorption capacity of the CNTs/rGO composite was 26.42 mg/g, which was comparatively higher than

graphene at 22.27 mg/g using NaCl solution with an initial concentration of 780 mg/L, volume flow-rate of 25 ml/min and 2.0 V cell voltage. In addition, the CNTs/rGO composite-based electrodes demonstrated considerably faster salt adsorption and desorption cycles within an average of 62 min compared with graphene-based electrodes, which required 112 min, for a single adsorption and desorption cycle as shown in Figure 1.13(b).

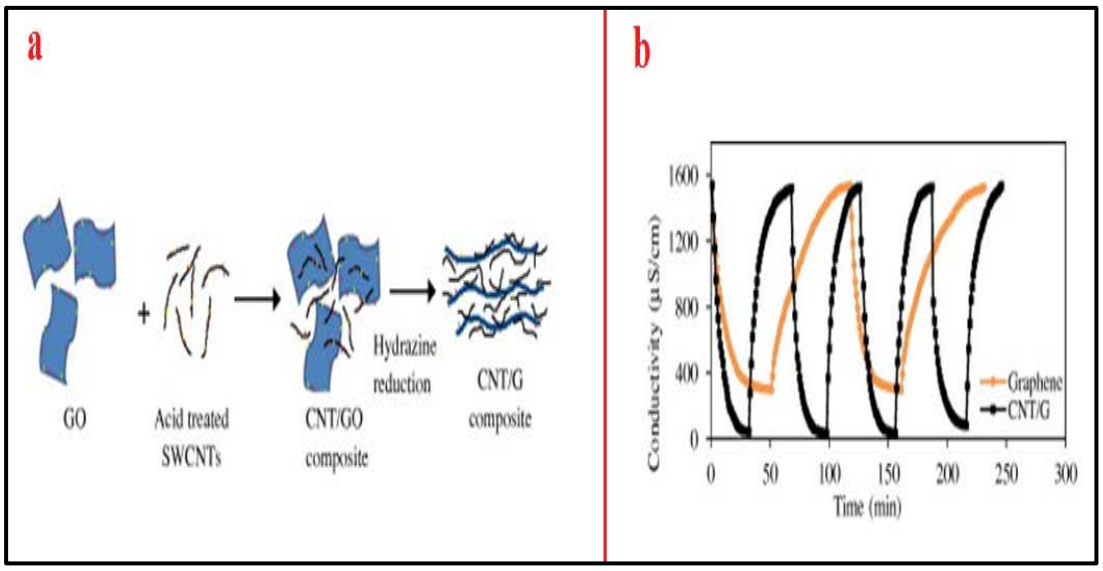

Figure 1.13:(a) Illustration of the CNT/rGO composite preparation process and (b) the CDI performance of graphene and the CNT/rGO composite using a 780 mg/L NaCl solution [212].

1.5 Aims of thesis

The scope of this thesis encompasses work to increase potable water production using the capacitive deionization (CDI) system as an eco-friendly and high energy efficient desalination. It was done by making 3D nanostructured electrodes and changing the direction of solution flow in a flow-through cell in the CDI system.

The specific aims of this research include:

- Use RVC for the first time as the substrate in a CDI system to reduce the resistance of solution flow through the electrode, increase the stability of composite electrode towards high flow-rate pressure, increase the possibility of ions to reach all electrode surfaces in a short time for electrosorption, and shorten the time of ions release from the electrode surface.
- Build 3D PEDOT microstructure electrodes, 3D nanoweb CNT electrodes and 3D hierarchical CNT/graphene electrodes for the first time in CDI technology then test the electrosorption performance of all electrodes.
- Improve the performance of a CDI system in terms of geometric volume and area.
- Design and make a simple flow-through cell that direct solution flow between electrodes in a CDI system then improve it using the concept of directing flow through the electrodes in a CDI system.

2 EXPERIMENTAL TECHNIQUES

2.1 Introduction

This chapter describes all of the techniques and instruments employed for the whole thesis that are involved with synthesis, characterization and applications as follows:-

- Synthesis and characterization of PEDOT coated RVC electrodes by electropolymerization methods (Chapter 3).
- Fabrication of a flow-through cell for a CDI system that allows solution to flow between electrodes (Chapter 3).
- Functionalization of commercial SWCNT by acid treatment (Chapter 4).
- Preparation of a-SWCNT coated RVC electrodes and their characterization (Chapter 4).
- Fabrication of another flow-through cell for the CDI system to allow solution to flow directly through the electrodes (Chapter 4).
- Synthesis and characterization of graphene oxide (GO) prepared from graphite (Chapter 5).
- Synthesis and characterization of reduced graphene oxide (rGO) prepared from GO (Chapter 5).
- Prepared composites of rGO with a-SWCNT then coated them on RVC electrodes and characterize them (Chapter 5).
- Testing of all composite electrodes prepared in a CDI system (Chapter 3, 4 and 5).

Specific experimental conditions relevant to each of the chapters above are provided in the respective Experimental sections within each Chapter.

2.2 Methods of synthesis and preparation of materials

The key components of this thesis are the use of PEDOT for the first time in a CDI system, the reduction of the resistance of SWCNT by functionalizing it by acid treatment, and the enhancement of its properties by forming composites with rGO.

2.2.1 Reagents and materials

The reagents and materials used in the work of this thesis are given below.

Reagents and materials	Grade/Purity	Supplier
3,4-Ethylenedioxythiophene monomer (EDOT)	99.9%	Sheng Chemical Ltd
Acetonitrile (ACN)	AR grade	Sigma-Aldrich
Lithium perchlorate ($LiClO_4$)	AR grade	Sigma-Aldrich
Nitric acid	70%	Sigma-Aldrich
Sodium chloride (NaCl)	AR grade	Sigma-Aldrich
Reticulated vitreous carbon (RVC)	Purified	ERG Materials and Aerospace Engineering
Single-walled carbon nanotubes Hipco	Purified	Carbon Nanotechnologies, Inc (Houston, TX)

Reagents and materials	Grade/Purity	Supplier
-N, N-Dimethylformamide (DMF)	AR grade	Sigma-Aldrich
Membrane filters (0.2 µm GTTP)		MILLIPORE
Graphite powder	Purified	Bay Carbon, Inc.
Potassium permanganate ($KMNO_4$)	AR grade	Sigma-Aldrich
Ethanol (C_2H_6O)	AR grade	Sigma-Aldrich
Sulphuric acid (H_2SO_4)	98%,w/v	Univar
Hydrogen peroxide (H_2O_2)	30% aqueous	Univar

2.2.2 Electropolymerization method

Three types of electrochemical methods are generally employed for the polymerization of EDOT monomer because it requires only small amounts of monomer, short polymerization time, and can yield both electrode-supported and freestanding film. These methods are: a constant current (chronopotentiometry), a constant potential (chronoamperometry), and a potential cycling method. The surface morphology of conducting polymers are affected by the electropolymerization method, as Hernandez- Perez et al. and Patra, et al., reported [105, 213]. The PEDOT possesses globular surface morphology when it is prepared at low current densities, low potentials and low potential ranges, and the morphology becomes porous at

higher current densities and higher potentials of preparation. In the case of potential cycling, preparation with high potential ranges produces a morphology that is rod-like and fibrous [105]. In addition, the film thickness was controlled by the period allowed for polymerization and the charge passed. The growth of the polymer is monitored by recording the change in current of the system as a function of time.

In Chapter 3, chronoamperometry and potential cycling methods were employed to synthesise PEDOT in a three-electrode system. All experiments were done using a potentiostat and cyclic voltammetric (eDAQ) EA 466 electrochemical system (eDAQ Pty Ltd) connected to a computer with general purpose electrochemical system Chart software version (v5.5.13) or Echem software version (v2.2.11) (Figure 2.1).

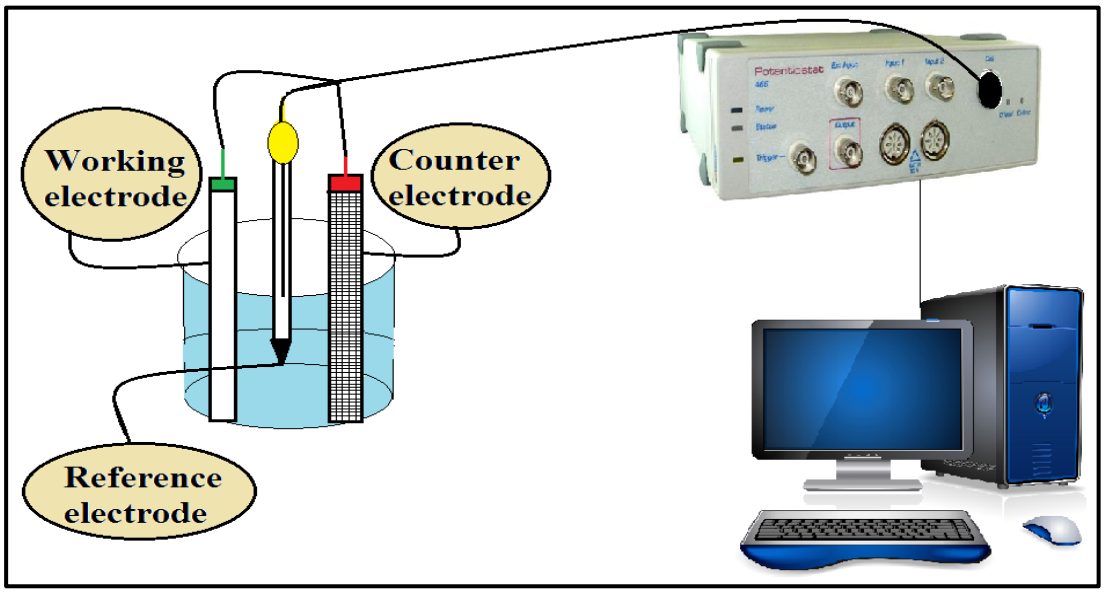

Figure 2.1: Three-electrode system for electropolymerization.

2.2.3 Functionalization of carbon nanotubes.

Oxidation is one of the most commonly used techniques for the purification of carbon nanotubes (CNT) [214, 215]. One of the most popular purification treatments is the use of strong acid [216, 217] which permits removal of a large part of the metallic impurities, cuts the tubes into shorter pieces and opens the CNT ends, improves separation of CNT from amorphous carbon, causes oxidative damage of the sidewalls which result in the production of defects in the CNT sp^2 structure, creates several functional groups on the surface of nanotubes at the tips and around the sidewalls of CNT such as carboxylic (¯COOH), carbonyl (¯CO), and hydroxylic (¯OH) [218-222]. Nitric acid (HNO_3) has been the most frequently utilized agent for oxidation of carbon nanotubes [223]. It can be used in two methods. The first method is called refluxing which uses diluted (2−6 M) HNO_3 for 6 to 48 hours [224]. The second method uses a mixture of concentrated sulphuric acid (H_2SO_4) and HNO_3, usually (3:1) by volume in an ultrasonic bath for 3 to 5 hours [225]. The refluxing method was adopted by many researchers because it is less destructive than concentrated nitric acid [223]. According to this article “Thermal and Electrical Properties of Carbon Nanotubes Purified by Acid Digestion” [226], HiPCO SWCNT oxidation by refluxing in 6 M HNO_3 for 6 hours at a temperature of 120 ºC improved the separation of SWCNT and the purification yield was 98.29% (Figure 2.2). Thus, we applied this method to functionalize SWCNT throughout this thesis.

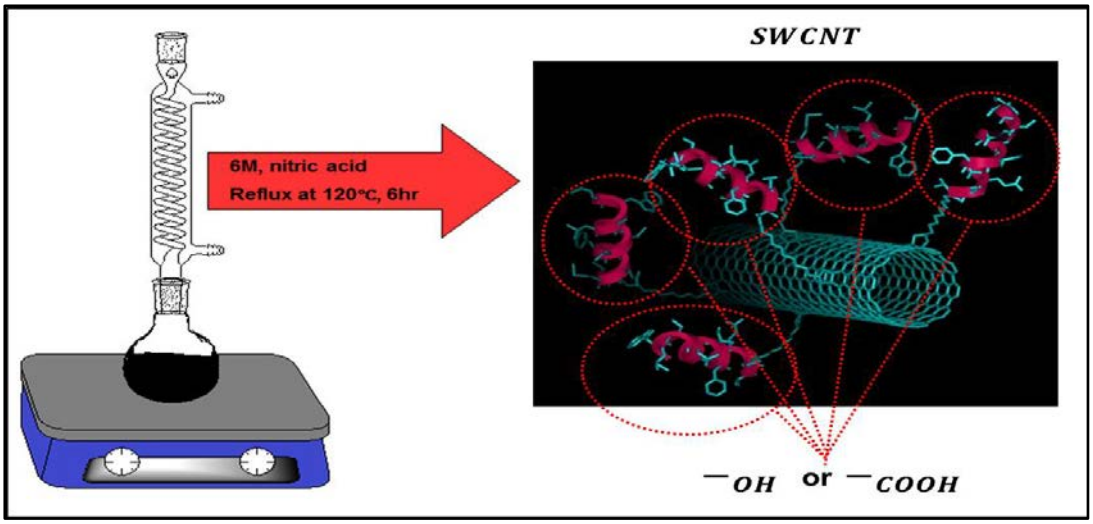

Figure 2.2: Refluxing method using diluted 6 M HNO_3 for 6 hours.

2.2.4 Dispersion of carbon nanotubes in solvent

CNT are materials practically insoluble and are difficult to disperse in most common solvents, especially in aqueous solutions [227-229]. There are three methodologies that have been reported to integrate the carbon nanotube with the biological milieu and improve the solubility of the tubes in aqueous and organic solvent [230-233]. The first procedure is a non-covalent functionalization approach which requires using ultrasonic energy in the presence of dispersions to break up large bundles of CNTs. The dispersant such as surfactants, polymers and biopolymers are used to interface between the hydrophobic and hydrophilic surfaces of the CNTs and solvent, respectively [233-242]. The second procedure involves direct dispersion into organic solvents such as N, N-Dimethylformamide (DMF) and N-Methyl-2-pyrrolidone (NMP) [243-245]. A quantitative study of SWCNT dispersion in different amine solvents was carried out by Landi et al.[244]. The SWCNT concentration after centrifugation in most of the organic solvents (such as DMF and NMP) was significantly less than 0.1 mg/ml. The third procedure is a

covalent approach which usually consists of chemical oxidation of CNTs using a concentrated acid (HCl, HNO_3, H_2SO_4 and HF) to produce a number of hydrophilic carboxylic acid residues on the CNTs surface. The presence of acid oxygenated groups increased SWCNT dispersibility in DMF and NMP solvents, and the SWCNT concentration after centrifugation was significantly less than 0.6 mg/ml [246].

2.2.5 Synthesis of graphene oxide (GO).

The most common method used today to produce graphene oxide from graphite is the Hummers method [190]. In Chapter 5 graphene oxide was synthesised using a modified Hummers methods as outlined by D.C. Marcano, et al. [197] and is described in that Chapter .

2.2.6 Reduction of graphene oxide.

Reducing graphene oxide to produce reduced graphene oxide (rGO) is an extremely vital process. There are a number of methods to achieve the reduction of GO, such as treating GO with hydrazine hydrate, exposing GO to hydrogen plasma for a few seconds, exposing GO to another form of strong pulsed light, heating GO in distilled water at varying degrees for different lengths of time, directly heating GO to very high levels in a furnace, and linear sweep voltammetry [194, 201, 210]. Recently, microwave radiation was used as a fast and simple way to reduce graphene oxide with no hazardous chemicals used, meaning no toxic waste [198]. Reduction of GO to produce rGO in this thesis was achieved by microwave radiation using a Panasonic Inverter ‘The Genius’ 1200W © conventional microwave, and is described in Chapter 5.

2.2.7 Sonication

Sonication (Figure 2.3) is a technique that applies ultrasound energy to the system to help the dispersion of particles. It can be applied by using an ultrasonic probe with strong agitation or an ultrasonic bath with soft agitation depending on the purpose of the experiment. In this thesis, functionalized SWCNT and rGO were dispersed in DMF solvent using a Branson homogenizer, Sonifier model S-450D equipped with a 13 mm step disruptor horn and a 3 mm tapered microtip, operating at a 20 kHz frequency. In addition, the sonication energy (*E*) in joules was calculated using:

$$\mathbf{E = P.t} \qquad \mathbf{(Eq\ 2.1)}$$

Where, *P* is the sonication power (Watt) and in this experiment the sonication power output is (100 W). *t* is sonication time (sec), respectively.

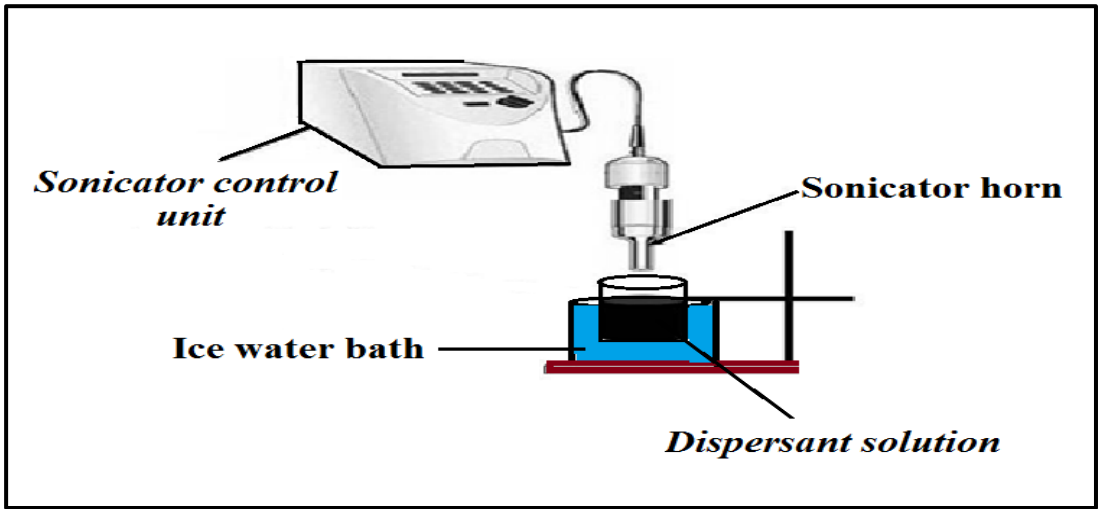

Figure 2.3: Schematic ultrasonic probe used in experiments.

2.3 Characterization techniques

2.3.1 Cyclic voltammetry

Cyclic voltammetry (CV) is a technique which is similar to linear sweep voltammetry (LSV). It is one of the most widely used techniques to study electrochemical reactions. It is able to rapidly provide considerable information on the kinetics of heterogeneous electron-transfer reactions and on the coupled chemical reactions. In addition, this technique is based on varying the applied potential at a working electrode in both forward and reverse directions at some scan rate while monitoring the current [247]. In CV, the potential is applied between the reference electrode (RE) and the working electrode (WE) and the current is measured between the working electrode and the counter (auxiliary) electrode (CE). This technique can be described as some function of a potential (E), current (i), and time (t) as shown in Figure 2.4. It is considered an electroactive technique because the applied potential forces a change in the concentration of an electroactive species at the electrode surface by electrochemically reducing or oxidizing it. In general [247, 248], an electrode provides the interface across which a charge can be transferred because the working electrode is where the reaction or transfer of interest is taking place. The reduction or oxidation of a substance at the surface of a working electrode, at the appropriate applied potential, results in the mass transport of new material to the electrode surface and the generation of a current.

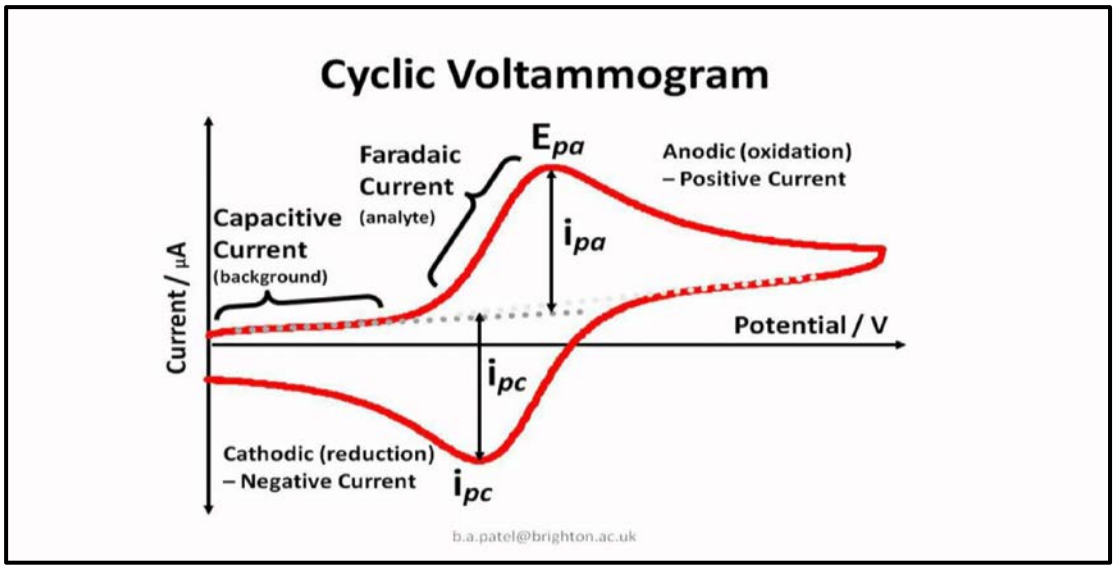

Figure 2.4: Cyclic voltammogram curve of 1 mM $[Fe(CN)_6]^{4-}/[Fe(CN)_6]^{3-}$ in 1 M NaCl; scan started from negative to positive potential.

The important parameters in a CV curve in Figure 2.4 are the peak potentials (E_{pc}, E_{pa}) and peak currents (i_{pc}, i_{pa}) of the cathodic and anodic peaks, respectively. If the electron transfer process is fast compared with other processes (such as diffusion), the reaction is electrochemically reversible, and the peak separation is given by [247, 248]:

$$\Delta E_p = E_{pa} - E_{pc} = 2.303\, RT/nF \qquad \text{(Eq 2.2.)}$$

Thus, for a reversible redox reaction at 25 °C with n electrons ΔE_p should be 0.0592/n V or about 60 mV for a one-electron transfer reaction. In practice this value is difficult to attain because of such factors as cell resistance. Irreversibility due to a slow electron transfer rate results in $\Delta E_p > 0.0592/n$ V, greater than 70 mV for a one-electron reaction.

For a reversible reaction, the concentration is related to peak current by the Randles–Sevcik expression (at 25 °C) [247]

$$i_p = 2.686\ 10^5 \times n^{3/2} A C_0 D^{1/2} \nu^{1/2} \qquad \text{(Eq 2.3.)}$$

Where i_p is the peak current in amps, A is the electrode area (cm^2), D is the diffusion coefficient ($cm^2\ s^{-1}$), C_0 is the concentration in mol cm^{-3}, and ν is the scan rate in V s^{-1}.

Equation (2.3.) indicates that i_p is proportional to bulk concentration, square root of scan rate and number of electrons transferred in the redox reaction. Practically, peak shape can be distorted by the capacitive current and the ohmic drop between electrodes. The capacitive current is defined by this equation [249]

$$i = AC_d \nu \qquad \text{(Eq 2.4.)}$$

Where A is the electrode area (cm^2), C_d is differential capacity of the electric double-layer at the specific potential (Fcm^{-2}) and ν is the scan rate in V s^{-1}.

The ratio of capacitive to faradic currents can be expressed as Equation 2.5 [250].

$$\frac{i_c}{i_p} = 2.3\ 10^{-8} \left(\frac{v^{0.5}}{C_0\ n^{3/2}}\right) \qquad \text{(Eq 2.5.)}$$

This suggests that the capacitive current increases as a function of scan rate and decrease in bulk concentration of electroactive species. In addition, the specific capacitance from CV curves can be obtained by using Equation 2.6 [249].

$$C = \frac{i*t}{m*E} \qquad \text{(Eq 2.6.)}$$

Where C is the specific capacitance (Fg^{-1}), i is discharge current (A), t is discharge time (s), E is the potential window (V) and m is the mass of the electrode (g).

Cyclic voltammetry has been used in this thesis to investigate the electrochemical properties of the PEDOT/RVC composite electrode, a-SWCNT/RVC composite electrode and mwGO/RVC electrode and CNT/mwGO/RVC composite electrode. Furthermore, the capacitance of RVC before and after coating with PEDOT or a-SWCNT or a-SWCNT composite with mwGO, the effect of increasing scan rate on electron transfer and the stability of the electrode have been studied. Experiments were performed in a three-electrode system consisting of a working electrode (WE), counter electrode (CE), and Ag/AgCl (3 M NaCl) reference electrode (RE). A potentiostat (eDAQ) EA 466 electrochemical system (eDAQ Pty Ltd) with Echem software version (v2.2.11) was used.

2.3.2 UV-Visible spectroscopy

UV-Visible spectroscopy or UV-Visible spectrophotometry (UV-Vis) is a common spectroscopic technique used to determine structure [251, 252]. In recent years, it has been used as a tool for analysing a few aspects of dispersions [251, 252]. It measures the response of a sample to ultraviolet and visible range of electromagnetic radiations. The basic principle of UV/Vis spectroscopy is shown in Figure 2.5. The principle of UV-visile spectroscopy relies on the Beer-Lambert law

that states that the solution's absorbance is proportional to the concentration of the absorbing species in the solution and the path length as in Equation (2.7) [251, 252]:

$$A=\log\left({}^{I_0}/_{I}\right) = \varepsilon * C * L \qquad \text{(Eq: 2.7)}$$

Where A is absorbance (no units), I_0 is incident light's intensity at a specific wavelength, I is transmitted intensity, ε is molar absorptivity (L/mol cm), C is concentration (mol/L) and L is pathlength (cm).

UV-Visible spectroscopy has been used in Chapters 4 and 5 to study the dispersal process by monitoring the levelling of the absorption intensity as a quick and simple way to investigate the stabilization of SWCNT and rGO in the dispersion, and it was also used to optimize the sonication time. Dispersions were studied contained in quartz cuvettes in a model Shimadzu UV-1800 spectrophotometer with UV probe (v.2.10 software) over the spectral range 350- 750 nm.

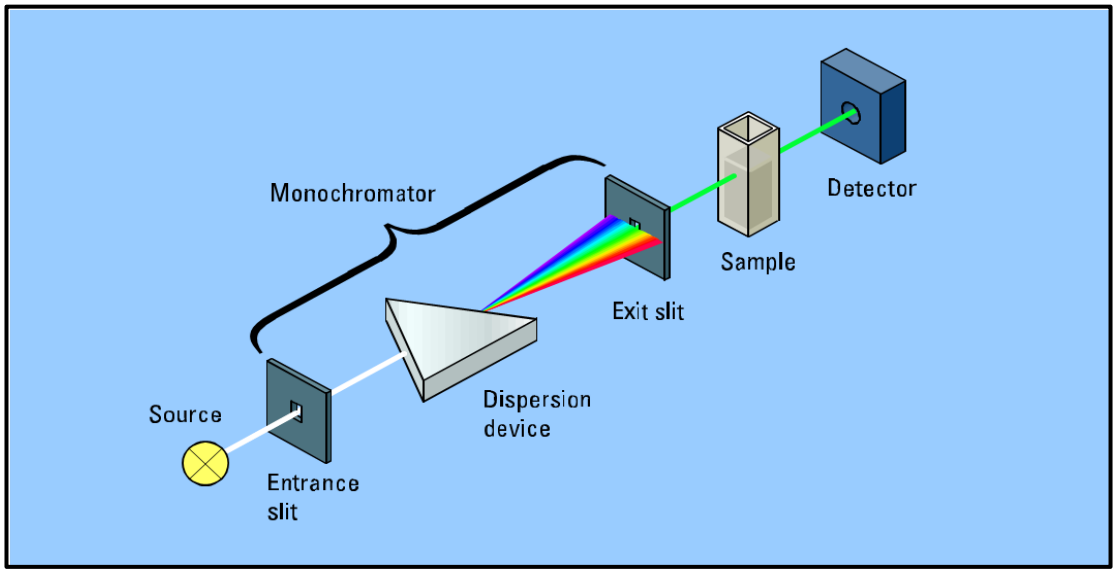

Figure 2.5: Schematic diagram of basic principle of UV/Visible spectroscopy system.

2.3.3 X-ray photoelectron spectroscopy (XPS)

X-ray photoelectron spectroscopy (XPS) which is also known as Electron Spectroscopy for Chemical Analysis (ESCA), is a widely used technique to measure the elemental composition, chemical state, empirical formula, and electronic state of the elements that exist within a material. The principle of XPS spectra involves irradiating a material with a beam of X-rays while simultaneously measuring the kinetic energy and number of electrons that escape from the top 10 to 100 Å (1 to 10 nm) and sending the resultant signals to a recorder to be displayed as a spectrum (Figure 2.6). In Chapter 5, XPS has been used to determine the functional groups in carbon binding to carbon, and hydrogen and oxygen in rGO and GO. The XPS is conducted using a SPECS PHOIBOS 100 Analyser installed in a high-vacuum chamber with the base pressure below 10–8 mbar, and X-ray excitation was provided by Al Ka radiation. The XPS binding energy spectra were recorded at the pass energy of 20 eV in the fixed analyser transmission mode. The XPS peak fitting was carried out using CasaXPS software.

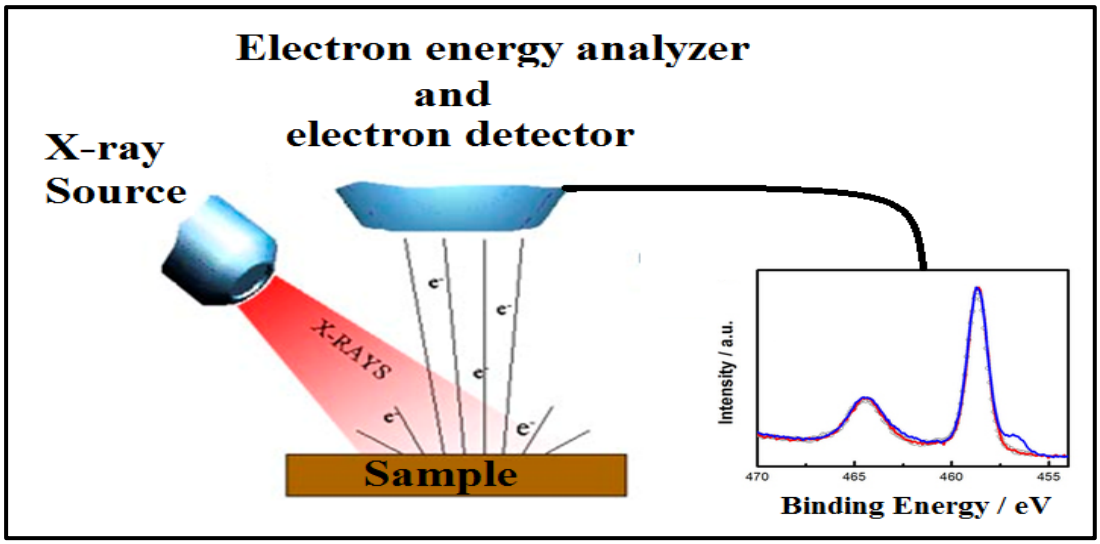

Figure 2.6: Schematic diagram of basic components of an XPS system.

2.3.4 Microscopy

The dispersion of a-SWCNT and mwGO in DMF were checked using a Fully Automated Upright Microscope System (Leica DM6000 B) as shown in Figure 2.7, including the Differential Interference Contrast (DIC) in combination with 5x magnification with real size 2517.94*1888.46 µm. The images were acquired using the Leica Application Suite (version 4.2 LAS) software. Dispersions were dropped onto glass slides and printed tracks were images on their substrates.

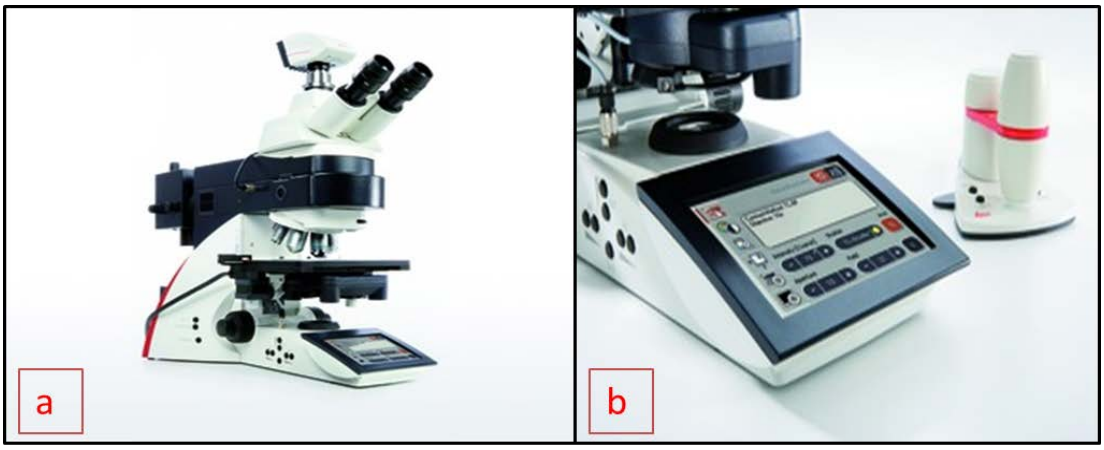

Figure 2.7: (a) Photo image of Leica DM 6000 Microscope, and (b) the Leica smart touchscreen function buttons located behind the focus knobs controls.

2.3.5 Scanning Electron Microscopy (SEM)

The Scanning Electron Microscope (SEM) is an electron microscope that produces high magnification images of a sample by scanning it with a focused beam of electrons. It is very useful due to its versatility in characterizing sample morphology, orientation of the crystalline structure and chemical composition. The principle of SEM can be simply explained as shown in Figure 2.8. A beam of

electrons is produced at the top of the microscope by an electron gun. The electron beam follows a vertical path through the microscope, which is held within a vacuum. The beam travels through electromagnetic fields and lenses, which focus the beam down toward the sample. Once the beam hits the sample, electrons and X-rays are ejected from the sample. The structure of composite electrodes and the thickness of PEDOT coated RVC in this thesis were observed by using a field emission scanning electron microscope (FESEM) JEOL7500F and cold-field emission gun Scanning Electron Microscopy (FEGSEM) equipped with a JEOL hyper-minicup Energy Dispersive Spectrometer (EDS). The FEGSEM was operated at accelerating voltages of 5 KV for Chapter 3 and 1.5 KV for Chapters 4 and 5, and a spot size setting of 8. Secondary and backscattered electron images and X-ray spectra were collected at a standard working distance (WD) of 8 mm. Samples were prepared by mounting small pieces of films onto a brass stub (11 mm × 5 mm) using double-sided conductive carbon tape.

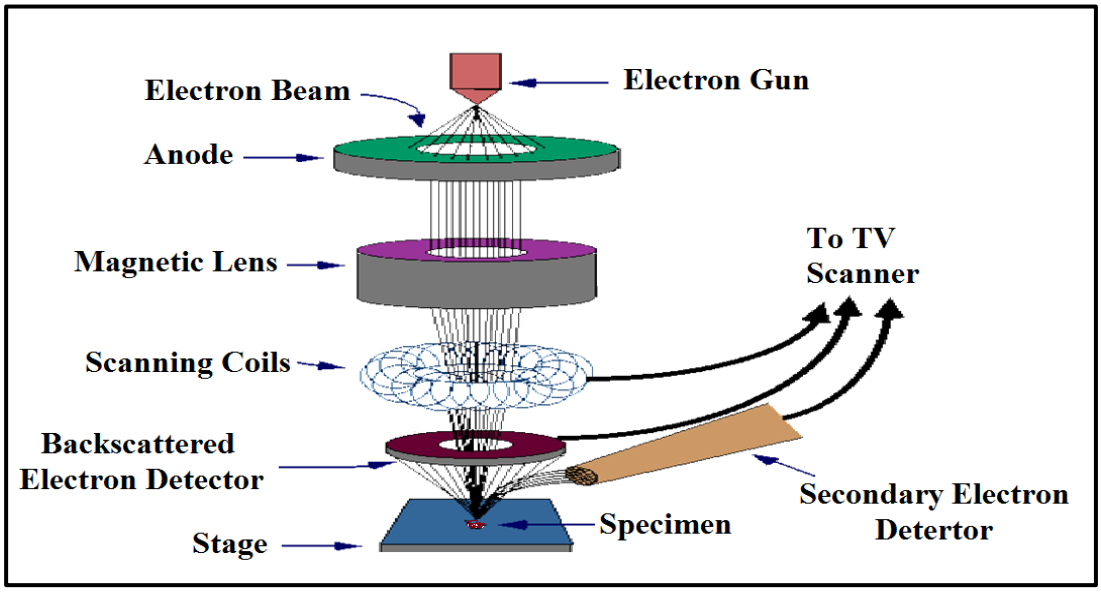

Figure 2.8: Schematic diagram of a Scanning Electron Microscope (SEM).

2.3.6 Raman spectroscopy

Raman spectroscopy is a spectroscopic technique used to observe rotational, vibrational and other low-frequency modes in a system. It relies on the scattering of light when the sample is irradiated by a monochromatic light source (usually a laser beam) which has a specific frequency. It probes molecular and crystal lattice vibrations and therefore is sensitive to the composition, bonding, chemical environment, phase, and crystalline structure of the sample material. These characteristics make it an exceptional method for unambiguously identifying materials in any physical form: gases, liquids, solutions, and crystalline or amorphous solids [253]. The vibrational frequency is measured and recorded as a scattering optical intensity versus vibrational frequency (cm^{-1}), as shown in Figure 2.9.

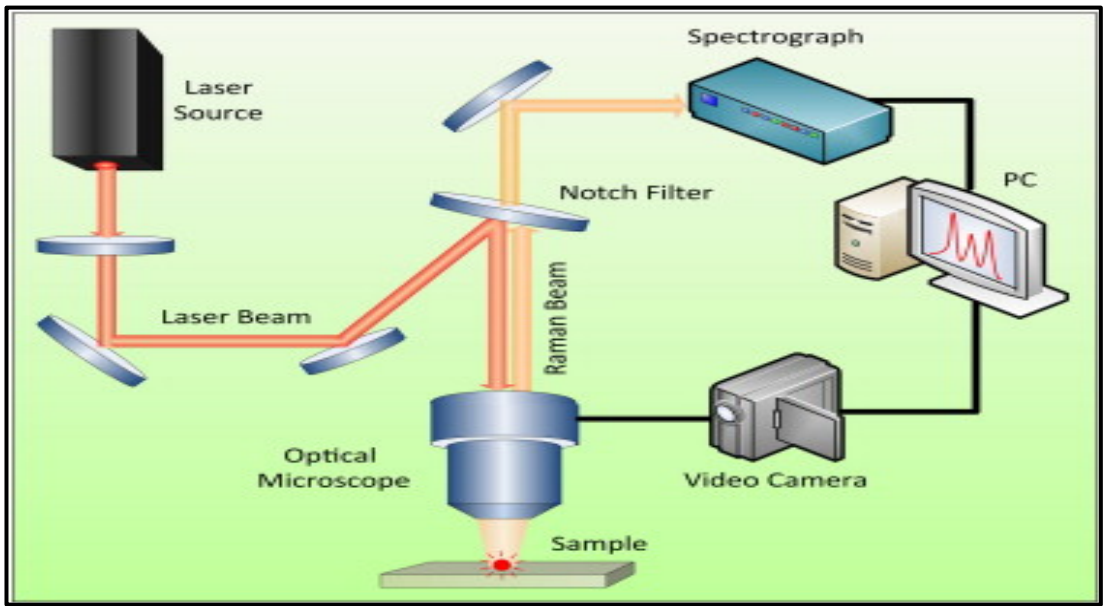

Figure 2.9: Basic principle of a Raman spectroscopy system [254].

In this thesis, Raman spectroscopy was employed to distinguish between graphite, GO, mwGO, CNT/mwGO composite and a-SWCNT by observing the D and G bands peak shape. Furthermore, the ratio and shifting of D and G bands are used to investigate the reduction of GO to mwGO and functionalization SWCNT to a-SWCNT. Moreover, it was used to obtain some information about the PEDOT structure. All these characterizations have been performed by Raman analysis using a Jobin Yvon Horiba HR800 Raman spectrometer equipped with LabSpec software and with a visible Raman microscope (Olympus BX41) and CCD detector. The excitation wavelength was 632.81 nm and spectra were obtained over 30 s at 1 cm^{-1} resolution. Moreover, the data analysis was carried out using Labspec V.5.45.09 software.

2.3.7 Thermogravimetric analysis (TGA)

The thermal stability and the amount of materials were determined by thermogravimetric analysis (TGA) curves which give the dependence of the weight loss of a sample as a function of temperature or time. Thermogravimetric analysis (TGA) was carried out using a Q500 (TA Instruments) (Figure 2.10 (a)) with the data analysis carried out using the Q Series software V. 2.5.0.255 (TA Instruments). An known amount of ~5 mg of each sample was placed into a platinum pan (Figure 2.10 (b)). The temperature range was between 25 °C to 750 °C at a ramp rate of 5 °C /min in air for PEDOT coated RVC electrode in Chapter 3, whereas and the temperature range was between 25 °C to 900 °C at a ramp rate of 2 °C /min in air for graphite, GO and rGO in Chapter 5. A combined gas flow of 10 ml min^{-1} Nitrogen (N_2) and 90 ml min^{-1} air was used.

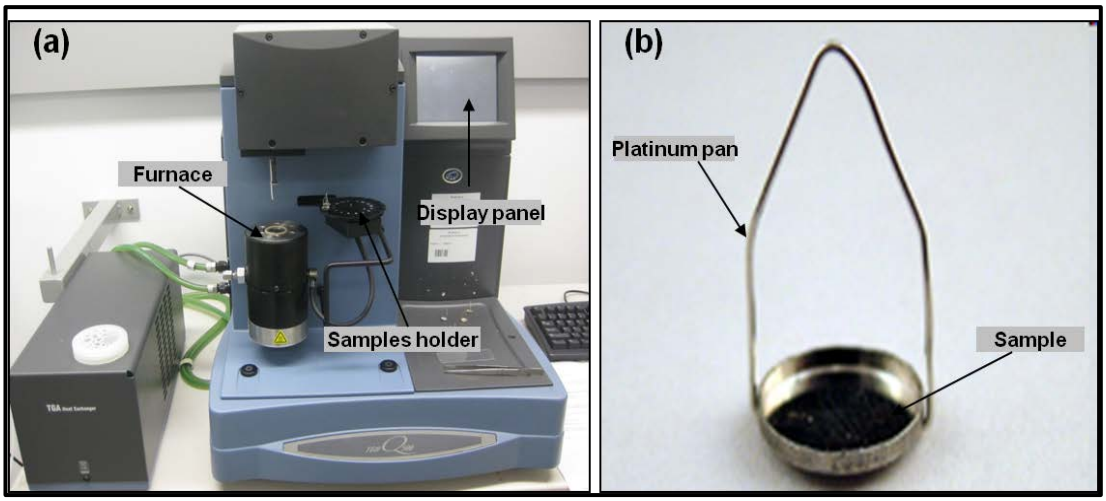

Figure 2.10: (a) thermogravimetric analyser (TA Instruments Q500) and (b) a platinum sample pan which was used to hold the samples inside the furnace.

2.3.8 X-ray diffraction (XRD)

X-ray diffraction (XRD) method (Figure 2.11) is one of the significant non-destructive analytical techniques used often to reveal information about the arrangement of atoms in a crystal structure, chemical composition, physical properties of solid material and all information that can be vital in material characterisation and quality control. This technique is based on constructive interference of monochromatic X-rays which are generated by filtered radiation from a cathode ray tube and directed toward the crystalline sample [255]. This interaction can be reflected such that the angle of reflection is equal to the angle of incidence. This behaviour is called diffraction and it is described by Bragg's Law [255]:

$$2d\sin\theta = n\lambda \qquad \text{(Eq 2.8.)}$$

Where θ is reflected X-ray beams at certain angles of incidence (theta), the variable d is the distance between atomic layers in a crystal (m), and λ is the wavelength of the incident X-ray beam (m) and n is an integer.

This law relates the wavelength of electromagnetic radiation to the diffraction angle and the lattice spacing in a crystalline sample. These diffracted X-rays are then detected, processed and counted by scanning the sample through a range of 2θ angles. All possible diffraction directions of the lattice should be attained due to the random orientation of the powdered material. Conversion of the diffraction peaks to d-spacings allows identification of the mineral because each mineral has a set of unique d-spacings. Typically, this is achieved by comparison of d-spacings with standard reference patterns. X-ray diffraction (XRD) was employed in this thesis in order to understand the crystallinity of the structure and to determine the interlayer distance between graphite, GO and mwGO nanosheets in Chapter 5. The XRD system (Philips 1825) measurements were taken with CuKα radiation (λ= 0.154) operating at 40 KeV and with a cathode current of 20 mA.

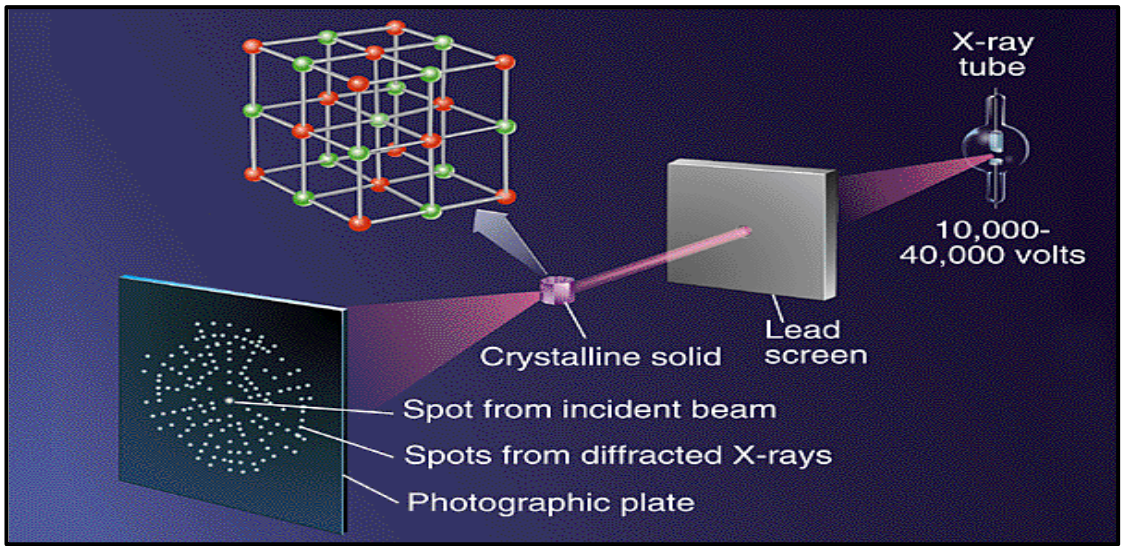

Figure 2.11: Basic principle of the X-ray diffraction (XRD) technique.

2.4 Capacitive deionization

2.4.1 CDI system components.

The CDI system consisted of a reservoir, (MasterFlex L/S® 25) pump tubing, a MasterFlex L/S® peristaltic pump for recirculating the salt solution into the system, an on-line flow-through cell to hold a conductivity sensor, an on-line (smart CHEM-LAB K=1.0) conductivity sensor used to measure solution conductivity, (smart CHEM-LAB Display and controls) conductivity meter used to monitor solution conductivity, (smart CHEM-LAB RS232G port) adapter used to receive data from the conductivity meter and send reading to a computer, integrated potentiostat (ER466, e-DAQ, Australia) used to apply electric current through the electrodes, a CDI unit cell and computer installed with e-Chart (ES500) and e-Chem (ES260), TPS communication, and Microsoft excel software to manipulate, recorded data, and draw curves. Figure 2.12 shows the principle components of the CDI system.

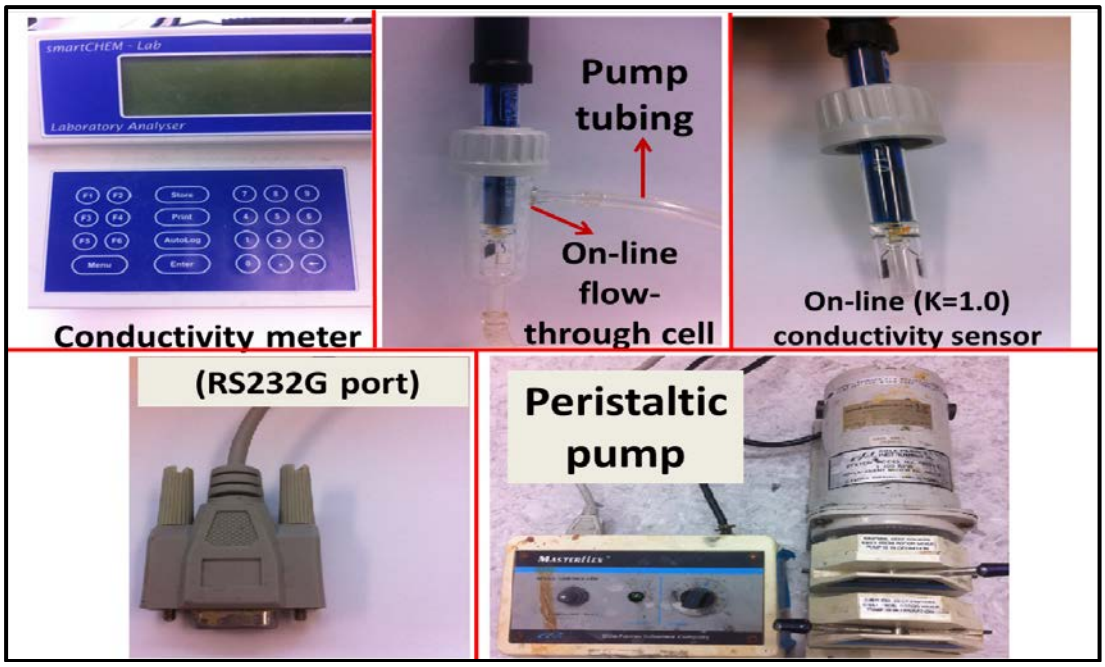

Figure 2.12: Photographs of pump tubing, peristaltic pump for recirculating the salt solution into the system, an on-line flow-through cell, an on-line conductivity sensor, conductivity meter, and (RS232G port) adapter.

2.4.2 Design and fabrication a flow-through cell

The flow-through cell which was used in the CDI system was designed using SolidWorks software, 2012 Version 5000, then built by printing using a Connex 350 3D printer (Figure 2.13), by (Objet). The designing and fabrication of the flow-through cell will be discussed in more detail in Chapters 3 (3.3.7.1) and Chapter 4 (4.3.10).

Figure 2.13: Photograph of a Connex 350 3D printer, by (Objet).

2.4.3 Measurement of amount of ion removal from the NaCl aqueous solution

NaCl concentration was determined in our laboratory by measuring the electrical conductivity of NaCl solution. The calibration curve linearity is shown in Figure 2.14. Conductivity linearly increased as NaCl concentration increased. The equation from fitting a line starting from the origin (0,0) to the calibration curve is as follows:

$$\boldsymbol{Cond = 1.9067 * Conc} \qquad (\boldsymbol{Eq\ 2.9})$$

Where Cond and Conc are the conductivity (μS/cm) and concentration (mg/L) of NaCl solution, respectively.

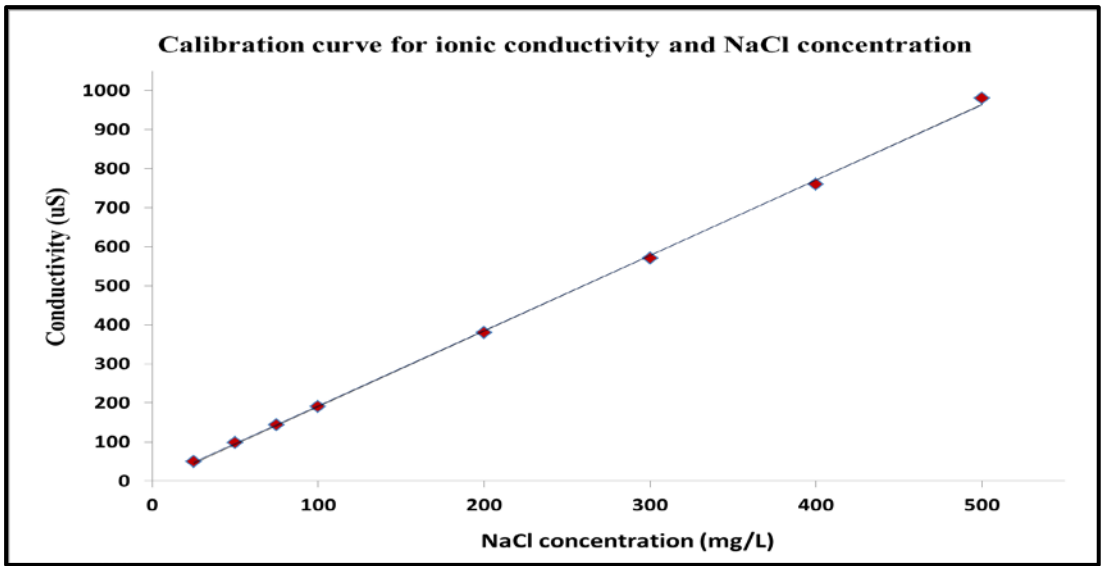

Figure 2.14 : Calibration curve linearity for ionic conductivity *vs* NaCl concentration.

Example calculation of the ion removal from NaCl solution

From the conductivity meter, the initial NaCl solution conductivity is 143.00 µS/cm and, after charging the electrode it became 138.59 µS/cm.

Ion removal from solution is calculated as follows:

As we know from equation (2.9),

Cond = 1.9067 * Conc , so

Conc= Cond/ 1.9067

Therefore,

Conc $_{initial}$ = (143.00)/ 1.9067= 75.00 mg/L

Conc $_{final}$ = (138.59)/ 1.9067= 72.69 mg/LHence, the ion removal from the NaCl solution = Conc $_{initial}$ - Conc $_{final}$ = 2.31 mg/L.

2.4.4 Electrode evaluation in the capacitive deionization

There are several parameters that need to be studied in order to evaluate a capacitive electrode in the capacitive deionization unit. In order to determine the optimum operational conditions, the effect of flow-rate and electric field for

desalination performance need to be considered as shown in Figure 2.15. Before starting the experiment to investigate the electrode in the unit cell, the relationship between conductivity and concentration of aqueous solutions is obtained according to a calibration curve made prior [33]. Then the best conditions of flow-rate and electric field at a solution temperature of 298 ^{o}K are evaluated [40]. Also, the total known volume must be maintained in order to calculate the electrosorption capacity [40]. After that, the solution conductivity is recorded during the process of charging and discharging the electrode. When the conductivity almost did not vary, the ions were adsorbed maximally. Then the electric field was removed, at which the conductivity returned to its initial value, demonstrating that the electrosorption is a reversible process. In this way the optimal voltage applied to the electrode to remove the ions from the solution can be determined, because the electrosorption capacity is dependent on applied voltage where higher ion removal is achieved with higher voltage.

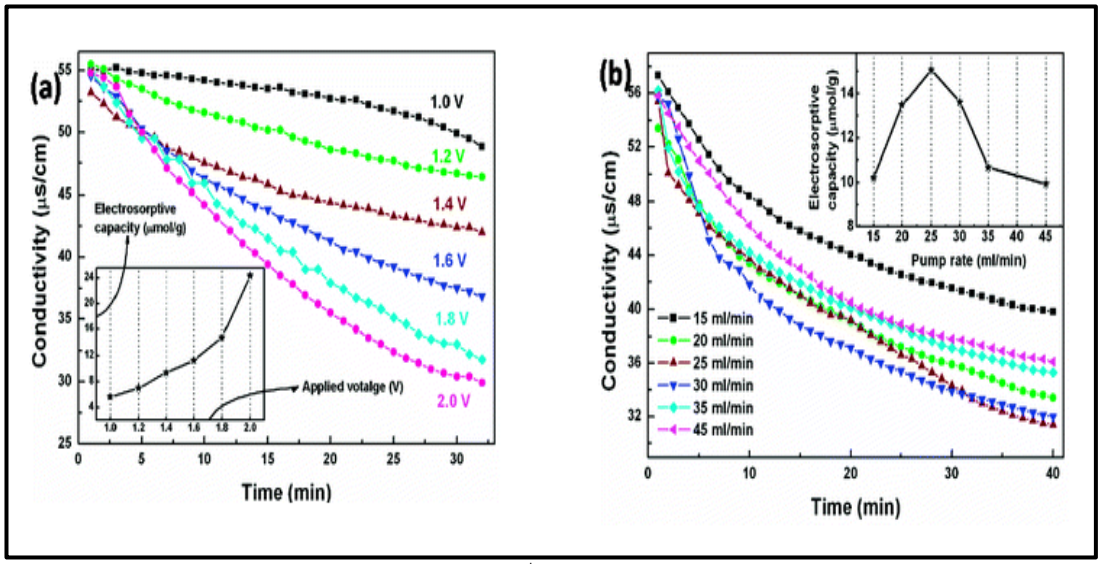

Figure 2.15: The electrosorption of Na^{+} onto GNFs electrode at (a) different bias potentials, (b) different flow-rates [33].

2.4.5 Electrosorption dynamics

Dynamics study is of great significance to evaluate the performance of electrode adsorption. This study describes the solute uptake rate, and evidently this rate controls the residence time of adsorptive uptake at the solid-solution interface [256, 257]. In order to investigate the controlling mechanism of electrosorption, the constants of sorption and intraparticle diffusion, a suitable kinetic model is needed to analyse the data. These models are the intra-particle diffusion model (IPD) proposed by Weber and Morris [258, 259], pseudo first-order model proposed by Lagergren [260], and pseudo second-order model [261]. The conformity between experimental data and the model predicted values is expressed by the correlation coefficients (r^2, values close or equal to 1). A relatively high r^2 value indicates that the model successfully describes the kinetics of NaCl adsorption. These models [256-261] are as follows:

For a rate constant of first-order sorption

$$\frac{dq_t}{dt} = \mathrm{k}_1(q_t - q_e) \qquad (\boldsymbol{Eq\ 2.10})$$

After integration by applying the initial conditions $q = 0$ at $t = 0$ and $q = q_t$at $t = t$, Eq. (2.10) becomes:

$$\mathrm{Log}\left(\frac{q_e}{q_t - q_e}\right) = \frac{K_1 t}{2.303} \qquad (\boldsymbol{Eq\ 2.11})$$

Equation (2.11) can be rearranged to obtain a linear form:

$$\log\ (q_t - q_e)\ = \log\ (q_e) - \frac{K_1 t}{2.303} \qquad (\boldsymbol{Eq\ 2.12})$$

Where q_t and q_e are the amounts of NaCl adsorbed (mg/g) at time *t* and at equilibrium respectively, and K_1 is the rate constant of the pseudo-first-order adsorption process (min^{-1}). The rate constant (K_1) was calculated from the slope of eq. (2.12). q_e was calculated by a trial-and-error method in conjunction with an optimization routine to maximize the correlation coefficient for Eq. (2.12) with the solver add in of Microsoft Excel.

The rate constant for pseudo-second-order sorption may be obtained from the following analysis:

$$\frac{dq_t}{dt} = k_2(q_e - q_t)^2 \qquad (\boldsymbol{Eq\ 2.13})$$

Integrating Eq. (2.13) and applying the boundary conditions, gives:

$$\frac{1}{(q_e - q_t)} = \frac{1}{(q_e)} + K_2 t \qquad (\boldsymbol{Eq\ 2.14})$$

Equation (2.14) can be rearranged to obtain a linear form:

$$\frac{t}{(q_t)} = \frac{1}{(h)} + \left(\frac{1}{(q_e)}\right) t \qquad (\boldsymbol{Eq\ 2.15})$$

Where $h = K_2 q_e^{\,2}$(mg $g^{-1}min^{-1}$) can be regarded as the initial adsorption rate as $t \rightarrow 0$ and K_2 is the rate constant of pseudo-second-order adsorption (g $mg^{-1}min^{-1}$). The plot of $\frac{t}{(q_t)}$ versus *t* should give a straight line if pseudo-second-order kinetics is applicable and the q_e, K_2 and *h* values can be determined from the slope and intercept of the above plot.

The rate parameter of intraparticle diffusion can be defined as:

$$q_t = f\,(t^{0.5}) \qquad (\boldsymbol{Eq\ 2.16})$$

The rate parameters for intraparticle diffusion (k_{id}) at different initial concentrations are determined using the following equation.

$$q_t = K_{id}\ (t^{0.5}) \qquad (\boldsymbol{Eq\ 2.17})$$

Where K_{id} is the intraparticle diffusion rate constant, (mg/gmin$^{0.5}$). The plot q_t versus $t^{0.5}$should give a straight line.

2.4.6 Electrosorpitive isotherm

The Langmuir and Freundlich isotherms are the two most common isotherms. They were employed for the simulation of the ion adsorption on electrodes. The Langmuir isotherm is applicable to localization of adsorbed ions with a limited adsorption amount [262] and the Freundlich isotherm is suitable for the description of ion adsorption with a wide variety of adsorption strength [263]. Langmuir (Eq. 2.18) and Freundlich isotherm (Eq. 2.19) are used to fit the experimental data for electrosorption of Na^+ and Cl^{-1} onto the electrode, respectively [262, 264].

$$q = \frac{q_m K_L C}{1 + K_L C} \qquad (\boldsymbol{Eq\ 2.18})$$

$$q = K_F C^{1/n} \qquad (\boldsymbol{Eq\ 2.19})$$

Where C is the equilibrium concentration (mg/l), q is the amount of adsorbed NaClin milligrams per gram of a-SWCNT, q_m is the maximum adsorption capacity corresponding to complete monolayer coverage (mg/g). K_L is the Langmuir constant related to binding energy, K_F is the Freundlich constant related to the adsorption capacity of adsorbent, and 1/n is the indication of the tendency of the adsorbate to be adsorbed.

3 : Novel three-dimensional PEDOT/RVC electrode structure for capacitive deionization.

3.1 Introduction

CDI researchers have focussed on the development of novel carbon materials [36, 45, 50, 52, 208, 265-268] such as activated carbon, carbon aerogel, carbon nanotubes, graphene, ordered mesoporous carbon, and their composites to make CDI electrodes with high specific surface area, high conductivity, reasonable microstructured pores, and high electrosorption capacity. In addition, conducting polymers have been combined with such carbon materials to improve the carbon electrode properties which lead to improvement of the CDI performance [163, 269, 270] because they have high electric conductivity and high surface area [271, 272]. All these electrodes were built as two-dimensional structure electrodes without significant thickness. However, a limited improvement in the electrosorption capacity is still far less than the theoretical value, which is mainly due to shortcomings such as the low effective surface area [273].

In this chapter, amongst conducting polymers, PEDOT (poly(3,4-ethylenedioxythiophene)) was chosen as active material for a CDI electrode because of its interesting properties such as high electrical conductivity, surface area and environmental stability [110], facile synthesis via electrochemical polymerization and other properties that have been discussed in Chapter 1. In addition, a novel PEDOT material will be used as a three-dimensional porous electrode with well-interconnected macropores, and numerous mesopores and micropores embedded in the reticulated vitreous carbon (RVC) walls because this improves ion diffusion by providing a decreased ion diffusion distance [273]. The presence of macropores serving as ion-buffering reservoirs guarantees a shorter ion diffusion distance [274,

275], which facilitates the rapid transportation of the ions into the interior of the bulk material. Moreover, it has been demonstrated that 3D porous carbon with an interconnected pore system shows an excellent performance in the field of electrochemistry [68, 69, 71, 275-277].

RVC as substrate was selected for PEDOT film deposition because it has tridimensional (3D) porous structure that provides high macroscopic surface area and other interesting characteristics such as a low density, high chemical inertness with low electrical and fluid flow resistance, and is also amenable to surface modification with conducting polymers [63, 78, 86, 278].

This chapter describes and discusses the electrodeposition of various amounts of PEDOT to coat RVC electrodes. These electrodes were characterised for their morphology, Raman spectrum, thermal stability and electrochemical properties. The electrodes tested using a flow-through cell fabricated using 3D printing. The electrodes were tested under various working conditions such as flow-rate and bias potential.

3.1.1 Aims of the work in this chapter

The aims of the research described in this chapter can be summarized as follows:

- Use PEDOT as materials and electrodes in CDI technology.
- Build 3D microstructure electrodes for use in CDI technology.
- Use RVC as the substrate in a CDI system to reduce the resistance of solution flow through the electrode, increase the stability of composite electrode towards high flow-rate pressure, increase the possibility of ions to reach all electrode surfaces in a short time for electrosorption, and shorten the time of ions release from the electrode surface.
- Improve the performance of a CDI system in terms of geometric volume and area by electrodeposition of different percentages of PEDOT on RVC electrodes.
- Design and make a simple flow-through cell that direct solution flow between electrodes in a CDI system.

3.2 Experimental

3.2.1 Chemicals and materials

Commercial 3,4-ethylenedioxythiophene monomer (EDOT) with purity 99.9% was purchased from Sheng Chemical Ltd, and was used as received. The following chemicals obtained from Sigma-Aldrich were also used as received: acetonitrile (ACN) (AR grade), lithium perchlorate ($LiClO_4$) (AR grade), concentrated nitric acid (70%) and sodium chloride (AR grade). The reticulated vitreous carbon (RVC) (60 ppi (normal pores per linear inch)) was purchased from ERG Materials and Aerospace Engineering and used as received. Milli-Q water with a resistivity of 18.2 $m\Omega\ cm^{-1}$ was used in all preparations.

3.2.2 Methods

3.2.2.1 Pre-treatment of the RVC electrode

All reticulated vitreous carbon (RVC) electrodes (length 4 cm * width 3.5 cm * thickness 0.3 cm (32.5 cm^2 or 4.2 cm^3) were cut from a block of RVC material, and soaked in 2M HNO_3 for 24 hours to remove any impurities [279]. Electrodes were thoroughly washed with distilled water to remove the acid. The pH of the effluent was checked periodically until the wash became neutral. All RVC electrodes were then soaked in methanol for 2 hours to remove any organic impurities [279]. The RVC electrodes were dried under a brief flow of nitrogen and kept in an oven at 110°C overnight. All RVC electrodes were weighed after drying.

3.2.2.2 Electrochemical polymerization of PEDOT on RVC electrode

In our work, PEDOT/RVC composite electrodes were synthesised by cyclic voltammetric and chronoamperometry. In both techniques before polymerizations, the RVC pieces were left in contact with the working electrolyte for at least 24 hours to ensure their complete wetting. In order to prepare the working electrodes, electrical contact was made by a hook of Pt wire. The electropolymerization was performed in an organic electrolyte, and the reference electrode was a Ag/AgCl (3 M NaCl) electrode and the counter electrode was a Pt mesh 4*4 cm^2. The electrolyte was an acetonitrile solution containing 0.01 M monomer, EDOT and 0.1 M supporting electrolyte salt ($LiClO_4$) [280, 281]. The solution was thoroughly deoxygenated by nitrogen (N_2) before the electropolymerization for 10 min prior to all electrochemical experiments at room temperature. PEDOT was deposited on the RVC working electrode by cyclic voltammetry using three-electrode systems in the voltage range between 0 to 1.3V at 50 mV/s scan rate. In addition, PEDOT films were galvanostatically deposited on the RVC working electrode with a constant voltage applied for various periods of time. The quantity of PEDOT-ClO_4 coating the RVC electrodes was determined by calculating the total charge passed in the electropolymerization. The charge values were read directly from the I-V curves by computer.

3.2.2.3 Physical characterisation

The thermal stability of the PEDOT on PEDOT/RVC electrodes and the amount of PEDOT coated on the RVC were determined by thermogravimetric analysis (TGA). Experiments were performed by using a Q500 (TA Instruments)

apparatus at a ramp rate of 5 °C/min in air, with a combined gas flow of 10 ml min^{-1} Nitrogen (N_2) and 90 ml min^{-1} air from 25 °C to 750 °C. Moreover, the morphology and the thickness of the PEDOT deposits on RVC electrodes were analysed by using a field emission scanning electron microscope (FESEM) at specific voltages of 0.5 KV. Furthermore, Raman spectra were measured on a Raman spectrometer equipped with a visible Raman microscope and CCD detector. The excitation wavelength was 632.81 nm and spectra were obtained over 30 s at 1.0 cm^{-1} resolution.

3.2.2.4 Electrochemical characterisation

The capacitance and the effect of different scan rates were determined by cyclic voltammetry (CV). A PEDOT/RVC composite electrode was used as the working electrode (WE) in 1 M NaCl aqueous solution and scanned in the voltage range between -0.2 to 0.8 V using a three-electrode system; RVC electrode and Ag/AgCl (3M NaCl) were used as counter electrode (CE) and reference electrode (RE), respectively. The scan rates ranging from 5 to 200 mV/s. Contacts to the WE and CE were made using Pt wire.

3.2.2.5 Measurement of amount of ion removal from the NaCl aqueous solution

NaCl concentration was determined by measuring the electrical conductivity of NaCl solution as described in Section 2.4.3.

3.3 Results and discussions

3.3.1 PEDOT deposited on RVC electrode

PEDOT can be polymerized using multiple different ways, but for the purposes of this work, electrochemical polymerization has been used to synthesize PEDOT. This method is important because it requires only a small amount of monomer, short polymerization time, and can yield both electrode-supported and free-standing film. This method utilizes electrochemical oxidation of the electron-rich EDOT-based monomers by three different techniques; namely, cyclic voltammetry, chronoamperometry and chronopotentiometry. In this project, chronoamperometry method was selected to grow thick PEDOT coated RVC electrodes and cyclic voltammetry was used to select the potential of EDOT monomer oxidation to form PEDOT.

3.3.1.1 Cyclic voltammetry

EDOT monomer was prepared in acetonitrile as electrolyte because it has the advantage of a higher conductivity than that prepared in aqueous solution [282]. Figure 3.1 shows the cyclic voltammograms related to the EDOT. It can be seen from Figure 3.1 that the EDOT oxidation started at 1.1 V for the anodic scan. Furthermore, the EDOT electropolymerization is characterized by cycles with a crossover of the reverse cathodic scan over the anodic scan, giving rise to what has been called the “nucleation loop” [283]. In particular we observe that the current of the reverse scan is higher than that of the forward scan in the region close to the switching potential, but it drops again to the level of the current–voltage curve of the forward scan. Such a kind of CV profiles have been interpreted as due to polymer

nucleation effects [284] or, more recently, to homogeneous reactions between an oligomeric follow-up product and the starting monomer [285]. Moreover an increase of both anodic and cathodic current intensities with increasing number of scans is also evident. This effect can be explained by considering the growth at the electrode surface of an electroactive polymer film, whose thickness increases regularly with the number of cycles [286]. Moreover, the RVC foam electrode was observed after polymerization to have a visible bluish colour on the foam skeleton and this has been reported in available literature [166].

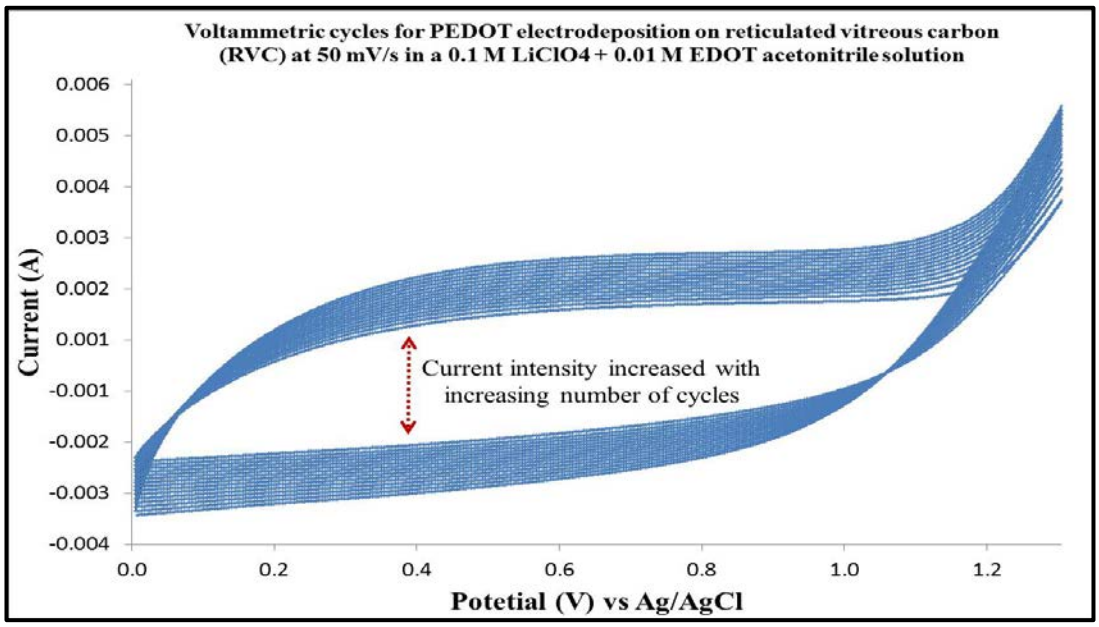

Figure 3.1: Cyclic voltammetry of RVC electrode in a solution containing 0.01 M EDOT and 0.1 M $LiClO_4$ in acetonitrile, using a three-electrode system; RVC electrode and Ag/AgCl (3M NaCl) were used as counter electrode (CE) and reference electrode (RE), respectively.

3.3.1.2 Polymerization Mechanism of PEDOT

The oxidation of EDOT to form PEDOT is similar to the oxidative polymerization of pyrrole [287]. The stepwise reaction mechanism of PEDOT is widely accepted for PEDOT oxidative polymerization [101, 288-290] which is

schematically shown in Figure 3.2. The first step generates a radical cation that has several resonance forms by oxidation of EDOT monomer. The second step is the combination of two radicals and subsequent deprotonation to form a neutral dimer. Substitution of the EDOT thiophene ring allows formation of new bonds. The dimer can be oxidized to form another positively charged radical that repeats the coupling and deprotonation steps with other monomeric or oligomeric cations. The alternating single and double bonds of the oligomers are π-conjugated, which delocalizes the electrons and decreases the oxidation potential. These stepwise reactions are repeated continuously to form the PEDOT polymer coated RVC electrode.

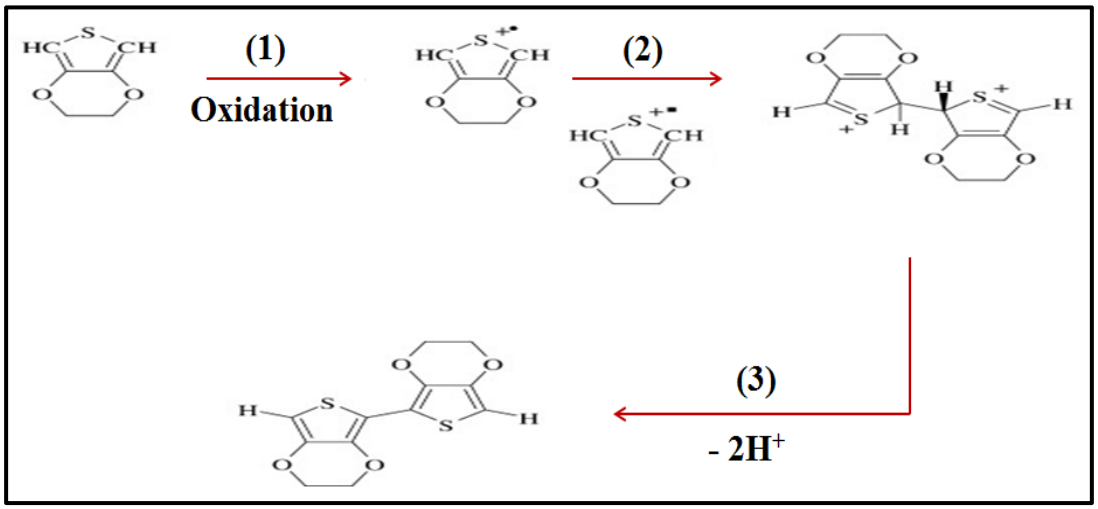

Figure 3.2: Scheme of oxidative polymerization mechanism of PEDOT.

3.3.1.3 Effect of applied constant potential on PEDOT electrosynthesis

Chronoamperometry was used to deposit PEDOT on RVC electrodes. The aim of this experiment is to study the effect of increasing the constant potential on electrochemical polymerization and to determine the best constant potential to be used for further experiments. These potentials were selected based on the CV of PEDOT growth (Figure 3.1) obtained previously, that showed no over-oxidation of

the polymer because polymer growth continued to increase with increasing number of cycles. Current–time curves for the electrodeposition of EDOT by potential steps 1.1V, 1.2V and 1.3V are shown in Figure 3.3. All these curves attain to the same charge consumed of 48 C. It is clear that the general features of these curves are similar to those reported in the literature [291-293]. The current starts to increase because the molecules of monomer diffuse from the solution to the electrode surface and, once they are oxidized, return to the solution where the oligomerization process occurs in the vicinity of the electrode surface. When an oligomeric high density region is established, clusters are deposited onto the electrode creating the growing nuclei. After that, the current increases until it reaches a current plateau. This region is generally attributed to nucleation and growth. Figure 3.3 also shows that PEDOT electrodeposition on RVC at a constant voltage of 1.1V was too slow and it took time (around 160 min) to attain a charge consumed of 48 C. It can be observed that when the constant potential applied was increased from 1.1 V to 1.2 V and 1.3 V, the current increased as expected. This led to a decrease in the time required to electrodeposit PEDOT on the RVC. For example, the same RVC electrode at a constant potential of 1.3V required 20 min to attain the same charge consumed of 48C. It is clear that the polymerization time decreased 8 times at 1.3 V compared with that at 1.1V. In addition, when the potential of deposition is increased, the porosity of PEDOT surface morphology is increased [105]. According to these reasons, the constant voltage of 1.3V was selected as the optimum potential to deposit PEDOT on RVC electrode using the potentiostatic mode in the work presented in Section (3.3.1.4.).

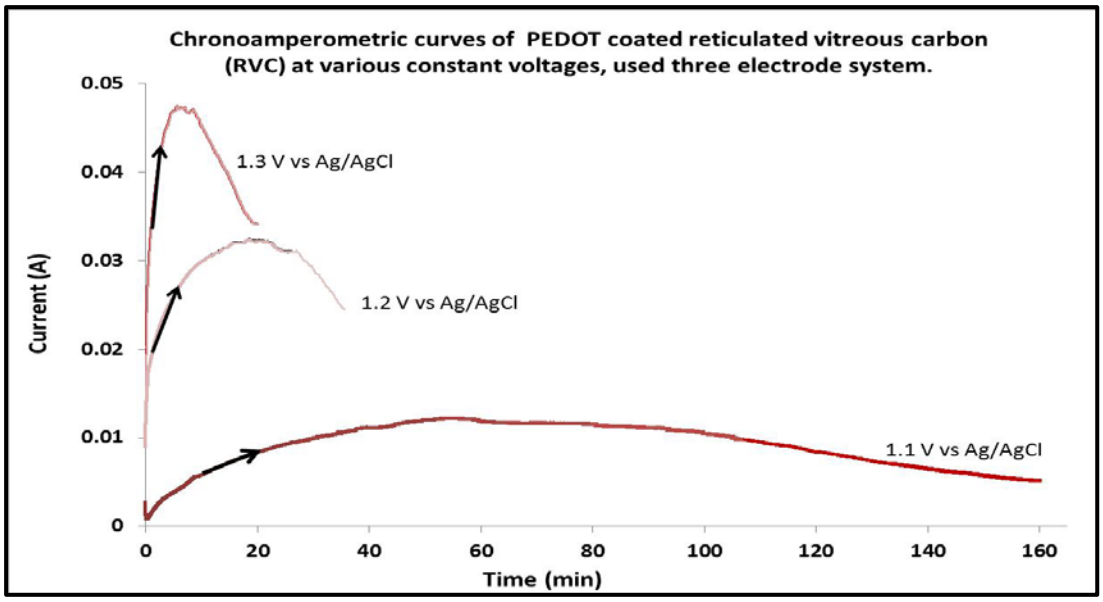

Figure 3.3: Chronoamperometric curves at various constant potential applied to coat RVC electrodes by PEDOT in a solution containing 0.01 M EDOT and 0.1 M $LiClO_4$ in acetonitrile, using a three-electrode system; RVC electrode and Ag/AgCl (3M NaCl) were used as counter electrode (CE) and reference electrode (RE), respectively.

3.3.1.4 Electrodeposition of different amounts of PEDOT on RVC electrodes.

The PEDOT films were electropolymerized onto (4*3.5*0.3 cm^3) RVC electrodes by applying a constant potential of 1.3 V vs Ag/AgCl until a polymerization time of 10, 20, 50, 70 and 120 min were reached. The aim of these experiments is to increase the amount of PEDOT on the RVC and consider the geometric volume of the PEDOT/RVC composite electrode when used in a capacitive deionization cell. Figure 3.4 shows a combination of chronoamperometric curves of PEDOT deposition on RVC electrodes and the arrows indicate the polymerization times for each electrode. It is clear that the chronoamperogram started at 0.19 A, then immediately rose sharply to 0.32 A within the first 5 min. After that the curve increased dramatically to reach 0.62 A after 35 min. The

chronoamperometric curve plateaued for 18 min then started to decrease steadily to 0.46 A when finally the current became almost stable. The charge consumed at each electrode was read directly from the I-V curve by computer and it was 20.64, 46.04, 112.71, 185.73 and 380.98 Coulombs (C) for polymerization times 10, 20, 50, 70 and 120 min, respectively. Table 3.1 shows the polymerization time, charge passed through the electrode, and the mass of PEDOT coating on the RVC electrode calculated using Equation 3.1. The PEDOT mass in each electrode increased with increase in polymerization time. It was 13, 29, 71, 117 and 240 mg for polymerization times 10, 20, 50, 70 and 120 min, respectively. The mass of a PEDOT coating on RVC electrodes was determined by the following equation [294, 295]:

$$m = \frac{(Q * M.wt_{EDOT}) + (Q * \gamma * M.wt_{ClO^4})}{n * F} \quad \text{(Eq 3.1)}$$

Where m is mass (g), $M.wt_{EDOT}$ is molecular weight (104.16 g/mol) of EDOT, $M.wt_{ClO_4}$ is molecular weight (99.45 g/mol) of ClO_4, Q is charge passed (C) on the working electrode, assuming the polymerisation efficiency was 100%, n is the number of electrons transferred which is 2.45 where two electrons are associated with polymerisation and 0.45 electrons (γ) are associated with doping of one monomer unit in PEDOT and F is the faraday constant (96485.34 C).

Example calculation the mass of PEDOT:ClO_4 from charge passed through the electrode:

If the charge passed through the electrode (Q) = 20.64 coulomb (C),

Then as we know from equation (3.1), ($m = \frac{(Q * M.wt_{EDOT}) + (Q * \gamma * M.wt_{ClO^4})}{nF}$)

so ($m = \frac{(20.64 * 104.16) + (20.64 * 0.45 * 99.45)}{2.45 * 96485.34}$)

m= 0.013 (g) = 13 (mg) PEDOT:ClO_4

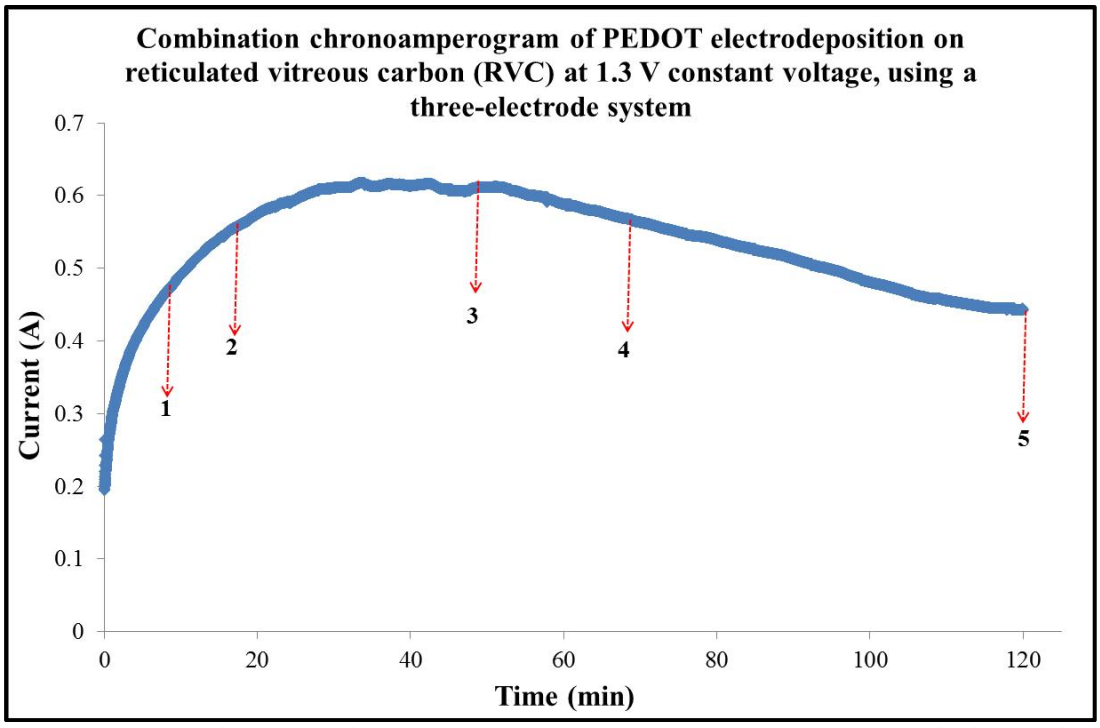

Figure 3.4: Combination chronoamperogram at 1.3 V constant potential obtained at RVC electrodes (4.2 cm^3) in a solution containing 0.01 M EDOT and 0.1 M $LiClO_4$ in acetonitrile, using a three-electrode system; RVC electrode and Ag/AgCl (3M NaCl) were used as counter electrode (CE) and reference electrode (RE), respectively.

Table 3.1: Charge consumed during polymerization, polymerization time and mass of PEDOT coating on RVC electrode calculated by Equation 3.1.

Sample	Polymerization time (min)	Charge consumed (C)	Mass of PEDOT-ClO_4 (mg)
PEDOT-10min/RVC	10	20.64	13
PEDOT-20min/RVC	20	46.04	29
PEDOT-50min/RVC	50	112.71	71
PEDOT-70min/RVC	70	185.73	117
PEDOT-120min/RVC	120	380.98	240

3.3.2 PEDOT surface properties

Scanning electron microscopy (SEM) was used to access information about PEDOT formation and its morphology along the RVC thickness. Figure 3.5 shows the SEM micrographs for 10 min electrodeposited PEDOT on RVC electrode. Figure 3.5 (a) confirms that 10 min polymerization was enough to uniformly cover PEDOT on the RVC electrode and the average size of the pores of 60 ppi RVC is about 350 µm. It is clear that the surface of PEDOT coating is rough (Figure 3.5 (b)) and highly porous (Figure 3.5 (c)). This morphology can enhance the performance of PEDOT because of high conductivity, increased electrode surface area and specific capacitance, and macroporous structure of RVC electrode. Figure 3.5(d) shows the cross-section of a region of PEDOT/RVC composite electrode and it can be observed that the average thickness of PEDOT covering the RVC is around 280 nm.

Figure 3.6 shows a SEM of PEDOT coated RVC electrode prepared with 120 min electropolymerization of EDOT. It is very clear that the original pores of the RVC electrode about 350 µm size are not significantly affected by the PEDOT

coating, and the average size of the composite electrode pores have become about 320 µm (Figure 3.6 (a)). The PEDOT possesses an extraordinary porous and loose structure with honeycomb-like fine structure. The fine structure of PEDOT shows a flower-like morphology, consisting of numerous thin flakes with numbers of macropores and micropores as seen in Figure 3.6 (b and c). The appearance of this structure is assumed to be related to the fast kinetics and will be useful for use as a CDI electrode.

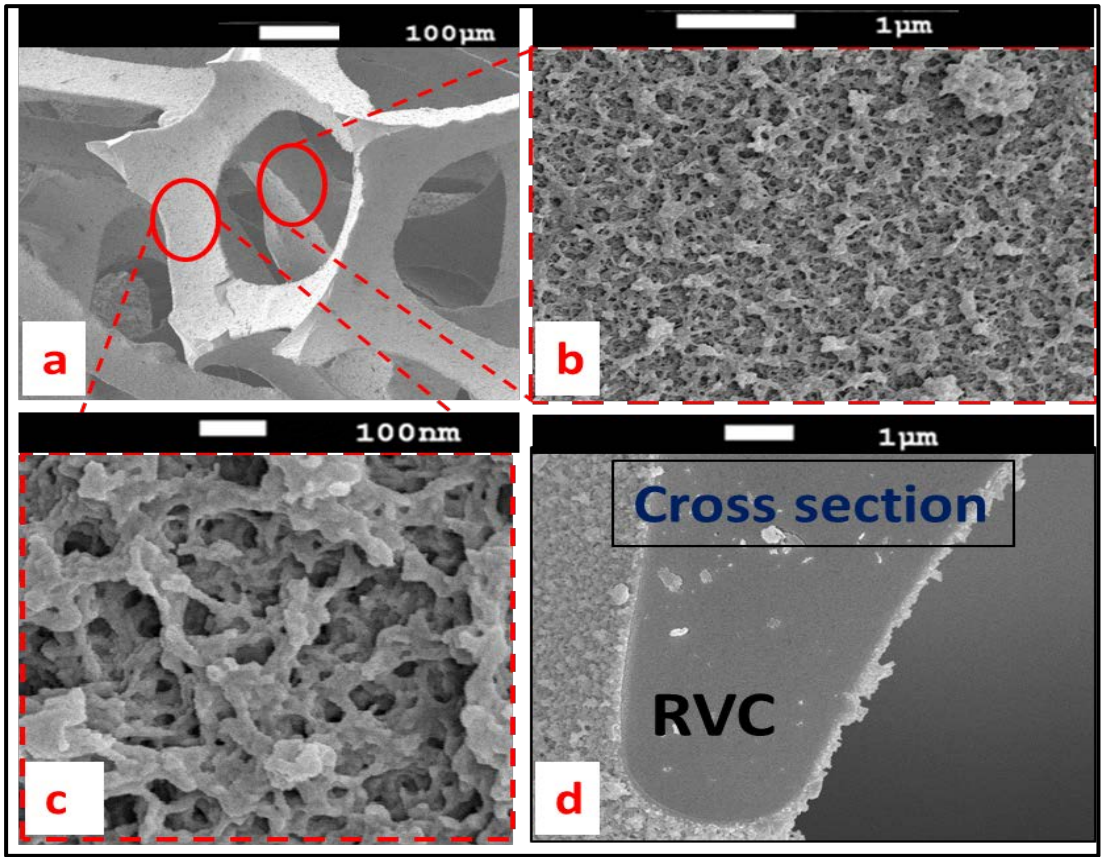

Figure 3.5: SEM of PEDOT coated RVC electrode for 10 min electropolymerization at 1.3V. Top surface (a,b,c) and cross-section (d).

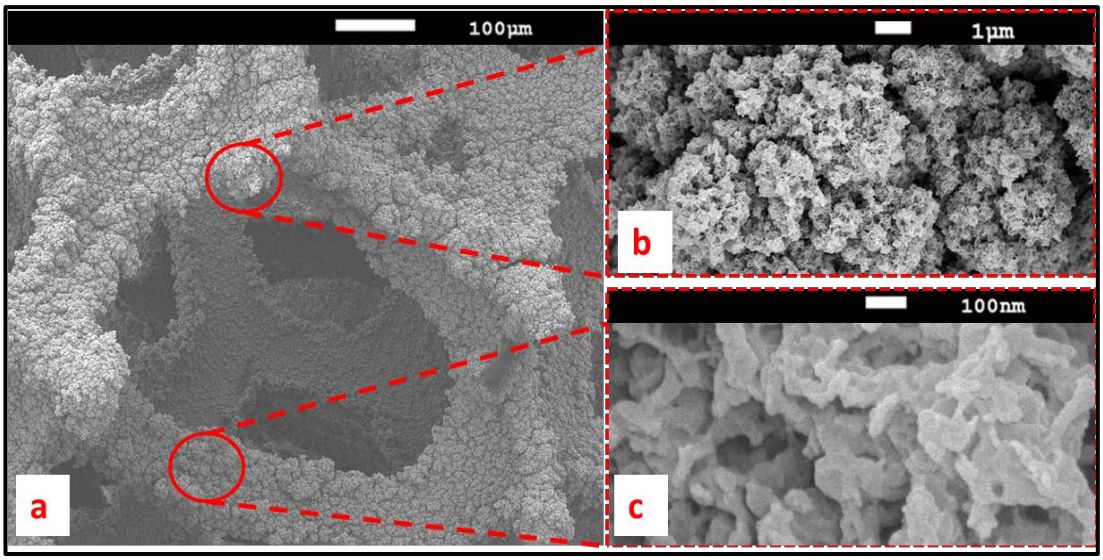

Figure 3.6: SEM of PEDOT coated RVC electrode for 120 min electropolymerization at 1.3V, showing the top surface.

The morphology of the electrosynthesised PEDOT on RVC electrode is affected by polymerization time. The PEDOT amount increased with increased polymerization time as discussed above. Figure 3.7 shows SEM images of the strut of the RVC electrode after coating by PEDOT at various polymerization times. It is clear that PEDOT of relatively smoother surface covered all the strut of RVC after 10 min polymerization (Figure 3.7 (a)) and the surface roughness was increased with increased polymerization time as seen in Figure 3.7 (c, e, g and i). After 20 min polymerization, a globular structure of PEDOT started growing. Moreover, the PEDOT globular structure increased upon increasing the polymerization time and also the porous morphology increased as a function of polymerization time. The thicknesses of PEDOT deposited on RVC electrodes were measured from the SEM image (Figure 3.7 (b, d, f, h and j)). The thicknesses of PEDOT were 0.28, 0.61, 1.12, 2.53 and 4.64 µm at 10, 20, 50, 70 and 120 min electropolymerization, respectively.

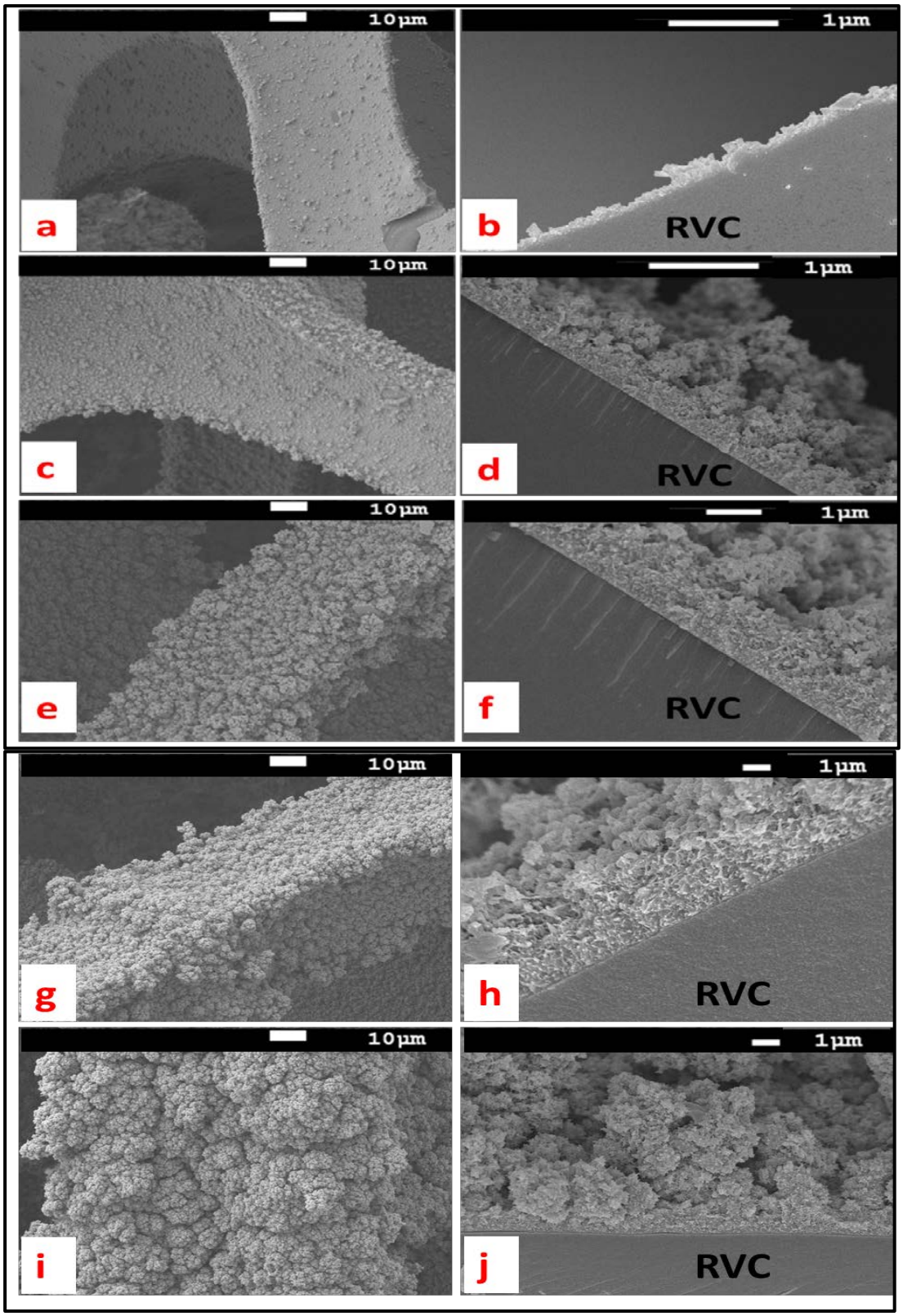

Figure 3.7: The top surface and cross-section of PEDOT coated RVC strut for 10 min polymerization (a,b), for 20 min polymerization (c,d), for 50 min polymerization (e,f), for 70 min polymerization (g,h) and for 120 min polymerization (i,j), respectively.

3.3.3 Thermogravimetric analysis

The thermal stability and the amount of PEDOT coated on RVC electrodes were determined from the thermogravimetric analysis (TGA) curves which give the dependence of the weight loss of a sample as a function of temperature or time. Figure 3.8 shows TGA curves of pure RVC electrode and various PEDOT/RVC composite electrodes. It can be seen that the TGA curve of the RVC electrode exactly matches those reported in literature [86, 296], where 10% of the initial weight loss occurred between 25 $^{\circ}$ and 250 ºC, then it was stable and did not show a dramatic decomposition in the tested temperature range between 250 ºC and 550 ºC followed by a major weight loss between 550 ºC and 700 ºC. The TGA curve of the PEDOT/RVC composite electrode consisted of three stages [297, 298]; volatilization, decomposition of PEDOT and carbonization reaction. All PEDOT/ RVC composite electrodes followed the same behaviour. The first 10% weight loss almost happened up to the temperature of 250 ºC (Stage 1). This was probably due to desorption of moisture and contaminant. Furthermore, the major weight loss between 550 ºC and 700 ºC (Stage 3) was most likely due to carbonization by breaking chemical bonds such as C-H. It is clear that all composite electrodes followed a similar decomposition with temperature in Stage 2. From 250 ºC a continuous degradation occurs until major decomposition occurred in the region between 350 ºC to 550 ºC. Therefore in this Stage 2, the amount of PEDOT in the various composite electrodes were calculated by loss in weight due to decomposition, and found to be 4, 9, 20, 31 and 56 % for 10, 20, 50, 70 and 120 min electropolymerization, respectively. In addition, almost no weight loss occurred after 700 ºC.

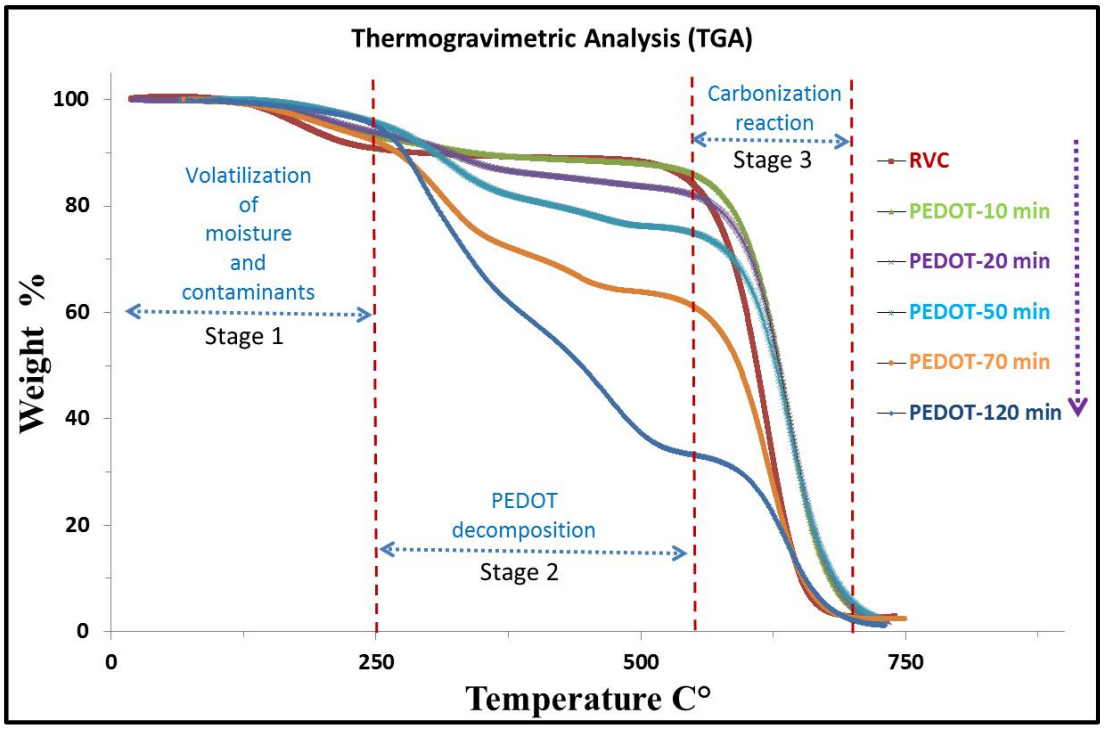

Figure 3.8: TGA curves of pure RVC electrode and various PEDOT/RVC composite electrodes.

3.3.4 Raman spectroscopy

The Raman spectrum of the RVC substrate is shown in Figure 3.9 and is in keeping with published reports for RVC electrodes [299, 300]. It has a typical two bands spectrum of disordered polycrystalline and noncrystalline graphitic carbons. The first band at 1360 cm^{-1} is called the D-band and the second band at 1600 cm^{-1} is called the G-band (graphitic) which is attributed to the graphite basal plane. Figure 9 shows the Raman spectra of RVC electrode after polymerizations that afford some information about the PEDOT structure. They confirm that the surface of RVC electrodes were coated by PEDOT. The principal assignaments of the main bands have been made considering the data reported in literature (Table 2) [283, 301-303]. Raman spectra of composite electrodes have seven strong bands that dominate the

spectrum which are related to the PEDOT vibrational spectrum. The most intense is at 1423 cm^{-1} which can be assigned to the symmetric $C_\alpha=C_\beta$ (-O) stretching. Asymmetric C=C stretching shifts from 1509 cm^{-1} to 1507 cm^{-1} and at 1364 cm^{-1} appears a peak related to $C_\alpha=C_\beta$ stretching. The asymmetric C_α-C_α- (inter-ring) stretching band is located at 1257 cm^{-1}. The C-O-C deformation, which appears at 1152, 1120 and 1085 cm^{-1} peaks, combines as one peak at 1098 cm^{-1}. Oxyethylene ring deformation peaks appear at 988 and 570 cm^{-1}. Also, the other peaks observed in the Raman spectrum of PEDOT coated RVC electrode are at 848 cm^{-1} (related to C–H bending of 2,3,5-trisubstituted thiophene due to α,α′ polymerization) and 685 cm^{-1} (symmetric C-S-C deformation). These results indicate that RVC electrodes do not affect the PEDOT structure.

Table 3.2: Calculated Raman band wavenumbers and vibrational assignments of PEDOT.

Description of the vibration	cm^{-1}	Description of the vibration	cm^{-1}
asym C=C str	1509	C-O-C def	1152, 1120 and 1085
CH_2 Scissoring	1477	Oxyethylene ring def	988
Sym C_α = C_β(-O) str	1426	ClO_4^-	933
C_β = C_β str	1365	C–H bending	806
C_α = C_α str	1252	Sym C-S-C def	690
C_α = C_α str	1236	Oxyethylene ring def	572

Key: str, stretching; def, deformation.

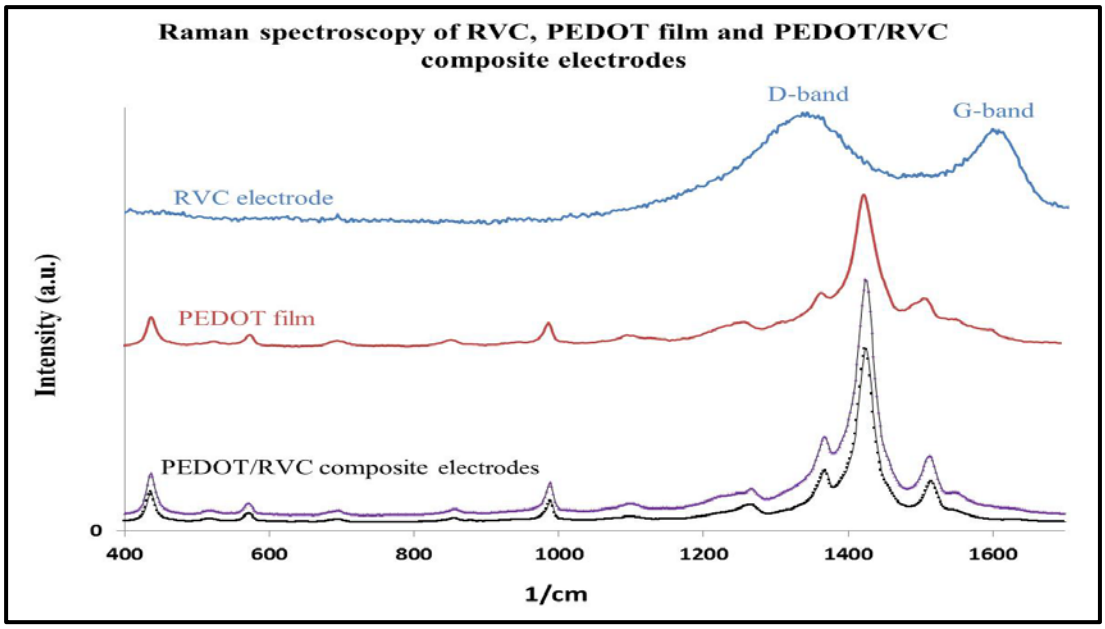

Figure 3.9: Raman spectra of PEDOT-ClO_4 grown by chronoamperometry at 1.3 V in acetonitrile containing 0.01 M EDOT and 0.1 M $LiClO_4$.

3.3.5 Electrochemical characterizations

Cyclic voltammetry was used to evaluate the electrochemical properties of the PEDOT/ RVC composite electrodes. In this chapter, the effect of coating RVC by PEDOT on electrode capacitance, the effect of increasing scan rate on electron transfer and capacitance and the stability of the electrode are considered.

3.3.5.1 Comparison between RVC before and after PEDOT coating.

Figure 3.10 (a) shows the cyclic voltammograms of 1 cm^3 RVC electrode and same electrode coated by PEDOT (PEDOT-120min/RVC electrode) at the scan rate of 5 mV/s. It is clear that the CV curve of RVC compared with PEDOT coated electrode is very small. The capacitance of the RVC electrode in terms of geometric volume as calculated using Equation (3.3) is 0.002 F/cm^3 (see Section 3.3.5.3). The current of PEDOT-120min/RVC composite electrode compared to a bare RVC

electrode of same geometric volume has increased by a factor of 2230. This is related to the large surface area of PEDOT compared to a RVC electrode according to the Randle-Sevcik relationship [304]. Figure 3.10 (b) shows the effect of increasing PEDOT in geometric volume of RVC on specific capacitance. It can be observed that the capacitance increased when polymerization time of PEDOT increased. The RVC geometric volume capacitance has increased by a factor of 220, 485, 1045 and 1710 at PEDOT coated RVC, where the PEDOT polymerization time was 10, 20, 50 and 70 min. The capacitance of PEDOT coated RVC electrodes at various polymerization time and various scan rates will be discussed more fully in Section 3.3.6.3.

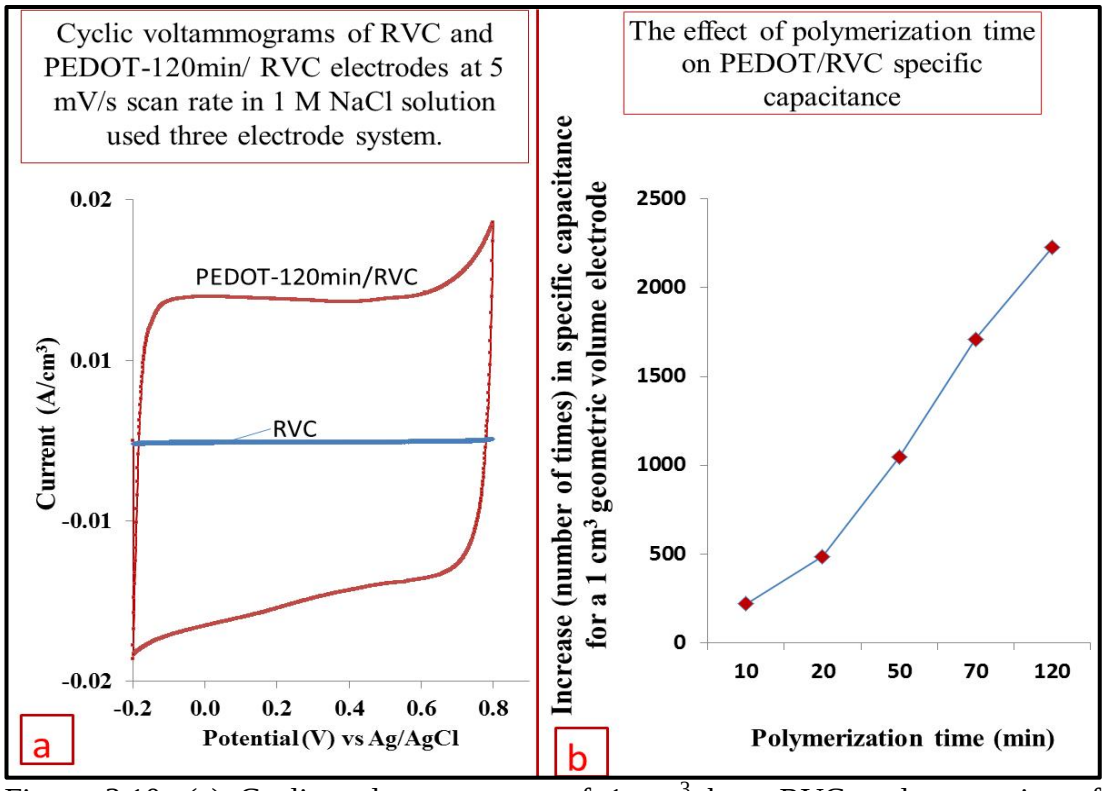

Figure 3.10: (a) Cyclic voltammograms of 1 cm^3 bare RVC and same size of PEDOT-120min/RVC composite electrode in 1M NaCl using a scan rate of 5 mV/s and Ag/AgCl reference electrode. (b) Effect of increasing polymerization time of PEDOT on the specific capacitance of PEDOT/RVC electrodes.

3.3.5.2 Effect of increasing scan rate on the electrode capacitance

In this study, the PEDOT-120min/RVC composite electrode was also selected for the same previous reasons. Figure 3.11 shows the cyclic voltammograms of PEDOT-120min/RVC composite electrode obtained at various scan rates of 5 to 200 mV/s. It can be noted that the shape of the CVs at scan rates up to 50 mV/s were nearly semi-rectangular and highly symmetrical (Figure 3.11 (a)) which indicates an ideal behaviour characteristic of double layered mechanism, fast charge/ discharge process, with insignificant ohmic resistance. The reason for its novel fast charge/discharge ability is that its granules are small and so encourages a large amount of meso-channels in the PEDOT/RVC composite, as shown in Figure 3.6, that can effectively reduce the diffusion length of ions (L) so as to reduce the diffusion time (t), which can be estimated as (L^2/D) where D is the diffusion coefficient [305]. This shape helps to achieve a constant specific capacitance [249]. Furthermore, as the scan rate increased the peak current also increased linearly (inset in Figure 3.11 (a)). This result is similar to those published in the literature [306, 307]. On other hand, when the scan rate was increased above 50 mV/s, the curves were characterized by non-rectangular shapes (Figure 3.11 (b)). This indicated resistance-like electrochemical behaviour because the electrode is very porous which hinders the migration of NaCl to the pores, and this becomes pronounced at increasing scan rates. This leads to a continuous decrease in the capacitance of electrodes with increasing scan rate; which is discussed in Section 3.3.6.3.

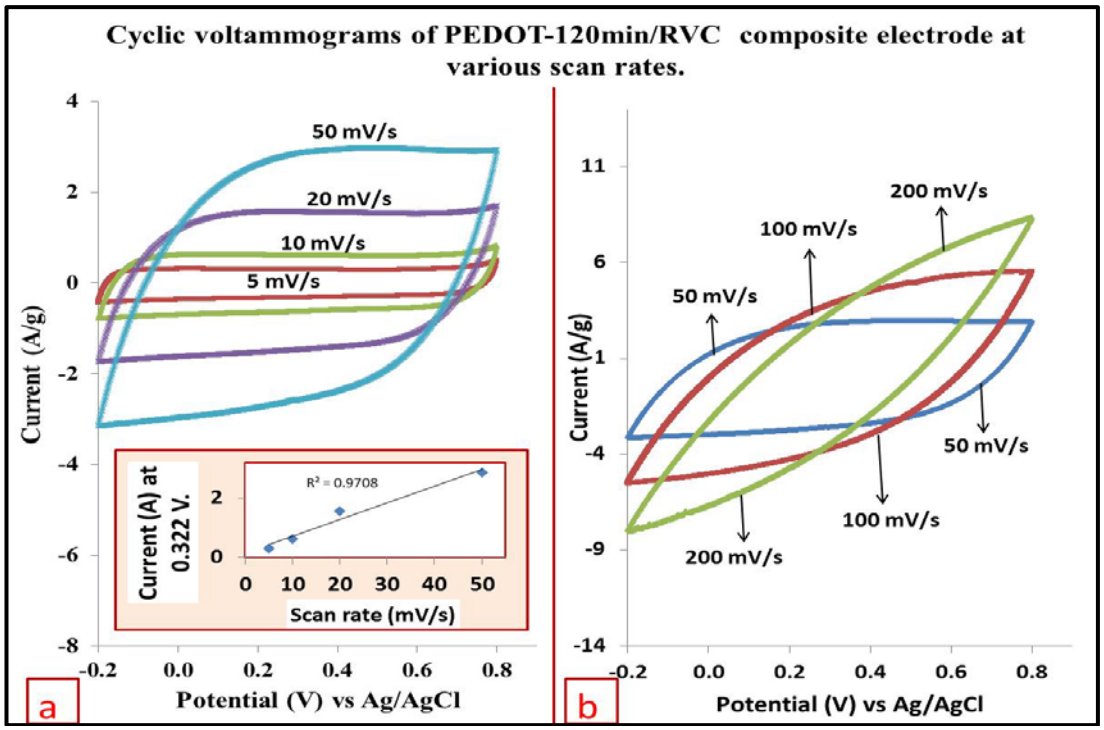

Figure 3.11: Cyclic voltammograms of PEDOT-120min/RVC electrode at: (a) 5 to 50 mV/s scan rates and (b) 50 to 200 mV/s scan rates in a three-electrode systems in 1 M NaCl solution.

3.3.5.3 Capacitance

The capacitive behaviour of the PEDOT resulted mainly from electrochemical double-layer charging. The specific capacitances of PEDOT/RVC electrodes were calculated from the CV curves of PEDOT coated RVC electrodes using a three-electrode system at different scan rates of 5 to 200 mV/s, as shown in Figure 3.12 (a). It is observed that PEDOT has high capacitive behaviour, and increasing the amount of PEDOT into the RVC electrode led to a decrease in the capacitance of the composite electrode. The specific capacitance of the PEDOT was significantly decreased from185.29 F/g to 86.56 F/g when the polymerization time of PEDOT in the composite electrode was increased from 10 to 120 min, determined at a low scan rate of 5 mV/s. The value of specific capacitance of PEDOT at PEDOT-10min/RVC

electrode was very close to the value of theoretical specific capacitance (210 F/g) [308]. Furthermore, the specific capacitances of PEDOT coated RVC electrodes, in all electrodes, were found to be very high compared with other PEDOT studies [308-310] at low scan rate but its capacitance markedly decreased at high scan rates. The specific capacitance of the PEDOT-10min/RVC was significantly decreased from 185.29 to 83.57 F/g as the potential scan rate was increased from 5 to 200 mV/s, as shown in Table 3.3. These results are in keeping with published reports for all cases of PEDOT [308, 311, 312]. It can be seen that the specific capacitance trend of all PEDOT electrodes decrease, when the scan rate was increased above 50 mV/s. It should be noted that the specific capacitance values in term of mass of all electrodes were calculated by Equation (3.2). As mentioned before, the aim of this chapter is to discuss the effect of increasing PEDOT amount in terms of geometric volume and area of the electrode on the capacitance results.

Figure 3.12 (b) shows the comparison cyclic voltammograms for the same PEDOT/RVC electrodes using current per gram of PEDOT and current per geometric volume of electrode. It is very clear that current behaviour in geometric volume unit was totally opposite to the current behaviour in units of gram. Therefore, the capacitances per unit geometric volume of PEDOT/RVC electrodes were calculated using Equation (3.3) and are presented in Table 3.3 as F/cm^3. The capacitance was 0.65 F/cm^3 for the PEDOT-10min/RVC and 6.18 F/cm^3 for the PEDOT-120min/RVC a low a scan rate of 5 mV/s. This indicates that the surface area of PEDOT coated in the RVC electrode was increased by increasing the amount of PEDOT, and the porous structure enhanced. Figure 3.12 (c) shows that the trend

of the capacitances in (F/cm^3) was completely opposite to the direction of the trend for capacitance per gram.

Furthermore, the capacitance per unit geometric area was calculated using Equation (3.4) and are reported in Table 3.3 as F/cm^2. It is expected that the capacitance (F/cm^2) behaviour of electrodes followed the capacitance (F/cm^3) behaviour. The capacitance has increased by a factor of 10 with increasing loading of PEDOT; that is, PEDOT-10min/RVC electrode compared with PEDOT-120min/RVC electrode.

The specific capacitance of a PEDOT coating on RVC electrodes was calculated according to the following equations [313, 314]:

$$C_{mass} = Q/(2*m*\Delta V) \quad (Eq\ 3.2)$$

$$C_{volume} = Q/(2*Z*\Delta V) \quad (Eq\ 3.3)$$

$$C_{area} = Q/(2*A*\Delta V) \quad (Eq\ 3.4)$$

Where C_{mass}, C_{volume} and C_{area} are capacitance of electrode in term of F/g, F/cm^3 and F/cm^2 respectively, Q is charge (C), m is mass (g), Z is geometric volume (cm^3), A is geometric area (cm^2) and V is voltage (V).

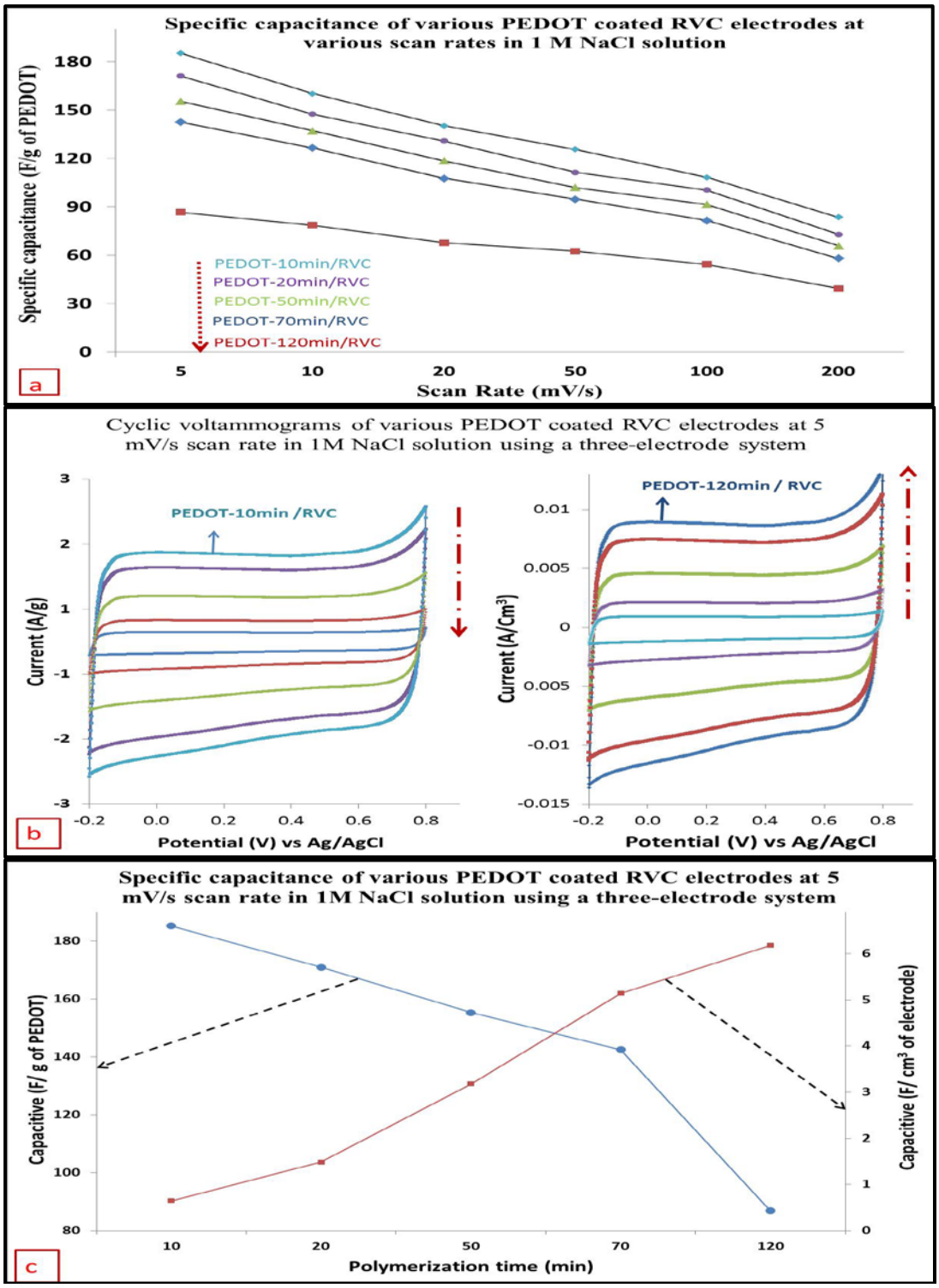

Figure 3.12: (a) The specific capacitance (F/g) of PEDOT/RVC electrodes at various scan rates. (b) Cyclic voltammograms of PEDOT/RVC electrodes using current per gram of PEDOT and current per geometric volume of electrode at 5 mV/s scan rate. (c) The specific capacitance of PEDOT/RVC electrodes in terms of F/g and F/cm^3 at 5 mV/s scan rate. Electrolyte: 1 M NaCl solution. Potential range: between -0.2 to 0.8 V vs Ag/AgCl using a three-electrode system.

Table 3.3: Specific capacitance of PEDOT/RVC electrodes measured in various units at various scan rates.

Composite electrode	PEDOT-10min /RVC	PEDOT-20min /RVC	PEDOT-50min /RVC	PEDOT-70min /RVC	PEDOT-120min /RVC
Scan rate (mV/s)	Capacitance F/g				
5	185.29	171.04	155.36	142.53	86.56
10	160.12	147.41	137.16	126.51	78.62
20	140.15	130.90	118.63	107.59	67.77
50	125.66	111.32	102.04	94.78	62.41
100	108.23	100.36	91.52	81.47	54.34
200	83.57	72.95	65.81	57.96	39.45
Composite electrode	PEDOT-10min /RVC	PEDOT-20min /RVC	PEDOT-50min /RVC	PEDOT-70min /RVC	PEDOT-120min /RVC
Scan rate (mV/s)	Capacitance F/cm^2				
5	0.08	0.19	0.41	0.66	0.80
10	0.07	0.17	0.36	0.59	0.73
20	0.06	0.15	0.31	0.50	0.63
50	0.06	0.12	0.27	0.44	0.58
100	0.05	0.11	0.24	0.38	0.50
200	0.04	0.08	0.17	0.27	0.36
Composite electrode	PEDOT-10min /RVC	PEDOT-20min /RVC	PEDOT-50min /RVC	PEDOT-70min /RVC	PEDOT-120min /RVC
Scan rate (mV/s)	Capacitance F/cm^3				
5	0.65	1.48	3.18	5.14	6.18
10	0.56	1.28	2.81	4.57	5.62
20	0.49	1.14	2.43	3.89	4.84
50	0.44	0.97	2.09	3.42	4.46
100	0.38	0.87	1.87	2.94	3.88
200	0.29	0.63	1.35	2.09	2.82

3.3.5.4 Cycling stability of PEDOT/RVC electrodes

Stability is one of the most critical characteristics and electrodes with poor mechanical and electrochemical stabilities may lose their function. The electrochemical cycling performance of the PEDOT/RVC electrodes was investigated for 200 cycles at 5 mV/s, as shown in Figure 3.13. It can be observed that the CVs' shape do not change much and are almost identical at the beginning and end of the stability test as shown in other studies [315]. The PEDOT-120min/RVC electrode shows quite good cycling stability and retains approximately 96% of its current density after 200 cycles. The loss may be due to the irreversible reactions of the PEDOT backbone, which represents a deterioration of the electrochemical reversibility [316]. The 3D mesoporous network structure can enable PEDOT to avoid shrinkage during continuous quick charging/discharging [317].

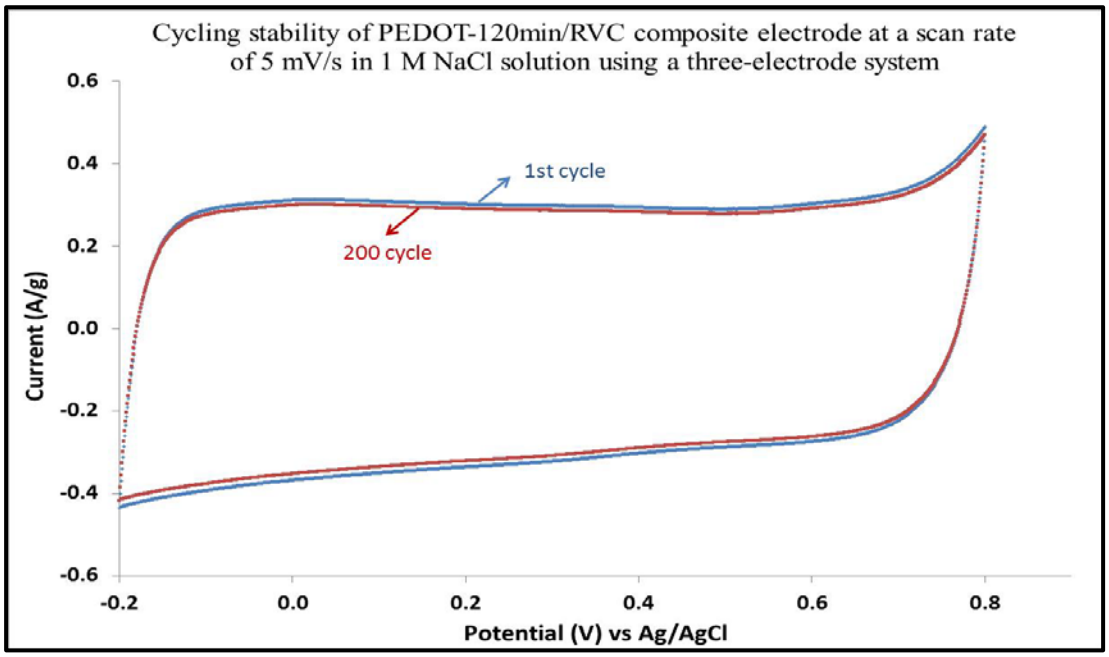

Figure 3.13: The electrochemical cycling stability of PEDOT-120min/RVC electrode in 1 M NaCl solution recorded in the potential range between -0.2 to 1.0 V vs Ag/AgCl using a three-electrode system at 5 mV/s scan rate for 200 cycles.

3.3.6 Construction of a capacitive deionization cell

Capacitive deionization experiments were carried out in a flow-through system, depicted in Figure 3.16 (a). The CDI unit cell consisted of a flow-through cell which has two parallel electrodes that allows aqueous solution to stream between them, and the spacing of 5 mm between the electrodes is maintained.

3.3.6.1 CDI flow-through open cell fabrication

Lawrence Livermore National Laboratories in USA, designed a CDI unit as a closed system to force water flow into all the pores of the electrodes [11]. It had a retaining plate, rubber gasket, electrode, rubber spacer and nylon spacer [40] and it usually was modified by researchers to make it suitable for their applications [5, 11, 34-39, 41, 43, 44, 46-52, 318, 319].

A flow-through electrode was prepared for use in this CDI cell and this electrode has low hydraulic resistance. This means that water flow will easily flow through all the pores of the electrodes in a CDI flow-through cell as shown in Figure 3.14 (b). This cell was designed in our laboratory and it was built by printing on a Connex 350 3D printer, by Objet. This printer built our cell with UEROBACK material over a period of three hours. After that, it was washed with water in readiness for use in the CDI system. The cell production was basic, easy and fast, very accurate and resulted in a strong product. In this cell, we avoided using rubber gaskets, nut tool, threaded rods and insulator layer between electrodes. Also, the electrical contact with electrodes was good and very easy. Furthermore, this cell has a rectangular external (Figure 3.14 (b)) and H-like internal (Figure 3.14 (c)) shapes. The dimensions of the outside cell was 57 mm *62 mm* 32 mm in height, length and

width, respectively. Each side had one 4 mm diameter hole for solution flow, one near the top and the other near the bottom. These holes are connected with 250 mm (MasterFlex L/S® 25) pump tubing to a peristaltic pump in a recirculating fashion (Figure 3.14 (a)). It is worth noting that the middle of both sides of the cell was fitted with 35mm * 35 mm glass windows to allow light to be directed through the cell to the electrodes. This was designed to be suitable for any future studies that need to use light for excitation of the electrodes. This glass was of dielectric material, transparent and allows all wavelengths to pass through it. Moreover, the H-shape was designed inside the cell to be suitable for holding a glass conductivity electrode (4mm thickness) inside the cell if needed for any relevant applications. The dimensions inside the cell were 50 mm *50 mm* 20 mm in height, length and width, respectively as shown in Figure 3.14 (c) (the top of the cell).

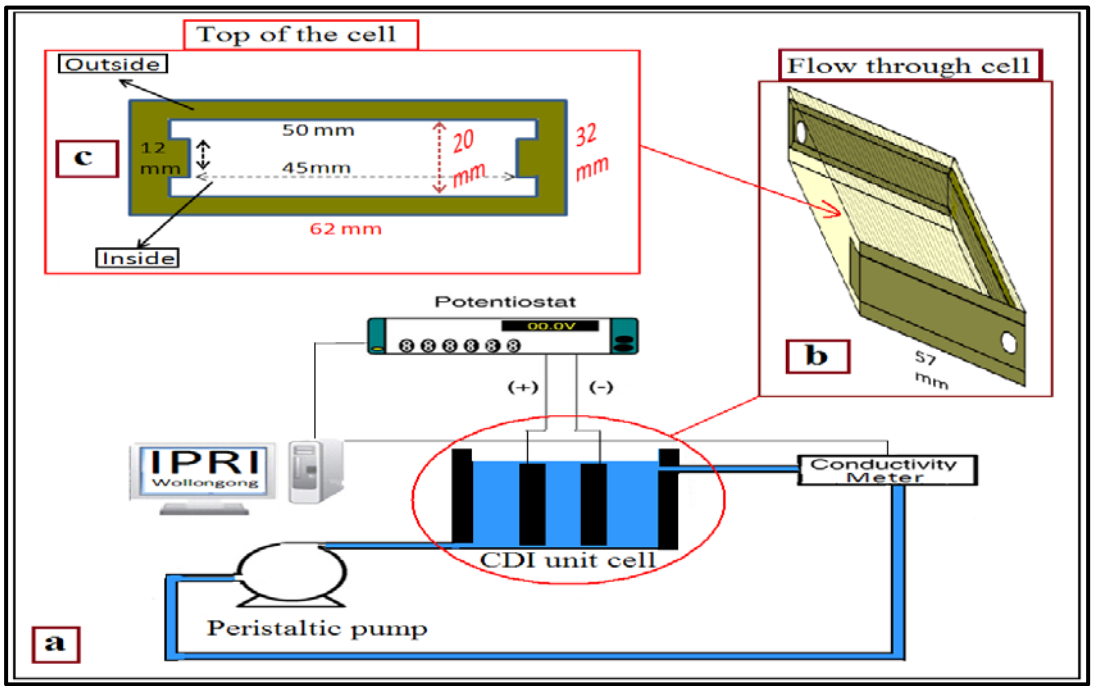

Figure 3.14: Schematic diagram of a capacitive deionization (CDI) cell.

3.3.7 Effect of working conditions on ion removal efficiency

The key factors that affect the performance of ion removal of NaCl onto the sites of PEDOT/RVC composite electrode, ie flow-rate and electrical voltage, were systematically investigated in this work. In this Section, the charge processes (voltage applied) were carried out for 2.5 min with 60 mL of the 75 mg/L NaCl solution (143 μS/cm) using a RVC electrode and Ag/AgCl electrode as counter and reference electrodes, respectively, and the solution temperature was maintained at 293 K.

3.3.7.1 Effect of applied voltage on ions removal

It is known that the oppositely charged ions are attracted to oppositely charged electrodes and the adsorption behavior of ion removal on the electrodes are affected by various direct electrical voltages applied [33]. In order to determine the greatest direct applied voltage that would be efficient in a CDI system, PEDOT-20min/RVC composite electrode (which has 29 mg PEDOT loading) was tested at four different applied voltages (0.6, 0.7, 0.8 and 0.9 V) at a volume flow-rate of 35 mL/min through a CDI cell (Figure 3.15 (a)). The stability of PEDOT in CVs that were discussed above in Section (3.2.1.l.) led to the selection of these voltages. Once the electric field was applied, the solution conductivity dropped dramatically because ions were attracted to the oppositely charged electrodes [33]. The CDI cell exhibited increased ions removal with increased applied voltage in the range of 0.6 V to 0.8 V. It was noticeable that the conductivity of NaCl solution decreased, once the electrode voltage was applied, to approximately 129.81 μS/cm, 126.89 μS/cm and 123.41 μS/cm at 0.6 V, 0.7 V and 0.8 V, respectively. The CDI process was very efficient at

0.8 V because of enhanced electrostatic forces, with a much poorer performance at 0.6 V. However, the conductivity change was not marked different at 0.9 V because the ions were adsorbed maximally at 0.8 V [33]. In the laboratory, when the electrical voltage was at 0.8 V, no visible gas bubbles appeared in the target solution, indicating that there was not any electrolysis of water taking place [268].

The electrosorption capacity, (calculated as explained in Section (3.3.9.)), shown in Figure 3.15 (b) gradually rose from 14.36 mg/g to 21.21 mg/g. It is obvious that the electrosorption capacity is dependent on applied voltage, and higher ion removal is achieved with higher voltage. The high electrical voltage results in high electrosorption capacity because of strong Coulombic interaction between the electrode and charged $Na^{+}$and Cl^{-}ions [40, 320]. However, the electrosorption capacity of the electrode at 0.9 V was exactly the same as the electrosorption capacity at 0.8V. Thus the optimum working voltage for all PEDOT/RVC electrodes as electrosorption electrodes was ascertained to be 0.8V and was selected for subsequent studies on the effect of flow-rate on ions removal in the CDI system; as reported in the next section.

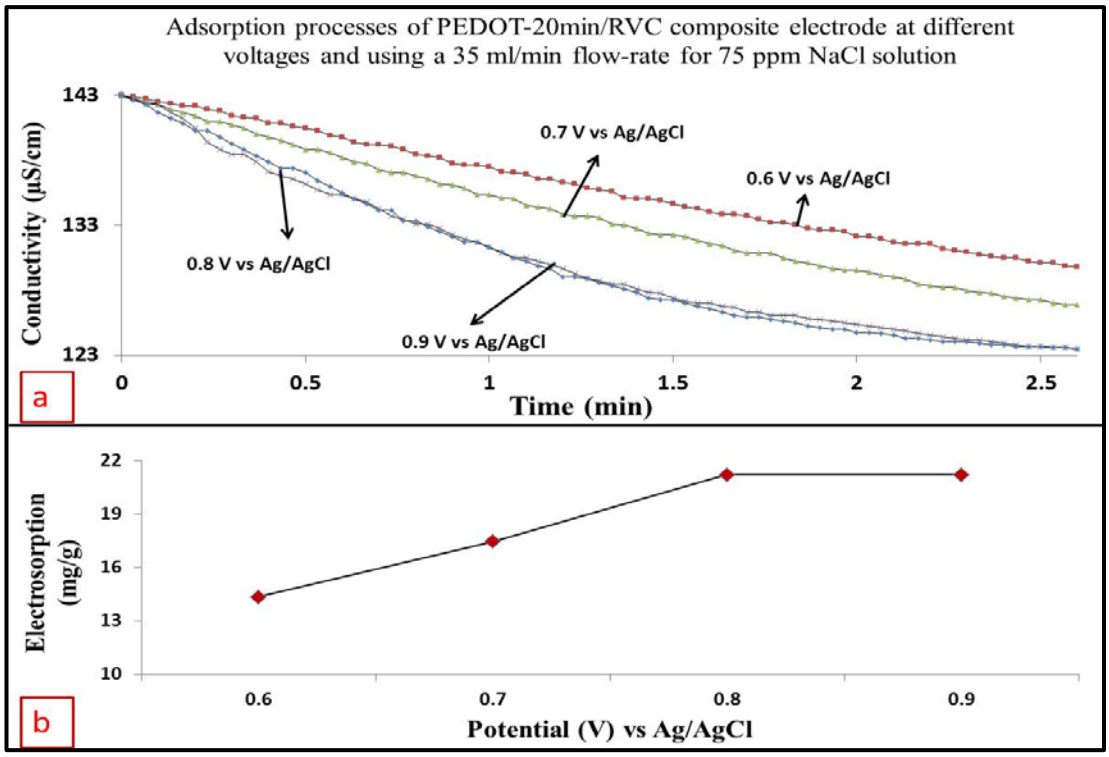

Figure 3.15: (a) Effect of applied voltage on electrosorption at a PEDOT-20min/RVC composite electrode using a 35 ml/min flow-rate and 75 mg/L NaCl feed solution. (b) Plot of electrosorption capacity as a function of electrical voltage.

3.3.7.2 Effect of flow-rate on ions removal

The effect of flow-rate on electrosorption performance of CDI was investigated using PEDOT-20min/RVC composite electrode by testing at seven different flow-rates (Figure 3.16). It is clear from the figure that at a lower flow-rate, such as 15 ml/min, the solution has a high conductivity 130.22 µS/cm because too low a pump rate will introduce a low pump force that is lower than the electrosorption force and therefore decrease the electrosorption amount [268]. The NaCl conductivity decreased when the flow-rate was increased up to 80 mL/min; which had a conductivity of 116.20 µS/cm after 2.5 min. This indicates accelerated adsorption of ions on the surface of the PEDOT/RVC electrode from the NaCl solution. However, it can be seen that the conductivity did not change significantly

when the flow-rate was increased from 80 mL/min up to 120 mL/min. This was due to the equilibrium between the electrostatic force of the electrode and the driving force in the flow-rate which did not significantly change when the flow-rate was increased. In this chapter the results showed that 80 mL/min was the optimum flow-rate.

Thus, methodical investigations have been done that demonstrated that an electrical voltage of 0.8 V and flow-rate of 80 ml/min were the optimum conditions and key factors which affected the NaCl ion removal performance onto the sites of the PEDOT/RVC electrode. These conditions were then applied to investigate the effect of PEDOT loading on NaCl ion removal efficiency as reported in the next section.

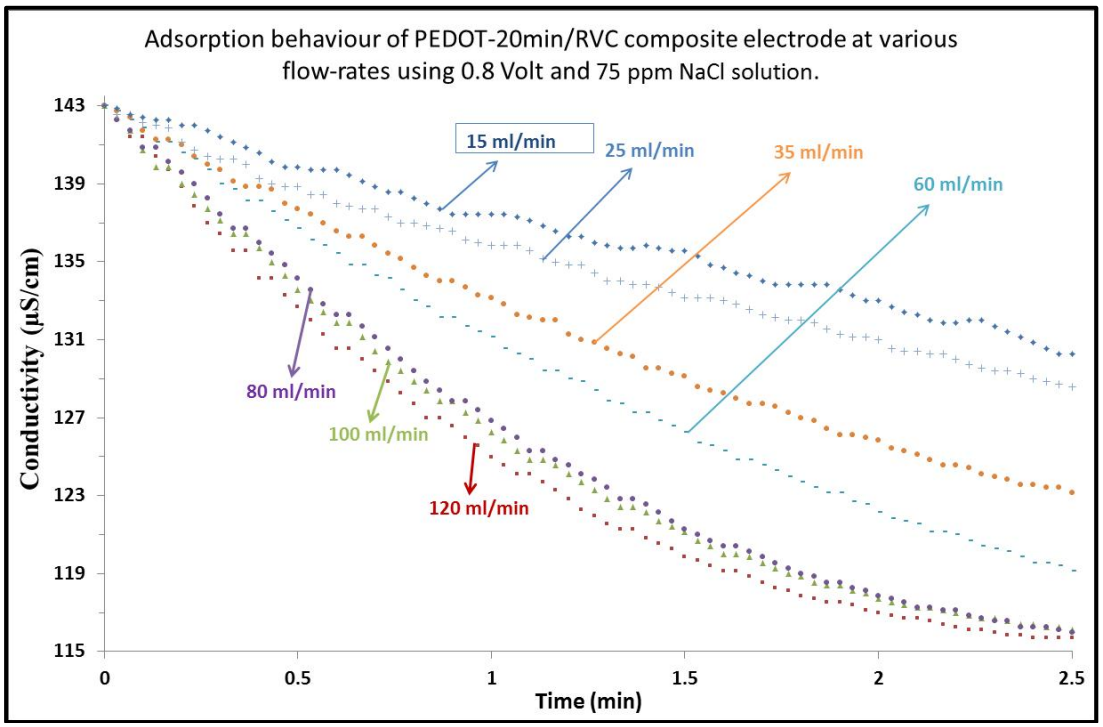

Figure 3.16: Effect of flow-rate on the electrosorption behaviour of PEDOT-20min/RVC composite electrode. Applied voltage: 0.8 V. Concentration of NaCl feed solution: 75 mg/L.

3.3.8 Effect of PEDOT loading of PEDOT/RVC electrode on ions removal

The CDI system was investigated with respect to the influence of increased loading of PEDOT into RVC electrodes on the ion removal performance (Figure 3.17). All experiments were performed with an electrical voltage of 0.8 V and a flow-rate of 80 mL/min through the CDI system, using 60 mL of the 75 mg/L NaCl solution, and solution temperature was maintained at 293 K. The adsorption processes at first took 5 minutes and the drop in conductivity increased with increasing amounts of PEDOT into the RVC electrode. This indicates that the increase of the amount of PEDOT loading leads to increase in the interaction between the charged surface of the electrode and charged Na^+ and Cl^- ions. The conductivity would gradually approach a constant minimum level, indicating that saturation was achieved. Notably, the highest drop in conductivity was around 54.21 μS/cm using the PEDOT-120min/RVC composite electrode. Furthermore, when the CDI system was under 0 V of applied voltage, the electrode can be quickly regenerated, that is, the adsorbed ions were desorbed from the electrodes due to the disappearance of electrostatic force. The discharge time was approximately 8 minutes; to release all the ions from the electrodes and return the solution conductivity to its initial level. These results suggest that the CDI process using PEDOT coated RVC electrodes have promise as an effective technology for desalination.

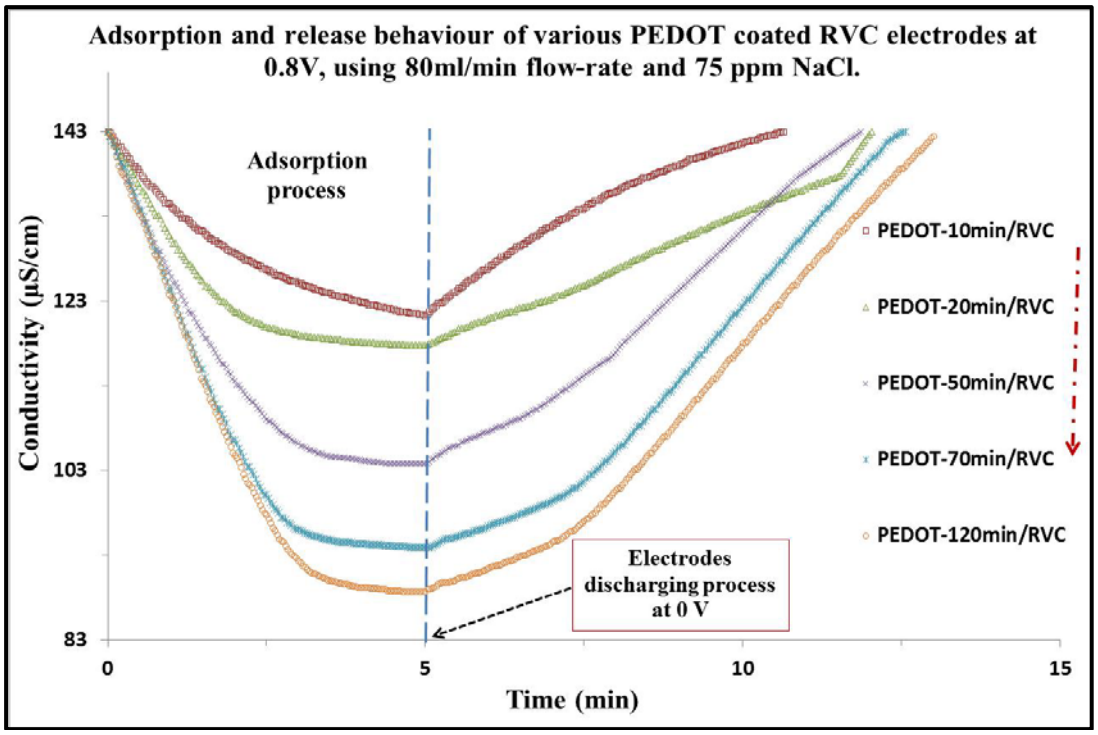

Figure 3.17: Effect of PEDOT loading of PEDOT/RVC electrode on ions removal efficiency using a CDI system. Applied voltage: 0.8 V. NaCl feed solution concentration: 75 mg/L. Flow-rate: 80 ml/min.

3.3.9 Electrosorption performance of PEDOT coated RVC electrode

This section calculates the electrosorption capacity of all electrodes applied in the previous Section (3.3.8.). The mass of PEDOT in the RVC electrodes, which have 4.2 cm^3 geometric volumes and 32.5 cm^2 geometric areas, are 13, 29, 71, 117 and 240 mg, respectively (as described in Section 3.3.1.4.). The variation of solution conductivity was monitored using a multi-function conductivity meter. Accordingly, the correlation between conductivity (µS/cm) and concentration (mg/L) was calibrated prior to experiments (Equation 2.9.).

The electrosorption performance of all PEDOT coated RVC electrodes are shown in Figure 3.18. The electrosorption per gram decreased with increasing mass

of PEDOT. Clearly, when the PEDOT-10min/RVC electrode had 13 mg of PEDOT, the electrosorption was 52.84 mg/g, and when PEDOT-120min/RVC electrode had 240 mg of PEDOT, the electrosorption was 6.52 mg/g (using Equation 3.5.). As mentioned before, our aim focuses on increasing the performance of the electrode in terms of geometric volume and area. Therefore, the electrosorption capacity per unit geometric volume and geometric area were calculated using Equation (3.6) and (3.7) respectively and are presented in Table 3.4 as mg/cm^3 and mg/cm^2 respectively. It is clear that, in these terms, electrosorption increased with increasing amounts of PEDOT on the RVC electrodes. When the PEDOT-10min/RVC electrode had 13 mg of PEDOT, the electrosorption was 0.05 mg/cm^2 or 0.16 mg/cm^3, and when PEDOT-120min/RVC electrode had 240 mg of PEDOT, the electrosorption was 0.12 mg/cm^2 or 0.41 mg/cm^3. It is worth mentioning that the electrosorption capacity of PEDOT-56/RVC electrode (6.52 mg/g) has better desalination performance than carbon materials such as activated carbon (1.42 mg/g), activated carbon nanofibre (4.64 mg/g), carbon nanotube (2.33 mg/g), ordered mesoporous carbon (0.54 mg/g), composite carbon nanotubes with carbon nanofibre (3.32 mg/g), reduced graphite oxide (3.23 mg/g) and composite ordered mesoporous carbon with carbon nanotubes (0.63 mg/g) [50, 265, 266, 320-322]. In summary, although the electrosorption performance of the PEDOT-10min/RVC electrode is best in term of mg/g of ion removal, it is the PEDOT-120min/RVC electrode that affords the best ion removal in term of geometric area or geometric volume of electrode; ie it removes the most ions in electrode terms. This is advantageous when the size of the electrode becomes a major consideration in designing a CDI system.

The electrosorption capacity of a PEDOT coating on RVC electrodes was calculated according to the following equations [209, 264, 268]:

$$M_{mass} = [(C_0 - C_f)^* V] / m \quad (Eq\ 3.5)$$

$$M_{volume} = [(C_0 - C_f)^* V] / Z \quad (Eq\ 3.6)$$

$$M_{area} = [(C_0 - C_f)^* V] / A \quad (Eq\ 3.7)$$

Where M_{mass}, M_{volume} and M_{area} are the electrosorption capacity of the working electrode in term of mg/g, mg/cm^3 and mg/cm^2 respectively. C_0 is the initial concentration of solution (mg/L), C_f is the final concentration of solution (mg/L) after adsorption, V is the volume of solution (L), m is the mass of materials (g), Z and A are volume of electrode and the geometric area, respectively.

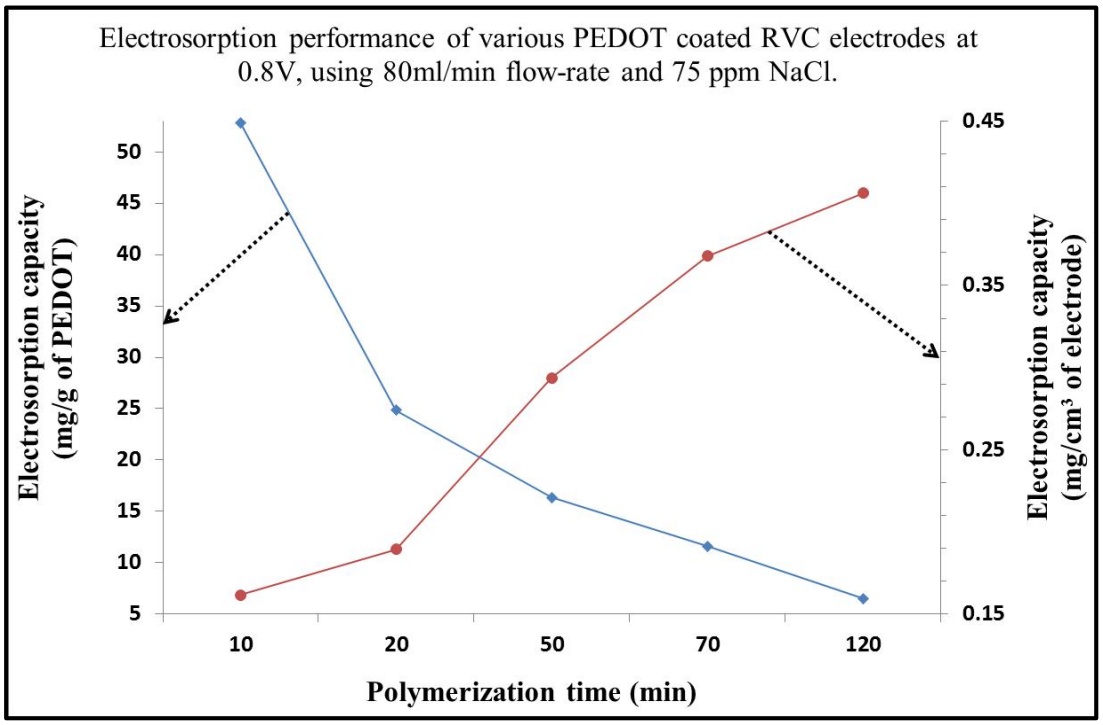

Figure 3.18: Effect of PEDOT loading of PEDOT/RVC electrodes on electrosorption as reported in terms of mass of PEDOT, and geometric volume of the PEDOT/RVC electrode.

Table 3.4: Electrosorption performance of PEDOT/RVC composite electrodes with different PEDOT loadings.

PEDOT/ RVC composite electrode	Electrosorption capacity		
	mg/g of PEDOT	mg/ cm^3 of electrode	mg/ cm^2 of electrode
PEDOT-10min/RVC	52.84	0.16	0.05
PEDOT-20min/RVC	30.86	0.19	0.06
PEDOT-50min/RVC	16.36	0.28	0.09
PEDOT-70min/RVC	11.62	0.32	0.11
PEDOT-120min/RVC	6.52	0.37	0.12

Example calculation of the electrosorption capacity of electrode in terms of (mg/g) and (mg/cm^3):

For a mass of electrode of 0.05 g (2.16 cm^3 geometric volume and 17.88 cm^2 geometric area), volume (v) and conductivity of NaCl solution of 0.06 L and 143.00 µS/cm respectively, and conductivity of NaCl solution after adsorption of 138.59 µS/cm, the electrosorption capacities are calculated as follows:

Section (2.4.3.) gives the equation for conductivity as (Cond = 1.9067 * Conc) so (Conc= Cond/ 1.9067). Hence:

Initial concentration, C_0= (143.00)/ 1.9067 = 75.00 mg/L

Final concentration, C_f = (138.59)/ 1.9067 = 72.69 mg/L

Therefore from equation (3.5): $M_{mass} = [(C_0 - C_f)* V] / m$

so, M_{mass} = [(75 – 72.69) * 0.06] / 0.05 = 2.77 mg/g

Or from equation (3.6): $M_{volume} = [(C_0 - C_f)* V] /Z$

so, M_{volume} = [(75 – 72.69) * 0.06] /2.16 = 0.06 mg/cm^3

Or from equation (3.7): $M_{area} = [(C_0 - C_f)* V] /Z$

so, M_{area} = [(75 – 72.69) * 0.06] /17.88 = 0.008 mg/cm^2

3.3.10 CDI stability

Regeneration of PEDOT-120min/RVC electrodes is a very important factor affecting their practical use in a CDI system. Figure 3.19 shows the electrosorption/regeneration cycles of PEDOT-120min/RVC electrode, which was conducted by repeating several charging and regeneration cycles. When no oxidation and reduction reaction occurs in electrosorption, the current is mainly consumed for charging the electrode to electroadsorb ions from the bulk solution [323]. As can be seen, the polarization of the electrode at 0.8 V leads to a decrease of solution conductivity. The conductivity sharply decreased because ions migrate onto the oppositely charged surface, and then continues to gradually decrease until the electrical double layer is completely formed at the electrode/electrolyte interface [267]. Moreover, the regeneration can be achieved upon electrode depolarization at 0.0 V. It can be noted that the process of regeneration can be carried out easily in a short time and the same pattern can be found in four repeated electrosorption–desorption cycles; each cycle takes 13 min, ie 5 min adsorption of ions and 8 min release of ions. Also, the recycling stability was very high for the reason that the decay of electrosorption capacity has not been observed. It demonstrates that the electro-adsorbed ions can be desorbed by removing an electric field, and then the PEDOT-120min/RVC electrode can be reused. Consequently, the electrosorption of ions using this electrode is a reversible process and that the amount of electro-adsorbed ions can be controlled, via manipulation of the electrical double layer formation at the electrode/ electrolyte interface.

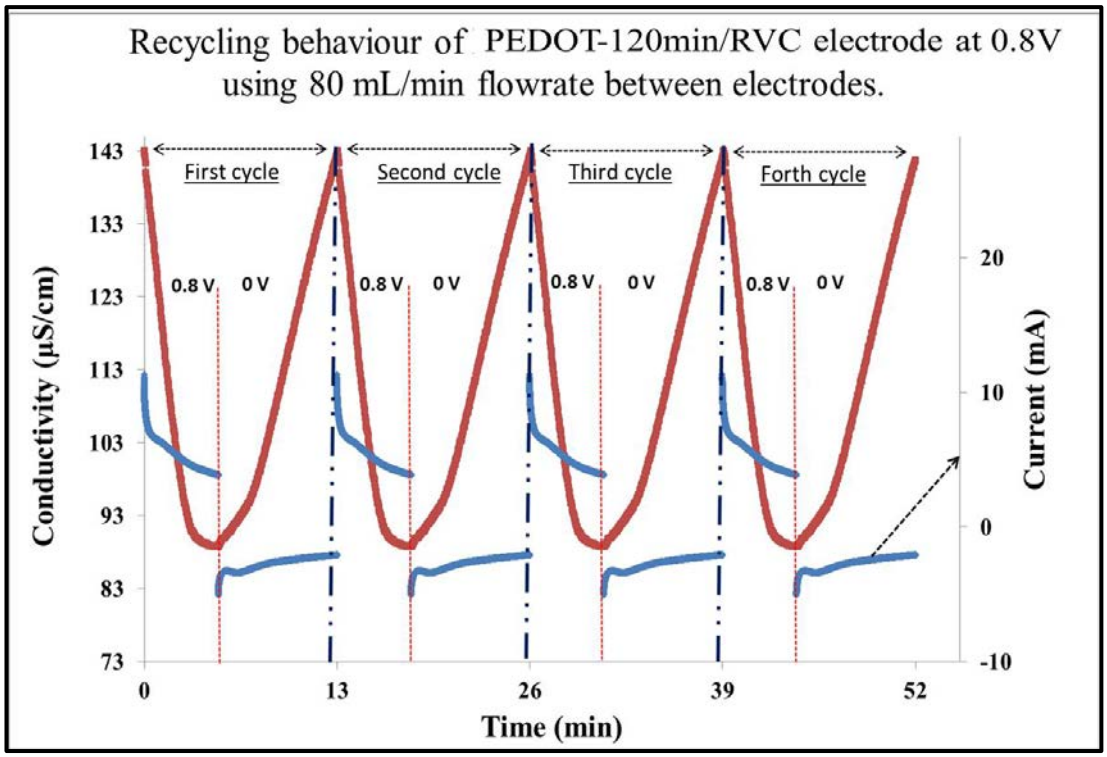

Figure 3.19: Multiple electrosorption–desorption and current response cycles for PEDOT-120min/RVC electrode upon polarization and depolarization at 0.8 V and 0.0 V, respectively. NaCl feed solution concentration: 75 mg/L.

3.3.11 Effect of NaCl concentration on electrosorption capacity

In this section the electrosorption behavior of PEDOT-120min/RVC electrode in various NaCl concentrations, 25, 50, 75, 100, 200, 300, 400 and 500 mg/L for 1 cycle desalination time (13 min) was investigated (Figure 3.20). This experiment was carried out at an electrical voltage of 0.8 V at a flow-rate of 80 ml/min through a CDI cell. The amount of NaCl removed increases as the initial concentration is raised, which is due to the enhanced mass transfer rate of ions inside the micropores and reduced overlapping effect by higher concentration of solution [324-326]. The electrosorpition sharply increases at concentrations up to 100 mg/L and continues to increase up to 500 mg/L. The electrosorption capacity of PEDOT-

120min/RVC electrde was 2.23, 4.31, 6.45, 8.58, 12.11, 14.41, 15.69 and 16.15 mg/g at 25, 50, 75, 100, 200, 300, 400 and 500 mg/L of NaCl solution respectively.

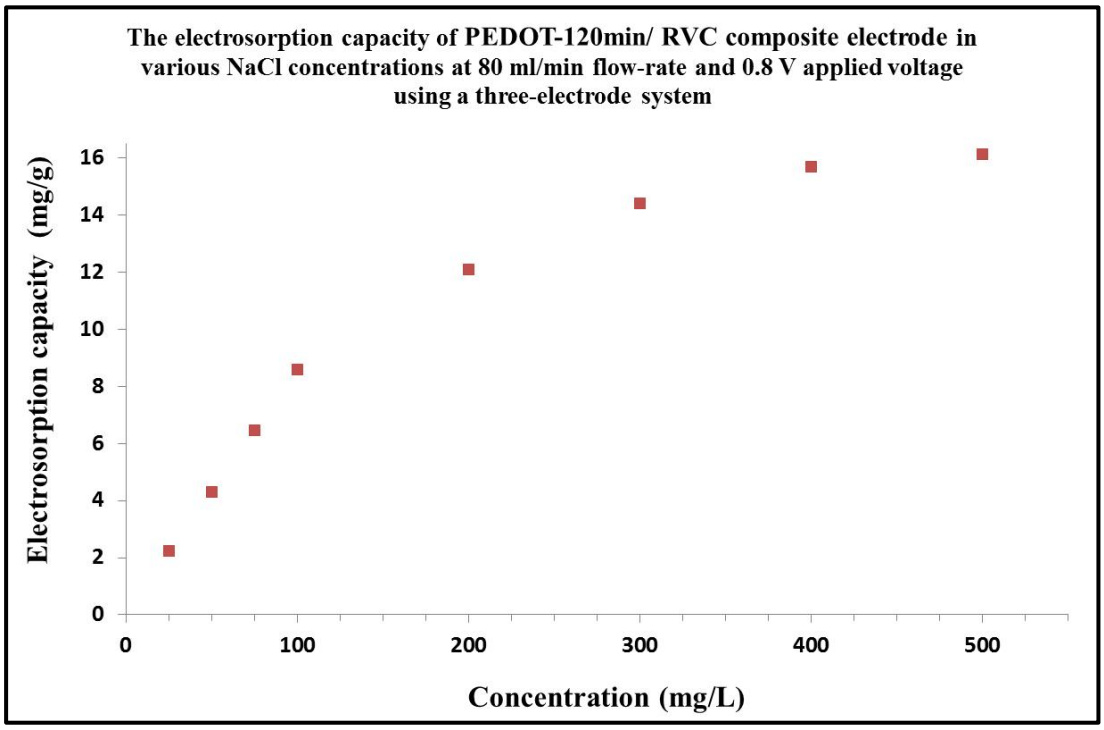

Figure 3.20: Electrosorption capacity of PEDOT-120min/RVC composite electrode at varous concentrations of NaCl feed solution. Applied voltage: 0.8V. Flow-rate: 80 ml/min.

3.3.12 Water production by CDI system

In this chapter, experiments were performed using a 75 mg/L NaCl feed solution. Therefore, water production calculations are hereby based on this feed concentration. From the above Section (3.3.11.), it can be concluded that, 1 g of PEDOT coated on 17.5 cm^3 RVC electrode (PEDOT-120min/RVC composite electrode) adsorbed 6.45 mg NaCl during 13 min using initial concentration of solution 75 mg/L and the solution concentration after 1 desalination cycle became

68.55 mg/L. In addition, the amount of salt electrosorbed will change with solution concentration as shown by the relationship between the electrosorption capacity and solution concentration (Figure 3.20). Figure 3.20 also shows that the electrosorption capacity, , however, appears to be linearly related to the NaCl concentration below 100 mg/L and this is confirmed by the straight line fit shown in Figure 3.21 (a) which affords Equation 3.8.

Electrosorption (mg/g) = 0.086 * Concentration **(Eq 3.8)**

From this equation (Eq 3.8), the concentration change after each desalination cycle will be known and this information can be used to obtain Figure (3.21 (b)). Figure 3.21 (b) shows the concentration change after each desalination cycle to reach less than 1 mg/L using 1 g of PEDOT which is coated on 17.5 cm^3 RVC electrode (PEDOT-120min/RVC composite electrode). It is clear that the total desalination process requires 49 cycles to reduce the concentration of solution from 75 mg/L to less than 1 mg/L. This means that water production, employing this electrode, needs 637 min (13 min * 49 cycles) to produce 1L of water containing NaCl concentration of less than 1 mg/L. Thus, the water produced per day is 2.26 L using 1 g PEDOT coated on 17.5 cm^3 RVC electrode or 129,176 L using $1m^3$ of same composite electrode (PEDOT-120min/RVC composite electrode). However, for low salt diet patients a salt concentration not exceeding 20 mg/L is recommended. Therefore, if a salt concentration of 20 mg/L is adopted as the goal, the water production will require 15 cycles that will require a total period of 195 min. This will translate to a water production of 421,978 L using $1m^3$ of composite PEDOT-120min/RVC composite electrode.

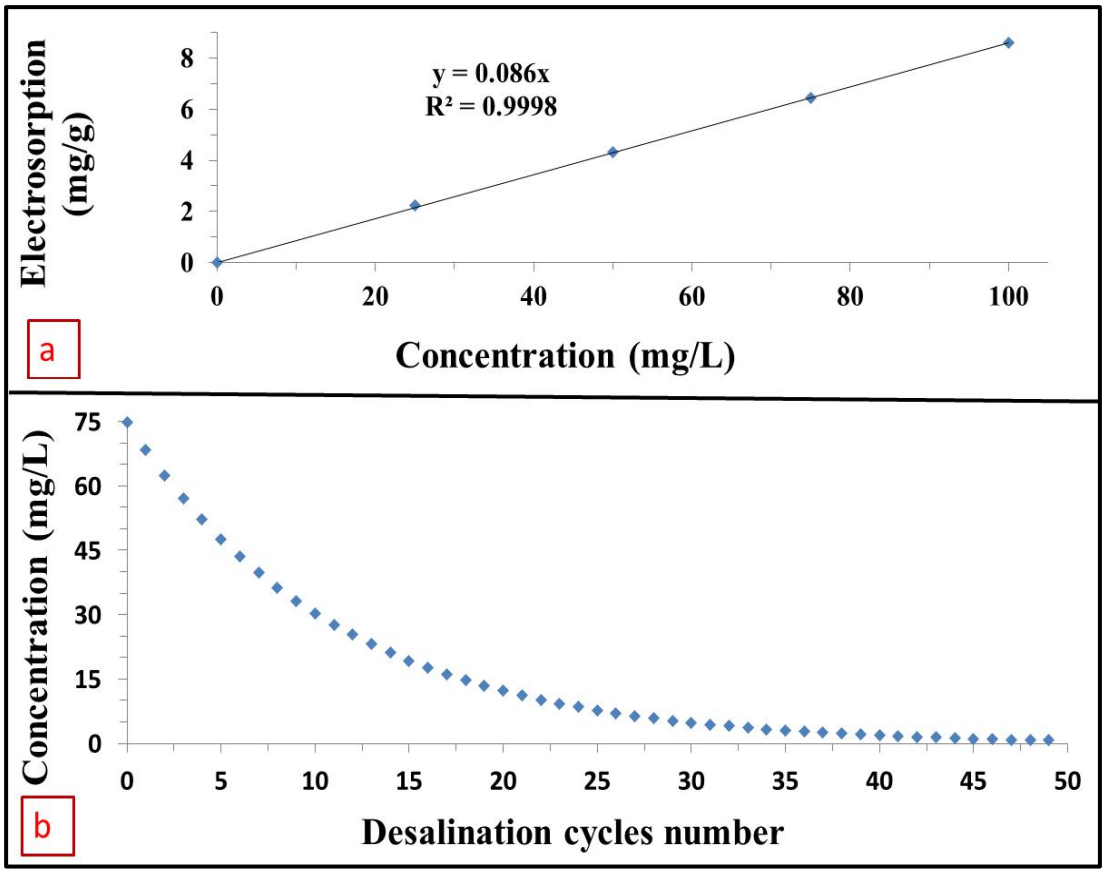

Figure 3.21: (a) Calibration curve of electrosorption vs concentration of NaCl feed solution. (b) Concentration of feed solution vs desalination cycles number for full desalination process to produce water of less than 1 mg/L NaCl concentration.

3.4 Conclusion

In this study, PEDOT/RVC composite electrodes with varying amounts of PEDOT loadings were considered for application as 3D microstructure electrodes. PEDOT was successfully deposited by electropolymerization on RVC and used for the first time as materials and electrodes in CDI technology. The aim of this chapter was achieved as demonstrated by the improved performance of the CDI electrode in terms of unit geometric volume and geometric area. It was shown that they have better desalting performance than carbon materials. The PEDOT/RVC electrode exhibited desirable macroporosity and microporosity characteristics that allow free movement of large amounts of salt ions. Thus, the adsorption/ regeneration of NaCl at PEDOT/RVC electrodes was facile with high efficiency achieved. Furthermore, the water production by $1m^3$ PEDOT-120min/RVC electrode from 75 mg/L NaCl feed solution was calculated to be 421,978 L/day of water of 20 mg/L NaCl final concentration. It has been shown that the capacitance of PEDOT-120min/RVC electrode compared with a bare RVC electrode had increased by a factor of 2230, and the electrochemical properties were ideal. The capacitance of PEDOT was found to be very high compared with other PEDOT studies. Raman spectroscopy and cyclic voltammetry suggests a strong interaction between the RVC and the backbone of the PEDOT chain. This improves the surface area and conductivity of the PEDOT/RVC composite electrode. Furthermore, all other aims of this chapter were achieved.

4 NOVEL SWCNT LOADED POROUS RVC ELECTRODES FOR CAPACITIVE DEIONIZATION.

4.1 Introduction

The successful use of 3D PEDOT/RVC in CDI systems led to the use of RVC electrodes again, in the work reported in this chapter, to build 3D nanoweb functionalized SWCNT electrode structures by coating the RVC with SWCNT using a dip coating method. The realisation of a high removal efficiency for capacitive deionization (CDI) is directly related to electrode materials with a high capacitance, large specific surface area for ion accumulation, good electrical conductivity, and suitable pore size. To date, carbon materials have been extensively studied as CDI electrodes [39, 327-337]. In particular carbon nanotubes (CNTs) have been used as CDI electrodes because they afford novel additional functional properties, such as structure, surface area, activity, and conductivity [20, 338-340]. These electrodes were made to be used as two dimension (2D) sheet electrodes. It is necessary to develop CNTs electrodes to be more effective electrodes in a CDI system. One of the effective ways is that CNTs electrodes could be constructed as three-dimensional (3D) structures. The advantages of this approach are high porosity, increased surface area, and efficient pathways for ion diffusion [341].

Reticulated vitreous carbon (RVC) has a three-dimensional (3D) structure and it can be used as a platform to support carbon materials. Here the RVC electrode is used to support a SWCNT coating for use as a 3D electrode in a CDI system. The resultant structure should increase the stability of composite electrodes towards high flow-rate pressure with low resistance to liquid flow, increase the possibility of ions to reach all electrode surfaces in a short time for electrosorption, and shorten the time of ions desorption from the electrode surface.

In this chapter, commercial SWCNT were functionalized to introduce carboxylic acid groups by acid treatment in order to facilitate dispersion in DMF and to convert SWCNT into hydrophilic materials to reduce the flow resistance of aqueous solutions through the electrodes. The SWCNT were characterised using Raman and Visible spectra. This acid treated SWCNT (a- SWCNT) was dispersed in DMF by sonication and the sonication time was optimized. In addition, the energy of sonication of each mg of a-SWCNT material was selected. The purpose of forming a-SWCNT solutions was in order to coat and fill the RVC electrode which was cleaned by dilute acid. a-SWCNT material coated RVC electrodes, with various coating levels up to filled electrode pores, were characterised for their morphology and electrochemical properties. These electrodes were tested in a capacitive deionization system and the performance of these electrodes in the system was investigated under various working conditions such as: flow-rate and bias potential which were optimized. Moreover, the effect of feed-stream directly through the electrode or between electrodes, and the effect of distance between electrodes in the CDI system were investigated. Furthermore, investigations of the electrosorption isotherm such as Langmuir and Freundlich models to describe how ions interact with electrodes, and electrosorption dynamics to evaluate the performance of electrodes. The basic and improved designs of flow-through cell made by 3D printing was also considered. All of these are very important to develop electrodes and effective technology for desalination.

4.1.1 Aims of the work in this chapter

The aims of the research described in this chapter can be summarized as follows:

- Prepare SWCNT materials to be used to build 3 D composite electrodes in a CDI system.
- Use RVC electrodes as substrates to reduce the resistance of solution flow through the electrodes.
- Improve the performance of the CDI system's adsorption/desorption cycle time by changing the electrode orientation in the CDI system hence directing the solution flow directly through the electrodes (Figure 4.1 (b)) as opposed to a flow between the electrodes (Figure 4.1 (a)).

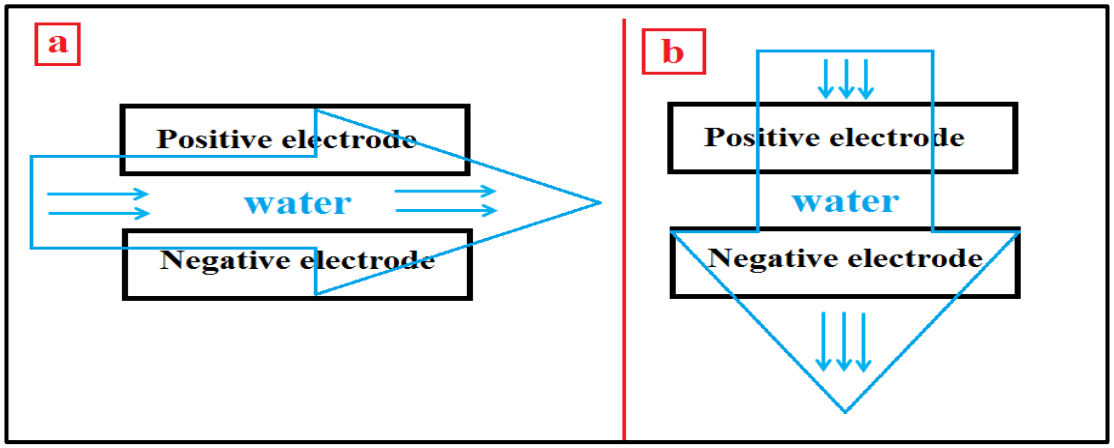

Figure 4.1: Schematic diagram of (a) flow-between and (b) flow-through electrodes systems in a CDI cell.

4.2 Experimental

4.2.1 Chemicals and Materials

Commercial single-walled carbon nanotubes (Hipco-CCNI /Lot # p1001) were purchased from Carbon Nanotechnologies, Inc (Houston, TX) and were used as received. The following chemicals obtained from Sigma-Aldrich were also used as received: -N, N-Dimethylformamide (DMF) (AR grade), concentrated nitric acid (70%) and sodium chloride (AR grade). The reticulated vitreous carbon (compressed 60, 45 and 30 ppi (pores per inch)) was purchased from ERG Materials and Aerospace Engineering and cleaned before use. Membrane filters (0.2 μm GTTP) was purchased from MILLIPORE and was used as received. Milli-Q water with a resistivity of 18.2 $m\Omega\ cm^{-1}$ was used in all preparations.

4.2.2 Methods

4.2.2.1 Functionalization of carbon nanotubes

As received SWCNT material was functionalized by a reflux method. In a typical procedure, 20 mg of the material was transferred into a round-bottom flask filled with 40 mL of 6 M nitric acid (HNO_3) and equipped with a magnetic stirring bar and a reflux condenser. The flask was immersed in an oil bath at a temperature of 120 °C for 6 hours. The acid treated SWCNT was then filtered and washed with water until the filtrate was neutral, then washed with 10 mL of methanol, followed with 10 mL of DMF. The functionalized material, henceforth referred to as acid treated SWCNT (a-SWCNT) was dried in an oven at a temperature of 105 °C for 48 hours.

4.2.2.2 Dispersion of a-SWCNT

A dispersion of 15 ml containing a-SWCNT 0.2% w/v in N,N-dimethylformamide (DMF), one of the best solvents reported for SWCNT dispersions [342] was obtained by using a Branson homogenizer, Sonifier model S-450D equipped with a 13 mm step disruptor horn and a 3 mm tapered microtip, operating at a 20 kHz frequency and 25% amplitude as the power output (100 W) , with pulse of two seconds on and one second off. The dispersion was sonicated in a water-ice bath to prevent the suspension from overheating. Homogeneity and birefringence of the dispersion were checked using an Olympus BH-2 microscope in transmission mode between crossed polarizers. In addition, the optimization of sonication time, sonication energy and solution stability will be discussed in the Results and Discussion section.

4.2.2.3 Pre-treatment of the RVC electrode

All reticulated vitreous carbon (RVC) electrodes (length 4 cm * width 1.8 cm * thickness 0.3 cm (2.16 cm^3) were cut from a block of RVC material, and were cleaned as described in Section 3.2.3.2. All RVC electrodes were weighed after drying.

4.2.2.4 a-SWCNT dip coated RVC Electrode

The dip coating method, which was used in our work, was kept simple and low cost [343]. All RVC electrodes which have 2.16 cm^3 volumes were immersed slowly into the 0.2 % w/v a-SWCNT solution to allow the air to escape and prevent the formation of air pockets; during this time the solution was seen to fill the whole RVC electrode via capillary action within a few seconds. After that all electrodes

were removed from the solution to dry them at room temperature before drying them in an oven at 100 ^{o}C for 2 hours. This procedure was repeated several times to study the maximum loading level of a-SWCNT on the RVC substrate. Figure 4.2 shows a schematic diagram of the full process of dip coating RVC in a-SWCNT solution. The process of the RVC electrode being soaked in solution and drying afterward in an oven overnight is shown schematically. The substrate, after dip coating, was dried at 100 °C in an oven for 2 h and then in a vacuum oven at 50 °C for 2 h to remove all organic solvents remaining in the micropores of the electrode. The weights of a-SWCNT loadings on the RVC electrodes were determined by weighing the electrodes before and after dip-coating.

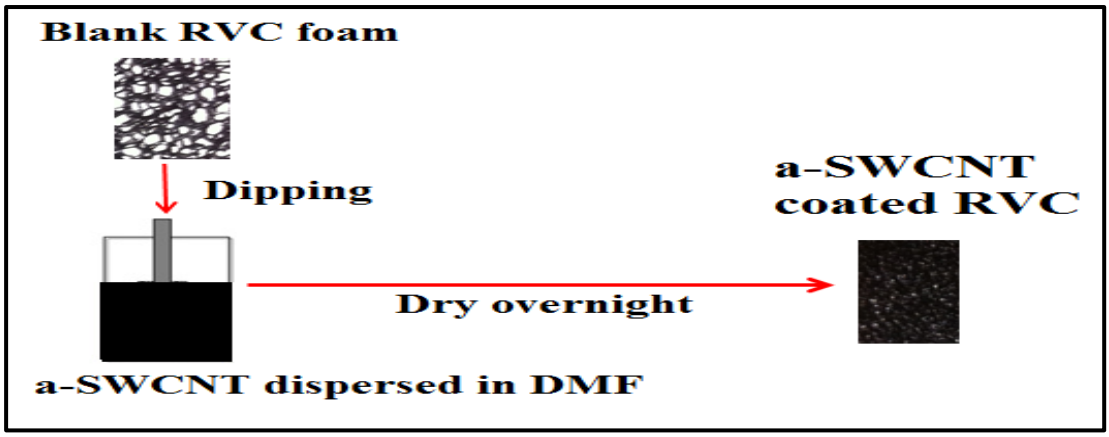

Figure 4.2: The full process of dip coating RVC in a-SWCNT solution.

4.2.2.5 Electrochemical characterisation

The capacitance of a-SWCNT was determined by cyclic voltammetry (CV). A a-SWCNT/RVC composite electrode was used as the working electrode (WE) in 1 M NaCl aqueous solution and scanned in the voltage range between -0.2 to 1.0 V useing a three-electrode system; RVC electrode and Ag/AgCl (3M NaCl) were used as counter electrode (CE) and reference electrode (RE), respectively. The scan rates

used were 5, 10, 20, 50, 100 and 200 mV/s, respectively. Contacts to the WE and CE were made using Pt wire.

4.2.2.6 Physical characterisation

The morphology of the a-SWCNT coated RVC electrodes were analysed by use of a field emission scanning electron microscope (FESEM) at specific voltages of 0.5 KV. Furthermore, a-SWCNT functionalization was characterised by: (1) Visible absorption spectra obtained using quartz cuvettes and (2) Raman spectra obtained with a Raman spectrometer equipped with a visible Raman microscope and CCD detector. The excitation wavelength was 632.81 nm and spectra were obtained over 30 s at 1.0 cm^{-1} resolution.

4.2.2.7 Measurement of amount of ion removal from the NaCl aqueous solution

NaCl concentration was determined by measuring the electrical conductivity of NaCl solution as described in Section 2.4.3.

4.2.2.8 Construction of a capacitive deionization cell

Capacitive deionization experiments were carried out in a flow-through system as described in Section (3.3.7.) and the details can be found in Section (3.3.7.1.).

4.3 Results and discussions

4.3.1 Characterisation of SWCNT after functionalization

Raman spectroscopy and Visible spectrophotometry were used to investigate the SWCNT surface after acid treatment.

4.3.1.1 Raman spectroscopy

Raman spectroscopy is a powerful technique for the characterization of the structure of carbon nanotubes[344]. It is known that the general characteristics of a Raman spectrum of CNTs have two bands appearing at 1582 cm^{-1} (G band) and 1350 cm^{-1} (D band). The shape and intensity of the D band corresponds to the sp^3 hybridized carbon atoms, and the G band is associated with the tangential vibration modes of CNT sidewall C-C bonds. The intensity ratio (R) of these D and G peaks (I_D/I_G) is often used to estimate the quality of the structure of the CNT sample [345-351]. In addition, the dominant second-order feature in SWCNT Raman spectra is the G' band which is located at about 2600 cm^{-1} and this is sensitive to charge transfer effects due to structural modifications of the nanotube walls induced by the attachment of different chemical species. Also, the M band appearing at about 1755 cm^{-1} is a second-order peak tentatively assigned to a combination mode of the G and the radial breathing mode (RBM) bands [344, 345]. The radial breathing mode (RBM) can be used to determine the nanotube diameter (d_t) through its frequency (ωRBM) [219, 352]. These features are unique to carbon nanotubes and occur at frequencies between 120 and 350 cm^{-1} for SWCNT for diameters in the range $\omega RBM = A/d_t + B$, where A = 234 cm^{-1}nm and B = 10 cm^{-1}, and where B is an upshift in ωRBM assigned to tube-tube interactions. For typical SWNT bundles in

the diameter range d_t = 1.5 ± 0.2nm and if the nanotube diameter is greater than 2 nm, the RBM spectrum is difficult to observe [219, 344, 352]. The mean diameter of SWCNT can be calculated by Equation (4.1):

$$\mathbf{d_t = \frac{248}{\omega}} \qquad (\mathbf{Eq\ 4.1})$$

Figure 4.3 shows the Raman spectra of raw single-walled carbon nanotubes (SWCNT) and after acid treatment with 6 M HNO_3.The intensity of the G band in raw SWCNT is considerably higher than the D band, due to the disorder-induced phonon mode of the carbon sixfold rings breathing vibration. On the other hand, the intensity of the G band after acid treatment decreases and the D band intensity slightly increases. The higher ratio explains the higher amorphous carbon content and defect formation. The intensity ratio of D and G bands of the raw and treated CNT samples are 0.0615 and 0.7452, respectively, (Table 4.1). It is worth mentioning that the M band almost completely disappeared. This observation leads to a conclusion that SWCNT after acid treatment have low amorphous carbon content and defects. Figure 4.3 also shows the RBM band of the raw and acid treated SWCNT. It can be observed that the absolute intensities of the radial breathing mode are drastically reduced after oxidation. The length of the raw SWCNT decreased after acid treatment; from 1.30 to 1.27 nm, 1.16 to 1.13 nm and 0.98 to 0.96 nm, respectively, as shown in Table 4.1. These changes indicate chemical alteration of the SWCNT.

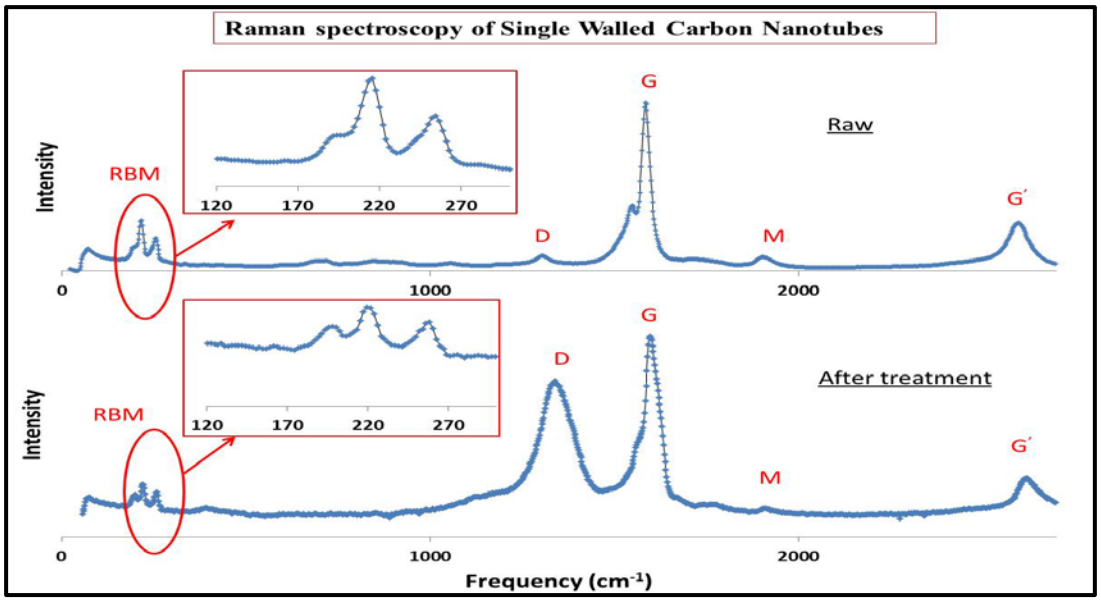

Figure 4.3: Raman spectra of single-walled carbon nanotubes before and after treatment by 6M HNO_3 for 6 hours at 120 °C.

Table 4.1 : Single-walled carbon nanotube (SWCNT) diameter and ratio of D to G bands before and after acid treatment

(SWCNT)	ω (cm^{-1})	d_t(nm)	I_D/I_G
Raw	191	1.30	0.0615
	213	1.16	
	254	0.98	
Treated	196	1.27	0.7452
	219	1.13	
	258	0.96	

4.3.1.2 Visible spectrophotometry

Visible spectrophotometry in the wavelength range from 400 nm to 750 was used to monitor sidewall perturbation of SWCNT before and after nitric acid treatment [353, 354]. The Visible absorption spectra of SWCNT and acid treated SWCNT (a-SWCNT) samples are shown in Figure 4.4. The boxes in the figure represent the approximate boundaries for metallic and semiconducting transitions

(the van Hove transitions). For metallic nanotubes, M_{11} represents the electronic transitions between the valence band and conduction band, and in semiconducting nanotubes, S_{22} is the electronic transition between the second valence to conduction bands [40, 355]. The SWCNT sample shows three distinct peaks at 505, 660 and 730 nm and they correspond to the second pair of van Hove singularities of the semiconducting and metallic nanotubes [354, 356-359]. The a-SWCNT sample does not show any distinct peaks in Figure 4.4. This implies that nitric acid treatment introduces structural defects or functional groups on SWCNT, which result in electronic band transition changes [354]. The changes observed in the van Hove singularities vanish in the spectra, and can be attributed to re-hybridization at carbon (sp^2 to sp^3) because the π electrons in the highest occupied molecular orbitals (HOMOs) are used to form new bonds to accommodate the carboxyl group [353, 354, 359].

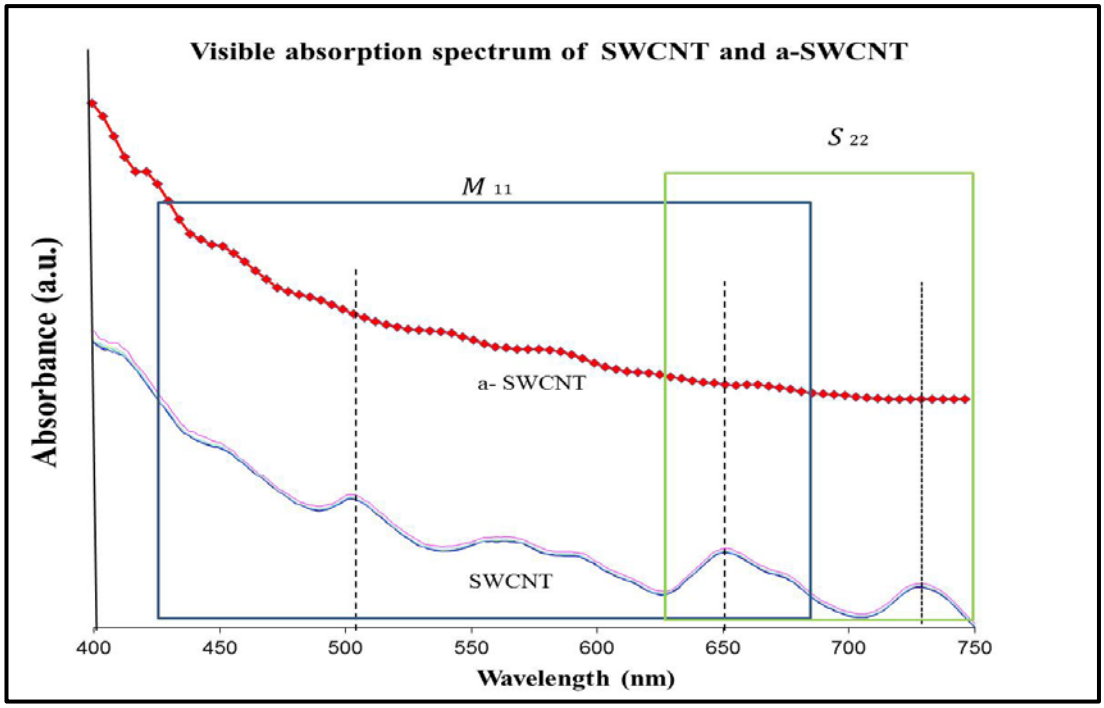

Figure 4.4: The Visible absorption spectra of dispersions containing 0.2%w/v pristine SWCNT and a-SWCNT which were measured after a 20- Fold dilution.

4.3.2 Dispersion of a-SWCNT in DMF

The optimum time of sonication required to effectively disperse CNTs needs to be determined, since excess sonication can shorten or create defects in the tubes that are detrimental to their inherent properties [232, 241, 360]. Visible spectroscopy can be used to study the dispersal process by monitoring the variation in absorbance during dispersal to determine the effectiveness of the dispersion and subsequently the stability [356, 357, 361]. In order to investigate the effect of sonication time on the dispersion of a-SWCNT in DMF, the sample was prepared as a 15 ml dispersion containing a-SWCNT 0.2% w/v in DMF; which is one of the best solvents reported for dispersing SWCNT [342]. In this experiment, a high concentration was used with a view to achieving high loading of a-SWCNT on the RVC electrodes. This leads to an increase in the viscosity of the solution which impedes efficient dispersion. Therefore, an increase in energy is needed to counteract this. Figure 4.5 (a) and (b) show the Visible spectra of a-SWCNT dispersions as a function of sonication time and the corresponding optical absorbance at λ (660 nm) was plotted as a function of sonication time, respectively. It can be seen that, the a-SWCNT spectra becomes more pronounced (higher absorbance) with longer sonication time, indicating that an increasing amount of a-SWCNT became dispersed with time. However, the absorption of the dispersion did not change dramatically after sonication beyond 30 min, indicating that the solution was saturated. The minimum amount of time required to effectively disperse the a-SWCNT was 30 min. The inset images in Figure 4.5 (a) suggest that homogenous dispersions have been obtained after 30 min sonication time. Also, it was observed that when the sonication time was increased, the colour of the solution became progressively black. From Figure 4.5 (c), the

minimum amount of energy required to effectively disperse 30 mg of the a-SWCNT was 180 KJ at 30 min. This means that 6 kJ was expended per mg of a-SWCNT in a 0.2% w/v solution. The sonication energy in Figure 4.5 (c) was calculated using equation (2.1).

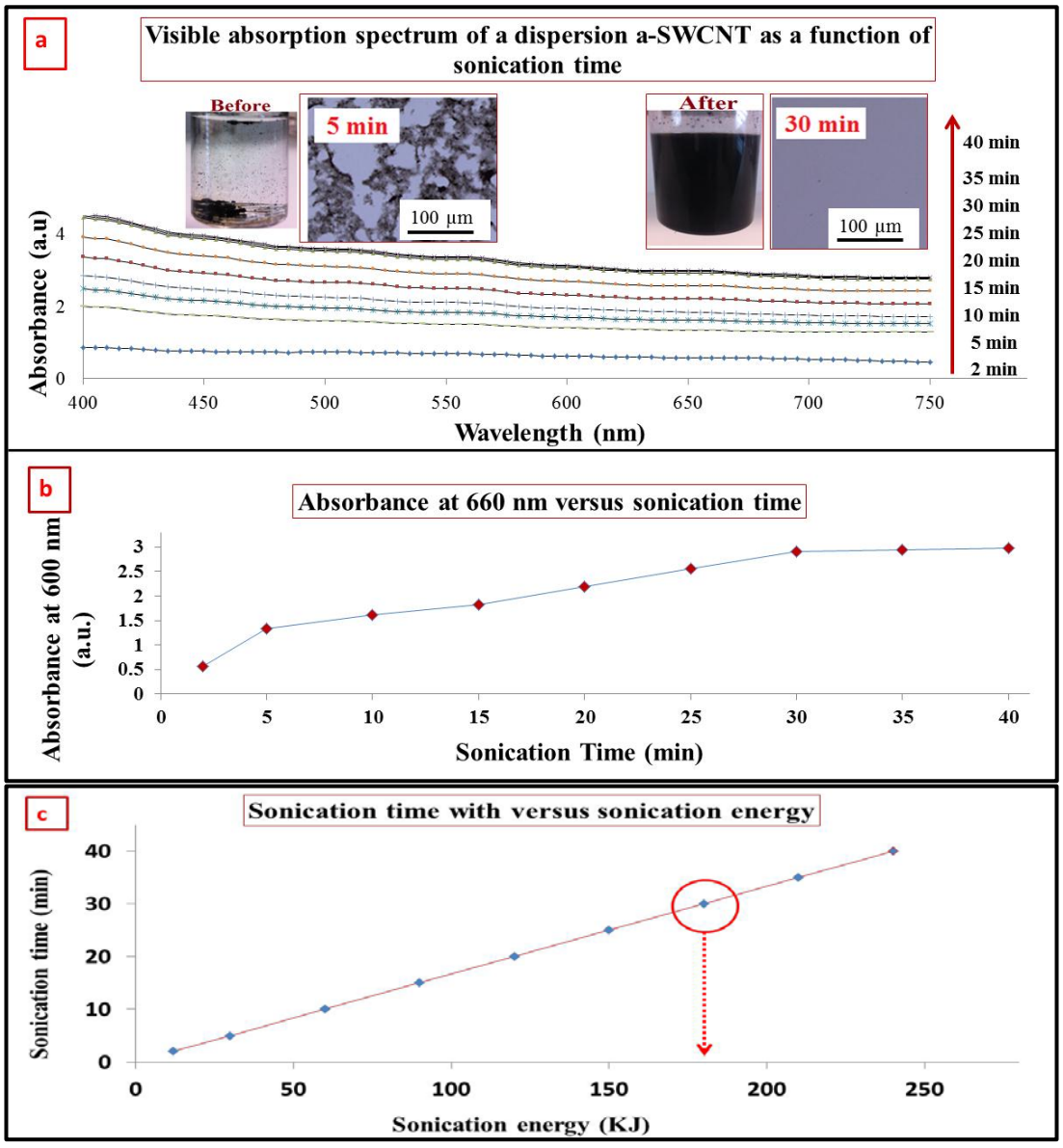

Figure 4.5: Effect of increasing sonication time on: (a) the Visible absorption spectrum of a dispersion containing 0.2% w/v a-SWCNT which was measured after a 20-fold dilution, where inset photo images are of 0.2% w/v containing a-SWCNT before sonication and after 30 minutes sonication and optical microscope image after 5 min and 30 min sonication time; and (b) Absorbance at 660 nm. (c) Effect of increasing sonication time on sonication energy. Arrows in (a) indicate the direction of increase in sonication time.

4.3.3 Optimization of RVC electrodes coated with a-SWCNT

The general purpose of this work is the optimization of the reticulated vitreous carbon (RVC) electrodes of different porosities coated with a-SWCNT. RVC electrode has a free void volume between 90% and 97%. Thus, RVC electrodes have a low flow resistance. Figure 4.6 (a, b, and c) shows photo images of three RVC electrodes with porosities of 60, 45 and 30 ppi (nominal pores per inch). It is clear that the free void volume of the RVC electrodes increases with decreasing ppi grade. The average pore sizes of the RVC electrodes were calculated from SEM images by measuring the distance between green lines in Figure 4.6 (d, e, and f) and they were 350, 700 and 900 μm for 60, 45 and 30 ppi, respectively. RVC electrode properties, discussed in Chapter 1, are dependent on the ppi grade. If the amount of pores per inch (ppi) increases, the electrode area per unit electrode volume will increase as well. According to previous reported properties of RVC [63, 87, 362], which are good surface area, conductivity and good mechanical strength, it is envisaged that the RVC electrode that has the largest number of pores per inch would be the best electrode for use in a CDI system. Therefore, in order to confirm that the smaller pores electrode is the best electrode for loading of a-SWCNT for use in a CDI system, we investigated the influence of all electrode capacitances of RVC electrodes with different pore sizes coated with the same amount of a-SWCNT. All RVC electrodes had the same geometric volume (dimensions of 4.0cm*1.8cm*0.3cm) and the same amount of a-SWCNT was coated, around 6 mg. The effect of different pores per inch was investigated in aqueous solution. Figure 4.6 (g) shows the capacitances of all electrodes that were calculated (using Equation 3.2.) from cyclic

voltammograms obtained at the potential scan rate of 5 mV/s. It can be seen that the highest specific capacitance was 267.24 F/ g for a-SWCNT coated RVC electrode with 60 pores per inch, and the specific capacitance decreased with a decrease in the amount of pores per inch. This is because the RVC electrode with 60 ppi has higher surface area per volume of electrode. The RVC 60 ppi electrode coated with a-SWCNT (6 mg) will be discussed in detail in its electrochemical behaviour evaluation using cyclic voltammetry (Section 4.3.6). In conclusion, therefore, 60 ppi RVC electrodes were selected as substrates to load a-SWCNT for use as electrodes in a CDI system.

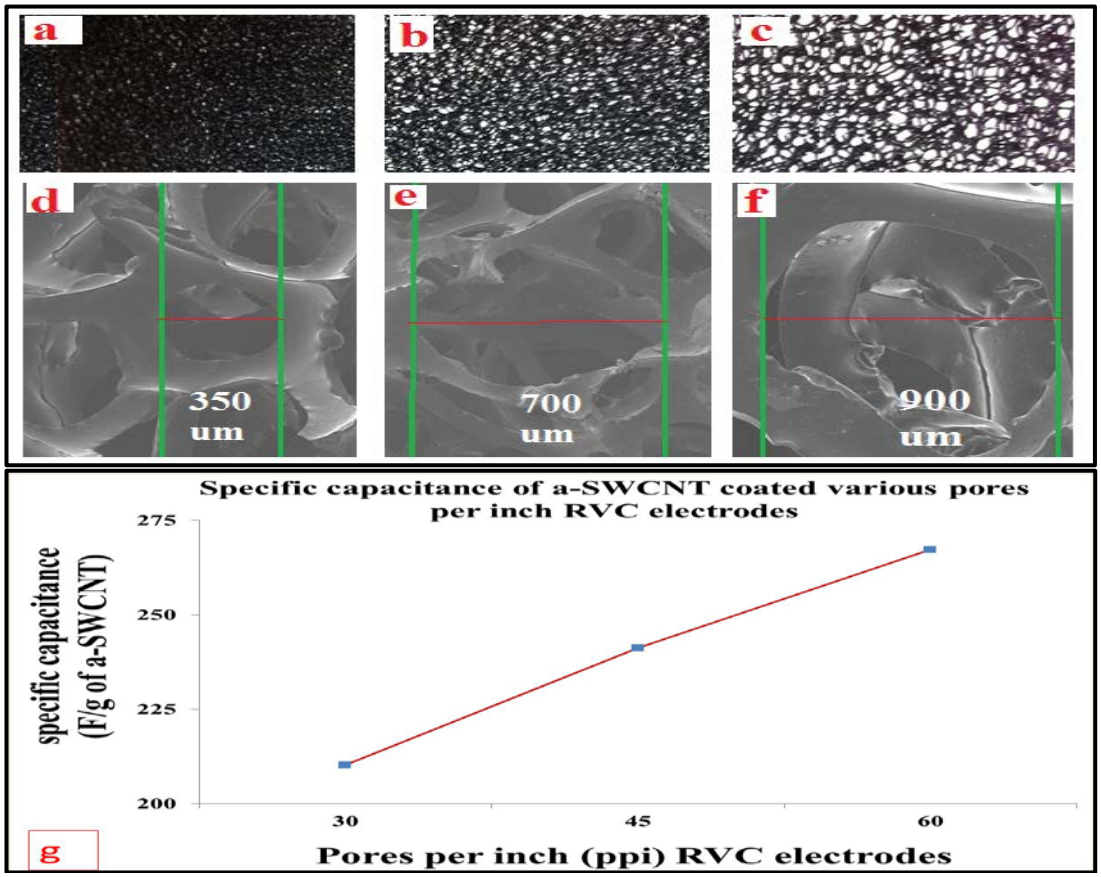

Figure 4.6: (a,b,c) Photo images and (d,e,f) SEM micrographs of 60, 45 and 30 ppi RVC samples, respectively. (g) The specific capacitance of a-SWCNT coated RVC electrodes of various porosities in 1 M NaCl solution calculated from cyclic voltammograms recorded in a voltage range between -0.2 to 1.0 V using a three-electrode system vs Ag/AgCl at 5mV/s scan rate.

4.3.4 Optimization of the loading level of a-SWCNT on RVC electrode

Figure 4.7 shows that the percentage of loading of a-SWCNT increased with repeated electrode immersion in the a-SWCNT solution. RVC electrodes, number 1, 2, 3 and 4 were repeatedly immersed in the solution 2, 5, 10 and 20 times, respectively, and the amounts of a-SWCNT loaded onto RVC to form a-SWCNT/ RVC composite electrodes were found to be 6 mg (3.63%wt), 23 mg (12.50 %wt), 34 mg (17.43% wt) and 50 mg (23.85% wt), respectively (Table 4.2). In the laboratory it was observed that the pores of this RVC electrode at 23.85%wt loading was completely filled by a-SWCNT as seen in the inset image in Figure 4.7 when tested with a light. All these electrodes, however, allowed liquid to flow through because the SWCNT filling itself is porous.

Table 4.2: RVC (2.16 cm ^{3}) electrodes before and after a-SWCNT coating.

Sample	1	2	3	4
RVC (mg)	159	161	161	162
After coating (mg)	165	184	195	212
Amount of a-SWCNT (mg) in sample	6	23	34	50
Amount of a-SWCNT in sample (% w/w)	3.63	12.50	17.43	23.58

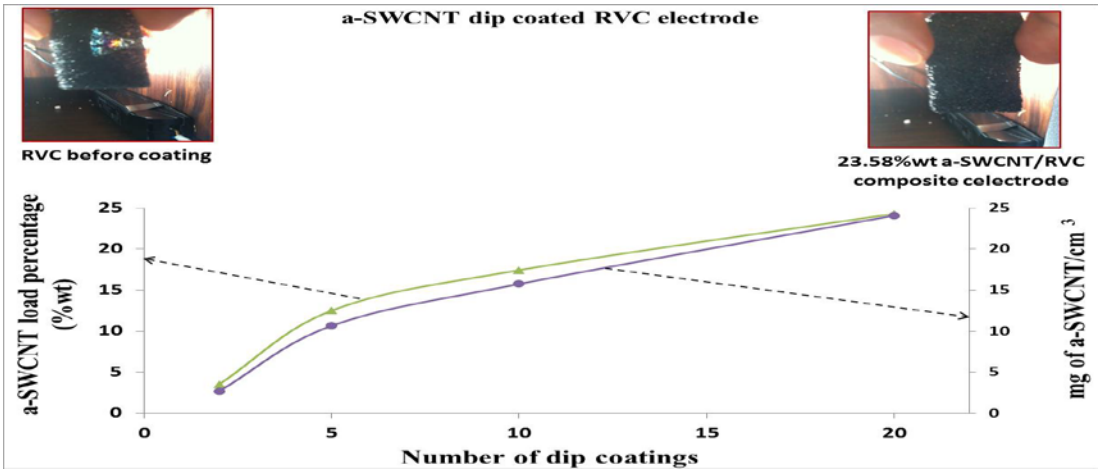

Figure 4.7: a-SWCNT loading of RVC as a function of number of dip coatings in a-SWCNT dispersion. Insets: images of RVC electrode before coating and after being completely filled (23.58 %wt a-SWCNT coated RVC electrode).

4.3.5 Scanning Electron Microscopy of a-SWCNT

The surface morphology of the a-SWCNT coated RVC electrode was examined using scanning electron microscopy (SEM). SEM images of the 23.58 %wt a-SWCNT coated RVC electrode is shown in Figure 4.8. It can be concluded that the a-SWCNT dispersed very well in DMF because no aggregation is seen on the surface and RVC pores appeared filled completely (Figure 4.8 (a)). The appearance of the top surface is like textile (Figure 4.8 (b)) because the nanotubes are irregularly spread on the RVC electrode and its pores, partly parallel and partly perpendicular to the surface. The SEM images in Figure 4.8 (c, d and e) show the a-SWCNT tubes became stronger and tougher due to the closer contact which improved ion transfer between nanotubes, which is consistent with previously reported results [363-365]. In addition, it shows that the void spaces or “pores” between the matted SWCNT tubes are of macroscale, and these void spaces can be considered as macropores, and are areas through which ions diffusion can freely take place. From the SEM image, SWCNTs nano-network structures act as useful nano-spacers for diminishing the aggregation of SWCNT. This 3-D porous structure exposes an extensive surface area that facilitates ions diffusion leading to a high performance of electrosorption. It maximises surface area, potentially allowing large capacitances to be obtained [366]. This also will lead to an increase in ions capture and conductive properties of a-SWCNT.

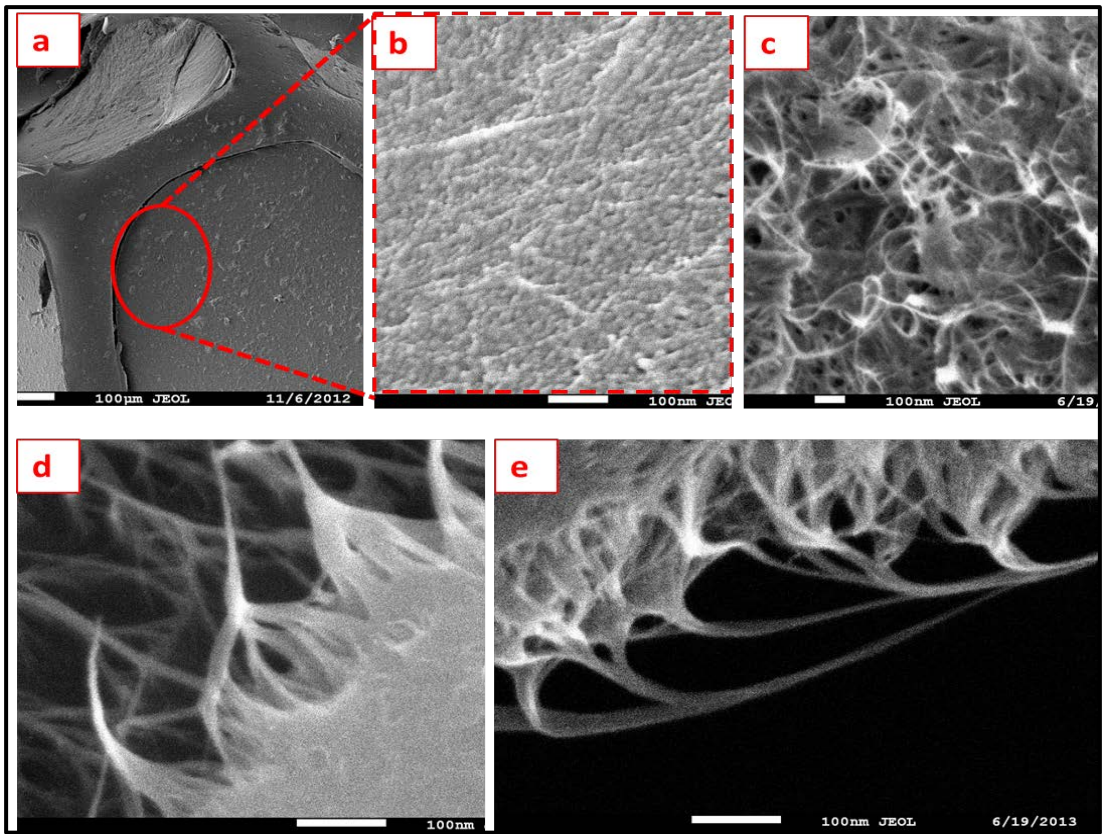

Figure 4.8: Scanning electron microscopy (SEM) images (a, and b) top surface, (c) cross-section and (d and e) 45° view of 23.58%wt a-SWCNT loading.

4.3.6 Electrochemical behaviour evaluation using cyclic voltammetry

In order to evaluate the electrochemical properties of the a-SWCNT coated RVC electrode, cyclic voltammetry was applied as it is one of the most widely used techniques to study electrochemical reactions. In this chapter, it is used to determine the effect of filling the pores of RVC by a-SWCNT on the capacitance, the effect of increasing scan rate on electron transfer and capacitance, and the stability of the electrode using 1 M NaCl solution recorded in the voltage range between -0.2 to 1.0 V vs Ag/AgCl in a three-electrode system with a RVC counter electrode.

4.3.6.1 The capacitance of RVC electrode before and after loading with a-SWCNT

The capacitance of the RVC electrode in 1M NaCl solution using three-electrode systems was discussed in Section (3.3.6.1.) and it was calculated using Equation (3.3) to be 0.002 F/cm^3. Figure 4.9 (a) shows the cyclic voltammograms of 1 cm^3 RVC electrode and the same electrode filled with 23.58 %wt a-SWCNT under the same conditions. The peak current (i_p) of 23.58 %wt a-SWCNT coated RVC electrode compared to a bare RVC electrode has increased by a factor of 1375. This is related to the large surface area of a-SWCNT compared to a bare RVC electrode according to the Randle-Sevcik relationship [304]. The specific capacitance of 23.58 %wt a-SWCNT coated RVC electrode was 2.75 F/cm^3. Figure 4.9 (b) shows that the specific capacitance of the electrode increased with increasing amounts of a-SWCNT in geometric volume. The specific capacitance was 0.56 F/cm^{3,} 1.02 F/cm^3 and 1.31 F/cm^3 for the electrode that had 3.63 %wt, 12.50 %wt and 17.43 %wt a-SWCNT coated on the RVC electrodes, respectively. The specific capacitance of 3.63 %wt, 12.50 %wt and 17.43 %wt a-SWCNT coated on the RVC electrodes compared to a bare RVC electrode has increased by a factor of 280, 510 and 655, respectively. Figure 4.9 (a) shows that the pseudo-capacitive behaviour at 0.5 V for the RVC electrode coated by a-SWCNT. This behaviour referred to the function group which created by the nitric acid treatment on SWCNT surface [368].

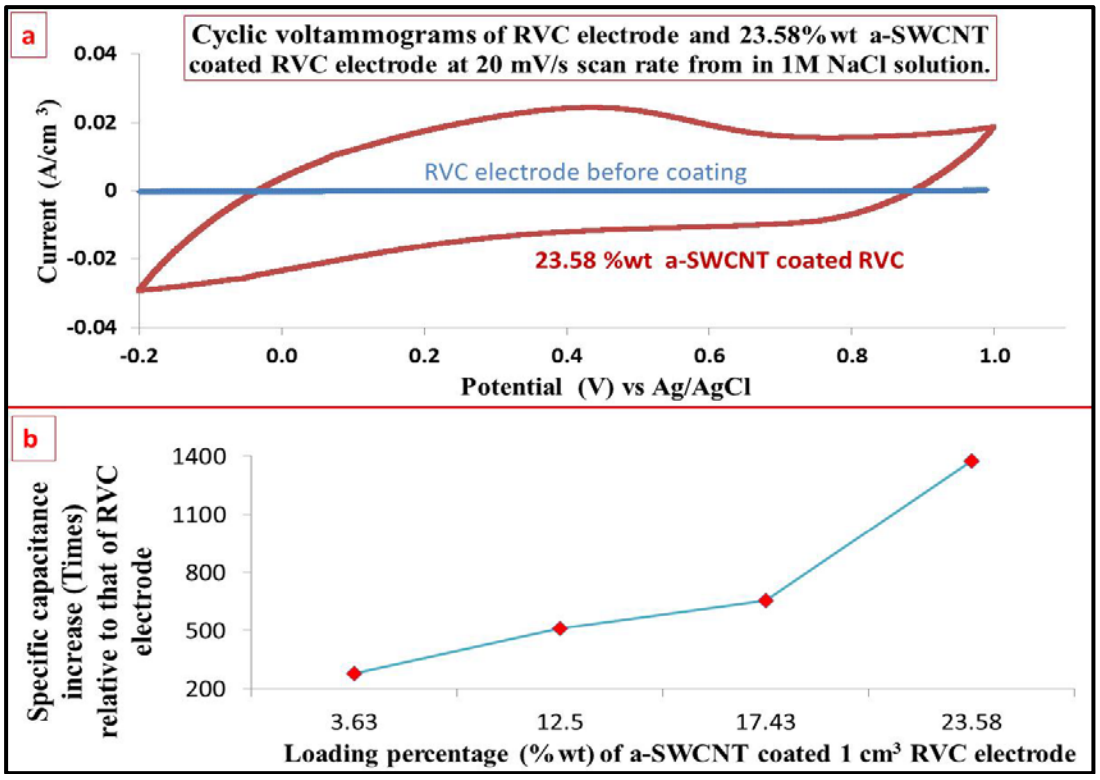

Figure 4.9: (a) Comparison cyclic voltammograms of 1 cm^3 bare RVC electrode and same size of 23.58 %wt a- SWCNT coated RVC electrode in 1 M NaCl scanned at 20 mV/s, and using a RVC counter electrode and Ag/AgCl reference electrode in a three-electrode system and (b) Effect of a- SWCNT loading of a- SWCNT/RVC composite electrodes on specific capacitance.

4.3.6.2. Effect of increasing scan rate on the electrode capacitance

The capacitive behaviour of the a-SWCNT resulted mainly from electrochemical double-layer charging along with a negligible contribution of pseudo-capacitance. In this study, the effect of different scan rates on electrode capacitance was investigated in 1M NaCl aqueous solution. Figure 4.10 (a) shows the cyclic voltammograms of 3.63 %wt a-SWCNT coated RVC working electrode obtained with various potential scan rates. It can be noted that electrochemical reactions occur in the potential range of (-0.2 to 0.4 V) for scan rates of 5 mV/s, resulting in redox peaks at about 0 and 0.2 V. However, the shape of the CVs at scan

rates 5 to 20 mV/s are close to rectangular and as we know, the achievement of a rectangular-shaped CV is the suggested ultimate goal in electrochemical double-layer capacitors (EDLC) [314]. The absence of Faradaic reactions at 0.5V indicates that the current response here absolutely comes from the electric double layer EDL formation [367]. The enhanced capacitance compared with raw SWCNT relates to the increased surface charge density from oxygen atoms with more negative electronic affinity [368]. According to the characteristics of the CV, it can be deduced that the contribution of carboxyl and carbonyl groups to CNTs is in the pseudo-capacitance, which increases apparent capacitance [341, 369]. It is clear that, the polarization caused by a high scan rate leads to the anodic peaks shifting toward high potential and the cathodic peaks moving toward negative potential simultaneously [341]. However, when the scan rate was increased to 50 mV/s, the curves were characterized by non-rectangular shape that indicated resistance-like electrochemical behaviour. This leads to a continuous decrease in the capacitance of electrodes with increasing scan rate.

Figure 4.10 (b) presents the capacitances of various a-SWCNT coated RVC electrodes as a function of the scan rate. It is observed that increasing the amount of a-SWNT in the RVC electrode led to a decrease in the specific capacitance of a-SWCNT. For example, the highest specific capacitance was 267.24 F/g for 3.63 %wt a-SWCNT and the lowest specific capacitance was 139.65 F/g for 23.58 %wt a-SWCNT at a scan rate of 5 mV/s. It seems also that a-SWCNT coated RVC electrodes gave, in all electrodes, a high capacitance at low scan rate, but its capacitance markedly decreased at high scan rates. For instance, the specific capacitance of 3.63 %wt a-SWCNT coated on RVC was 267.24 F/g, 239.58 F/g,

207.40 F/g, 132.69 F/g, 84.77 F/g and 51.15 F/g at 5, 10, 20, 50, 100 and 200 mV/s, respectively (Table 4.3). It is expected that the capacitive volume should increase with increasing scan rates because it is found in all cases of carbon nanotubes [221, 314, 341, 367, 368, 370-372]. This characteristic has been attributed to the resistance of the electrolyte and the inner resistance of ion diffusion with certain carbon micro-pores being surface partially accessible to electrolytes. This becomes significant under relatively high scan rates due to the differential depletion of the electrolyte concentration [372-374]. It can be seen that the specific capacitance trend of 3.63 %wt electrode sharply decreases when the scan rate is above 20 mV/s. For other electrodes, the specific capacitance trend decrease is more pronounced, when the scan rate is increased above 50 mV/s. The specific capacitance values of all electrodes were calculated using Equation (3.2.).

Figure 4.13 (c and d) show cyclic voltammograms of a-SWCNT composite electrodes with different loadings of a-SWCNT in terms of current per gram of a-SWCNT and current per geometric volume of electrode respectively. It is observed that increasing the amount of a-SWNT in the RVC electrode led to a decrease in the current per gram of a-SWCNT (Figure 4.10 (c)) but, in contrast, led to an increase in the current per geometric volume of electrode (Figure 4.10 (d)). Hence, the effect of the geometric volume of the electrode on the results will now be discussed. The calculated capacitance per unit geometric volume of porous electrode are presented in Figure 4.10 (e) and Table 4.3 as F/cm^3. This is not the same as per unit volume of active material (ie SWCNT) alone. The capacitance of the electrode per geometric volume (F/cm^3) was calculated using Equation (3.3). Figure 4.10 (e) shows that the capacitances of various a-SWCNT coated RVC electrodes increase with increase in

the amount of a-SWCNT in the geometric volume. The specific capacitance, obtained at 20 mV/s, was 0.56 F/cm^{3,} 1.02 F/cm^3, 1.31 F/cm^3 and 2.75 F/cm^3 for the electrode that had 3.63 %wt, 12.50 %wt, 17.43 %wt and 23.58 %wt a-SWCNT coated on the RVC electrodes, respectively. This indicates that the surface area of a-SWCNT coated in the RVC electrode had increased. In addition, the effect of the geometric area of the electrode on the results will now be considered. The calculated capacitance per unit geometric area of porous electrode are presented in Table 4.3 as F/cm^2. The capacitance of electrode per geometric area (F/cm^2) was calculated using Equation (3.4.). The increase of SWCNT loading level could increase the active area resulting in higher specific capacitance. In Table 4.3, the capacitance obtained at 20 mV/s was 0.07 F/cm^2, 0.12 F/cm^2, 0.16 F/cm^2 and 0.33 F/cm^2 for the electrode that had 3.63 %wt, 12.50 %wt, 17.43 %wt and 23.58 %wt a-SWCNT coated on the RVC electrodes, respectively. This indicates that the surface area of a-SWCNT coated in the RVC electrode had increased.

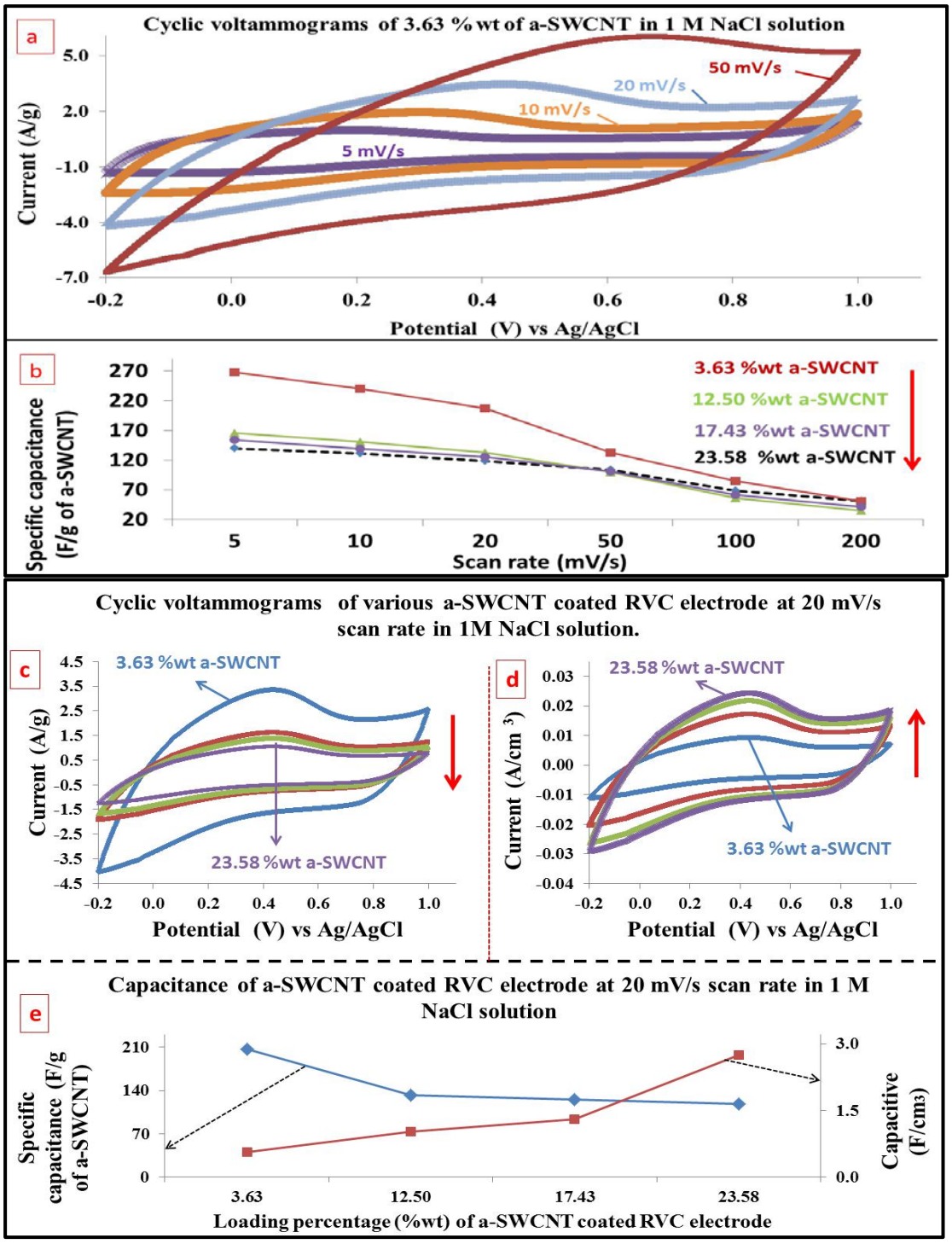

Figure 4.10: (a) Cyclic voltammograms of 3.63 %wt a-SWCNT coated RVC electrode, and (b) specific capacitance of various a-SWCNT coated RVC electrodes at various scan rates in 1 M NaCl solution in the voltage range between -0.2 to 1.0 V vs Ag/AgCl using a three-electrode system. Cyclic voltammograms of a-SWCNT coated RVC electrodes at 20 mV/s, in terms of (c) current per gram of a-SWCNT, and (d) current per geometric volume of electrode. (e) Capacitance of the electrodes per gram of a-SWCNT and per geometric volume of the electrode.

Table 4.3: Specific capacitance of various a-SWCNT coated RVC electrodes by F/g of a-SWCNT, F/area of electrode and F/ volume of electrode, in 1 M NaCl solution at various scan rates.

Sample		3.63 %wt a-SWCNT coated RVC					
Scan rate (mV/s)		**5**	**10**	**20**	**50**	**100**	**200**
Specific Capacitance	**(F/g)**	267.24	239.58	207.40	132.69	84.78	51.15
	(F/cm^2)	0.09	0.08	0.07	0.03	0.03	0.02
	(F/cm^3)	0.72	0.64	0.56	0.36	0.23	0.14
Sample		12.50 %wt a-SWCNT coated RVC					
Scan rate (mV/s)		**5**	**10**	**20**	**50**	**100**	**200**
Specific Capacitance	**(F/g)**	165.20	150.33	132.16	99.12	56.17	34.69
	(F/cm^2)	0.21	0.18	0.12	0.07	0.04	0.02
	(F/cm^3)	1.76	1.46	1.02	0.55	0.31	0.17
Sample		17.43 %wt a-SWCNT coated RVC					
Scan rate (mV/s)		**5**	**10**	**20**	**50**	**100**	**200**
Specific Capacitance	**(F/g)**	153.79	138.94	125.20	100.77	61.07	41.23
	(F/cm^2)	0.29	0.23	0.16	0.08	0.04	0.02
	(F/cm^3)	2.42	1.93	1.31	0.67	0.37	0.19
Sample		23.58 %wt a-SWCNT coated RVC					
Scan rate (mV/s)		**5**	**10**	**20**	**50**	**100**	**200**
Specific Capacitance	**(F/g)**	139.65	131.27	117.70	103.34	68.43	51.67
	(F/cm^2)	0.39	0.37	0.33	0.29	0.19	0.14
	(F/cm^3)	3.23	3.04	2.75	2.39	1.58	1.20

4.3.6.2 Cycling stability of a-SWCNT/RVC electrodes

The electrochemical cycling performance of the electrodes with various amounts of a-SWCNT coated on the RVC electrode was investigated for 200 cycles by cyclic voltammetry, as shown in Figure 4.11. It is clear that they all exhibit excellent cycling performance during the first 200 cycles and the results show that a lower amount of a-SWCNT on the RVC electrode exhibits a much better stability. After 200 cycles, the 3.63 %wt, 12.50 %wt, 17.43 %wt and 23.58 %wt a-SWCNT coated RVC electrodes maintained 98%, 95%, 94% and 91% of their capacitances respectively. The main initial loss of stability can be attributed to the decrease in the redox activity of the redox process. The decrease in the capacitance of each electrode can be attributed to the decrease of the pore structure of the electrode and to the increase of the ratio of C to O attributed to the phenolic hydroxyl groups on the electrodes [369]. Consequently, the capacitance decreased with the cycle number due to the increase in the number of oxygen-containing functional groups on the electrode. The results show that a lesser amount of a-SWCNT on the RVC electrode exhibits a much higher discharge capacity and excellent cycling stability.

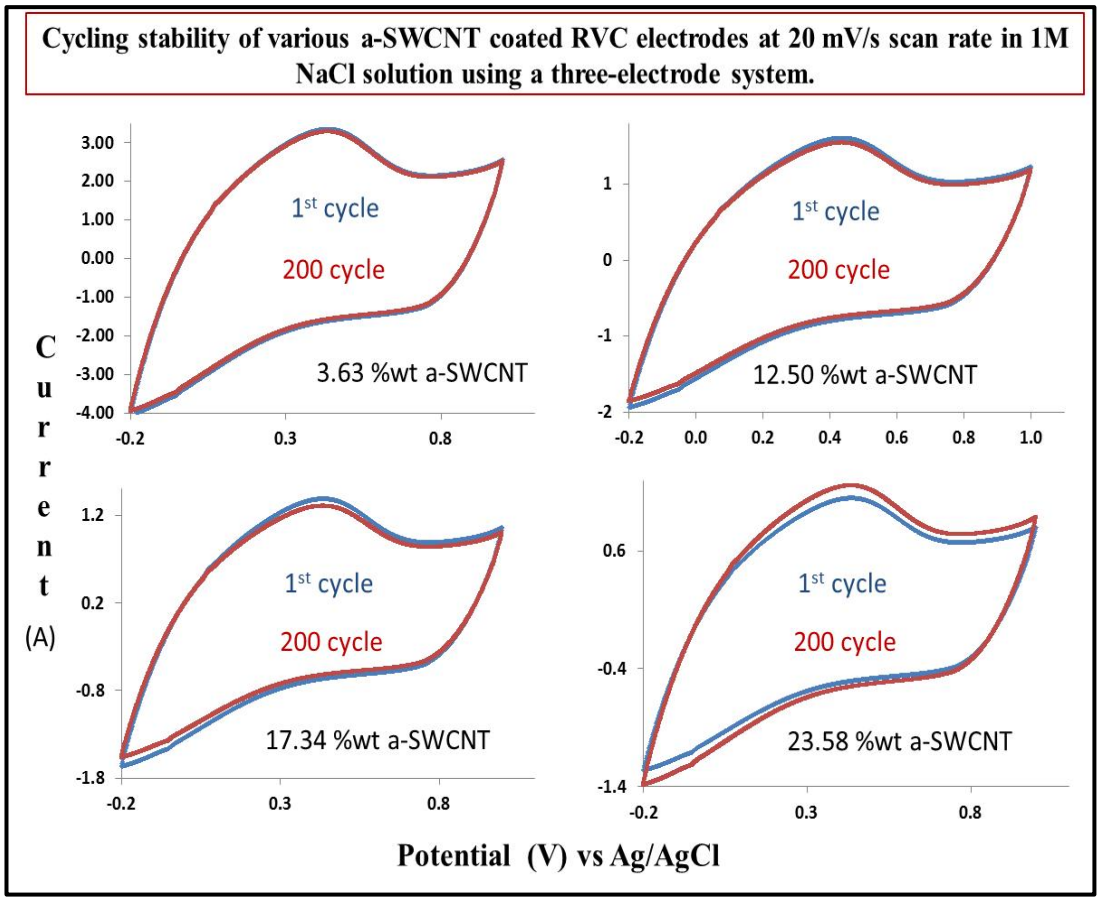

Figure 4.11: The electrochemical cycling stability of a-SWCNT coated RVC electrodes, with different a-SWCNT loadings, in 1 M NaCl solution recorded after 200 cycles in the voltage range between -0.2 to 1.0 V vs Ag/AgCl using a three-electrode system at 20 mV/s scan rate.

4.3.7 Effect of working conditions on ion removal efficiency

The key factors that affect the performance of ion removal of NaCl onto the sites of a-SWCNT, ie flow-rate and electrical voltage, were systematically investigated in this work. These experiments were carried out with 60 mL of the 75 mg/L NaCl solution (143.00 μS/cm measured conductivity) using a RVC electrode and Ag/AgCl electrode as counter and reference electrodes, respectively, and the solution temperature was maintained at 293 K.

4.3.7.1 Effect of applied voltage

The 3.63 %wt a-SWCNT/RVC was used as working electrode in the CDI system. The magnitude of the applied voltage ranged from 0.9 V to 1.5 V. Conductivity variations of the NaCl solution with applied voltage and operating time are shown in Figure 4.12 (a); and Figure 4.12 (b) represents the electrosorption capacity (calculated as explained in Section (3.3.9.)) as a function of electrical voltage. The ion removal characteristics were affected by various applied voltages. Once the electric field was applied, the salt concentration dramatically dropped because ions were attracted by oppositely charged electrodes [33]. As the applied voltage increased in the range of 0.9 V to 1.5 V, the ion removal amount increased and the electrosorption capacity gradually rose from 3.15 mg/g to 8.92 mg/g. It is obvious that the electrosorption capacity is dependent on applied voltage, and higher ion removal is achieved with higher voltage. As expected, high electrical voltage results in high electrosorption capacity because of strong Coulombic interaction between the electrode and charged $Na^{+}$and Cl^{-}ions [40, 320]. When the electrical voltage was at 1.5 V, no visible gas bubbles appeared in the target solution, indicating that there was not any electrolysis of water taking place [268]. Electrolysis of water was not found when the voltage between the two electrodes was more than 1.2 V because of the existence of the resistance in the whole circuit [375]. It is noticeable that the conductivity of NaCl solution decreases once the cell voltage is applied, to approximately 141.34 μS/cm, 141.61 μS/cm, 142.43 μS/cm and 142.67 μS/cm at 1.5V, 1.3V, 1.1V and 0.9 V, respectively. The CDI process was very efficient at 1.5 V because of enhanced electrostatic forces, with a much poorer performance at 1.1 V. When the conductivity almost did not vary, it indicated that

the ions were adsorbed maximally [33]. When the electric field was switched off, the conductivity returned to its initial value, demonstrating that the electrosorption was a reversible process. It is known that the CDI process is closely related to the electrical voltage.

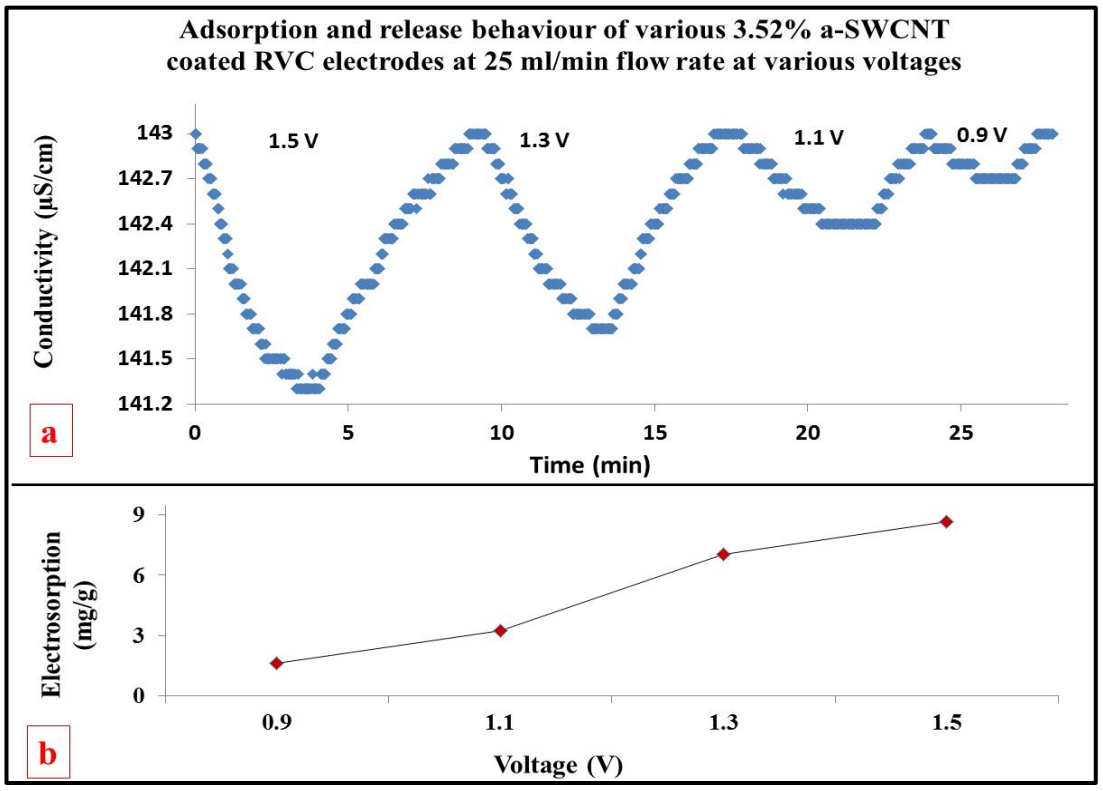

Figure 4.12: (a) Conductivity variations of NaCl solution with applied voltage and operating time. (b) The electrosorption as a function of applied voltage.

4.3.7.2 Effect of flow-rateon electrosorption

The effect of increasing flow-rates on the electrode's ability to adsorb ions was investigated over a range of the flow-rates ranging from 25 mL/min to 75 mL/min through a CDI cell. Figure 4.13 shows the ion removal characteristics at various flow-rates. It is obvious that the efficiency of NaCl ions removal using 3.63%wt a-SWCNT and 12.50%wt a-SWCNT coating RVC electrodes decreased when the flow-rate was increased above 50 mL/min as shown in Figure 4.13 (a and

b). The maximum conductivity decrease of the NaCl from an initial value of 143 μS/cm, using the 3.63%wt a-SWCNT/RVC and 12.50 %wt a-SWCNT/RVC electrodes in the CDI unit system, was to around 140.72 μS/cm and 140.14 μS/cm respectively, at a flow-rate of 25 and 50 mL/min. The conductivity at a flow-rate of 75 mL/min was decreased to 141.33 and 140.82 μS/cm using the 3.63%wt a-SWCNT/RVC and 12.50 %wt a-SWCNT/RVC electrodes, respectively. These results indicate that flow-rates above 50 mL/min would lead to lower electrosorption. This is because too high a pump rate will introduce a high pump force that is greater than the electrosorption force and therefore decrease the electrosorption amount [209, 268]. In addition, the conductivity characteristics related to flow-rates did not significantly change when the flow-rate was increased from 25 to 50 mL/min. This was due to the equilibrium between the electrostatic force of the electrode and the driving force in the flow-rate [209, 268]. Therefore, the electrosorption amount did not significantly change in both cases. It is clear that when the loading level of a-SWCNT increased in the RVC electrodes to 17.43%wt and 23.58%wt (Figure 13 (c and d)), the efficiency of the conductivity at low flow rate (25 ml/min) was worse. The reason is that a low pump rate would result in an obvious co-ions effect which will depress the electrosorption process [209, 268]. Furthermore, the results showed that 50 mL/min was the optimal flow-rate as shown in Figure 4.13 (c and d).

Thus, methodical investigations have been done that showed an electrical voltage of 1.5 V and flow-rate of 50 ml/min are the optimum conditions and key factors which affected the NaCl ion removal performance onto the sites of a-SWCNT. These conditions were then applied to investigate the effect of a-SWCNT loading on NaCl ion removal efficiency as reported in the next section.

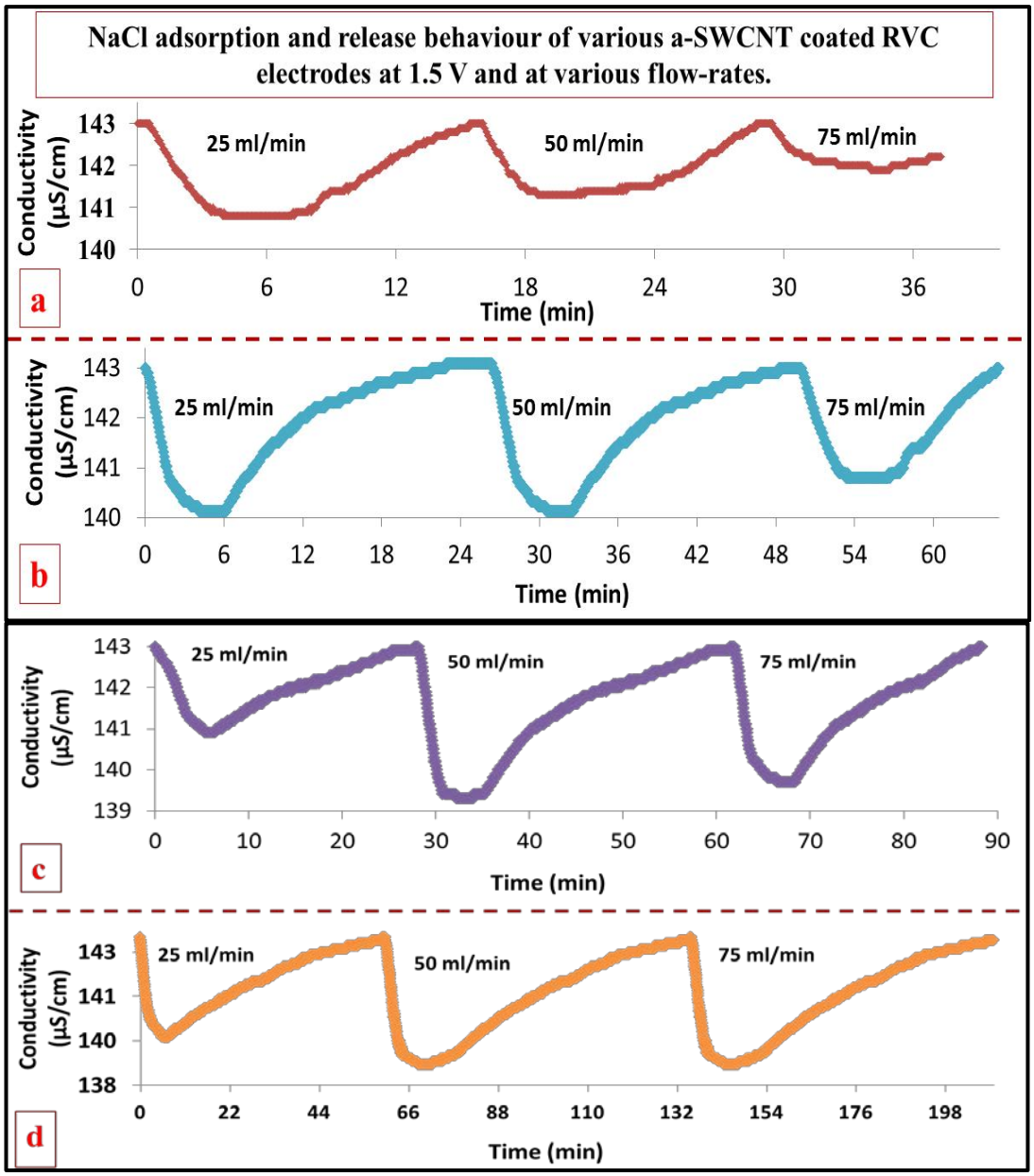

Figure 4.13: Variations of the conductivity of NaCl solution with various applied flow-rates and operating time. (a) 3.63 %wt, (b) 12.50 %wt, (c) 17.43 %wt and 23.58%wt a-SWCNT coated RVC electrodes.

4.3.8 Effect of a-SWCNT loading on electrosorption

The CDI system was investigated with respect to the influence of increased loading of a-SWCNT of a-SWCNT/ RVC composite electrodes on the ion removal performance. The loading levels were 3.63, 12.50, 17.43 and 23.58 %wt,

respectively. All experiments were performed with an electrical voltage of 1.5 V and a flow-rate of 50 mL/min through the CDI system, using 60 mL of the 75 mg/L NaCl as feed solution, and the solution temperature was maintained at 293 K.

Figure 4.14 (a) depicts the CDI process at various a-SWCNT coated RVC electrodes. As expected, once the electrical voltage was applied, the conductivity decreased for all electrodes because ions were attracted by opposite charges on the electrodes [33]. Then the conductivity would gradually approach a constant minimum level, indicating that saturation was achieved. These adsorption processes at first took 6 minutes. It is clear that the drop in conductivity of the solution increased with increasing amounts of a-SWCNT on the RVC electrode. This indicates that the increase in the amount of a-SWCNT leads to increase in the interaction between the charged surface of the electrode and charged Na^+ and Cl^- ions. Notably, the highest drop in conductivity was around 4.41 μS/cm using the electrode which had 23.58 %wt a-SWCNT. For other electrodes the conductivity decreased from 143.00 μS/cm to 141.34 μS/cm, 140.32 μS/cm and 139.29 μS/cm with a-SWCNT loadings of 3.63 %wt, 12.50 %wt and 17.43 %wt, respectively. Furthermore, when the CDI system was under 0 V of applied voltage, the electrode can be quickly regenerated, that is, the adsorbed ions were desorbed from the electrodes due to the disappearance of electrostatic forces. The discharge time was approximately 30 minutes; to release all the ions from the electrodes and return the solution conductivity to its initial level. These results suggest that the CDI process using a-SWCNT coated RVC electrodes has promise as an effective technology for desalination.

Electrosorption removal of NaCl by our CDI system was measured from the data in Figure 14 (a). Accordingly, the correlation of conductivity (μS/cm) with concentration (mg/L) was calibrated prior to experiment see previous Equation (2.9.). The electrosorption performance of a-SWCNT is shown in Figure 14 (b). The electrosorption decreased with increasing mass of a-SWCNT. Clearly, when the 3.63%wt a-SWCNT/RVC electrode had 6 mg of a-SWCNT, the electrosorption was 8.39 mg/g, and when the 23.58%wt a-SWCNT/RVC electrode had 50 mg of a-SWCNT, the electrosorption was 2.77 mg/g. On the other hand, if the electrosorption of electrodes in terms of geometric volume or geometric area of the a-SWCNT coated RVC electrodes was considered, the electrosorption increased with increasing amounts of a-SWCNT. When the 3.63%wt a-SWCNT/RVC electrode had 6 mg a-SWCNT, the electrosorption was 0.003 mg/cm^2 or 0.02 mg/cm^3, and when the 23.58%wt a-SWCNT/RVC electrode had 50 mg a-SWCNT, the electrosorption was 0.008 mg/cm^2 or 0.06 mg/cm^3. Also it is clear that the electrosorption became more stable above an electrode loading of 12.50 %wt a-SWCNT. Table 4.4 shows more details of the electrosorption in terms of mass, area and volume for each a-SWCNT coated RVC electrode.

In summary, although the electrosorption performance of the electrode with 3.63 %wt a-SWCNT loading is best in terms of mg/g of ion removal, it is the electrode with 23.58 %wt a-SWCNT loading that affords the best ion removal in terms of geometric area or geometric volume of electrode; ie it removes the most ions in electrode size terms. This is advantageous when the size of the electrode becomes a major consideration in designing a CDI system. Having designed a simple CDI system and investigated its electrosorption performance, attention was then

turned towards refining the CDI system with an improved cell design. This work is now reported in the next section.

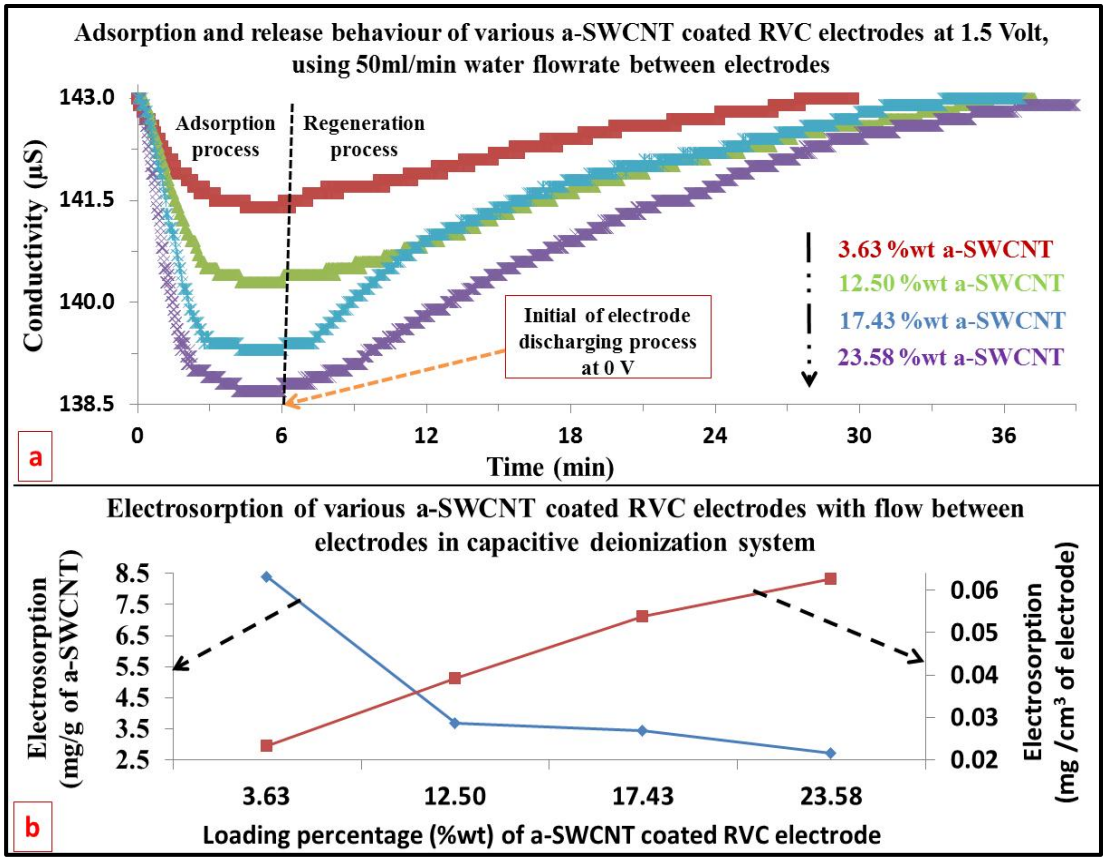

Figure 4.14: (a) Adsorption and release behaviour and (b) the electrosorption capacity in terms of mass of a-SWCNT and in terms of geometric volume of composite electrode of various loadings of a-SWCNT on RVC electrode using the CDI system.

Table 4.4: Electrosorption capacity of various a-SWCNT coated RVC electrodes

Sample	a-SWCNT in sample (% wt)	Electrosorption capacity		
		mg/g of a-SWCNT	mg/ cm^3 of electrode	mg/ cm^2 of electrode
1	3.63	8.39	0.02	2.8E-03
2	12.50	3.69	0.03	4.8E-03
3	17.43	3.42	0.05	6.5E-03
4	23.74	2.77	0.06	7.6E-03

4.3.9 Effect of CDI cell configuration on ions removal efficiency

CDI systems are most often designed such that the feed stream to be desalinated flows primarily between the two porous electrodes [44, 51, 167, 209]. This separation between electrodes must serve as both a flow channel and a structure to prevent electrical shorts between the two porous electrodes. Flow-between (FB) electrodes in CDI systems require long desalination times [376]. Therefore, an attempt was made to change the location of the electrodes so as to flow the feed stream directly through the electrode pores to reduce desalination time. This flow system, now called flow-through electrode (FT) cell often uses low hydraulic resistance and high surface area porous electrodes, consisting of micron-scale and nano-scale pores [376]. According to Suss et al [376], when carbon aerogel is used in a FT cell, the mean sorption rate increases 4 to 10 times higher than typically achieved with a FB cell. This is because the the FT cell allows ion transport from the microscale pore bulk to the nano-scale pores which maximize the surface area [376]. Figure 4.15 (a and b) is a schematic representation of a typical FB charging electrodes configuration through a porous separator element and FT capacitive desalination cell taht allows the feed solution to flow directly through the electrode pores, respectively.

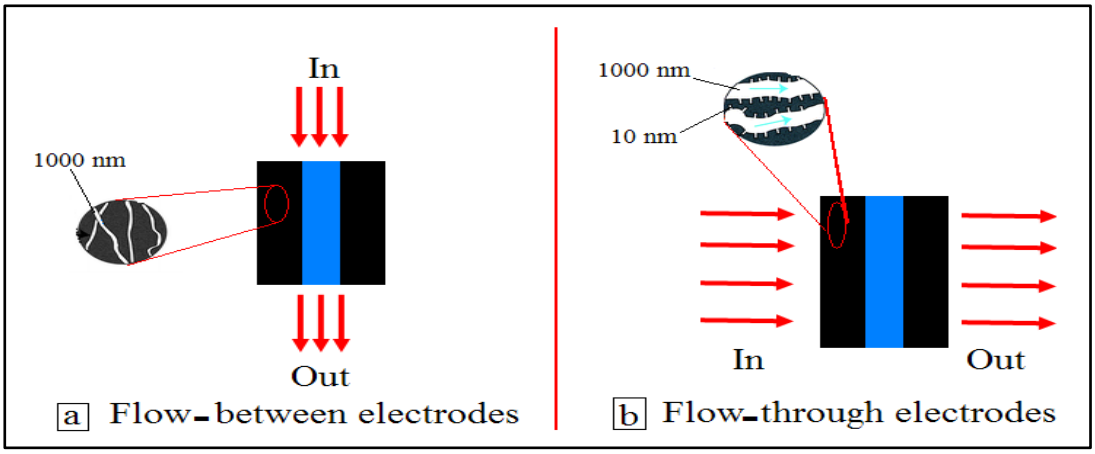

Figure 4.15: Schematic diagram of flow-between and flow-through electrodes in CDI cell.

Further experiments, therefore, were carried out to compare the performance of the FB cell with that of the FTE cell. All experiments used 60 mL of the 75 mg/L NaCl solution that was re-circulated at 50 mL/min as feed solution in the CDI system under an applied voltage of 1.5 V. An a-SWCNT 50 mg coated RVC electrode (23.58 %wt) was used as the working electrode. Also, the distance between electrodes in both configurations was 5 mm. Figure 4.16 shows the effect of feed stream directly through the electrode or between electrodes on desalination time. It is clear that for one desalination cycle, 39 minutes were required for the flow between electrodes configuration and 18 minutes for the flow directly through electrodes configuration. In fact, the time required for desalination decreased more than two times when the flow-through electrodes configuration was applied. In both systems, the adsorption process took 6 minutes, and the rest of the time was required to regenerate the electrodes. This means that the release of salt from the electrode required 12 minutes and 33 minutes for flow-through electrodes and flow-between electrodes, respectively. This improvement in the salt removal and regeneration

process can be attributed to the facilitated ion transport at the electrode solution interface and faster electron transport within the electrode that resulted in the 3 times faster desalination cycle when the solution was flowed directly through the electrodes. It is very important to draw attention to the shape of the conductivity curve although the amount of conductivity decrease was the same in both systems. The conductivity after 6 minutes in both systems was 138.59 µS/cm. This can be attributed to the flowing force of ion transport to the electrode interface that was same in both systems.

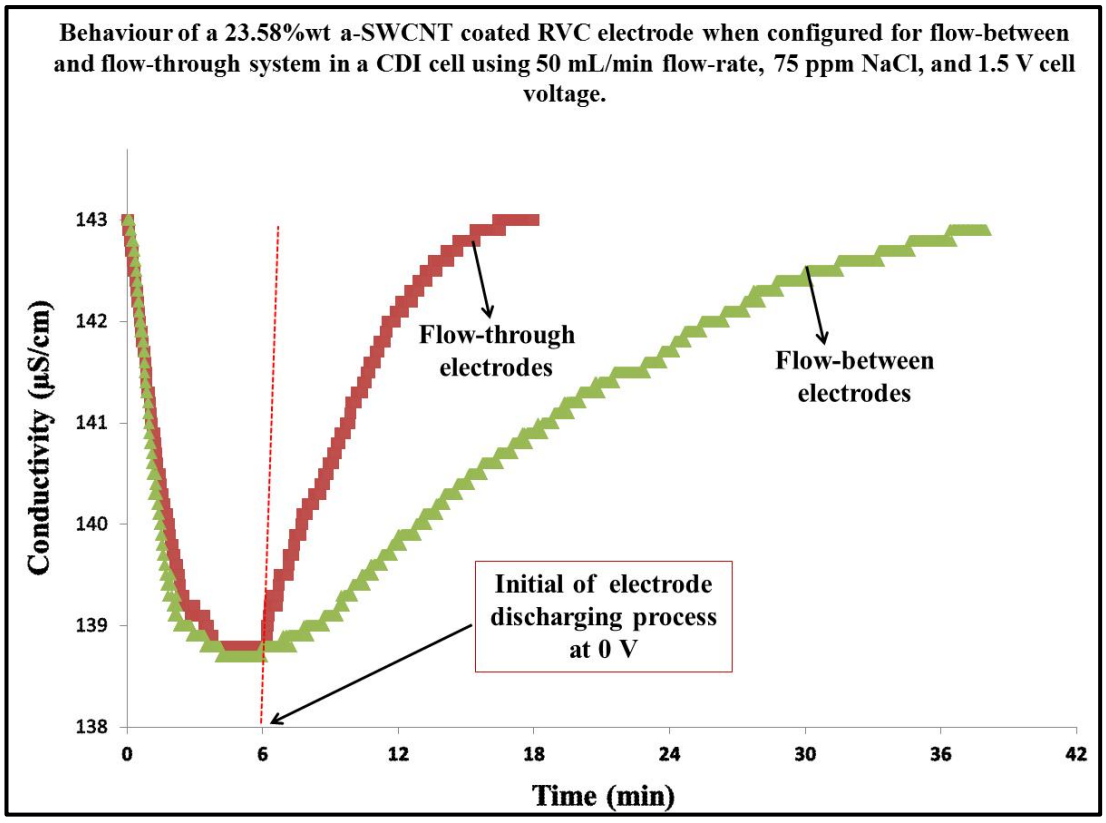

Figure 4.16: Comparison of the NaCl adsorption and release behaviour of 23.58 %wt of a-SWCNT coated RVC electrode when configured for flow-between and flow-through system in a CDI cell.

4.3.10 New design for flow-through cell

The three times faster desorption cycle in a CDI system using flow-through electrodes encouraged efforts to design a new CDI cell with a flow-through electrode system. Figure 4.17 shows the schematic of a new design made in our laboratory. It was built on a Connex 350 3D printer, by Objet. This time the flow-through cell was produced using MED610 material printed over a period of three hours. This cell was rectangular shaped outside and the dimensions were 50 mm *70 mm*28 mm in height, length and width, respectively (Figure 4.17 (a)). Each side had one 4 mm diameter hole in the middle that served as inlet and outlet ports for re-circulating the fluid flow by pumping. When entering the cell, the solution was passed through a flow distributor chamber, 40 mm *20 mm* 10 mm in height, length and width respectively, that had 45 (0.35 mm diameter) holes in the exit side that helped to direct flow onto the whole electrode surface (Figure 4.17 (b)). A similar chamber was constructed for the outlet end. The cell was designed inside to fit a series of electrodes and separate between them. The dimensions of each location and each separating space were 50 mm * 22 mm* 5 mm and 50 mm * 20 mm* 5 mm in height, length and width, respectively. This flow-through cell can hold up to 5 electrodes at any one time.

The total volume of solution was increased in this cell to 70 ml while the old cell was 60 ml. This means that the total amount of NaCl salt dissolved in our solution (75 mg/L = 143.00 µS/cm) increased from 4.50 mg to 5.25 mg. It is very important to mention that the volume of solution is one parameter in the electrosorption capacity equations (Eq 3.5, Eq 3.6 and 3.7). This means that the

volume of electrosorption capacity will increase in the new cell compared with the old cell if the electrode adsorption saturate at the same conductivity value. For example, if the adsorption of the electrode (50 mg) saturate after the NaCl conductivity dropped from 143.00 to 138.59 µS/cm (3.31 mg/L), then the absolute amount of NaCl adsorbed by the electrode in the new cell is 0.16 mg and in the old cell is 0.14 mg; resulting in electrosorption capacities of 2.77 mg/g and 3.23 mg/g respectively.

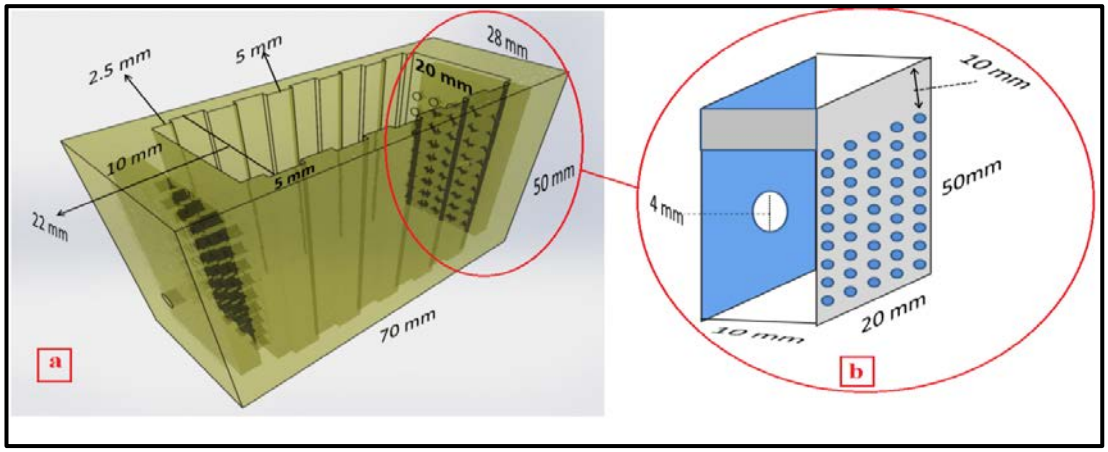

Figure 4.17 : Schematic of a flow-through cell (a) and cross-section of flow distributor chamber (b).

4.3.11 Effect of flow-rate and voltage on ions removal efficiency

In the new system, the total volume of solution was increase to 70 ml. The concentration and the electrical voltage were as for the previous experiments; 75 mg/L NaCl solute ion and 1.5 V. The flow-rate was investigated to study the NaCl removal using the best performance electrode in the old system which was the 23.58 %wt a-SWCNT coated RVC electrode. The distance between electrodes was 5 mm. According to the old system, the best performance for water purification was at 50 ml/min flow-rate. This information led to this investigation of electrode performance

at flow-rates below and above 50 ml/ min as shown in Figure 4.18. It is obvious from the results that the best conductivity decrease was achieved when the flow-rate was 50 mL/min. When the flow-rate was above or below 50 ml/min, the conductivity decrease was less, leading to lower electrosorption capacity. This is due to the fact that a low pump rate would result in an obvious co-ions effect which will depress the electrosorption process, while a high pump rate will introduce a high pump force that is greater than that of electrosorption force and therefore decrease the electrosorption amount [268]. Thus, an optimized flow-rate for the CDI process was found to be 50 mL/min.

In the next sections, all experiments were performed with 70 mL of the 75 mg/L NaCl solution at 50 mL/min flow-rate through the CDI system under the applied voltage of 1.5 V.

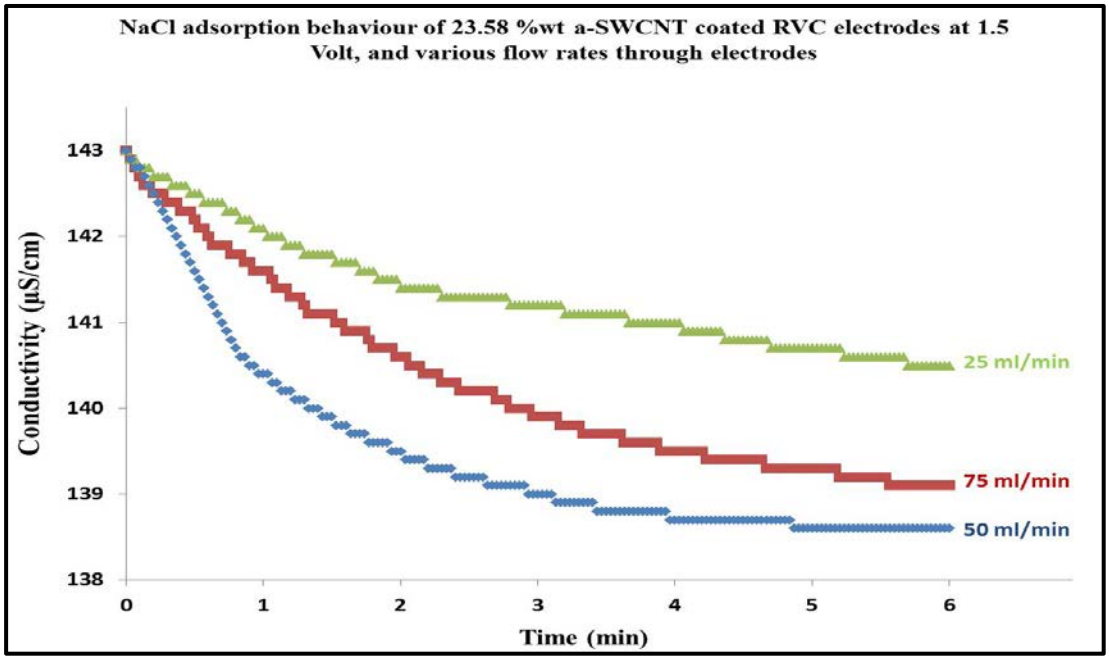

Figure 4.18: Conductivity variations of NaCl solution with various flow-rates, as a function of operating time.

4.3.12 Effect of distance between the electrodes on efficiency of electrosorption

It is known that increasing the space between a pair of electrodes results in an increase in electrical resistance between the electrodes that, in turn, leads to decrease in the electrical current [377, 378]. Therefore the next phase of studies was directed towards the effects of current density and space between electrodes on the efficiency of electrosorption. The space between electrodes was varied from 5 mm to 15mm then to 25 mm, respectively, and the counter electrode was RVC electrode, and the working electrode was 23.58 %wt a-SWCNT coated RVC electrode. Figure 4.19 shows the current and conductivity behaviour of 23.58 %wt a-SWCNT coated RVC electrodes for various gaps between electrodes. It was as expected, the current density decreased with an increase in the gap between electrodes. When the distance between electrodes was 5, 15 and 25 mm, the current at the start was found to be 4.56, 2.20 and 1.11 mA, respectively (Table 4.5). Table 4.5 also gives more details about start current, current stability, charge of electrode, the time of highest conductivity, and the energy output for each distance between electrodes. Furthermore, the energy output of the CDI system was affected by an increase in the space between electrodes. It is clear that if the space increases, the energy output increases. The energy output at 5, 15, and 25 mm was 0.67, 0.91 and 1.42 J/C, respectively. The energy can be calculated according to Equation (4.2) [379].

$$E = Q * V \qquad \textbf{(Eq 4.2)}$$

Where E is energy (J), Q is charge (C) and V is constant voltage (V).

It is very interesting that the ion removal characteristics were affected by various distances between electrodes. As the distance increased, the ion removal amount was not affected in the range of distances from 5mm to 15 mm but was less when the gap between electrodes was 25 mm. However the adsorption time required increased when the distance was increased in all cases. One deionisation cycle took 7 min at 5 mm distance between electrodes but when the distance was increased to 15 mm the ions adsorption/ desorption cycle took 55 min as shown in Figure 4.19. According to the above, the best design should have a small space between electrodes because this will: reduce the time of water purification, afford efficient energy output, decrease the electrical resistance between the electrodes and increase the electrical current.

Table 4.5: The current of the CDI system for different inter-electrode distances used 1.5V applied voltage.

Distance between electrodes (mm)	Time required for adsorption (min)	Initial current (mA)	Stable current (mA)	Charge (C)	Energy (J)
5	6	4.56	1.02	0.45	0.67
15	25	2.20	0.27	0.61	0.91
25	60	1.11	0.16	0.95	1.42

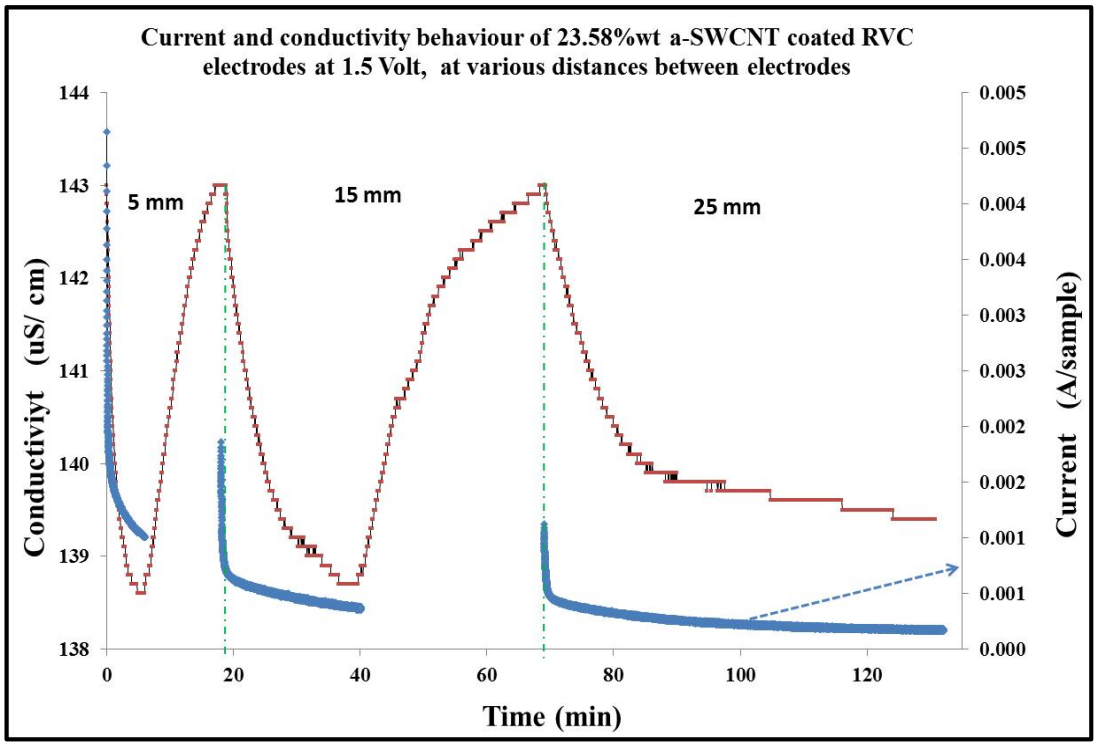

Figure 4.19: The effect of distance between electrodes (5 mm, 15 mm and 25 mm) on the current and conductivity behaviour of 23.58 %wt a-SWCNT coated RVC electrode at 1.5 Volt and 50 ml/min flow-rate.

4.3.13 Adsorption/ desorption performance of a-SWCNT loaded RVC electrodes

Having determined that the optimum distance between electrodes is 5 mm, the optimum applied voltage is 1.5 V and optimum flow-rate is 50 mL/min, as reported in the previous section, these conditions were used in further studies to compare the desalination performance of a range of electrodes with different amounts of a-SWCNT coated on the RVC. Figure 4.20 (a) shows the CDI process at all loading levels of a-SWCNT in RVC electrodes. It is clear that the electrosorption behaviours of all electrodes in the new cell followed the old cell in Section (4.3.8.); ie the drop in conductivity increases with increasing amounts of a-SWCNT on the

electrode. At the a-SWCNT 23.58 %wt coated RVC electrode, a better electrosorption performance was achieved and the conductivity significantly dropped about 4.41 μS/cm in the electrosorption process. For all electrodes the conductivity would gradually approach a minimum constant level, indicating that saturation had occurred. These adsorption processes took 6 minutes. During discharging of the CDI system under 0 V of applied voltage, the solution conductivity returned to about its initial value (143 μS/cm), meaning ions were released from the double layer region back into the solution because of the disappearance of electrostatic forces (as discussed in Section (4.3.8.)). The regeneration by discharging the CDI cells was completed at 0 V after 18 min for the electrode with the highest amount of a-SWCNT in the sample (23.58 %wt). This result is in keeping with earlier results reported in Figure 4.14 (a).

Figure 4.20 (b) shows the electrosorption of various a-SWCNT coated RVC electrodes in terms of the mass of a-SWCNT and the volume of electrode. It is clear from the figure that the electrosorption decreased with the increase in weight of a-SWCNT loading. Clearly, when the sample had 3.63 %wt a-SWCNT the electrosorption capacity was 10.40 mg/g and when the sample had 23.58 %wt a-SWCNT, the electrosorption capacity was 3.23 mg/g. On the other hand, if the electrosorption of electrodes was considered in terms of geometric area or geometric volume, the electrosorption increased with increase in the amount of a-SWCNT. For example, when the sample had 3.63 %wt a-SWCNT, the electrosorption was 0.03 mg/cm^3 or $0.003mg/cm^2$ and when the sample had 23.58 %wt a-SWCNT, the electrosorption was 0.08 mg/cm^3 or 0.009 mg/cm^2, (Table 4.6). Table 4.6 also gives more details about electrosorption in terms of mass, geometric area, and geometric

volume for each a-SWCNT coated RVC electrode which were calculated according to Equation (3.5), Equation (3.6) and Equation (3.7).

Table 4.6: Electrosorption capacity of various a-SWCNT coated RVC electrodes.

Sample	a-SWCNT in sample (wt %)	Electrosorption capacity		
		mg/g of a-SWCNT	mg/ cm^3 of electrode	mg/ cm^2 of electrode
1	3.63	10.40	0.03	3.5E-03
2	12.50	3.99	0.05	5.1E-03
3	17.43	3.67	0.06	7.2E-03
4	23.58	3.23	0.08	9.4E-03

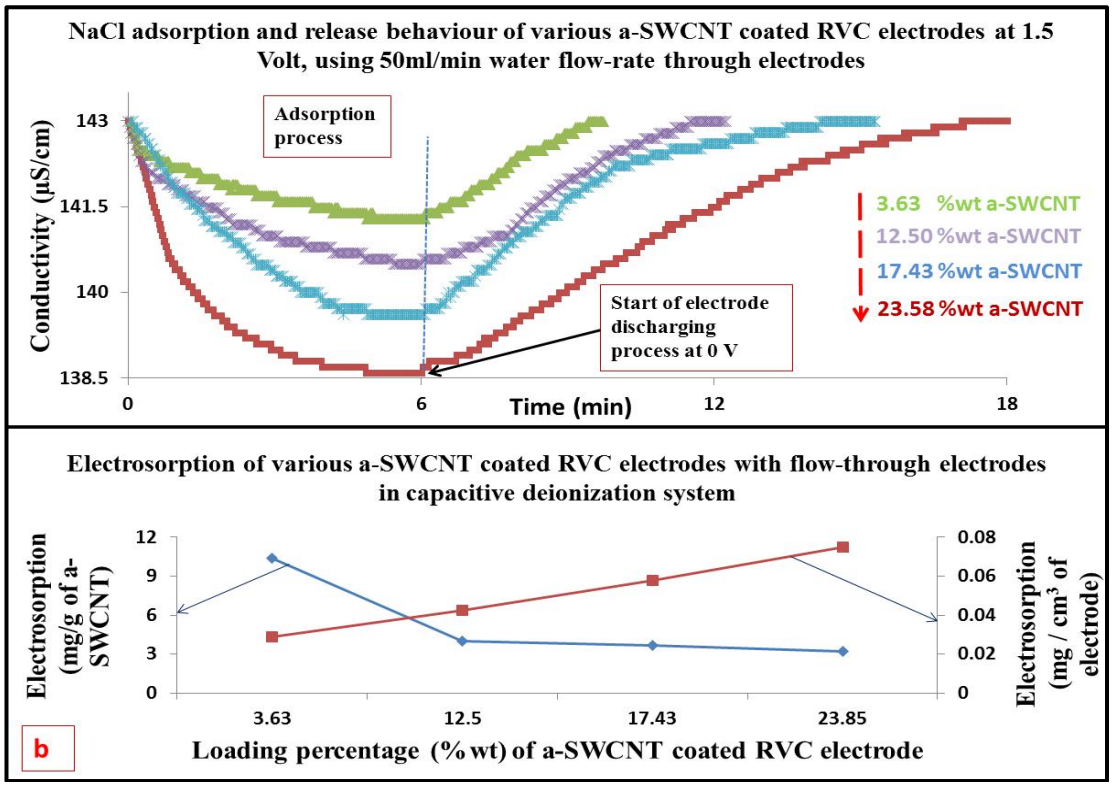

Figure 4.20: (a) Adsorption and release behaviour, and (b) the electrosorption capacity in terms of mass of a-SWCNT and the geometric volume of electrode of various a-SWCNT coated RVC electrode coatings of a-SWCNT (wt%): 3.63%, 12.50%, 17.43% and 23.58%.

4.3.14 Comparison between new cell (flow feed through electrode) and old cell (flow feed between electrode)

This section compares the results of electrosorption capacity and the time of one desalination cycle, obtained with various a-SWCNT coated RVC electrodes, for the two different flow cells (flow feed through electrodes and flow feed between electrodes), as shown in Table 4.7. All these data are obtained from section 4.3.8. and section 4.3.13 using 75 mg/L NaCl feed solution. It is clear that, the electrosorption capacity of all electrodes in the new cell was increased. For example, the electrosorption capacity for 3.63 %wt a-SWCNT was increased from 8.39 mg/g to 10.40 mg/g using flow feed between electrodes and flow feed through electrodes, respectively. This means that electrosorption capacity increased 23.96% (see example calculation below). In fact, the time required for one desalination cycle decreased around three times after using flow feed through electrodes. The time of one desalination cycle decreased from 30 min to 10 min, from 36 min to 12 min, from 37 min to 15 min, and from 39 min to 18 min using 3.63 %wt a-SWCNT, 12.50%wt a-SWCNT, 17.43%wt a-SWCNT and 23.58%wt a-SWCNT coated RVC electrodes, respectively.

Table 4.7: Electrosorption capacities and the time of one desalination cycle of various a-SWCNT coated RVC electrodes obtained by comparing the performance between flow feed between (FB) electrodes and flow feed through (FT) electrodes with NaCl feed solution (75 mg/L)

a-SWCNT in RVC electrode (wt %)	Flow direction	Electrosorption	# Enhancement in electrosorption	Time of one desalination cycle
		mg/g of a-SWCNT	%	min
3.63	FT	10.40	23.96	10
	FB	8.39		30
12.50	FT	3.99	8.13	12
	FB	3.69		36
17.43	FT	3.67	7.31	15
	FB	3.42		37
23.58	FT	3.23	16.61	18
	FB	2.77		39

see example calculation below

Example calculation enhancement related of electrosorption capacity in new cell using flow feed through (FT) electrodes compared with flow between (FB) electrodes.

For the 3.63% a-SWCNT/RVC electrode, the electrosorption capacity 1 desalination cycle is considered.

Thus:

Electrosorption capacity for the FT cell = 10.40 mg/g

Electrosorption capacity for the FB cell = 8.39 mg/g

Therefore,

$$\text{Enhancement} = \left(\frac{(\text{electrosorption using FT cell} - \text{electrosorption using FB cell})}{\text{electrosorption using FB cell}}\right) * 100$$

$$= = \left(\frac{(10.40 - 8.39)}{8.39}\right) * 100 = 23.96\%.$$

4.3.15 CDI cycling stability

Regeneration of a-SWCNT coated RVC electrodes is a very important factor affecting practical use in CDI systems. 23.58 %wt a-SWCNT electrode was used in this study because it afforded the highest electrosorption capacity in terms of geometric volume using the flow feed through cell. Figure 4.21 shows the electrosorption/regeneration cycles of the 23.58 %wt a-SWCNT coated RVC electrode, which was conducted by repeating several charging and regeneration cycles. When no oxidation and reduction reaction occurs in electrosorption, the current is mainly consumed for charging the electrode to electro-adsorb ions from the bulk solution [323]. As can be seen, the polarization of the electrode at 1.5 V leads to a decrease of solution conductivity. The conductivity sharply decreased because ions migrate onto the oppositely charged electrode surface, and then continues to gradually decrease until the electrical double layer is completely formed at the electrode/electrolyte interface [267]. Moreover, the regeneration can be achieved upon the electrode depolarization at 0.0 V. It is noted that the process of regeneration can be carried out easily in a short time and the same pattern can be found in four repeated electrosorption–desorption cycles, each cycle takes 17 min, ie 6 min ion adsorption and 11 min release of ions. Also, the recycling stability was very high for the reason that the decay of electrosorption capacity has not been observed. It demonstrates that the electro-adsorbed ions can be desorbed by removing an electric field, and then the a-SWCNT coated RVC electrode can be reused. Consequently, the electrosorption of ions using this electrode is a reversible process and that the amount of electro-adsorbed ions can be controlled, via manipulation of the electrical double layer formation at the electrode/ electrolyte interface.

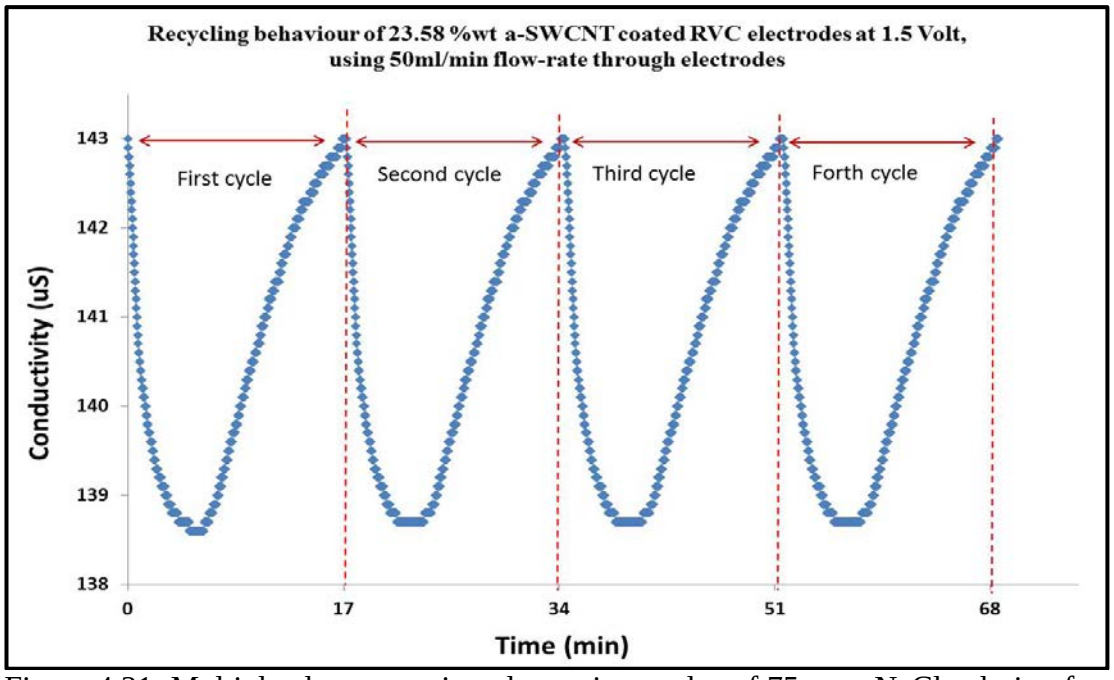

Figure 4.21: Multiple electrosorption–desorption cycles of 75 ppm NaCl solution for 23.58 %wt a-SWCNT coated RVC electrode. Polarization and depolarization was performed at 1.5 V and 0.0 V, respectively.

4.3.16 Electrosorption dynamics

The pseudo first-order, pseudo second-order, and intraparticle diffusion dynamic models for NaCl adsorption onto the 23.58 %wt a-SWCNT coated RVC electrode at a voltage 1.5 V and flow-rate of 50 ml/min using flow feed through cell are shown in Figure 4.22. The electrosorption of NaCl onto the electrode was very rapid within the first minute, then it became dynamic adsorption and after three minutes the electrode gradually approached saturation as shown in Figure 4.22 (a). The time required to reach sorption equilibrium was 6 minutes which may be due to the higher rate of diffusion of ions onto the a-SWCNT particle surface. When the Weber and Morris model, applying Equation (2.17), [258] is used to study intraparticle diffusion of ions into the electrode, it is clear that the plot of q_t versus $t^{0.5}$ shows three multi-linear regions as shown in Figure 4.22 (b).This behaviour is

quite common in an electrosorption process [208, 209, 268, 324, 380] and it indicates that more than one step is effective in the electrosorption process. When voltage was applied, the first stage adsorption was occurring rapidly because the surface diffusion was transported from the bulk solution to the external surface of the sorbent [381]. The second linear stage represents a gradual adsorption stage where intraparticle diffusion of sorbate molecules move into the interior of sorbent particles, and the third linear stage indicates that a low adsorption stage has occurred where intraparticle diffusion starts on the interior sites of the sorbent [381]. In general, the slope of the line in stage 2 is called the intraparticle diffusion rate constant, k_{id} [382]. The rate parameters, k_{id}, together with the correlation coefficients are listed in Table 4.8, they are 1.66 mg/gmin$^{0.5}$ and 0.981, respectively.

Pseudo-first-order and pseudo-second-order processes were studied within the first three minutes in Figure 4.22 (c) and (d), respectively. To evaluate the kinetics of the electrosorption process, the pseudo first-order and pseudo second-order models were tested to interpret the experimental data. The slopes and intercepts of plots of log (*qe–qt*) versus *t* were used to determine the first-order rate constant k_1 and equilibrium adsorption density q_e is shown in Figure 4.22 (c). The linear fit has a relatively high r^2 value however close inspection of the model fit and experimental observations in Figure 4.22 (c) suggests that application of Equation (2.12) is appropriate as experimental observations are linear when plotted in this manner. A comparison of the results with the correlation coefficients is shown in Table 4.8. The correlation coefficients for the pseudo-first- order kinetic model obtained was 0.994 and the rate constant (k_1) of the pseudo-first-order was 0.82 min^{-1}. Also the

theoretical q_e values found from the pseudo-first-order kinetic model gave reasonable values (3.19 mg/g).

Pseudo second-order adsorption parameters q_e and k_2 in Eq. (4.15) were determined by plotting t/q_t versus t as shown in Figure 4.22 (d). This figure shows poor agreement between experimental data and the second-order kinetic model used Equation (2.15). Table 4.8 lists the computed results obtained from the second-order kinetic model. The correlation coefficient for the second-order kinetic model obtained was poor (0.950) and the rate constant (k_2) of the pseudo-second-order was 0.12 g/mg min. The calculated *qe* values also did not give reasonable values with the experimental data; it was 4.72 mg/g. Furthermore the correlation coefficients (R^2) for the pseudo first-order kinetic model fits are 0.996, much higher than the correlation coefficients derived from pseudo second-order model fits. Given the good agreement between model fit and experimentally observed equilibrium adsorption capacity, in addition to the large correlation coefficients, this suggests that NaCl adsorption has obeyed pseudo first -order kinetics rather than pseudo second -order kinetics and that NaCl ions were not adsorbed onto the a-SWCNT surface via chemical interaction [381]. Similar trends have been reported in the literature for the adsorption of NaCl ions from aqueous solutions by other adsorbents [208, 209, 268, 320, 324, 332, 380].

Table 4.8: Comparison between the adsorption rate constant, qe, estimated and Correlation Coefficients associated with pseudo-first-order and pseudo-second-order Rate Equations and Intraparticle Diffusion.

pseudo-first-order			pseudo-second-order				intraparticle diffusion	
q_e (mg/g)	K_1 (min^{-1})	R^2	q_e(mg/g)	K_2 (g/mg min)	R^2	h (mg/g min)	K_{id} (mg/g $min^{0.5}$)	R^2
3.19	0.82	0.994	4.72	0.123	0.950	2.74	1.66	0.981

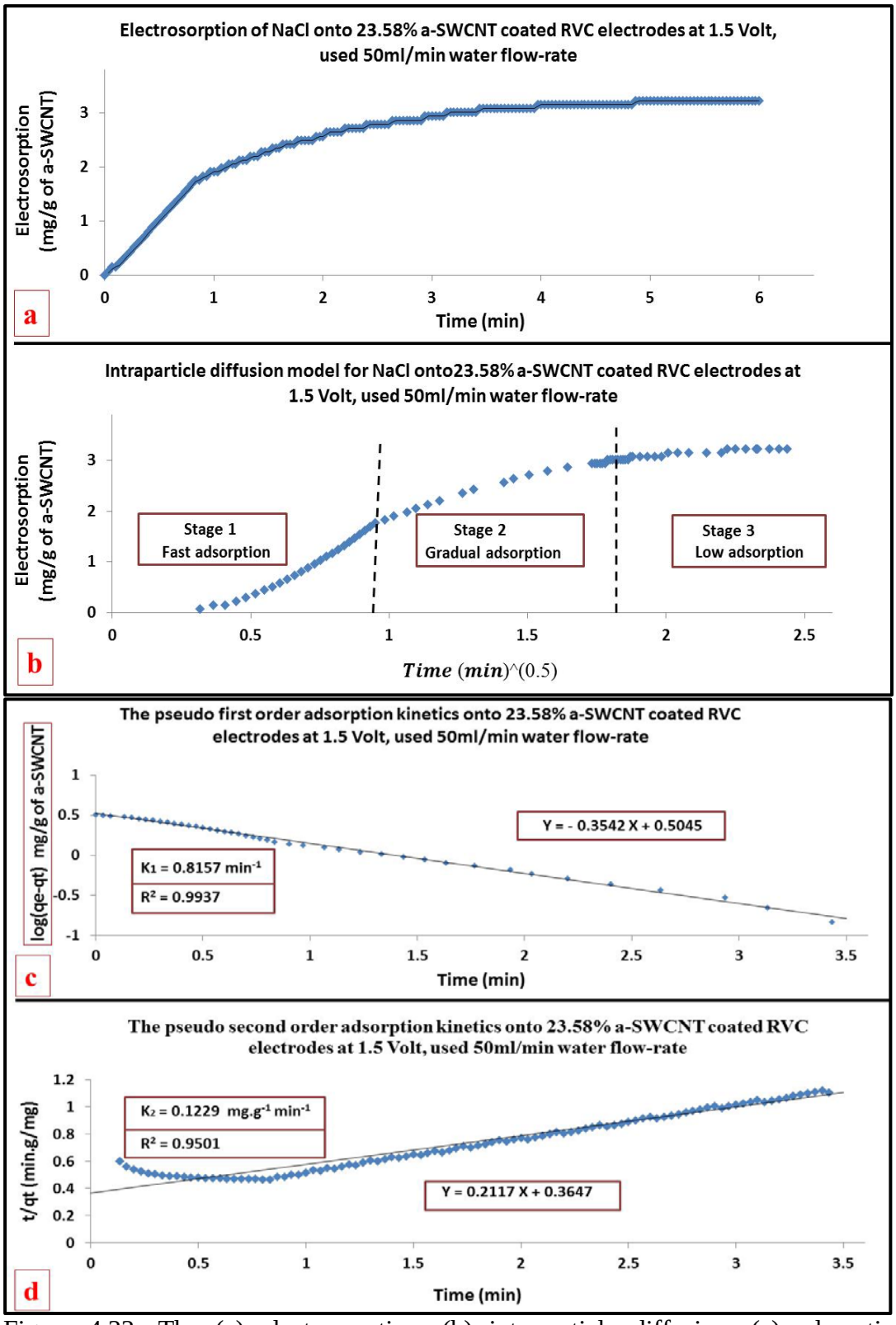

Figure 4.22: The (a) electrosorption, (b) intraparticle diffusion, (c) adsorption kinetics pseudo-first-order, and (d) adsorption kinetics pseudo-second-order, of NaCl onto23.58 %wt a-SWCNT coated RVC electrode at 1.5 V and 50 mL/min flow-rate.

4.3.17 Electrosorption isotherms

Electrosorption isotherms are essential to estimate the electrosorption behaviour of Carbon electrodes. This experiment was carried out at an electrical voltage of 1.5 V with different initial concentrations of NaCl at a flow-rate of 50 ml/min through a CDI unit cell, to obtain the electrosorption isotherm. The electrosorption of NaCl onto a-SWCNT (23.58 %wt) coated RVC electrode was evaluated at a constant temperature of 298 °K for the isotherm. The initial concentrations of NaCl solutions were 25 mg/L, 50 mg/L, 75 mg/L, 100 mg/L, 200 mg/L, 300 mg/L, 400 mg/L and 500 mg/L, respectively, as shown in Figure 4.23.The electrosorption of a-SWCNT was affected at different initial solution concentrations. When the solution was very dilute, the adsorbed NaCl amount inclines to zero. The removal amount of NaCl increases as the initial concentration is raised, which is due to the enhanced mass transfer rate of ions inside the micropores and reduced overlapping effect by higher concentration of solution [324-326]. The electrosorption capacity of SWCNT (23.58 %wt) coated RVC electrode was 8.89 mg/g at 500 mg/L feed concentration.

Langmuir (Eq. 2.18) and Freundlich (Eq. 2.19) isotherms were used to fit the experimental data for electrosorption of Na^{+} and Cl^{-1} onto the electrodes. Table 4.9 shows the determined parameters and regression coefficients R^2, K_L and K_F of Langmuir and Freundlich isotherms respectively for NaCl electrosorption using a-SWCNT (23.58 %wt) coated RVC electrode as electrosorption electrode. It was found that the electrosorption for this electrode obeys both the Langmuir isotherm and the Freundlich isotherm models, according to the R^2 values (better than 99.9%

confidence level). The regression coefficients were 0.997 and 0.989 for the Langmuir isotherm and Freundlich isotherm, respectively. This phenomenon suggests that the monolayer adsorption was the primary adsorption mechanism during the electrosorption process [209, 332]. The K_L and K_F values of a-SWCNT electrode was 0.01 and 0.28, respectively. Normally, a higher value of n between 1 and 10 represents more beneficial adsorption [268] and the value of n in this electode was 1.77. Hence, the a-SWCNT electrode with high value of n exhibits a high potential electrosorption capability. In such a system, the adsorbed layer is extremely thin and the amount adsorbed is only a fraction of the monolayer capacity. Therefore, the electrosorption of the a-SWCNT/RVCelectrode in CDI follows the monolayer adsorption [208]. Additionally, in order to estimate the maximum electrosorption amount of a-SWCNT, the parameter q_m in the Langmuir isotherm model was considered as the maximum adsorption capacity, so the results suggest that the maximum adsorption capacity was improved as the bias concentration rose. The equilibrium electrosorption capacity of this electrode, at a polarization of 1.5 V and a flow-rate of 50 ml/min, was 13.08 mg/g.

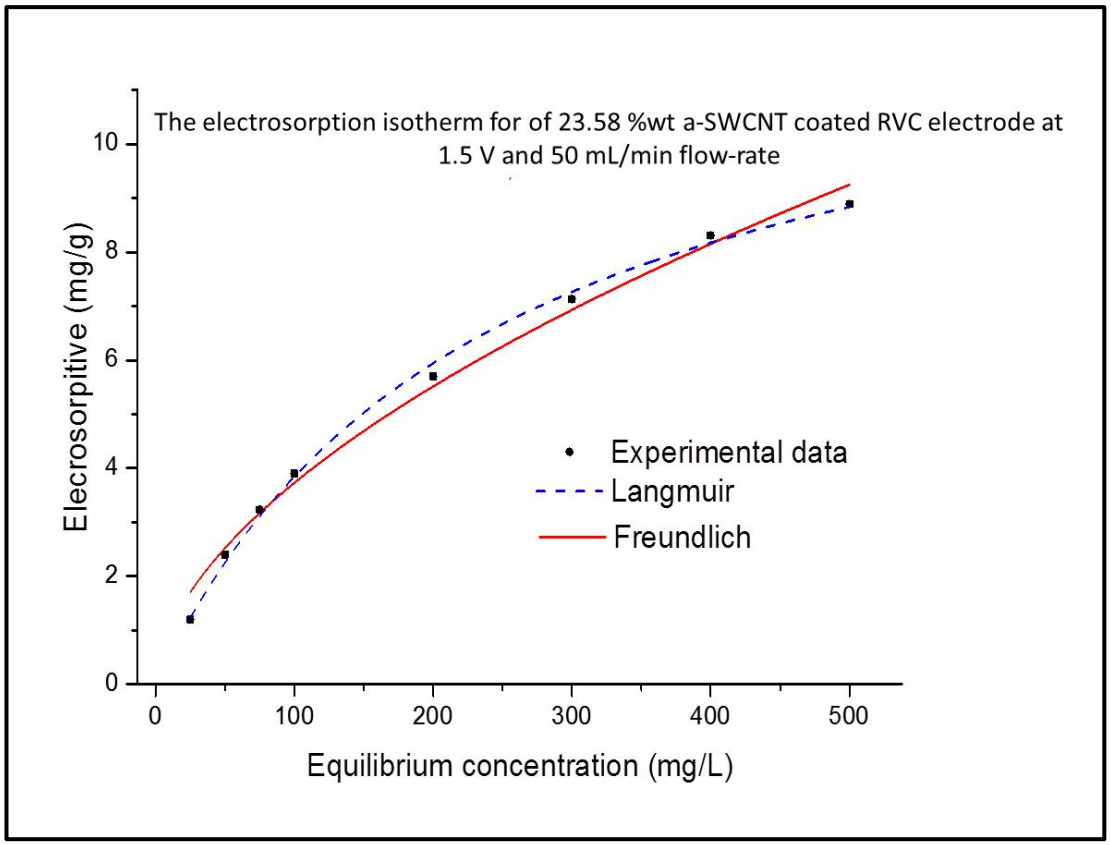

Figure 4.23: The electrosorption isotherm for 23.58 %wt a-SWCNT coated RVC electrode at 1.5 V and 50 ml/min NaCl flow-rate.

Table 4.9: Determined parameters of regression coefficients R^2, K_L and K_F of Langmuir and Freundlich isotherms for NaCl electrosorption by using a-SWCNT (23.58 %wt) coated RVC electrode as electrosorption electrode.

Isotherm	**parameter**	**Value**
Langmuir	q_m	13.08
	K_L	0.01
	R^2	0.997
Freundlich	K_F	0.28
	n	1.77
	R^2	0.989

4.3.18 Comparison of present work with previous published research studies

In this section, a-SWCNT coated RVC electrodes electrosorption capacities were compared with several other carbon materials such as activated carbon (AC), activated carbon nanofibre web (ACF) [265], carbon nanotubes (CNT) [321], composite carbon nanotubes with carbon nanofibre (CNT/CNF) [322], reduced graphite oxide (rGO) [320], and carbon aerogels (CA) [50] that have been studied as CDI electrode materials. Table 4.10 lists the electrosorption capacity, mass and dimensions of electrode materials, and other basic information for CDI systems of all previous carbon electrode materials. It can be observed that all researchers measured electrosorption capacity by mg of NaCl per gram of active material and they ignored measuring it by geometric area or geometric volume. This leads to comparison of all electrosorption capacities by the weight of activated carbon materials in the electrode. However, our research was focussed on improving the electrosorption capacity in terms geometric area and geometric volume. It can be seen that 3.63 %wt of a-SWCNT coated RVC gave the highest amount of electrosorption capacity (10.40 mg/g) than that of other electrode materials. Also the electrode that had 23.58 %wt a-SWCNT coated on the RVC still had high electrosorption capacity (3.23 mg/g) compared with CNT electrode material (2.33 mg/g). It is worth mentioning that the time required for one adsorption cycle in the CNT electrode material, which was 100 min, was decreased more than 16 times when the a-SWCNT coated RVC electrode was used (6 min). This means that the amount of pure water produced is increased more than 16 times when the a-SWCNT coated RVC electrode is used.

The electrosorption capacity of activated carbon nanofibre web (ACF) was consistently higher than that of AC, CA, CNT, CNT/CNF, rGO and all a-SWCNT

coated RVC electrodes except the 3.25 %wt SWCNT coated RVC, as shown in Table 4.10. Unfortunately, this ACF electrode functioned with very low flow-rate (5ml/min) and needed a long time to complete one cycle of adsorption (150 min). The main differences between the CDI electrodes include the energy consumed in the CDI system. It is known that the energy consumed increases with increase in the time required for the adsorption processes and increase in the cell voltage [379]. Table 4.10 shows the applied cell voltages and time for one adsorption cycle. It is noted that the applied cell voltage for all a-SWCNT coated RVC electrodes was 1.5 V as also for the AC, CA and rGO electrodes. The differences between these electrodes were the time for one adsorption cycle which was 6 min for a-SWCNT coated RVC electrode, 30 min for AC and rGO, and 840 min for CA. It is observed that the energy consumed in the CDI system with a-SWCNT coated RVC electrode is much less compared with other electrodes. Also, if one compares the time per adsorption cycle of a-SWCNT coated RVC (6 min) with other electrodes in Table 4.10, one can see that the time is much shorter which leads to energy saving.

Table 4.10: Comparison of electrosorption capacity of various carbon electrodes and electrodes developed in this thesis.

	Carbon electrodes						**Electrodes developed in this thesis (SWCNT/RVC) using new cell**			
	AC	CA	CNT	CNT/ CNF	rGO	ACF	3.63 %wt	12.50%wt	17.43 %wt	23.58 %wt
Electrosorption capacity (mg/g)	1.42	2.56	2.33	3.32	3.23	4.64	10.40	3.99	3.67	3.23
Electrosorption capacity (mg/cm^3)	-	-	-	-	-	-	0.029	0.043	0.058	0.075
Electrosorption capacity (mg/cm^2)	-	-	-	-	-	-	0.039	0.057	0.078	0.10
Mass of materials (g)	1.50	4.30	0.12	0.85	1.50	0.31	0.006	0.023	0.034	0.050
Electrode length & width (cm)	14*7	16*8	8*8	8.7 Diameter	14*7	7*5	4*1.8			
Electrode thickness (mm)	0.3	0.8	0.03	0.3	0.3	0.2	3.0			
Applied voltage (V)	1.5	1.5	1.2	1.2	1.5	1.6	1.5			
Flow-rate (ml/min)	20	400	40	14	20	5	50			
Solution volume (ml)	200	500	50	40	200	50	70			
Initial conductivity of NaCl solution (µS/cm)	145	101	100	100	145	192	143			
Time of electrosorption cycle (min)	30	840	100	45	30	150	6			
Reference	[320]	[50]	[321]	[322]	[320]	[265]				

4.4 Conclusions

In summary, SWCNT material was functionalized by reflux method in nitric acid, and it was characterised by Raman spectroscopy and Visible spectra. The concentrate (0.2 % w/v) of functionalized SWCNT (a-SWCNT) was dispersed in DMF solvent by ultrasonic probe and the sonication energy was 6 KJ per mg. After that, RVC electrodes were loaded with a-SWCNT to different levels including until pores of the RVC were filled. A unique 3D electrode has been constructed and explored as a novel CDI electrode. All 3D electrodes were evaluated for their electrochemical properties by cyclic voltammetry. SWCNT coated RVC electrode was used as electrode in CDI methodical investigations that showed that an electrical voltage of 1.5 V and flow-rate of 50 ml/min were the optimum conditions and that they were key factors which affected the NaCl ion removal performance onto the sites of a-SWCNT. The CDI system was investigated with respect to the influence of increased loading of a-SWCNT of a-SWCNT/ RVC composite electrodes on the ion removal performance. These results suggest that the CDI process using a-SWCNT coated RVC electrodes have promise as an effective technology for desalination. Subsequently, an improved CDI system was designed to accept solution flowing through the electrodes and its effect on desalination cycle time was studied. It is clear that for one desalination cycle, 42 minutes was required for the flow-between electrodes configuration and 18 minutes for the flow through electrodes configuration. The three times faster desorption cycle in a CDI system using flow-through electrodes encouraged efforts to design a new CDI cell with a flow-through electrode system. The electrosorption capacity of all electrodes in the new cell was increased and the time required for one desalination cycle decreased as well. The

electrosorption capacity for 3.63 %wt a-SWCNT was increased from 8.39 mg/g to 10.40 mg/g using flow feed between electrodes and flow feed through electrodes, respectively. This means that electrosorption capacity increased 23.96%. In fact, the time required for one desalination cycle decreased around three times after using flow feed through electrodes. In addition, the ion removal characteristics were affected by various distances between electrodes. As the distance increased, the ion removal amount was not affected in the range of distances but the adsorption time required increased when the distance was increased in all cases. It observed that NaCl adsorption has obeyed pseudo first -order kinetics rather than pseudo second -order kinetics. It was found that the electrosorption for 23.58%wt a-SWCNT electrode obeys both the Langmuir isotherm and the Freundlich isotherm models. This phenomenon suggests that the monolayer adsorption was the primary adsorption mechanism during the electrosorption process. The maximum electrosorption capacity result for 23.58 %wt a-SWCNT electrode was 8.89 mg/g at 500 mg/L feed concentration, as compared with a theoretical maximum value of 13.08 mg/g calculated using the Langmuir isotherm model. In conclusion, all the aims of this chapter were achieved.

5 PERFORMANCE ENHANCEMENT OF CAPACITIVE DEIONIZATION (CDI) SYSTEM BY MODIFIED 3D SWCNT/RVC ELECTRODES USING MICROWAVE IRRADIATED GRAPHENE OXIDE (MW GO).

5.1 Introduction

The CNT/RVC electrode described in Chapter 4 was a success as an electrode in a CDI system because it had increased stability at high flow-rate pressure, increased the possibility of ions to reach all of the electrode surface in a short time for electrosorption, and shortened the time of ions desorption from the electrode surface. The goal of the work in this chapter is to increase the electrosorption capacity of CNT/RVC electrode. This can be achieved by firstly improving the pore structure and surface area. Both play a significant key role in the electrical double-layer capacitance in a CDI system. This could occur by uniform distribution of macropores that provide better electrochemical accessibility, and facilitates rapid and easy ion transport.

Graphene material has recently become a material of interest in various applications such as capacitive deionization (CDI), supercapacitor, optical detection, electrochemical biosensing, nanoelectronic circuits, energy, battery, and analytical applications [208-212, 383-393]. This is because graphene has an impressive theoretical surface area (2630 m^2/g) [177, 178], high theoretical specific capacitance (550 F/g) [212, 394], a theoretical electrical conductivity as high as 7200 S/m [207], mean pore diameter and total pore volume reaching to 4.38 nm and 0.44 cm^3/g, respectively [212] and other interesting properties. These intriguing properties enable graphene to be considered for significant enhancement of carbon nanotube coated RVC electrodes by acting as conductive bridges for the pores between the CNT particles. Moreover, according to Zhang et al. graphene sheets decreased the aggregation of the CNTs bundle and thereby increase the actual accessible area [167]. In addition, the CNT with graphene will build 3D multilayer architecture

pores inside the film which are responsible for providing many more available spaces to accommodate ions during electrosorption [211, 395].

CNTs and graphene combinations have been used to prepare electrodes for CDI systems [167, 211, 212]. Significant property enhancement has been observed in these materials where graphene sheets are intercalated with CNTs to enhance the electron transfer between the graphene sheets as the salt solutions are inherently resistive. In addition, the spacing between the graphene sheets is increased which improves solution flow and facilitates access of ions to these electrode materials. When these composite electrodes are compared with CNT or graphene electrodes alone, the electrical conductivity, accessible surface area, specific capacitance volumes, electrochemical stability and electrosorption capacity are improved resulting in low energy consumption for the CDI system. All of them used the Hummer's method to prepare GO from graphite and were exfoliated by low power sonication or thermal treatment. These electrodes were made to be used as two dimension (2D) sheet electrodes with no significant electrode thickness (0.02 cm).

In this chapter, the electrodes were made as novel three-dimensional (3D) electrodes with electrode thickness (0.3 cm) using reticulated vitreous carbon (RVC) electrode as substrate. In addition, graphene oxide (GO) nanosheets were synthesised through a modified Hummer's method and microwave irradiation was used as a fast way to reduce and exfoliate (GO) nanosheets. After that, the microwave irradiated graphene oxide (mwGO) was dispersed with functionalized CNT in amide solvent (DMF) at various ratios and then used to coat RVC electrodes by a dip coating method. The sonication time was optimized by monitoring with Visible spectra. In addition, the energy of sonication of each mg of composite material was selected.

Composite electrodes were characterised for their morphology and electrochemical properties. These electrodes were tested in a capacitive deionization system using a feed stream flowing directly through the electrodes. The performance of these electrodes in the system was investigated under various working conditions such as: flow-rate and bias potential which were optimized. Furthermore, investigations of the electrosorption isotherm such as Langmuir and Freundlich models to describe how ions interact with electrodes, and electrosorption dynamics to evaluate the performance of electrodes. All of these characteristics are very important for developing electrodes and effective technology for desalination.

5.1.1 Aims of the work in this chapter

The aims of the research described in this chapter can be summarized as follows:

- Synthesis of graphene oxide (GO) nanosheets through a modified Hummer's method and use microwave irradiation to reduce and exfoliate (GO) nanosheets.
- Prepare composites of microwave irradiated graphene oxide (mwGO) with functionalized single-walled carbon nanotubes (a-SWCNT) to improve the conductivity, surface area and ions diffusions in the CNT material.
- Build novel 3D CNT/mwGO/RVC composite electrodes without binder, which would usually reduce the specific capacitance.
- Test the electrosorption performance of 3D CNT/mwGO/RVC composite electrodes and compare with the best performing 3D CNT/RVC electrode from Chapter 4.

5.2 Experimental

5.2.1 Chemicals and Materials

Commercial single-walled carbon nanotubes (Hipco-CCNI /Lot # p1001) were purchased from Carbon Nanotechnologies, Inc (Houston, TX) and graphite powder was purchased from Bay Carbon, Inc. which was used as received. The following chemicals obtained from Sigma-Aldrich were also used as received: -N, N-Dimethylformamide (DMF) (AR grade), concentrated nitric acid (70%) (AR grade), potassium permanganate ($KMNO_4$) (AR grade), ethanol (C_2H_6O) (AR grade), and sodium chloride (AR grade). In addition, the following chemicals obtained from Univar were also used as received: concentrated sulphuric acid (H_2SO_4, 98%,w/v) (AR grade), hydrogen peroxide (30% aqueous H_2O_2) (AR grade), and concentrated (36%, w/v) hydrochloric acid (HCl) (AR grade). The reticulated vitreous carbon (compressed 60 ppi (pores per inch)) was purchased from ERG Materials and Aerospace Engineering and used as received. Membrane filters (0.2 µm pore size GTTP) was purchased from MILLIPORE and cleaned. Milli-Q water with a resistivity of 18.2 $m\Omega\ cm^{-1}$ was used in all preparations.

5.2.2 Methods

5.2.2.1 Functionalization of carbon nanotubes

As received SWCNT material was functionalized by a reflux method as described in Section 4.2.2.1.

5.2.2.2 Synthesis of graphene oxide (GO)

Graphene oxide was synthesised using a modified Hummer's method as outlined by Marcano et al. [197]. In detail, 1 g of graphite powder was added to 60 ml of concentrated H_2SO_4 and mixed thoroughly for a few minutes. Then 3.5 g of $KMNO_4$ was added in small aliquots so as the temperature did not exceed 100 °C. This mixture was left stirring overnight for 18 h. From 300 to 500 ml of distilled H_2O was added (ice bath condition) to hydrolyse the intercalation compound that forms graphite oxide. Lastly, 30% aqueous H_2O_2 (drop wise, approximately 3 ml) was added until a complete colour change was observed. Finally, the mixture was filtered and washed with HCl solution, water, and ethanol. After vacuum filtration the slurry was dried in a vacuum oven overnight at 50 °C.

5.2.2.3 Exfoliation and reduction of graphene oxide using microwave irradiation

Exfoliated and reduced GO (mwGO) were formed by using a conventional microwave oven (1200 W). After irradiation, the GO glowed red hot accompanied by fuming and sparking, leading to a remarkable volume expansion caused by the violent expulsion of the volatile species from the interlayer spaces of the graphene intercalation compounds [396, 397].

5.2.2.4 Dispersion of microwave irradiated graphene oxide (mwGO) and acid treated Single-Walled Carbon Nanotubes (a-SWCNT)

A dispersion of 5 ml containing mwGO 0.1% w/v in DMF, one of the best solvents reported for GO dispersions because it can be coupled to an amphiphilic oligoester to produce amphiphilic graphene oxide that is dispersible [194, 397], was obtained by using a Branson homogenizer, Sonifier model S-450D equipped with a 13 mm step disruptor horn and a 3 mm tapered microtip, operating at a 20 kHz frequency and 25% amplitude as the power output (100 W) , with pulse of two seconds on and one second off. The dispersion was sonicated in a water-ice bath to prevent the suspension from overheating. In addition, the optimization of sonication time, sonication energy and solution stability will be discussed in the Results and Discussion section (Section 5.3.4.2). Furthermore, functionalised SWCNT 0.2% w/v was dispersed in DMF and optimised as described in Section 4.2.2.2.

5.2.2.5 Preparation of a-SWCNT/mwGO composite coating solution.

The fabrication of a-SWCNT/mwGO composite material coated RVC electrode involves the following steps (Figure 5.1). The dispersion containing a-SWCNT and mwGO solution were mixed via a combination of probe sonication for 30 minutes at 30% amplitude (1s on / 2s off pulse) and bath sonication for 30 minutes [167] and as optimised for the individual components. The a-SWCNT/mwGO composites were prepared using the weight ratios 90% a-SWCNT: 10% mwGO, 80% a-SWCNT: 20% mwGO and 70% a-SWCNT: 30% mwGO which were the weight ratios optimised in our laboratory, one of which (90% a-SWCNT: 10% mwGO) afforded the highest specific capacitance for the composite material in

an electrode and that also gave the highest capacity for electrosorption. This is discussed later in the Results and Discussion section.

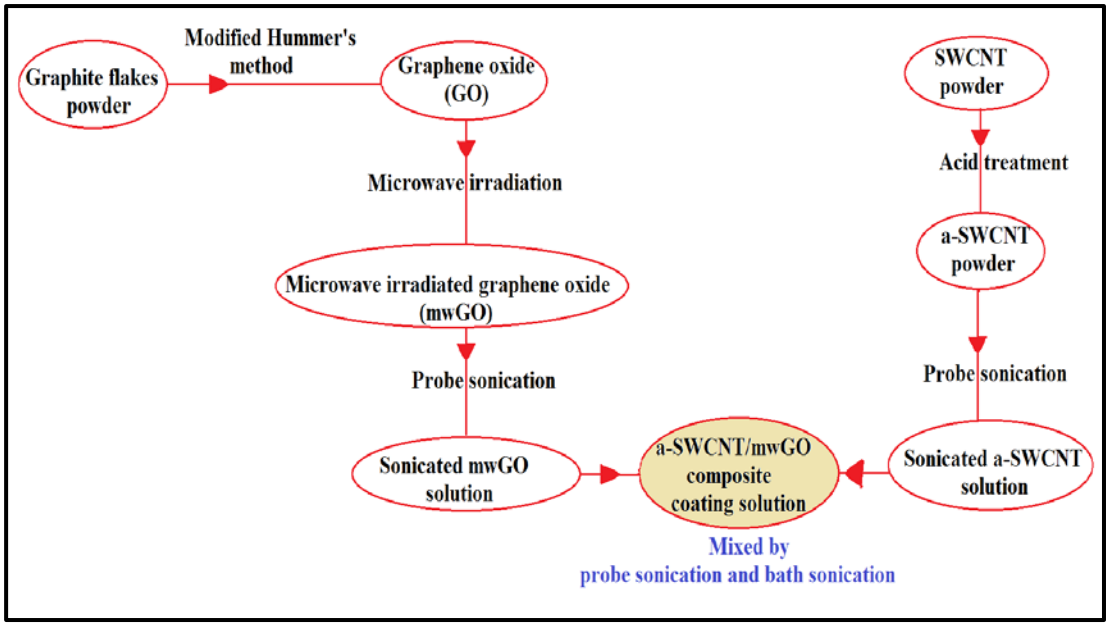

Figure 5.1: Schematic diagram of the preparation process of composite a-SWCNT/mw GO coating solution.

5.2.2.6 Pre-treatment of the RVC electrode

The best pores per inch (ppi) RVC electrode used as substrate for loading carbon material for use in a CDI system was optimized in Section 4.3.3. It was the 60 ppi RVC electrode because it leads to an increase in the conductivity of the electrode which readily allows the movement of electrical charge, and has higher capacitance and surface area. Therefore, 60 ppi RVC electrodes were selected as substrates to load a-SWCNT/mwGO composite material for use as electrodes in a CDI system. All RVC electrodes (length 4 cm * width 1.8 cm * thickness 0.3 cm) (2.16 cm^3) were cut from a block of RVC electrode, and were cleaned as described in Section 3.2.2.2. All RVC electrodes were weighed after drying.

5.2.2.7 a-SWCNT, mwGO, and a-SWCNT/mw GO composite dip coated RVC electrodes

All electrodes which are a-SWCNT, mwGO, or a-SWCNT/mwGO composites with RVC, were made by the dip coating method as described in Section 4.2.2.4. They were immersed slowly into the composite solution to allow the air to escape and prevent the formation of air pockets. Figure 5.2 shows a schematic diagram of the full process of dip coating RVC in a composite solution of 9 CNT: 1 mw GO. In addition, the process of the RVC electrode being soaked in solution and drying afterward in an oven overnight is shown schematically. The substrate, after dip coating, was dried at 100 °C in an oven for 2 h and then in a vacuum oven at 50 °C for 2 h to remove all organic solvents remaining in the micropores of the electrode.

Table 5.1 presents the weights of material loadings on the RVC electrodes as determined by weighing the electrodes before and after dip-coating. The 9 a-SWCNT/ mwGO composite material weights coated on RVC electrodes were 10, 30 and 50 mg, and all the other composite materials weights coated on RVC electrodes were 50 mg including a-SWCNT and mwGO material coated RVC electrodes. A maximum of 50 mg loading was used because previous work (Chapter 4) showed that 50 mg was the highest amount of CNT material that can be loaded into the RVC electrode and it afforded the highest capacitance and electrosorption capacity in terms of geometric volume. Initial investigations were done (Table 5.1 (a)) to determine which electrode material gave the best performance with maximum 50 mg

loading. Subsequent experiments (Table 5.1 (b)) were performed on the best electrode to confirm that 50 mg loading indeed gave the best result.

In future discussions, these composite electrodes, depending on the ratio of a-SWCNT in the sample, will be identified as 9-CNT/mwGO/RVC (9 a-SWCNT: 1 mwGO coated RVC electrode), 8-CNT/mwGO/RVC (8 a-SWCNT: 2 mwGO coated RVC electrode), 7-CNT/mwGO/RVC (7 a-SWCNT: 3 mwGO coated RVC electrode), CNT /RVC (10 a-SWCNT: 0 mwGO coated RVC electrode), and mwGO/RVC (0 a-SWCNT: 10 mwGO coated RVC electrode).

Table 5.1: Details of carbon materials coated on RVC (2.16 cm^3) electrodes.

samples	Ratio in coating solution		Material weight (mg)
	a-SWCNT	mw GO	
(a)			
CNT/RVC	10	0	50
9-CNT/mwGO/RVC	9	1	50
8-CNT/mwGO/RVC	8	2	50
7-CNT/mwGO/RVC	7	3	50
mwGO/RVC	0	10	50
(b) 9-CNT/mwGO/RVC			
1	9	1	10
2	9	1	30
3	9	1	50

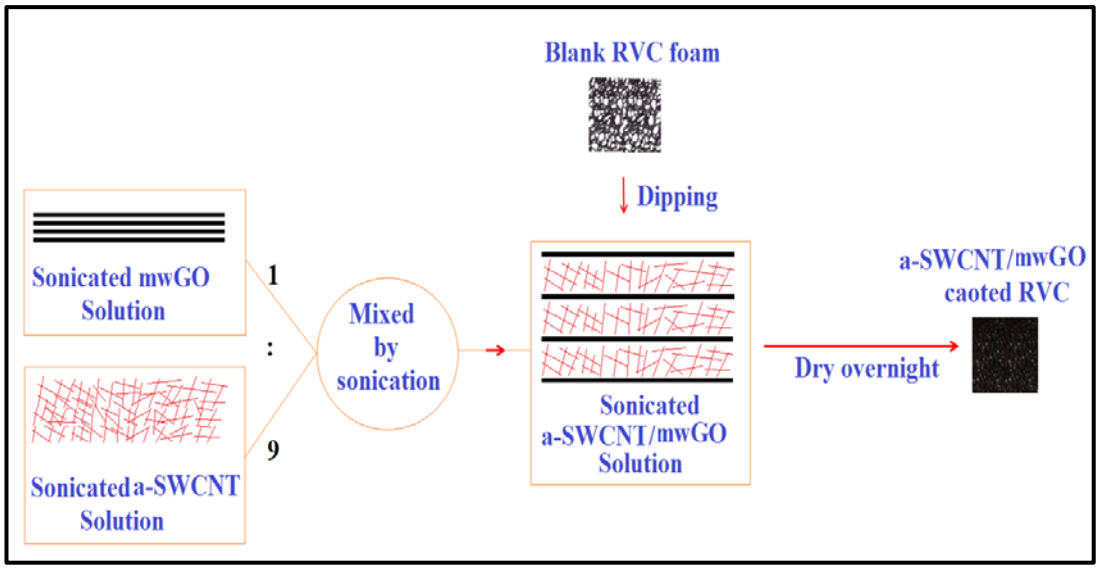

Figure 5.2: Schematic diagram of the preparation process of ratio 9:1 composite a-SWCNT/mw GO coated RVC electrode.

5.2.2.8 Electrochemical characterisation

The capacitance of a-SWCNT, mwGO, and a-SWCNT/mwGO composite electrodes were determined by cyclic voltammetry (CV). A a-SWCNT/RVC, mwGO/RVC or a-SWCNT/mw rGO/RVC composite electrode was used as the working electrode (WE) in 1 M NaCl aqueous solution and scanned in the voltage range between -0.2 to 1.0 V using a three-electrode system; RVC electrode and Ag/AgCl (3M NaCl) were used as counter electrode (CE) and reference electrode (RE), respectively. The scan rates used were 5, 10, 20, 50, 100 and 200 mV/s, respectively. Contacts to the WE and CE were made using Pt wire.

5.2.2.9 Physical characterisation

The morphology of the a-SWCNT, mwGO, and a-SWCNT/mwGO composite coated RVC electrodes were characterised using a field emission scanning electron microscope (FESEM) at a specific voltage of 1.0 KV. Furthermore, a-SWCNT and GO functionalization characterization was done by: (1) Visible absorption spectra obtained using quartz cuvettes, (2) Raman spectra measured with a Raman spectrometer equipped with a visible Raman microscope and CCD detector at the excitation wavelength of 632.81 nm where spectra were obtained over 30 s at 1.0 cm^{-1} resolution, and (3) X-ray photoelectron spectroscopy (XPS) to determine the functional groups in carbon binding to carbon, and hydrogen and oxygen in GO and mwGO. The XPS binding energy spectra were recorded at the pass energy of 20 eV in the fixed analyser transmission mode. X-ray diffraction (XRD) was employed in order to understand the crystallinity of the structure and to determine the interlayer distance between nanosheets. The XRD measurements were taken with CuKα radiation (λ= 0.154) operating at 40 KeV and with a cathode current of 20 mA. In addition, the thermal stability of the graphite, GO and mwGO materials was determined by thermogravimetric analysis (TGA). Experiments were performed by using a Q500 (TA Instruments) apparatus at a ramp rate of 5 °C/min in air, with a combined gas flow of 10 ml min^{-1} Nitrogen (N_2) and 90 ml min^{-1} air from 25 °C to 800 °C.

5.2.2.10 Measurement of amount of ion removal from the NaCl aqueous solution

NaCl concentration was determined by measuring the electrical conductivity of NaCl solution as described in Section 2.4.3.

5.2.2.11 Construction of a capacitive deionization cell

Capacitive deionization experiments were carried out in a new design of a flow-through electrodes system as described in Section (4.3.11.). In the system, the total volume of solution was 70 ml of the NaCl solution, the distance between electrodes was 5 mm, and solution temperature was maintained at 293 K. A RVC electrode was used as counter electrode.

5.3 Results and discussion

5.3.1 Characterisation of a-SWCNT after functionalization

a-SWCNT were prepared and characterised as described in Section (4.3.1.1.) and (4.3.1.2.).

5.3.2 Dispersion of a-SWCNT in DMF

The Visible spectra of a-SWCNT dispersions as a function of sonication time between 350 and 750 nm were discussed in Section (4.3.2.1.). In addition, the minimum amount of energy required to effectively disperse the a-SWCNT was 180 KJ at 30 min as described in Section (4.3.2.2.), and the stability of dispersion was also discussed in Section (4.3.2.3.).

5.3.3 Chemical conversion of graphite to graphene oxide

The most common source of graphite used for chemical reactions, including its oxidation, is flake graphite, which is a naturally occurring mineral that is purified to remove heteroatomic contamination [398]. The reaction of graphite with sulfuric acid (H_2SO_4) in the presence of $KMnO_4$ is shown in Equation (5.1). Graphite bisulfate (GB) ($C_{24}^{s}HSO_4^-.2H_2SO_4$), was prepared using a chemical method in the presence of strong oxidants by the intercalation of graphite with a mixture of potassium permanganate and concentrated sulfuric acid [399].

$$5C_{24} + KMnO_4 + 17H_2SO_4 \rightarrow C_{24}^{s}HSO_4^-.2H_2SO_4 + MnSO_4 + 4KHSO_4 + H_2O \qquad \text{Eq 5.1}$$

At the same time, rapid bubbling occurs due to the release of carbon dioxide from the reaction according to Equation (5.2) [399]:

$$5\,C + 4KMnO_4 + 8H_2SO_4 \rightarrow 5\,CO_2 + 4MnSO_4 + 4KHSO_4 + 6H_2O \qquad \text{Eq 5.2}$$

Water was added to hydrolyse the intercalation compound to form graphite oxide. H_2O_2 was added after hydrolysis to decompose permanganate ions into manganese (IV) ions where after the manganese (IV) ions were removed by vacuum filtration. The result was washed with HCl solution to ensure no undesirable manganese hydroxides were formed, which can get trapped in between the graphene/graphite layers [400]. The inset in Figure 5.3 (b) shows an optical image of graphene oxide, after washing and vacuum drying, at the bottom of a glass vial.

5.3.3.1 Surface chemistry of graphene oxide (GO)

Energy-dispersive X-ray (EDX) spectra, Fourier-Transform Infrared (FTIR) spectra, and X-ray diffraction patterns (XRD) were used to confirm the successful oxidation of the graphite flakes to form GO using strong acid.

5.3.3.1.1 Energy-dispersive X-ray spectroscopy

Figure 5.3 (a and b) show the SEM images and corresponding EDX spectra of graphite flakes powder and as-prepared GO respectively. The smooth leaf structure of graphite flakes was completely changed into the uniform rough and porous structure containing valleys and elevated regions which reflect vast amounts of sheet stacking after the chemical oxidation process, which can be clearly seen from the scanning electron microscopy (SEM) images of graphite and as-prepared GO given as insets in Figure 5.3 (a) and (b), respectively. The crystal structures of

graphite flakes powder and as-prepared GO are identified using X-ray diffraction (XRD) patterns (Figure 5.3 (c)). Graphite flakes exhibit a strong and sharp peak at 26.6^0 indicating a higher ordered structure, that corresponds to a basal spacing d_{002} = 0.343 nm (described by Bragg's Law (Eq 2.8.). The pattern of graphene oxide, on the other hand, exhibits a 001 reflection at low-angle region (10.8^0) corresponding to a basal spacing of d_{001} = 0.820 nm and the broader peak at 2Ɵ =20.7º corresponding to the (d_{002} = 0.435 nm) crystal plane of graphite and amorphous carbon [198, 401]. These results are similar to those of other GO precursors [198, 402] and it can be attributed to the introduction of oxygen-containing functional groups into the carbon lattice during the oxidation [403]. The interlayer spacing of GO is higher than the interlayer spacing of graphite flakes (d-spacing= 0.343 nm). In addition to SEM images and XRD, the corresponding EDX spectra in Figure 5.3 (b, for GO) reveal the formation of a new structure with a higher oxygen content of 30.1 wt % O (the oxygen content of graphite is too low to be detected (Figure 5.3 (a)) and lower C/O ratio of 2.3; indicating the oxidation of graphite flakes and formation of GO. The higher oxygen content of GO than that of graphite is due to the formation of epoxide, carboxylic acid and hydroxyl groups on the edges and the basal planes of the carbon structure, respectively [404]. In addition to the C and O atoms in Figure 5.3 (b), no peaks exist in the EDX spectra of GO; which indicates that no impurities, presence of sulphur and manganese, have been left as residuals of H_2SO_4 and $KMnO_4$ used in the preparation procedure.

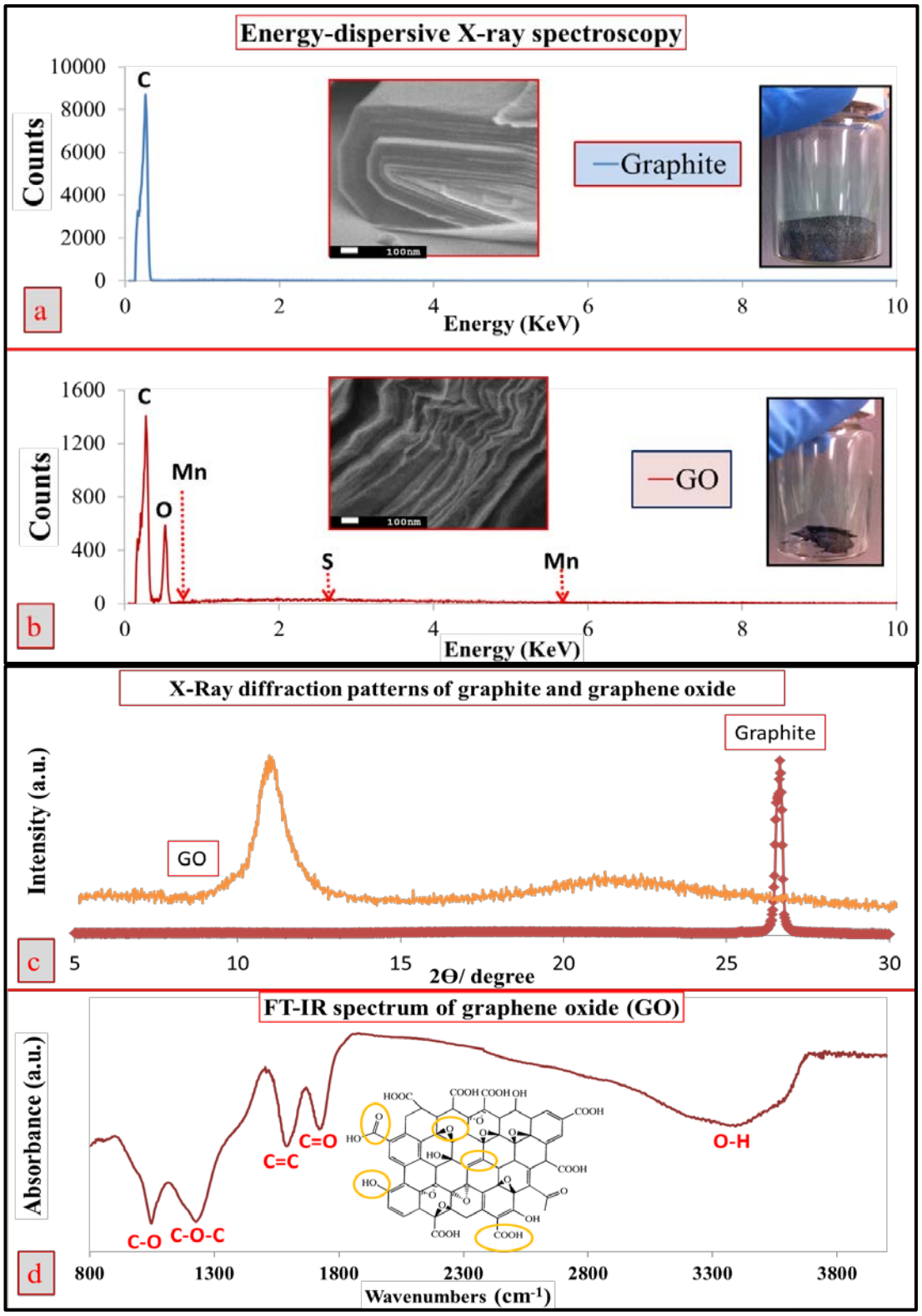

Figure 5.3: (a and b) Energy-dispersive X-ray (EDX) spectra, (c) the X-ray diffraction (XRD) patterns of the graphite flakes powder and graphene oxide (GO) film respectively, and (d) Fourier-Transform Infrared (FT-IR) spectrum for graphene oxide film. Inset shows scanning electron microscopy (SEM) and optical images of the (a) graphite flakes powder and (b) the GO film.

5.3.3.1.2 Fourier-Transform Infrared spectroscopy (FTIR)

The Fourier-Transform Infrared (FTIR) spectrum of the graphene oxide obtained in these steps confirms the successful oxidation of the graphite as evidenced by the presence of oxygen-containing functional groups as shown in Figure 5.4 (d). The presence of different types of oxygen functionalities in graphene oxide was confirmed by the broad and wide peak at 3386 cm^{-1} that can be attributed to the -OH stretching vibrations of the hydroxyl (C-OH) groups and water, and the epoxy (C-O-C) groups peak at 1228 cm^{-1} [405-407]. These groups usually are present throughout the basal planes of GO [408]. In addition, the sharp intense peak at 1587cm^{-1} can be ascribed to (C=C) benzene rings, and the absorption bands at 1720 and 1047 cm^{-1} can be ascribed to the stretching vibration of carboxyl (C=O) and alkoxy (C–O) groups [204, 407, 409, 410], respectively, which usually were distributed at the edges of these two dimensional nanostructures [408].

5.3.4 Microwave assisted exfoliation and reduction of graphene oxide

Microwave irradiation as a convenient and rapid heating source has been used to prepare exfoliated graphite (EG) [396, 397] and exfoliated graphene oxide [198]. In addition, microwave assisted reduction of GO can be achieved by treating the GO precursor in a microwave oven for less than 1 min [198, 411]. This facile and efficient process has provided a straightforward method to generate what we will call mwGO (microwave exfoliated graphene oxide). Therefore, microwave irradiation was used to exfoliate and reduce graphene oxide. The GO powders were treated in a microwave oven for 10 s. Upon microwave irradiation, a large volume expansion of

the GO film, accompanied by ‘violent fuming’ was observed. As can be seen from the inset in Figure 5.4 (e), the GO powder in the glass vial (inset Figure 5.4 (d)) has dramatically expanded yielding a black and fluffy mwGO powder. Zhu et al. demonstrated that further treatment of the mwGO powders with the microwave induced sparking and even burning [411]. The scanning electron microscopy (SEM) in Figure 5.4 (b) shows that the graphene sheets expanded, leading to the development of an accordion type structure of highly 3D macropores folded with each other, forming an interconnected network with minimal re-stacking compared with GO before microwave irradiation in Figure 5.4 (a) [198, 396] that are transparent to the electron beam and ions salts. In addition, the SWCNT can be sandwiched into the layers more easy [412]. Furthermore, the XRD spectra, Figure 5.4 (c), shows one distinct broad peak for mw GO at $2\Theta = 20.7^{o}$ corresponding to the (d_{002} = 0.435 nm) crystal plane of graphite and the sharp peak at $2\Theta = 10.8^{o}$ is much more suppressed as a result of the rapid expansion of GO layer. This result is similar to those of other mw GO precursors [198] and it can be ascribed to the removal of some of functional groups of graphene oxide and successful exfoliation of graphene [167, 403, 413-415]. In addition to XRD and SEM images, the corresponding EDX spectra reveal the formation of a new structure with the lower oxygen content of 9.9 wt % O and higher C/O ratio of 9.1 indicating the reduction of graphene oxide and formation of reduced graphene oxide (rGO). The lower oxygen content of rGO than that of GO is due to the release of epoxide, carboxylic acid and hydroxyl groups on the edges and the basal planes of the carbon structure, respectively.

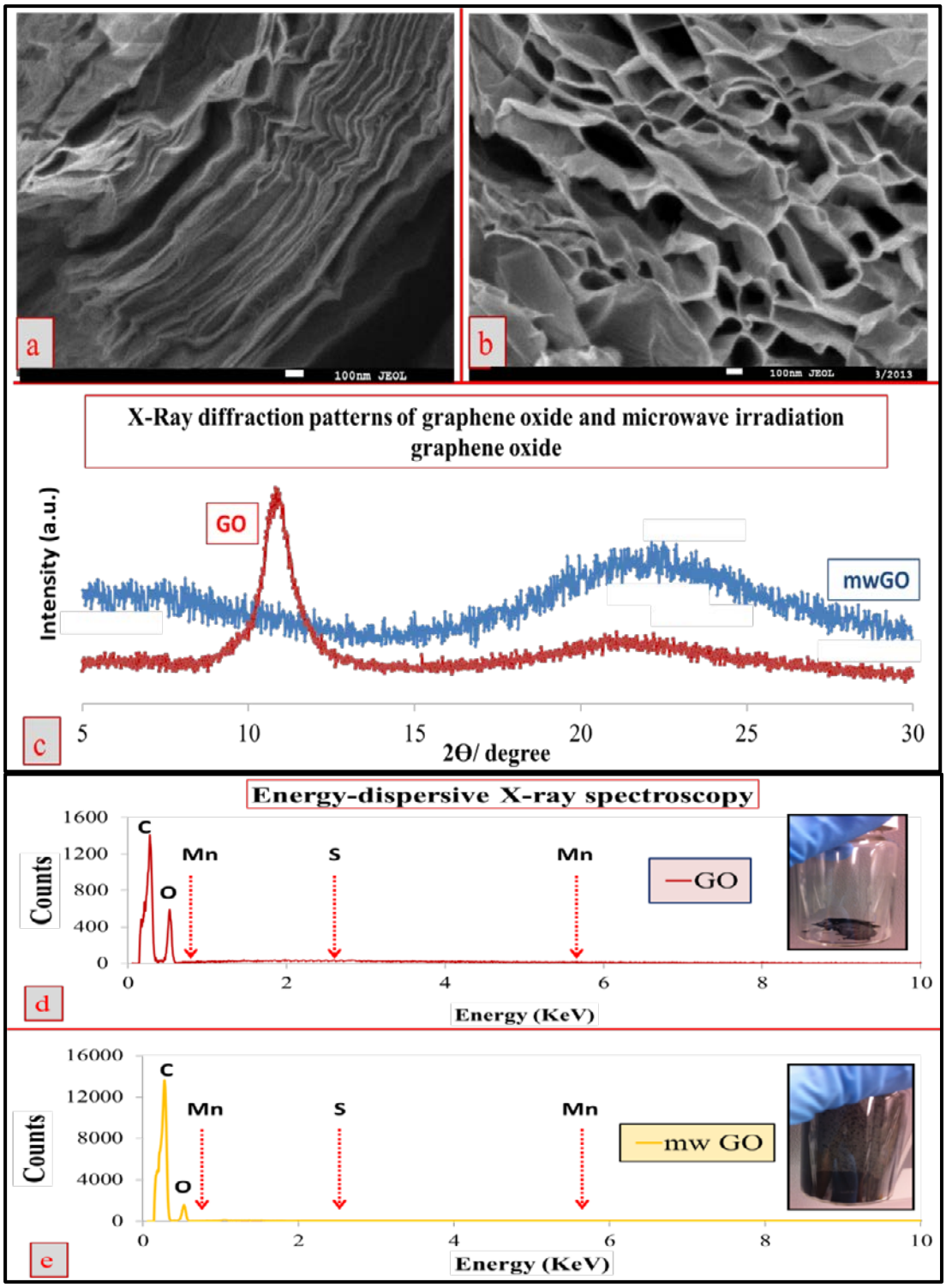

Figure 5.4: (a and b) Scanning electron microscopy (SEM) images of GO and mwGO, respectively, (c) the X-ray diffraction (XRD) patterns of GO and mwGO and (d and e) Energy-dispersive X-ray (EDX) spectrum of graphene oxide (GO) film and microwave irradiated graphene oxide. Inset shows optical images of the (d) GO film and (e) mwGO.

5.3.4.1 Surface chemistry of graphene oxide (GO) after microwave irradiation.

The chemical changes brought about by microwave irradiation in graphene oxide were investigated by Raman spectra, thermogravimetric analysis (TGA), XPS, and XRD spectra to confirm the graphene oxide (GO) reduction and exfoliation by microwave irradiation.

5.3.4.1.1 Raman spectra

Raman spectroscopy is a powerful diagnostic tool, the most direct and non-destructive technique to characterize the structure and quality of carbon materials [416-419] and in particular to investigate the defects and ordered and disordered structure of graphite and graphene. Many scientific papers mention that there are three typical peaks always attributed to D, G and 2D bands of graphite, graphene oxide and reduced graphene oxide that are observed at about 1350, 1580 and 2680 cm^{-1}, respectively [419-425]. The 2D band is always a strong band in graphene even when there is no D band present, and it does not represent defects. Figure 5.5 shows the Raman spectra of natural graphite flakes, as-prepared GO, and GO after microwave irradiation. It is clear from the Raman spectra that graphite exhibits two peaks at G and 2D bands. The chemical oxidation on graphite to produce graphene oxide (GO) results in the appearance of a D band at a lower wavenumber than that of the G band coupled with the disappearance of the 2D band peak. The D band peak of GO is associated with the breathing modes of rings or κ-point phonons of A_{1g} symmetry of graphene oxide occurring at 1321 cm^{-1}; while the G band peak, associated with first order scattering of the stretching vibration mode E_{2g} observed for carbon sp^2 atoms domains, occurs at 1587 cm^{-1} [426]. The integrated intensity

ratio (I_D/I_G) of these two Raman bands has been demonstrated to depend upon the physical state of the graphitic carbon, and can reveal the ordered and disordered crystal structures of graphene. As expected, after microwave irradiation, there is a slight shift in both D and G band peaks to 1330 cm^{-1} and 1590 cm^{-1} respectively, and the ratio of the I_D/I_G band decreased from 1.26 to 1.08. This decrease suggests a slight reduction of the GO [422-425]. In addition, the reduction of GO by microwave irradiation has good advantage over chemical reduction by ultrasonic dispersion or rapid thermal expansion followed by chemical reduction because chemical reduction often involve highly toxic chemicals, require long reduction time, or require high-temperature treatment [427, 428].

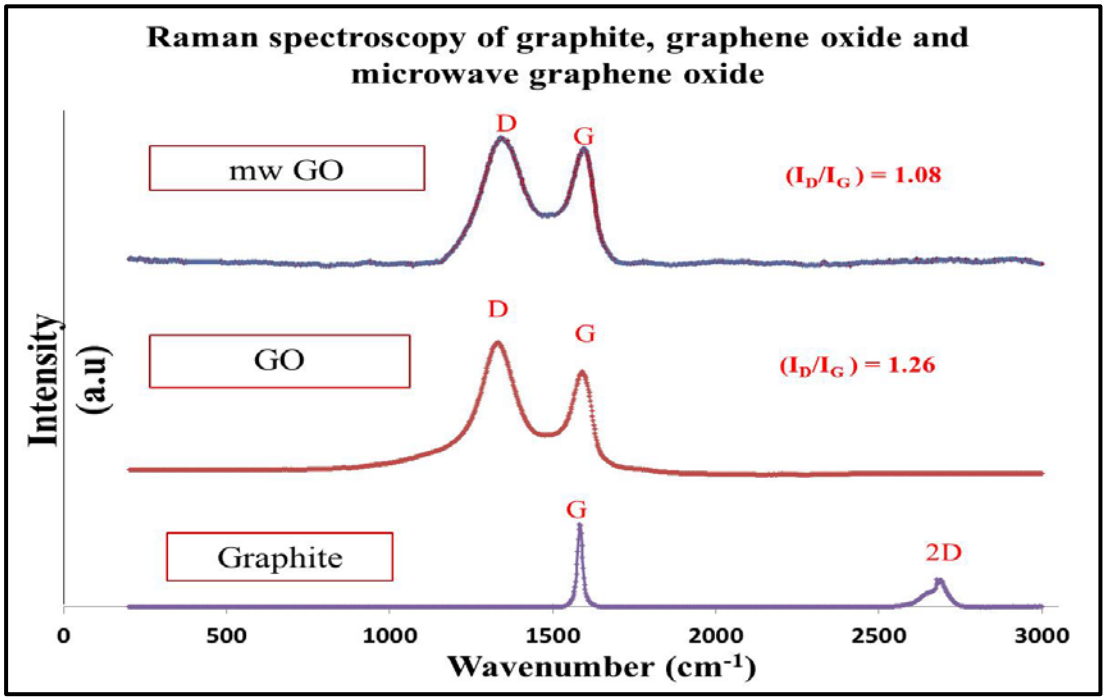

Figure 5.5: Raman spectroscopy of flake graphite, graphene oxide and microwave reduced graphene oxide.

5.3.4.1.2 X-ray photoelectron spectroscopy (XPS) spectra

X-ray photoelectron spectroscopy (XPS) was employed to investigate the surface chemical states of graphene oxide (GO) and microwave irradiated graphene oxide (mwGO) powder by observing changes in the binding energy of C1s peaks. Figure 5.6 shows a comparison of XPS spectra that depict the range of binding energies scanned from 280 to 294 eV, which presents information on the main chemical components in our samples from the detected peaks (C1s spectra) of both samples. It can be seen that in Figure 5.6 (a), the C1s XPS spectrum of graphene oxide clearly indicates a considerable degree of oxidation with three components corresponding to carbon atoms in different functional groups [415]: the non-oxygenated C at 284.4 eV corresponds to C1s of sp^2 (C=C), the carbonyl carbon (C=O) at 287.2 eV, and the carboxylate carbon (O-C=O) at 288.4 eV. Based on the XPS analysis, the as-prepared GO had an atomic ratio for carbon/oxygen of 2.91. After microwave irradiation of GO (Figure 5.6 (b)), the percentage of C=C band increased from 34.21% to 56.47%, revealing remarkable restoration of the graphitic structure of reduced GO, while the C/O atomic ratio of mwGO was found to be 5.32. The XPS results show that the oxygen containing groups have been significantly removed by the exposure to the microwave irradiation as reported for graphite oxide and graphene oxide [198, 405, 411]. It must also be noted that the slight shift of the de-convoluted peaks for mwGO is due to the enhanced regular structure as compared to the GO [197].

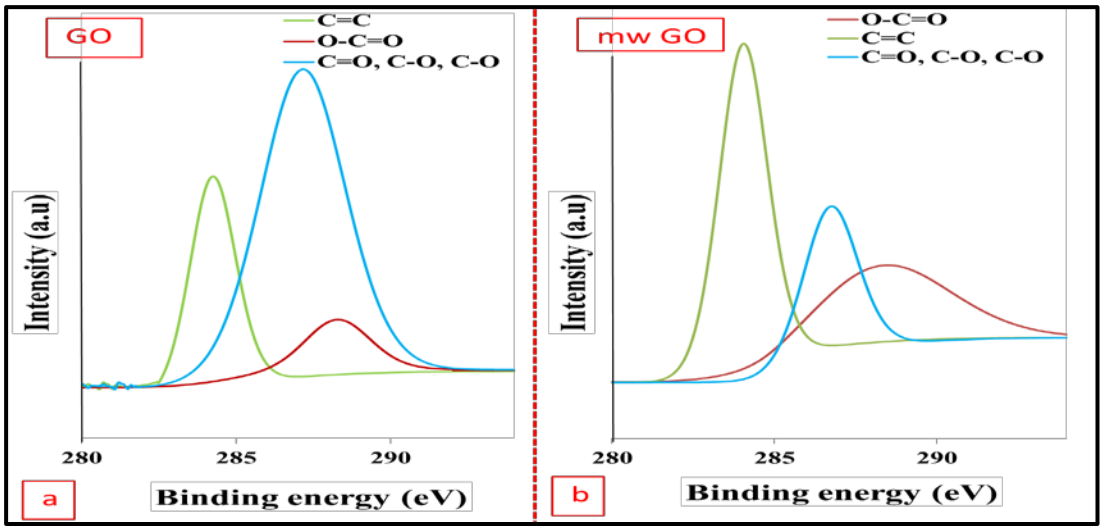

Figure 5.6: X-ray photoelectron spectroscopy (XPS): comparison of the C1s spectra for (a) graphene oxide (GO) and (b) microwave irradiated graphene oxide (mwGO).

5.3.4.1.3 Thermogravimetric analysis (TGA)

Thermogravimetric analysis (TGA) was used to study the thermal stability of natural graphite flakes, graphene oxide (GO), and microwave irradiated graphene oxide (Figure 5.7). The thermogravimetric analysis (TGA) curves were based on the mass loss during the heating in air. It is clear that pristine graphite is very thermally stable, only 4.8 wt% mass loss occurred upon heating to 600 °C as mentioned in the Song et al. paper [429]. For graphene oxide (GO), three significant weight loss events are apparent, as shown in Figure 5.7. The first one is below 120 °C, related to the weight loss of intercalated water that was not removed from drying. The second one, between 120 °C and 300 °C, corresponds to the removal of oxygen-containing functional groups, such as C-O, C=O and O-C=O [197, 403, 430]. This major weight loss is related to degradation and decomposition, whereas the third weight loss that occurs at approximately 530 °C is due to the bulk pyrolysis of the carbon skeleton [403, 431]. This pyrolysis is also observed in mwGO at 565 °C and in graphite at 680

°C. The TGA analysis indicates incomplete reduction of the functional groups by microwave because roughly 15 wt% of oxygen containing groups did not undergo reduction.

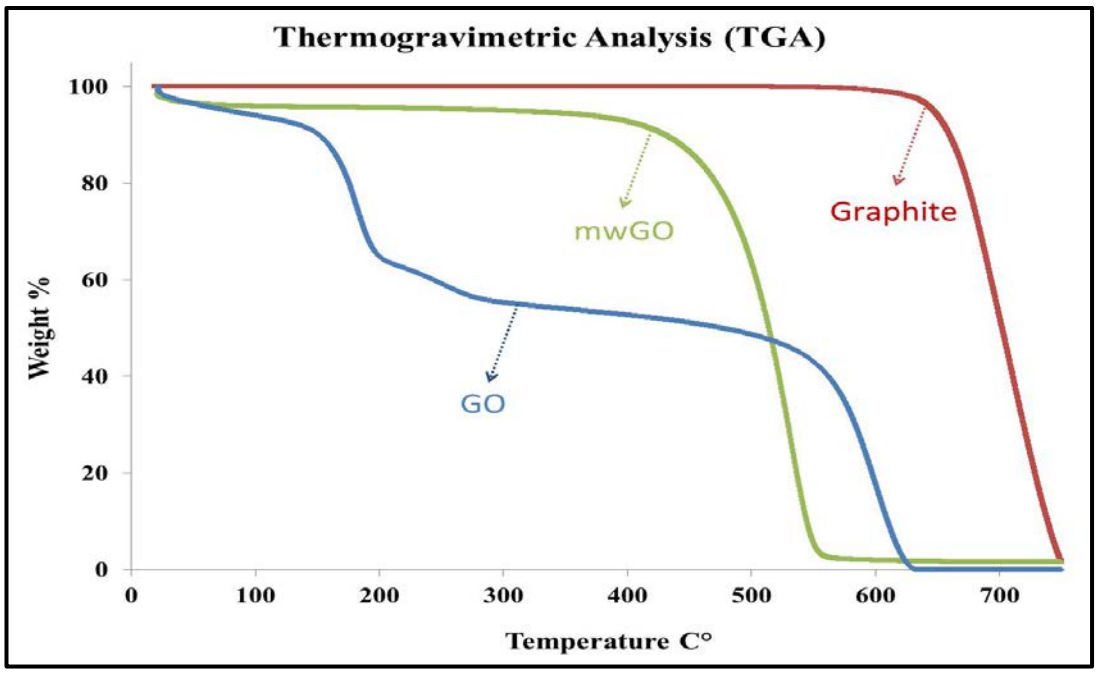

Figure 5.7: Thermogravimetric analysis (TGA) of natural graphite flakes, graphene oxide (GO), and microwave irradiated graphene oxide.

5.3.4.2 Dispersion of mwGO in DMF

In recent years, sonication has been extensively used as an exfoliation and dispersion strategy to produce graphene sheets in a liquid phase [432]. The first parameter to be investigated was the effect of sonication time on the dispersion of mwGO in DMF. The sample was prepared as a 15 ml dispersion containing mwGO 0.1% w/v in DMF; which is the best solvent reported for GO dispersions because it gave the highest spacing between GO sheets of up to 1.05 nm and the smallest GO sheet thickness, down to 0.83 nm [433]. The optimum time of sonication required to effectively disperse mwGO needed to be determined because excess sonication can

shorten or create defects in the sheet. Visible spectroscopy was used to study the dispersal process by monitoring the levelling of the absorption intensity; as a quick and simple way to investigate the stabilization of mwGO in the dispersion. The Visible spectra of mwGO dispersions, as a function of sonication time, between 300 and 1100 nm are shown in Figure 5.8 (a). All mwGO solutions were diluted 5 times by DMF before measuring their Visible spectra; using 1 cm path length quartz cuvettes for all the measurements and the baseline for DMF. The corresponding optical absorbance of the supernatant at 660 nm was plotted as a function of sonication time, and is represented in Figure 5.8 (b). Peak intensities were read directly from the as-measured absorption spectrum. It can be seen that, the mwGO bands become more pronounced with longer sonication time, indicating that an increasing amount of mwGO became dispersed with time. The minimum amount of time required to effectively disperse the mwGO was 35 min. However, the absorption of the dispersion did not change dramatically after sonication beyond 35 min, indicating that the solvent was saturated. In addition, the inset photographs in Figure 5.8 (a) show the mwGO dispersion before and after 35 min sonication time. It can be observed that when the sonication time was increased, the colour of the solution became progressively black indicating that homogenous dispersions have been obtained. It is known that energy is a factor that affects complete dispersion. The Visible absorbance of mwGO dispersions as a function of sonication energy is shown in Figure 5.8 (c). The figure shows the sonication energy used to disperse 15 mg of mwGO in 15 ml DMF. It is clear that the energy increased with sonication time. The energy was 12 KJ at 2 min and was 90 KJ at 15 min. The minimum amount of energy required to effectively disperse the mwGO was 210 KJ at 30 min

because the absorbance of the dispersion remained constant beyond the sonication energy of 210 KJ. This energy, shown in Figure 5.8 (c), was for 35 mg in DMF (0.1 % w/v). This means that 14 kJ was expended per mg of mwGO in a 0.1% w/v solution. The sonication energy (E) in joules was calculated using equation (2.1).

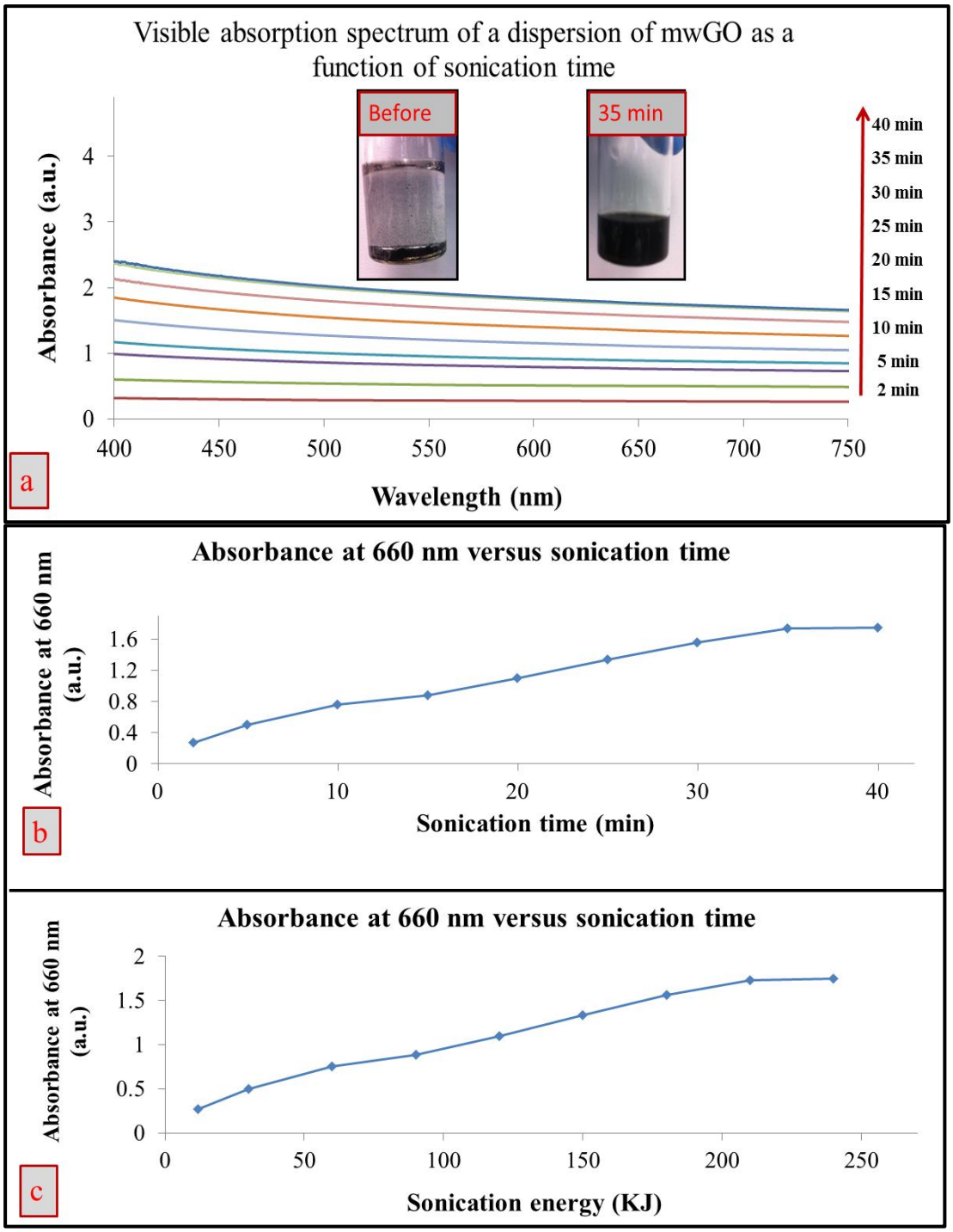

Figure 5.8: Effect of increasing sonication time on: (a) the Visible absorption spectrum of a dispersion containing 0.1% w/v mwGO which was measured after a 5-fold dilution, where inset photo images are of 0.1% w/v containing mwGO before sonication and after 35 minutes sonication, and (b) Absorbance at 660 nm *vs* sonication time. Arrows in (a) indicate the direction of increase in sonication time. (c) Effect of increasing sonication energy on absorbance at 660 nm for 0.1 % w/v mwGO dispersions.

5.3.5 Electrodes surface morphology

Figure 5.9 shows the surface morphology of the 9-CNT/mwGO/ RVC, 8-CNT/mwGO/ RVC, 7-CNT/mwGO/ RVC, mwGO/ RVC electrodes using scanning electron microscopy (SEM). The deposition in all composite electrodes are clearly visible and are homogeneously on the surface and pores of the RVC substrate as shown in Figure 5.9 (a, f and i). The representative SEM image which was taken from a 45^0 view of the 9-CNT/mwGO/ RVC electrode in Figure 5.9 (b) shows that the appearance of the top surface of the composite material coating is like a textile because the CNTs and mwGO are regularly spread on the RVC electrode and its pores, partly parallel and partly perpendicular to the surface. In addition, CNTs are dispersed in a highly tangled fashion with each other and systematically distributed like a web, showing the obvious domination of CNTs in the composite and with the CNTs uniformly wrapped on/ in between the curled graphene sheets. The cross-section of the composite electrode shown in Figure 5.9 (c) indicates a layered structure and the CNTs are uniformly sandwiched between the GO sheets making a multilayered 3D network structure with a highly porous architecture inside the electrode where graphene nanosheets conductively bridge the pores between the CNT particles. In addition, it reveals that CNTs and graphene sheets are distributed evenly throughout the resultant structure. It is clearly apparent that many gaps interface between graphene sheets and CNTs to form an open pore system (Figure 5.9 (d)) favourable for easy electrolyte ions access to the surface of mwGO and CNTs to form electric double layers [434] and may increase surface area [435]. This is due to the enhanced van der Waals forces and friction, which is consistent with previously reported results [363-365]. In addition, Figure 5.9 (d) shows that the void

spaces or “pores” between the matted CNT tubes are in the order of microns, and these void spaces can be considered as macropores and are areas through which ions diffusion can freely take place thus enhancing electrosorption. From the SEM image, CNTs nano-network structures act as useful nano-spacers for diminishing the face-to-face aggregation of CNTs. This 3-D porous structure exposes extensive surface areas that facilitate the ions diffusion leading to a high performance of electrosorption [436]. Moreover, the strands of CNTs adhere to each other to form smaller aggregation bundles (10-30 nm) compared with usual CNTs diameters (50-80 nm) [437] and bundles of CNTs in CNT/RVC electrode (25-50 nm). This decrease in aggregation bundles of CNTs is expected when combining graphene sheets with CNTs according to data reported by Zhang et al. [167]. The tightly wrapped nanotube bundles lead to a reduced electrode resistance [438] and maximises surface area, potentially allowing large capacitances to be obtained [366]. These will lead to an increase in ions capture and conductive properties of 9-CNT/mwGO/RVC electrode.

It is obvious from the top view of 8-CNT/mwGO composite materials (Figure 5.9 (g)) that nanotube bundles are still dominant and highly tangled, wrapped in the composite. The strands of CNTs adhere to form bigger aggregation bundles compared with 9-CNT/mwGO composite materials. The cross-section of this composite electrode shown in Figure 5.9 (h) indicates a layered structure and the CNTs are uniformly sandwiched between the GO sheets making a multilayered 3D network structure with good porous architecture inside the composite electrode. Obviously, the graphene nanosheets restacking and gaps interfacing between graphene sheets and CNTs to form a favourable open pore system was decreased.

This leads to difficult electrolyte ions access to the surface and minimises surface area when compared with 9-CNT/mwGO composite material. This phenomenon could possibly be due to the minimization of surface area and specific capacitance. It is clear that, from Figure 5.9 (j), when the mwGO ratio reaches to 3 in the composite, the graphene nanosheets dominate in the composite and the cross-section surface was completely changed into the 3D uniform rough multilayer and porous structure containing voids with carbon nanotubes distributed in them; but are difficult to clearly image. This structure leads to reduced electrolyte accessibility to the surface area. In contrast, Figure 5.9 (k) shows the top surface of mwGO/RVC electrode. The top surface of mwGO has rippled and crumpled structures and wrinkled structures with clear aggregation, and the stacked structure of the nanosheets in the cross-section image of mwGO (Figure 5.9 (l)) can be clearly observed. The cross-section SEM reveals a curled morphology consisting of rippled structures. As a result, graphene sheets with curled or wrinkled morphologies will present the greatest difficulty for electrolyte access to the surface area. Therefore, the specific capacitance in mwGO/RVC is expected to be the smallest, comparing amongst all composite electrodes.

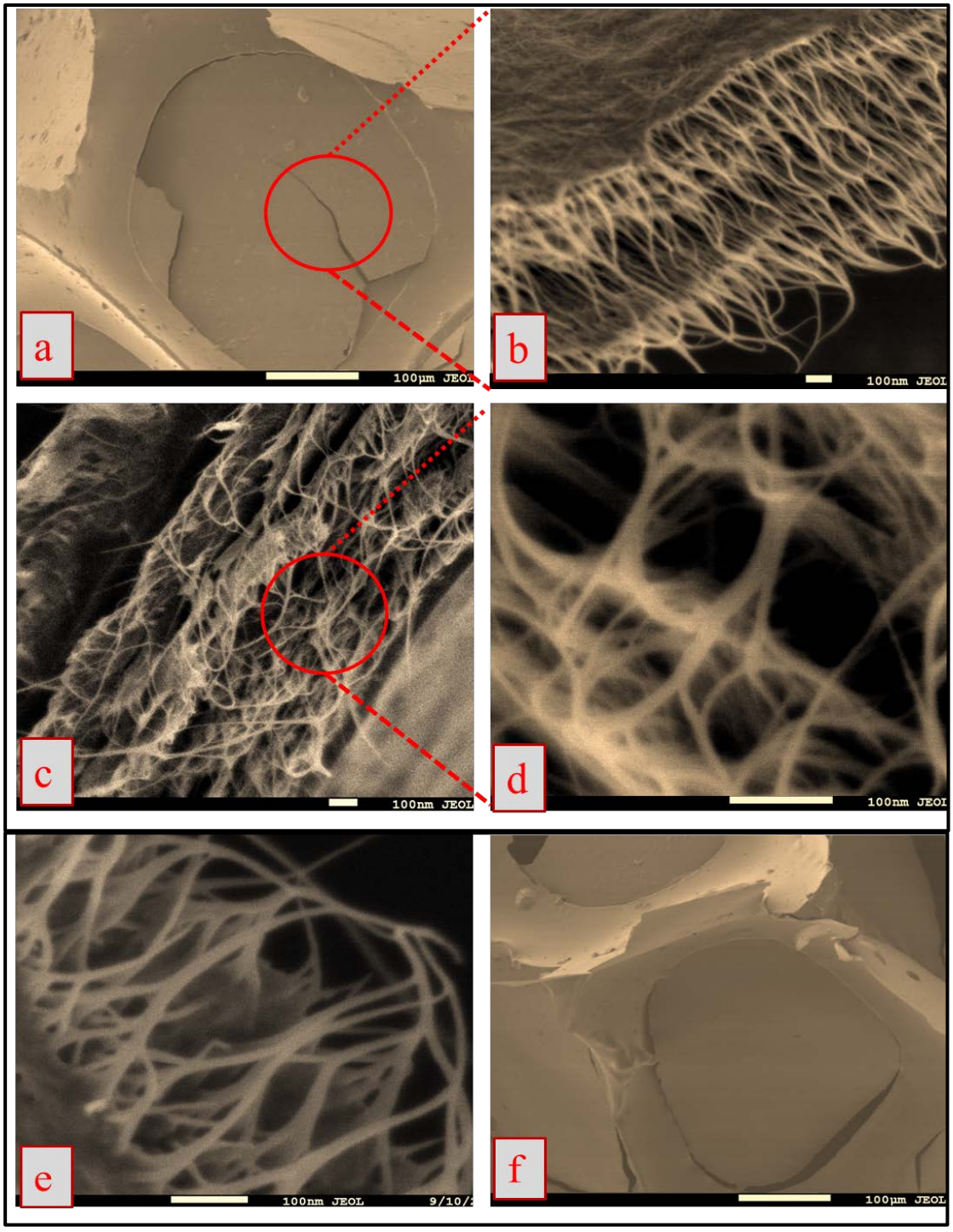
a
100µm JEOL
b
100nm JEOL
c
100nm JEOL
d
100nm JEOL
e
100nm JEOL
f
100µm JEOL

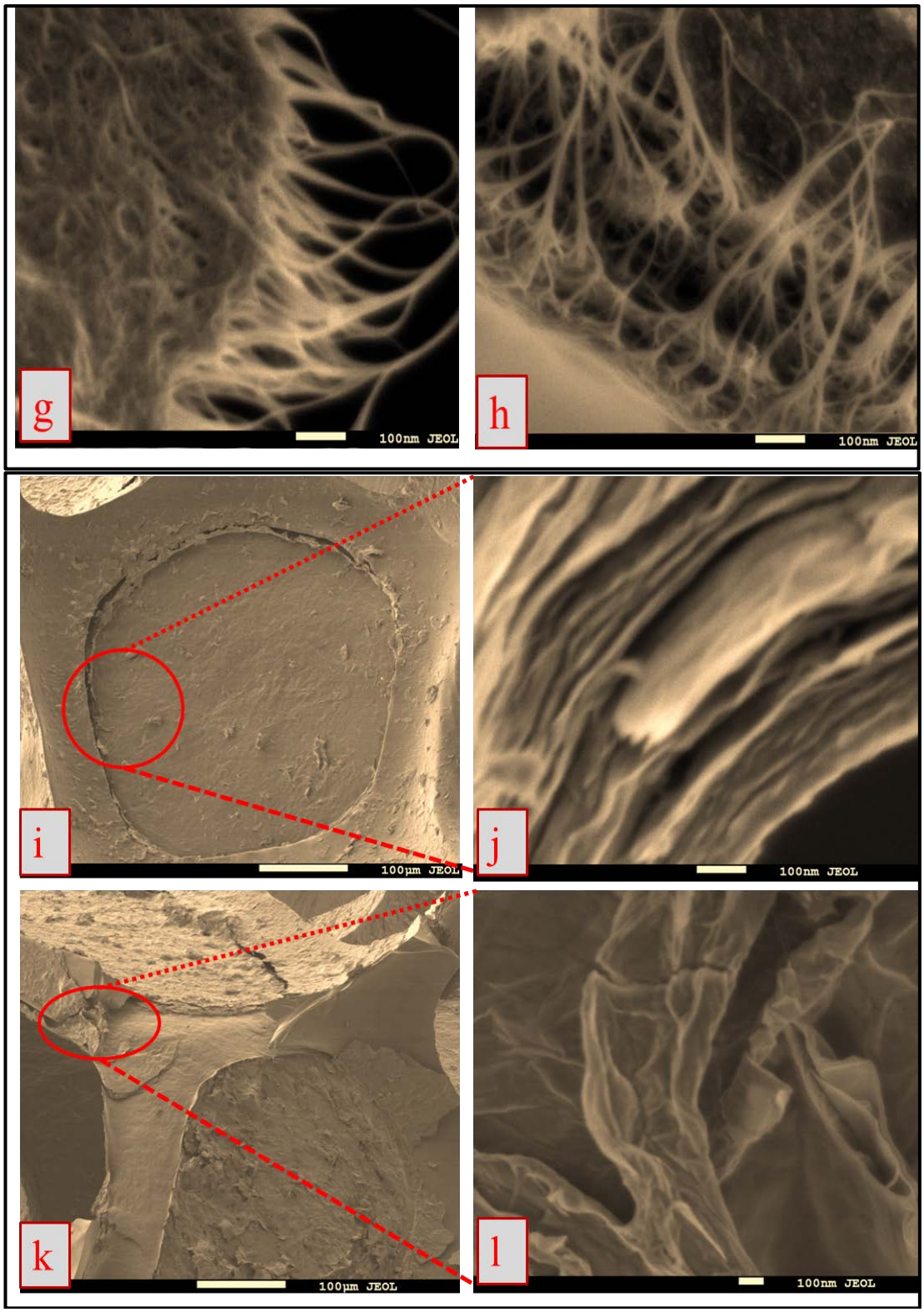

Figure 5.9: Scanning electron microscopy (SEM) images (a) top surface, (b) 45º view, (c, d, e) cross-section of 9-CNT/mwGO/RVC electrode; (f) top surface, (g) 35º view, (h) cross-section of 8-CNT/mwGO/RVC electrode; (i) top surface, (j) 45º view of 7-CNT/mwGO/RVC electrode; and (k) top surface, (l) 45º view of mwGO electrode.

5.3.6 Electrochemical behaviour of electrodes studied using cyclic voltammetry

In order to evaluate the electrochemical properties of all of the coated RVC electrodes, cyclic voltammetry (CV) was applied as it is one of the most widely used techniques to study electrochemical reactions. In this chapter, it is used to determine the effect of increasing the ratio of mwGO in CNT/mwGO/RVC electrodes on the capacitance, the effect of increasing scan rate on electron transfer and the stability of electrodes using 1 M NaCl solution recorded in the voltage range between -0.2 to 1.0 V vs Ag/AgCl in a three-electrode system. A RVC electrode was used as counter electrode, and mwGO/RVC, CNT/RVC, 7-CNT/mwGO/RVC, 8-CNT/mwGO/RVC and 9-CNT/mwGO/RVC electrodes were used as working electrodes, respectively.

5.3.6.1 Capacitive behaviours of mwGO/RVC, CNT/RVC, and various CNT/mwGO/RVC composite electrodes.

Electrochemical capacitance has been widely examined as the most common factor to govern the capacitance. The capacitive behaviour of these electrodes resulted mainly from electrochemical double-layer charging along with a negligible contribution of pseudo-capacitance. The capacitance of all materials coated RVC electrodes were investigated by integrating the curve area of the CV curve. Figure 5.10 presents the CV curves of mwGO, CNT and various ratios of mwGO in CNT/mwGO composite materials coated RVC electrodes at 5 mV/s scan rate in terms of current per gram of materials. In all cases, the CV curves have one pair of redox peaks that occurs in the potential range of (-0.2 to 0.4 V), probably owing to a

small quantity of oxygen-containing functional groups in all electrodes [395]. In addition, the CV curves obtained are quasi-rectangular, with distortions also apparent indicating a pseudo capacitance type behaviour with no significant Faradaic reaction being observed for any electrode; indicating that ions are adsorbed on the electrode surface by forming an electric double layer due to Coulombic interaction rather than electrochemical reaction [210, 314, 315, 367]. It is worth noting that in Figure 5.10 the current density of mwGO is much lower than that of CNT and CNT/mwGO. Therefore, the specific capacitance of mwGO coated RVC electrode has the lowest specific capacitance (87.21 F/g) amongst all the electrodes. This specific capacitance was very small compared with other studies for reduced graphene oxide under the same conditions (140 F/g) [209, 212]. The low specific capacitance of mwGO indicates low exposure of surface area since specific capacitance is proportional to the electrolyte-accessible surface area. This experimental result could be explained by that the graphene sheets are loosely stacked or folded with each other to construct interconnected 3D macropores in mwGO/RVC electrode as shown in SEM image (Figure 5.2 (b)) that leads to formation of aggregates, and the distance between interlayers of sheets (0.435 nm) is too small to allow the hydrated sodium ions (radius = 0.358 nm) access. This leads to the poor exposure of surface area for forming the electric double layer with electrolytes. Therefore, the mwGO agglomerates show a relatively low specific capacitance.

The CV curve of CNT/RVC electrode was discussed in Section (4.3.6.3.) and the specific capacitance at 5 mV/s was calculated using Equation (3.2) to be 139.65 F/g. This capacitance was increased when the mwGO material was combined with CNT material at less than 2 parts in 10, as shown in Figure 5.10. The inset in

Figure 5.10 shows that the highest specific capacitance was obtained from the 9-CNT/mwGO/RVC electrode and the calculated specific capacitance was 179.39 F/g, which represents a 29 % increase compared with the CNT/RVC electrode. This enhancement could be attributed to the synergistic effect of CNT and mwGO. The incorporation of mwGO into CNT forms an advantageous network structure that conductively bridges the pores between the CNT particles, which can facilitate rapid transport of the electrolyte ions within the electrode materials and increase the surface area of electrode. This surface area increased because of the large external active surface area of mwGO sheets and because of the diameter of bundling of CNTs in CNT/mwGO/RVC composite electrode being smaller than 25 nm. This is smaller than the diameter of bundling of CNTs alone, which was discussed in Section (4.3.5.).

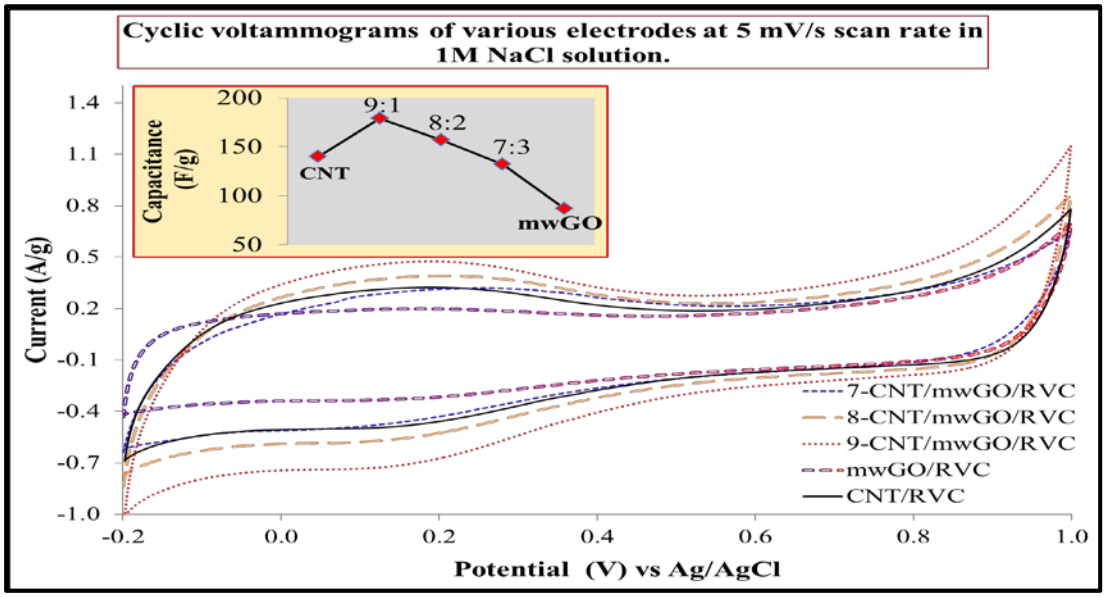

Figure 5.10: Comparison cyclic voltammograms and (inset) specific capacitance for mwGO/RVC, CNT/RVC, 7-CNT/mwGO/RVC, 8-CNT/mwGO/RVC and 9-CNT/mwGO/RVC electrodes in 1 M NaCl solution recorded in the voltage range between -0.2 to 1.0 V vs Ag/AgCl in a three-electrode system at 5 mV/s scan rate.

The inset in Figure 5.10 shows that the trends of the specific capacitance of electrodes decrease with further increase in mwGO content in the CNT/mwGO/RVC composite electrodes. The specific capacitances of 8-CNT/mwGO/RVC and 7-CNT/mwGO/RVC electrodes, which were calculated using Equation (3.2), were 156.47 and 132.60 F/g, respectively. The decrease in specific capacitance could be ascribed to the low specific surface area of mwGO. Furthermore, excessive mwGO will cover most of the CNT surface, which makes the transport of the electrolyte ions into the porous structure of CNT difficult, resulting in a low specific capacitance. It is interesting to note that the specific capacitance of the CNT/RVC electrode was higher than the specific capacitance of 7-CNT/mwGO/RVC electrodes. These specific capacitance results suggest that the electrosorption capacity performance of 9-CNT/mwGO/RVC electrode will be better than all other electrodes. Moreover, the specific capacitance result of mwGO/RVC electrode, being lower than that of the other electrodes, suggests to not apply this electrode in the CDI system selected for experiments because the electrosorption capacity will be very small compared with CNT/RVC and CNT/mwGO/RVC composite electrodes.

5.3.6.2 The effect of increasing loading level on capacitive behaviours.

In the previous section it was reported that the highest specific capacitance was obtained at the 9-CNT/mwGO/RVC electrode. This led to the selection of this electrode for study on the effect of increasing loading level of composite materials in geometric area terms and geometric volume terms on its capacitive behaviours. In this study, the capacitive behaviours of all 9-CNT/mwGO/RVC electrodes which had similar geometric volume (2.16 cm^3) of RVC electrodes with various amounts of

composite materials coated, 10, 30 and 50 mg, were investigated by CV. The maximum loading amount of composite material was set at 50 mg because it was observed in the laboratory that at this level the pores of the RVC electrode was completely filled; as evidenced by the top view SEM image (Figure 5.9 (a)).

Figure 5.11 (a and b) show cyclic voltammograms, at 5 mV/s, of composite electrodes with different loadings of 9-CNT/mwGO composite material in terms of current per gram of composite material and current per geometric volume of electrode respectively. It was expected that the CV behaviours of all composite electrodes would be in keeping with earlier results reported for the CNTs electrodes in Sections (4.3.6.3.); ie increasing the amount of composite material in the RVC electrode led to a decrease in the current per gram of 9-CNT/mwGO composite (Figure 5.11 (a)) but, in contrast, led to an increase in the current per geometric volume of electrode (Figure 5.11 (b)). The capacitance results per unit gram of composite material and per unit geometric volume of electrode are presented in Figure 5.11 (c) as F/g and F/cm^3 respectively. The capacitance of the electrode per mass (F/g) and geometric volume (F/cm^3) were calculated using Equation (3.2.) and Equation (3.3.), respectively. It is observed in Figure 5.11 (c) that increasing the amount of 9-CNT/mwGO composite material in the RVC electrode led to a decrease in the capacitance of 9-CNT/mwGO composite material. For example, the highest specific capacitance was 298.98 F/g for the 10 mg of composite material loaded and the lowest specific capacitance was 179.39 F/g for 50 mg composite loaded, determined at a scan rate of 5 mV/s. On the other hand, Figure 5.11 (c) also shows that the capacitances in terms of geometric volume of these electrodes increase with increase in the amount of composite. The capacitance, obtained at 5 mV/s, was 1.39

F/cm^3, 2.93 F/cm^3 and 4.13 F/cm^3 for the electrode that had 10, 30 and 50 mg 9-CNT/mwGO composite coated on the RVC electrodes, respectively.

Furthermore, the capacitance of electrode per geometric area (F/cm^2) was calculated using Equation (3.4.). It is expected that increasing the amount of composite material in the electrode would lead to a decrease in the porosity of the RVC electrode which, in turn, would lead to an increase in the geometric area. This results in an increase in the capacitance of the electrode. The capacitance obtained at 5 mV/s was 0.17 F/cm^2, 0.36 F/cm^2 and 0.50 F/cm^2 for the electrode that had 10, 30 and 50 mg 9-CNT/mwGO composite material coated on the RVC electrodes, respectively. These results indicate that the surface area of composite material coated in the RVC electrode had increased.

From these results and Chapter 4 results, it can be generalised that the specific capacitance in geometric area and volume increases with increasing amounts of material on the electrode. However, the capacitance is significantly higher when expressed in terms of geometric volume.

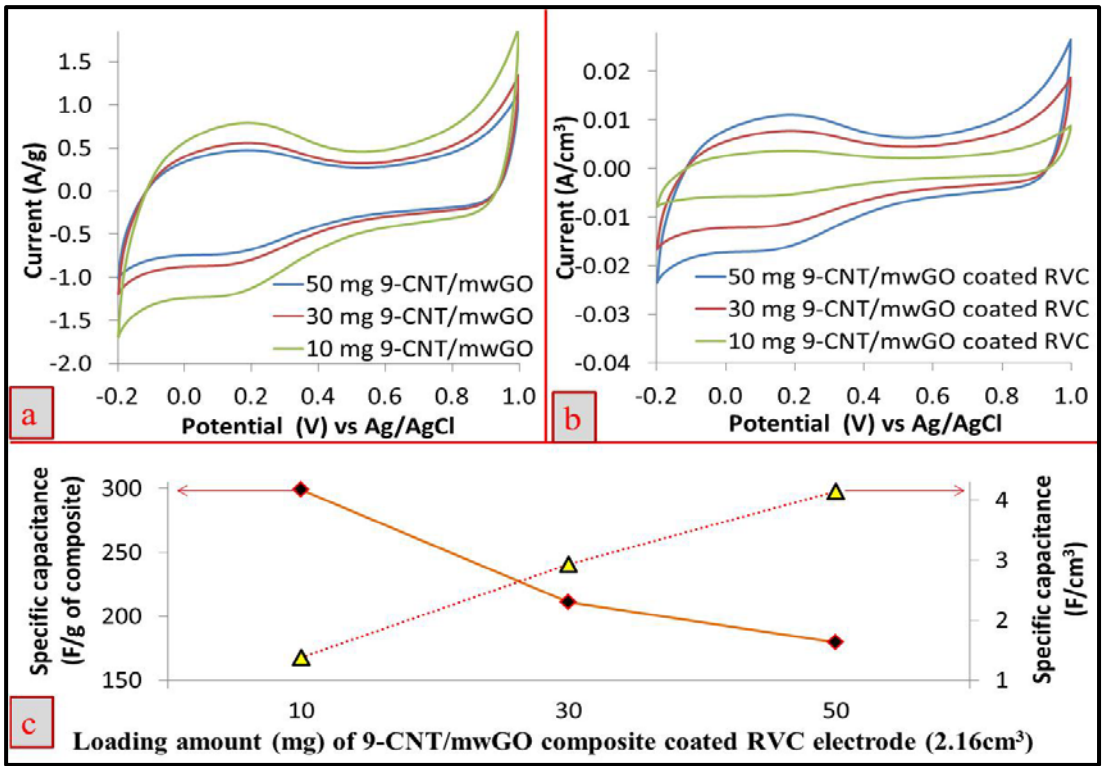

Figure 5.11: Cyclic voltammograms of 9-CNT/mwGO composite coated RVC electrodes in 1 M NaCl solution recorded in the voltage range between -0.2 to 1.0 V vs Ag/AgCl using a three-electrode system at 5 mV/s, in terms of (a) current per gram of composite, and (b) current per geometric volume of electrode. (c) Capacitance of the electrodes per gram of composite and per geometric volume of the electrode.

5.3.6.3 Effect of increasing scan rate on the electrode capacitance

The effect of different scan rates on electrode capacitance was investigated in aqueous NaCl solution. Figure 5.12 presents the CV curve of 9-CNT/mwGO/RVC electrode as a function of the scan rate. The shape of the CVs at scan rates 5 and 50 mV/s (Figure 5.12 (a)) are close to rectangular and as we know, the achievement of a rectangular-shaped CV is the suggested ultimate goal in high electrochemical double-layer capacitors (EDLC) [314]. According to the characteristics of the CV, it can be deduced that the contribution of carboxyl and carbonyl groups to CNTs is in the pseudo-capacitance, which increases apparent capacitance [341, 369]. This

suggests that there is an intimate contact between the electrolyte and the active material, and which results in excellent charge transfer kinetics due to the porous and cross-linked structure formed. It is clear that the polarization caused by a high scan rate leads to the anodic peaks shifting toward high potential and the cathodic peaks moving toward negative potential simultaneously [341]. However, when the scan rate was increased above 50 mV/s (Figure 5.12 (a)), the curves were characterized by non-rectangular shapes that indicated resistance-like electrochemical behaviour. This is because the electrode is very porous which hinders the migration of NaCl to the pores and this becomes pronounced at increasing scan rates of CV [341]. This leads to a continuous decrease in the capacitance of electrodes with increasing scan rate (Figure 5.12 (b)); which is discussed in Section 4.3.6.3. This characteristic has been attributed to the resistance of the electrolyte and the inner resistance of ion diffusion with certain carbon micro-pores whose surface is only partially accessible to electrolytes. This becomes significant under relatively high scan rates due to the differential depletion of the electrolyte concentration [372-374]. It can be seen that the specific capacitance trend of the electrode sharply decreases when the scan rate is above 50 mV/s. It is expected that the capacitive volume should increase with increasing scan rates because it is found in all cases of carbon nanotubes and graphene composite with carbon nanotubes [221, 314, 341, 367, 368, 370-372]. Furthermore, the stability of the CV curve was very high; 99% stable after 200 cycles as shown in Figure 5.12 (c). In addition, Table 5.2 shows the specific capacitance for all electrodes at various potential scan rates in terms of F/g of material, F/ cm^2 geometric area of electrode and F/cm^3 geometric volume of electrode, in 1 M NaCl solution at various scan rates; which were calculated using Equations (3.2, 3.3. and

3.4.). It is clear for all electrodes that a high capacitance is obtained at low scan rate, but the capacitance markedly decreased at high scan rates. For instance, the specific capacitance of 9-CNT/mwGO/RVC electrode was 179.39 F/g (0.50 F/cm^2 or 4.13 F/cm^3) and 67.79 F/g (0.19 F/cm^2 or 1.57 F/cm^3) at 5 and 200 mV/s scan rates, respectively. It is apparent from Table 5.2 that the behaviour of specific capacitance in terms of geometric volume and geometric area followed the specific capacitance in term of mass of materials with respect to scan rate. This was expected because the mass of materials was similar in all electrodes (50 mg). It is interesting to note that the specific capacitance per geometric area of the mwGO coated RVC electrode at 50 mV/s scan rate was 0.17 F/cm^2. This specific capacitance increased around 9 times compared with the same mwGO prepared as buckypaper (0.019 F/cm^2), tested under the same conditions using 1M $NaNO_3$ solution [198].

It is important to note that the capacitance of the RVC electrode per geometric volume under the same conditions at a scan rate of 20 mV/s was discussed in Section (4.3.6.1.). The RVC was 0.002 F/cm^3 and the capacitance had increased by a factor of 1060 when the same electrode was filled completely by functionalized CNT material. It can be observed from Table 5.2 that the capacitance of the RVC electrode had increased by a factor of 1775 when filled completely with 9-CNT/mwGO material. This is related to the large surface area of 9-CNT/mwGO/RVC compared to a RVC electrode according to the Randles-Sevcik relationship [304].

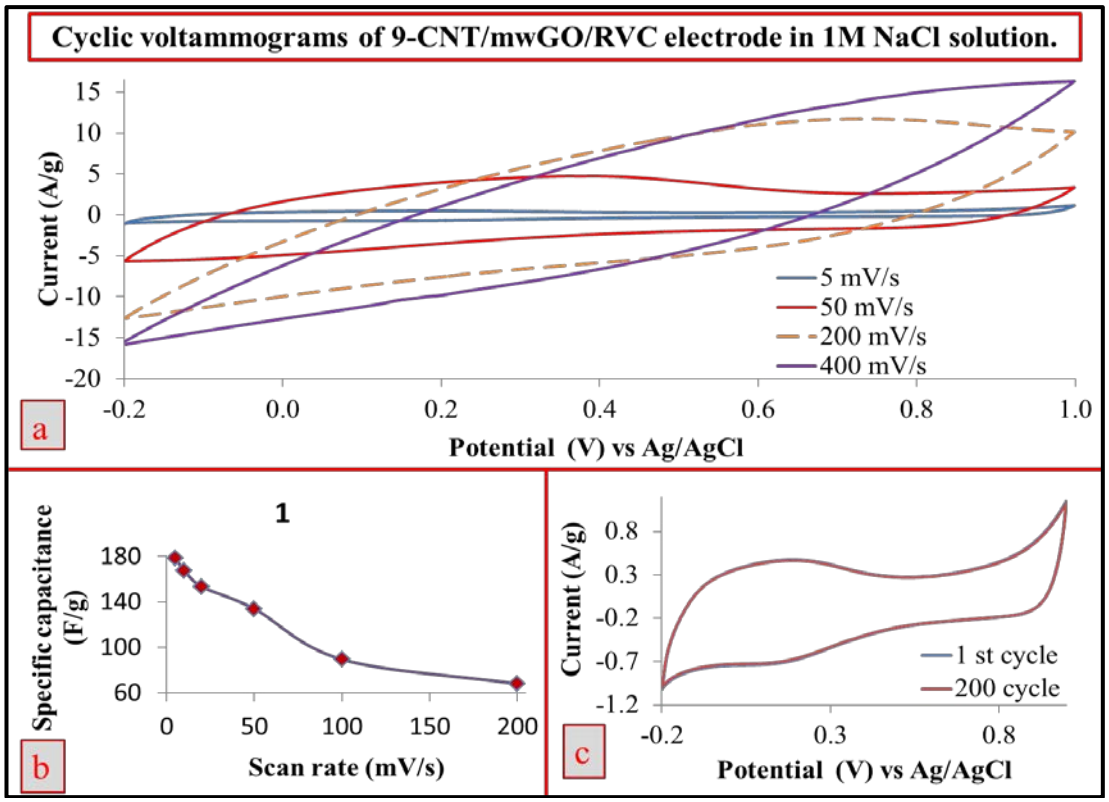

Figure 5.12: (a) Cyclic voltammograms and (b) specific capacitance at various scan rates, and (c) the cyclic voltammograms stability scanned at 20 mV/s using 9-CNT/mwGO/RVC electrode in 1 M NaCl solution recorded in the voltage range between -0.2 to 1.0 V vs Ag/AgCl in a three-electrode system.

Table 5.2: Specific capacitance of various electrodes in terms of F/g of material, F/area of electrode and F/ volume of electrode, in 1 M NaCl solution at various scan rates.

Sample		**mwGO/RVC**					
Scan rate (mV/s)		**5**	**10**	**20**	**50**	**100**	**200**
Specific Capacitance	**(F/g)**	**87.21**	**75.87**	**69.77**	**61.05**	**47.97**	**34.88**
	(F/cm^2)	**0.24**	**0.21**	**0.19**	**0.17**	**0.13**	**0.10**
	(F/cm^3)	**2.02**	**1.75**	**1.61**	**1.41**	**1.11**	**0.81**
Sample		**CNT/RVC**					
Scan rate (mV/s)		**5**	**10**	**20**	**50**	**100**	**200**
Specific Capacitance	**(F/g)**	**139.65**	**131.27**	**117.70**	**103.34**	**68.43**	**51.67**
	(F/cm^2)	**0.39**	**0.37**	**0.33**	**0.29**	**0.19**	**0.14**
	(F/cm^3)	**3.23**	**3.04**	**2.75**	**2.39**	**1.58**	**1.20**
Sample		**9-CNT/mwGO/RVC**					
Scan rate (mV/s)		**5**	**10**	**20**	**50**	**100**	**200**
Specific Capacitance	**(F/g)**	**179.39**	**167.69**	**153.42**	**133.79**	**89.20**	**67.79**
	(F/cm^2)	**0.50**	**0.47**	**0.43**	**0.37**	**0.25**	**0.19**
	(F/cm^3)	**4.13**	**3.88**	**3.55**	**3.09**	**2.06**	**1.57**
Sample		**8-CNT/mwGO/RVC**					
Scan rate (mV/s)		**5**	**10**	**20**	**50**	**100**	**200**
Specific Capacitance	**(F/g)**	**156.47**	**143.95**	**131.43**	**112.66**	**73.54**	**57.89**
	(F/cm^2)	**0.44**	**0.40**	**0.37**	**0.31**	**0.21**	**0.16**
	(F/cm^3)	**3.62**	**3.33**	**3.04**	**2.61**	**1.70**	**1.34**
Sample		**7-CNT/mwGO/RVC**					
Scan rate (mV/s)		**5**	**10**	**20**	**50**	**100**	**200**
Specific Capacitance	**(F/g)**	**132.60**	**112.71**	**106.08**	**92.82**	**59.67**	**39.78**
	(F/cm^2)	**0.37**	**0.31**	**0.30**	**0.26**	**0.17**	**0.11**
	(F/cm^3)	**3.07**	**2.61**	**2.45**	**2.15**	**1.38**	**0.92**

5.3.7 Adsorption performance of 9-CNT/mwGO coated RVC electrode.

Having determined that the optimum applied voltage was 1.5 V and optimum flow-rate was 50 mL/min, as reported in Chapter 4 for CNT/RVC electrode, these conditions were used in further studies to compare the desalination performance of a range of electrodes with different amounts of 9-CNT/mwGO composite materials coated on the RVC electrode. All experiments were performed with the total volume of NaCl solution kept at 70 ml and the concentration was 75 mg/L (143 μS/cm). Figure 5.13 (a) shows the CDI process at all loading levels of composite in a similar geometric volume (2.16 cm^3) of RVC electrodes; 10, 30 and 50 mg loadings. It was expected that the electrosorption behaviours of all composite electrodes would be in keeping with earlier results reported for the CNT electrodes in Sections (4.3.8. and 4.3.13.); ie the drop in conductivity of the test saline solution would increase with increasing amounts of material on the electrode because ions were attracted by oppositely charged electrodes when an electric field was applied [33]. A better electrosorption performance was achieved at 50 mg coated RVC electrode and the conductivity significantly dropped by about 5.21 μS/cm in the electrosorption process. Figure 5.13 (b) shows the electrosorption of various 9-CNT/mwGO/RVC electrodes in terms of the mass of 9-CNT/mwGO and the volume of electrode which were calculated according to Equation (3.5) and Equation (3.6) (calculated as explained in Section (3.3.9.)). It is clear from the figure that the electrosorption decreased with composite material increase in weight. Clearly, when the RVC electrode was loaded with 10 mg of composite, the electrosorption capacity was 9.91 mg/g and when same electrode was loaded with 50 mg of composite, the electrosorption capacity became 3.82 mg/g. On the other hand, if the electrosorption

of electrodes was considered in terms of geometric volume, the electrosorption increased with increase in the amount of composite material. For example, when the RVC electrode was loaded with 10 mg of composite, the electrosorption was 0.05 mg/cm^3 and when the RVC electrode was loaded with 50 mg of composite, the electrosorption was 0.09 mg/cm^3. This result and Chapter 4 results lead to generalization that the electrosorption capacity increases with increasing amounts of material on the electrode. Thus, the effect of loading of composite materials 8-CNT/mwGO and 7-CNT/mw GO onto RVC electrodes on the ion removal was not investigated.

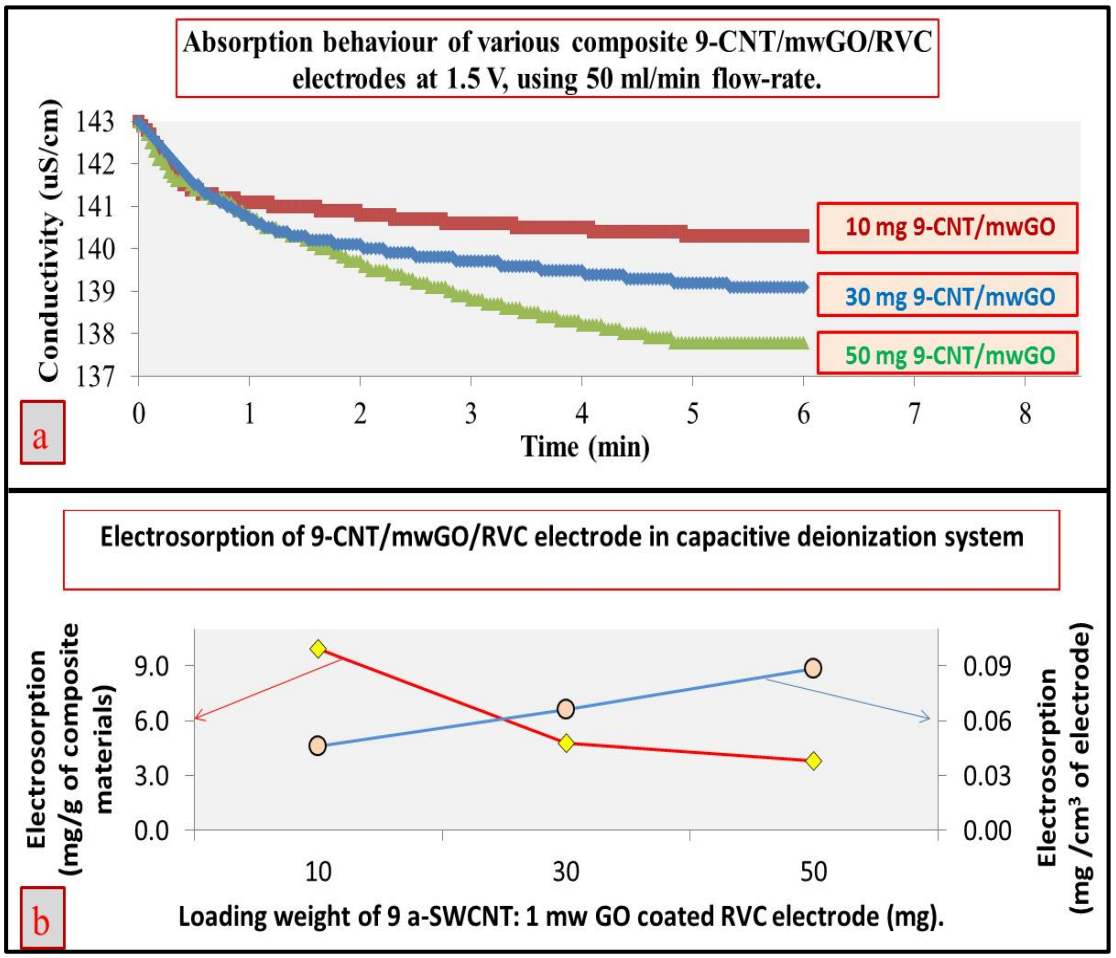

Figure 5.13: (a) Adsorption behaviour, and (b) the electrosorption capacity in terms of mass of composite material loading and the geometric volume of electrode of various 9-CNT/mwGO/RVC electrodes. Loadings (mg): 10, 30 and 50.

5.3.7.1 Optimization of conditions for ion removal efficiency

From the results obtained in Chapter 4 for the a-SWCNT/RVC electrode that afforded an optimized ion removal efficiency at a 50 ml/min flow-rate and 1.5 V cell voltage, the best NaCl removal performance for a capacitive deionization (CDI) system using the 9-CNT/mwGO/RVC electrode was determined with respect to variations about this flow-rate and this electrical voltage. The electrode that had 50 mg of composite coated on the RVC was selected for this study because it had the highest electrosorption capacity in terms of geometric volume. The flow-rates below and above 50 ml/ min and the cell voltage just below 1.5 V were investigated as shown in Figure 5.14 (a and b). Cell voltages above 1.5 V were not investigated because saving energy is one of our targets. It is obvious from the results that the best solution conductivity decrease was achieved when the flow-rate was 50 mL/min. When the flow-rate was above or below 50 ml/min, the conductivity decrease was less, leading to lower electrosorption capacity. This is due to the fact that a low pump rate would result in an obvious co-ions effect which will depress the electrosorption process, while a high pump rate will introduce a high pump force that is greater than that of electrosorption force and therefore decrease the electrosorption amount [268]. In addition, the ion removal characteristics were affected by various applied voltages. As the applied voltage increased, the ion removal amount increased and a higher ion removal was achieved with 1.5 V. Thus, the optimized flow-rate and cell voltage for the CDI process were found to be 50 mL/min and 1.5 V, respectively.

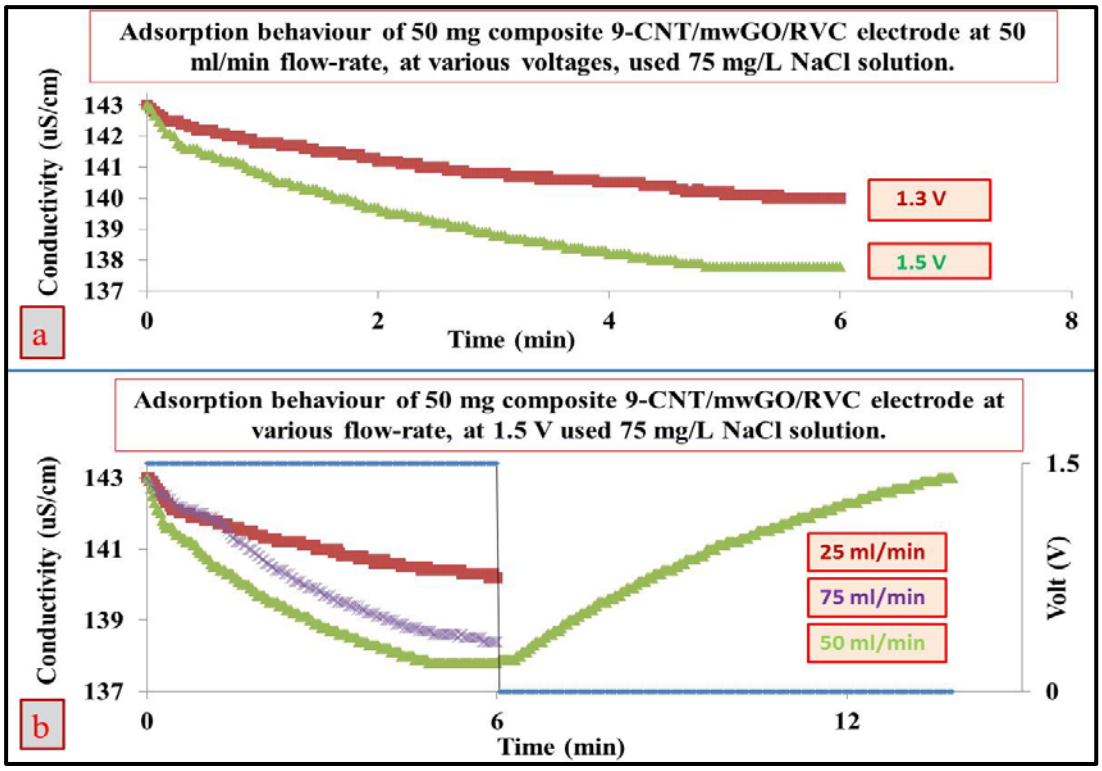

Figure 5.14: Conductivity variations of NaCl solution with various (a) applied voltages and (b) applied flow-rates, with respect to operating time; using the 9-CNT/mwGO/RVC electrode loaded with 50 mg composite material.

5.3.8 Capacitive deionization (CDI) system

5.3.8.1 Adsorption/ desorption performance of various ratios of CNT/mwGO loaded RVC electrodes.

The CDI system was investigated with respect to the influence of increasing ratios of mwGO in CNT/mwGO composite materials coated RVC electrodes on the ion removal performance. The ratio levels were 10:0, 9:1, 8:2 and 7:3 CNT:mwGO, respectively, and the mass of materials coated on all RVC electrodes was 50 mg. All experiments were performed with the same previous conditions as in Section (5.3.8.); at 1.5 V and 50 mL/min flow-rate with 6 min adsorption processes. Figure 5.15 (a) shows the CDI process for all composite coated RVC electrodes. As expected, once

the electrical voltage was applied, the solution conductivity dramatically decreased for all electrodes because ions were attracted by opposite charges on the electrodes [33]. Then the conductivity would gradually approach a constant minimum level, indicating that saturation was achieved [211]. During discharging of the CDI system under 0 V of applied voltage, the solution conductivity returned to about its initial value (143 μS/cm), meaning ions were released from the double layer region back into the solution because of the disappearance of electrostatic forces. It is clear that the highest drop in conductivity was by around 5.2 μS/cm using the 9-CNT/mwGO/RVC electrode. The second largest drop in conductivity was by around 4.8 μS/cm using the 8-CNT/mwGO/RVC electrode. The drop in conductivity for the CNT/RVC electrode was higher than that of the 7-CNT/mwGO/RVC electrode. It is notable that the 9-CNT/mwGO/RVC electrode saturation was achieved after 5min whereas CNT/RVC electrode saturation was achieved after 6 min. It is interesting also to note that the regeneration by discharging the CDI cells was completed, at 0 V, after 13 min for the electrode with the least amount of mwGO ratio in the sample; ie 9-CNT/mwGO/RVC. This means that the time saving of one electrosorption–desorption cycle with the 9-CNT/mwGO/RVC electrode was 27.78 %; compared with the CNT/RVC electrode which required 18 min. In addition, the electrosorption removal of NaCl by the 9-CNT/mwGO/RVC electrode in terms of mass of the electrode (3.82 mg/g) increased 18.27 % compared with that of the CNT/RVC electrode (3.23 mg/g). This improvement in electrosorption amount in the 9-CNT/mwGO/RVC electrode can be attributed to complicated and many factors including: increasing specific surface area, specific capacitance, more accessible

interlayer, pore microstructure and pore size distribution which can play important roles in affecting electrosorption capacity [211, 212, 439].

Figure 5.15 (b) shows the electrosorption performances of all electrodes which were measured from the data in Figure 5.15 (a). The variation of solution conductivity was monitored instantly by a multi-function conductivity meter. Accordingly, the correlation of conductivity (μS/cm) with concentration (mg/L) was calibrated prior to experiments; see previous equation (2.9.). Furthermore, the 8-CNT/mwGO/RVC electrode also afforded better CDI system performance than the a-SWCNT/RVC electrode; as evidenced by time saving of 11.11 % and 8.98% better electrosorption removal of NaCl. Table 5.3 also gives more details of the electrosorption in terms of mass, area and volume for each composite electrode; which were calculated according to Equation (3.5), Equation (3.6) and Equation (3.7) respectively. It is clear that the electrosorption behaviours of all composite electrodes in terms of area and in terms of volume followed the electrosorption behaviours of composite electrodes in term of mass of electrode because all the parameters were held constant; mass of material, electrode area and volume. These results suggest that the CDI process using 9-CNT/mwGO/RVC electrodes have promise as an effective technology for desalination.

Table 5.3: Electrosorption of NaCl by CNT/mwGO/RVC electrodes with various ratios of CNT, time of one desalination cycle.

Ratio of a-SWCNT in electrodes	Electrosorption			*Enhancement percentage in electrosorption	Time of one desalination cycle
	mg/g	mg/cm^2	mg/cm^3	%	min
7	3.01	8.4E-03	0.07		17
8	3.52	9.9E-03	0.09	8.98	16
9	3.82	1.1E-02	0.10	18.27	13
10	3.23	9.4E-03	0.08		18

*Comparing with CNT/RVC electrode.

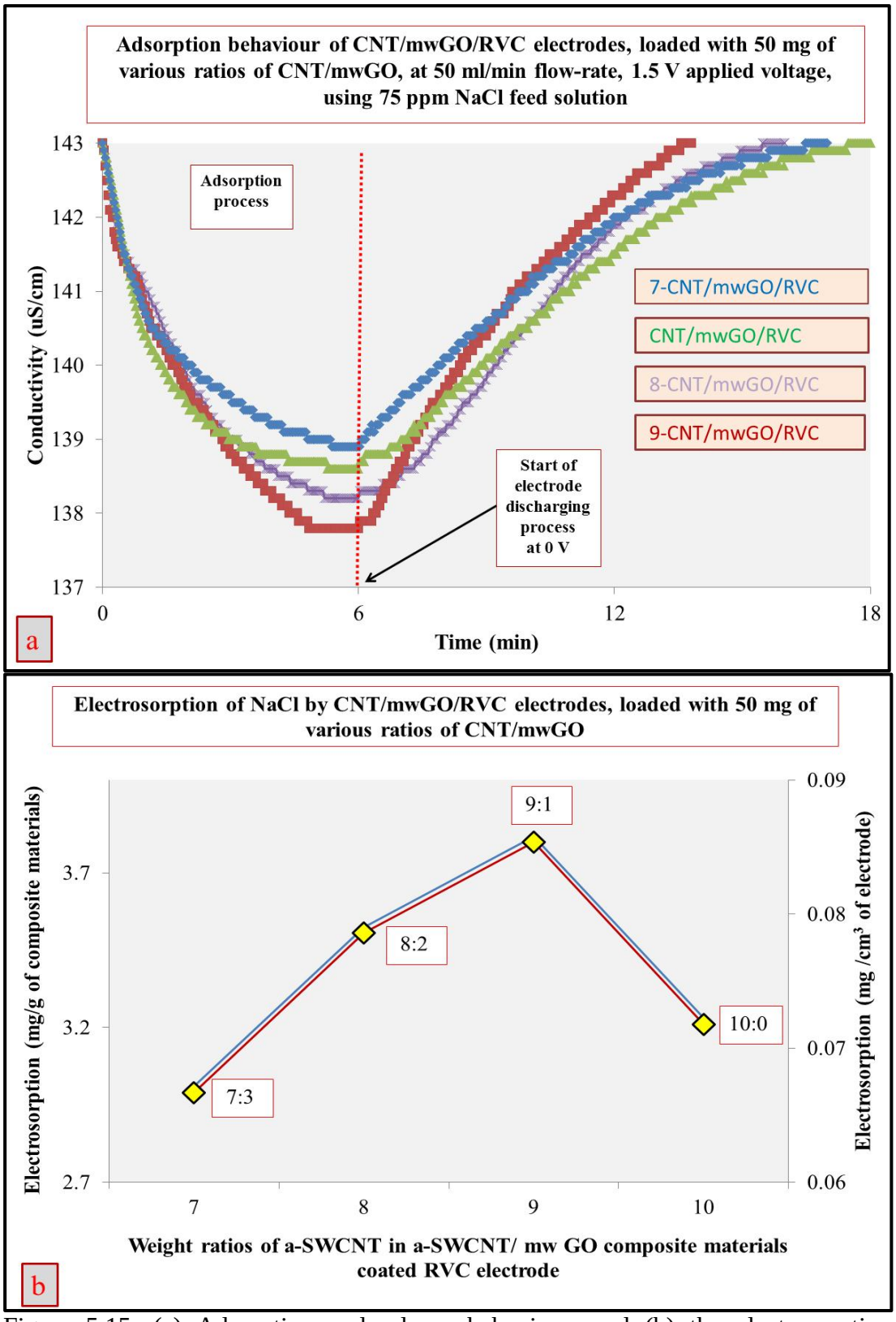

Figure 5.15: (a) Adsorption and release behaviour, and (b) the electrosorption capacity in terms of mass of CNT/mwGO and the geometric volume of electrode of various ratios 10, 9, 8 and 7 CNT in CNT/mwGO/RVC electrodes.

5.3.8.2 Electrosorption dynamics

The performance of electrodes adsorptions are evaluated by dynamics study which describes the solute uptake rate, and evidently this rate controls the residence time of adsorptive uptake at the solid-solution interface [256, 257]. From Chapter 4, it was shown that the NaCl adsorption by CNT/RVC electrode had obeyed pseudo first-order kinetics and that those NaCl ions were not adsorbed onto the CNTs surface via chemical interaction. Therefore, this section will investigate the controlling mechanism of electrosorption and the constants of sorption of pseudo first-order kinetics. The pseudo first-order kinetics model has been discussed in Section (3.3.15.) as proposed by Lagergren [260], and the conformity between experimental data and the model predicted values is expressed by the correlation coefficients (r^2, values close or equal to 1). The electrosorption dynamic and pseudo-first-order dynamic models for NaCl adsorption onto CNT/RVC, 9-CNT/mwGO/RVC, 8-CNT/mwGO/RVC and 7-CNT/mwGO/RVC electrodes at a voltage of 1.5 V, flow-rate of 50 ml/min, and constant temperature of 298 °K are shown in Figure 5.16. The electrosorption of NaCl onto all electrodes except the 9-CNT/mwGO/RVC electrode was very rapid within the first minute, then it became dynamic adsorption and after three minutes the electrode gradually approached saturation as shown in Figure 5.16 (a, b, and d). The time required to reach adsorption equilibrium was 6 minutes. However, the electrosorption of NaCl onto 9-CNT/mwGO/RVC electrode was very rapid within the first half minute. This could be because the external surface area of bundled CNT in this electrode is higher than other electrodes, thus increasing the possibility of ions to reach the surface easily. The SEM image of this electrode which was shown in Section (5.4.1) supports this

reason. After that, the electrosorption of NaCl onto this electrode becomes dynamic adsorption for four minutes and then followed by electrode saturation as shown in Figure 5.16 (c). The time required to reach adsorption equilibrium was 5 minutes, which may be due to the higher rate of diffusion of ions onto the electrodes particle surface.

The Pseudo-first-order kinetics for all electrodes was studied within the first four minutes as shown in Figure 5.16 (e, f, g and d), respectively. To evaluate the kinetics of the electrosorption process, the pseudo first-order model was tested to interpret the experimental data. The slopes and intercepts of plots of log ($qe–qt$) versus t were used to determine the first-order rate constant k_1 by Equation (2.12). In all electrodes, methods that are based on linearization of the models and correlation coefficients (r^2) of around 0.99 confirm that all electrodes followed Pseudo-first-order dynamics. Similar trends have been reported in the literature for the adsorption of NaCl ions from aqueous solutions by other adsorbents [208, 209, 268, 320, 324, 332, 380]. A comparison of the rate constant k_1 results, with the correlation coefficients is shown in Table 5.4. The rate constant (k_1) of the pseudo-first-order kinetics was 0.816, 0.525, 0.555, and 0.639 min^{-1} for CNT/RVC, 9-CNT/mwGO/RVC, 8-CNT/mwGO/RVC and 7-CNT/mwGO/RVC electrodes, respectively. It is clear that the relationship between the rate constant and electrosorption is an inverse relationship; when the electrosorption capacity increased, the rate constant decreased. Also the theoretical q_e values found from the pseudo-first-order kinetics model gave reasonable values (3.19, 3.66, 3.45 and 2.75

mg/g for CNT/RVC, 9-CNT/mwGO/RVC, 8-CNT/mwGO/RVC and 7-CNT/mwGO/RVC electrodes, respectively).

Table 5.4: Comparison between the adsorption rate constant (k_1) and correlation coefficients of pseudo-first-order kinetics, and the estimated theoretical and experimental (q_e) of maximum electrosorption with pseudo-first-order model.

a-SWCNT: mw GO	R^2	K_1 (min^{-1})	Theoretical q_e (mg/g)	Experimental q_e (mg/g)
7:3	0.990	0.639	2.75	3.01
8:2	0.987	0.555	3.45	3.52
9:1	0.992	0.525	3.66	3.82
10:0	0.994	0.816	3.19	3.23

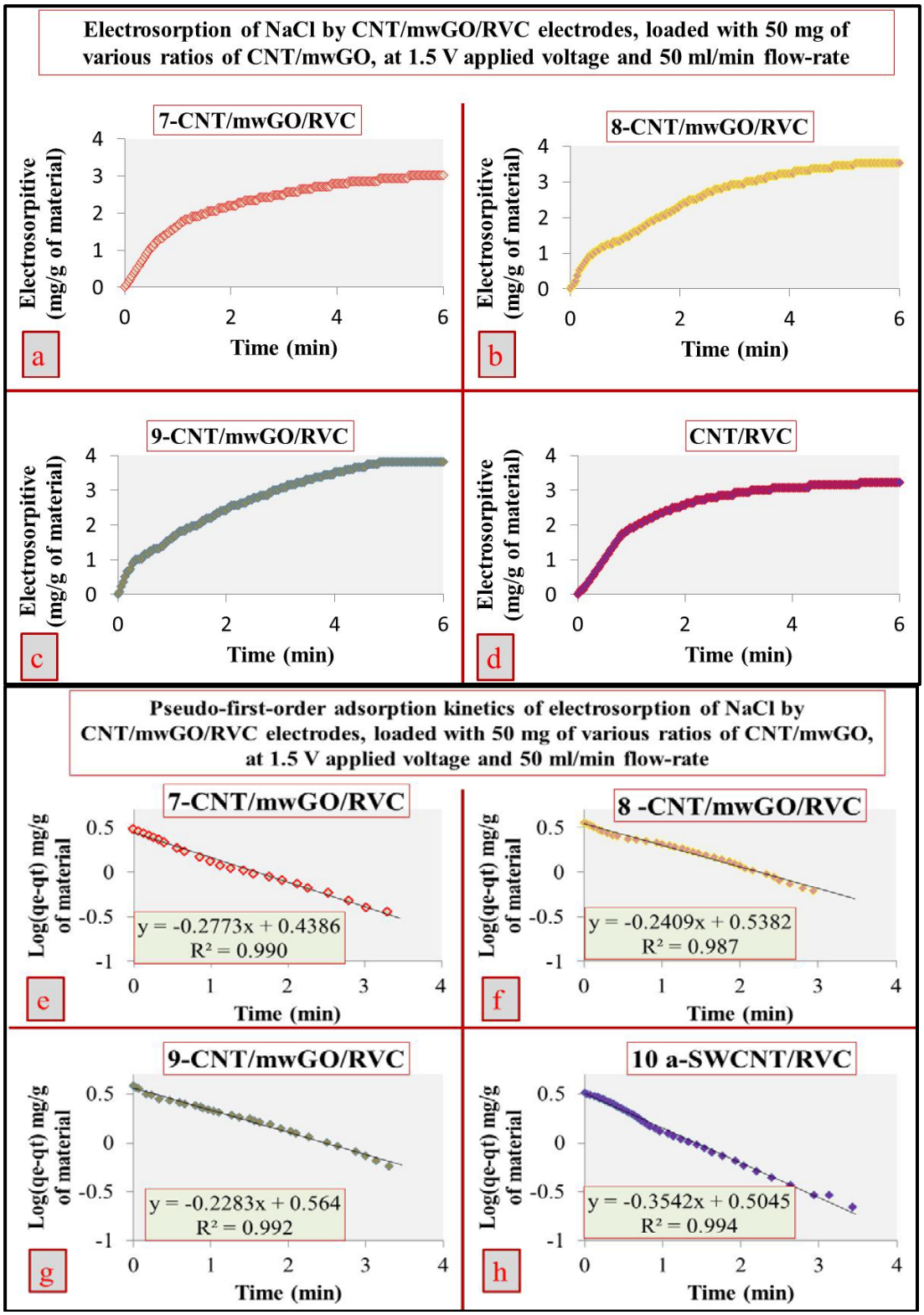

Figure 5.16: (a, b, c, d) Electrosorption and (e, f, g, h) pseudo-first-order adsorption kinetics of NaCl electrosorption onto CNT/RVC, 9-CNT/mwGO/RVC, 8-CNT/mwGO/RVC and 7-CNT/mwGO/RVC electrodes, respectively, at 1.5 V and 50 mL/min flow-rate. Results have been derived from Figure 5.15 (a) (adsorption process).

5.3.8.3 CDI cycling stability

Regeneration of electrodes plays a significant role in their commercialisation for use in CDI systems. In this section, several charging and regeneration cycles for the 9-CNT/mwGO/RVC electrode, which was selected for this study because it has highest electrosorption capacity amongst all electrodes, are shown in Figure 5.17. This experiment was performed with the same previous conditions as in Section (4.3.7.). Figure 5.17 clearly shows that no oxidation and reduction reactions occur in electrosorption. This means that the current is mainly consumed for charging the electrode to electro-adsorb ions from the bulk solution [323], and the electrical double layer is completely formed at the electrode/electrolyte interface [267]. In addition, the conductivity changes are reproducible for the five cycles of electrosorption and desorption, confirming that the CDI could be regenerated very well without any driving energy and secondary pollution, which is critical for large scale applications. It is noted that the process of regeneration can be carried out easily in a short time and the same pattern can be found in four repeated electrosorption–desorption cycles; each cycle takes 13 min, ie 6 min ion adsorption and 7 min release of ions. Also, the recycling stability was very high (100%) for the reason that the decay of electrosorption capacity has not been observed. This high stability behaviour of the CNT/GO electrode in a CDI system is reported in other research as well [211].

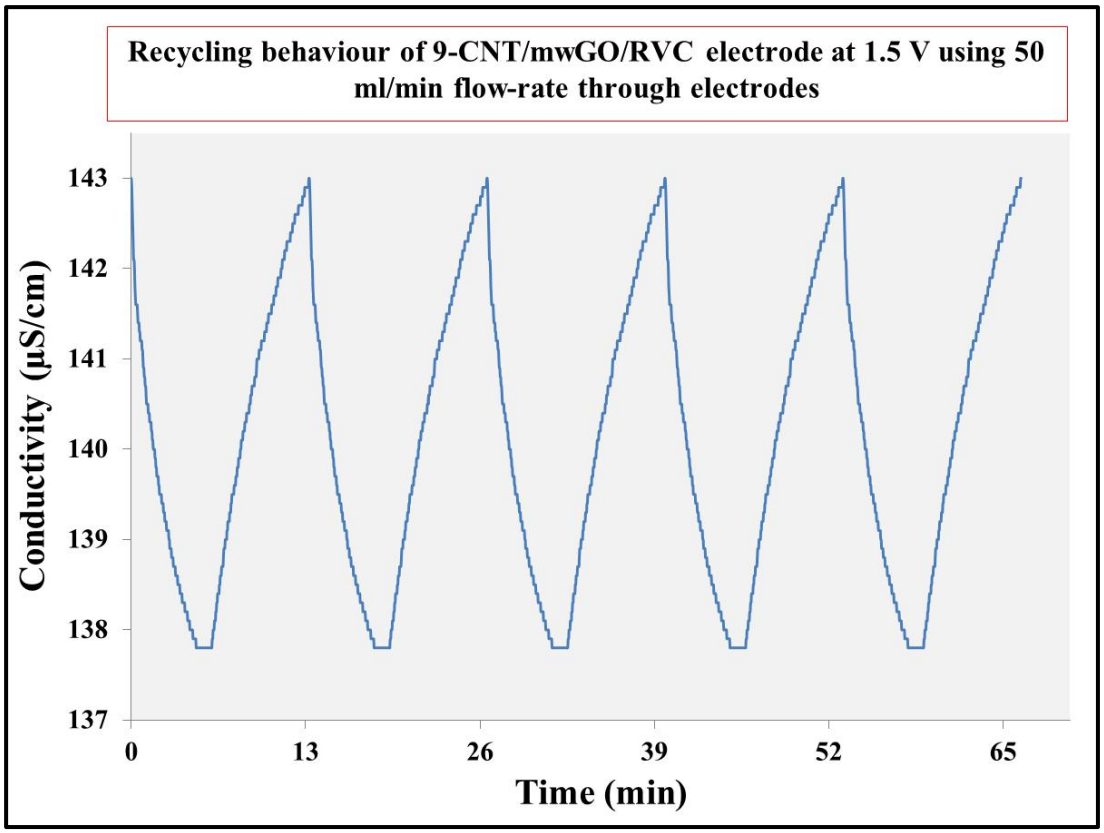

Figure 5.17: Multiple electrosorption–desorption cycles of 75 ppm NaCl solution for 9-CNT/mwGO/RVC electrode upon polarization and depolarization at 1.5 V and 0 V, respectively.

5.3.8.4 Electrosorption isotherm

Electrosorption isotherms can be used to describe how ions interact with carbon electrodes. The Langmuir and Freundlich isotherms are the two most common isotherms and they were employed for the simulation of the ion adsorption on the 9-CNT/mwGO/RVC electrode. The electrosorption isotherms of NaCl onto the 9-CNT/mwGO/RVC electrode were evaluated and compared with those of the CNT/RVC electrode which were discussed in Chapter 4. This experiment was carried out using the same conditions of different initial concentrations of NaCl solutions; 25, 50, 75, 100 , 200, 300, 400 and 500 mg/L, respectively, as shown in Figure 5.18. It is clear that the electrosorption capacity behaviour of 9-

CNT/mwGO/RVC electrode followed the electrosorption capacity behaviour of CNT/RVC electrode. In both electrodes, the removal amount of NaCl increases as the initial concentration is raised. This is due to the enhanced mass transfer rate of ions inside the micropores [324-326]. The electrosorption capacity of 9-CNT/mwGO/RVC and CNT/RVC electrodes were 10.84 and 8.89 mg/g, respectively, at 500 mg/L feed concentration. This indicates that combining mwGO with CNT materials increased the number of sites for adsorption in the 9-CNT/mwGO/RVC electrode under an electric field. Langmuir (Eq. 2.18) and Freundlich (Eq. 2.19) isotherms were used to fit the experimental data for electrosorption of Na^+ and Cl^- onto the electrodes. The Langmuir isotherm is applicable to localization of adsorbed ions with a limited adsorption amount [262] and the Freundlich isotherm is suitable for the description of ion adsorption with a wide variety of adsorption strength [263].

Table 5.5 shows the comparison between Langmuir and Freundlich isotherms for NaCl electrosorption using 9-CNT/mwGO/RVC and CNT/ RVC electrodes. It was found that the electrosorption isotherm in both electrodes obey both the Langmuir isotherm and the Freundlich isotherm models, according to the R^2 values (better than 99.9% confidence level). The regression coefficients for CNT/RVC were 0.997 and 0.989, and for 9-CNT/mwGO/RVC electrode were 0.995 and 0.981 for the Langmuir isotherm and Freundlich isotherm, respectively. This phenomenon suggests that monolayer adsorption was the primary adsorption mechanism during the electrosorption process [209, 332]. The K_L values of both electrodes were 0.01, and K_F values of CNT/RVC and 9-CNT/mwGO/RVC electrodes were 0.28 and 0.32, respectively. Normally, a higher value of n between 1 and 10 represents more

beneficial adsorption [268] and the volume of n for both electodes was around 1.74. Hence, the electrodes with high value of n exhibit a high potential for electrosorption capability. In such a system, the adsorbed layer is extremely thin and the amount adsorbed is only a fraction of the monolayer capacity. Therefore, the electrosorption of both electrodes in CDI follows the monolayer adsorption [208]. Additionally, as a standard procedure, in order to estimate the maximum electrosorption amount of electrodes, the parameter q_m in the Langmuir isotherm model was considered as the maximum adsorption capacity, so the results suggest that the maximum adsorption capacity was improved as the bias concentration rose. The equilibrium electrosorption capacity of this electrode, at a polarization of 1.5 V and a flow-rate of 50 ml/min, was 13.08 and 16.59 mg/g using CNT/RVC and 9-CNT/mwGO/RVC electrodes, respectively. The results suggest that the maximum adsorption capacity for NaCl on the 9-CNT/mwGO/RVC electrode was improved compared with CNT/RVC electrode. The maximum electrosorption capacity at equilibrium, for a concentration of 500 mg/L NaCl, for CNT/RVC electrode is much higher than the electrosorption capacity of multi-walled carbon nanotubes (MWCNTs) [332] and activated carbon (AC) [264]; which were 3.10 mg/g and 9.72 mg/g, respectively. This indicates that the surface area and average pore size in CNT/RVC electrode are larger, where the the surface area in MWCNTs and AC electrodes were 153 and 1153 m^2/g [264, 332], respectively. In addition, The maximum electrosorption capacity of CNT/RVC electrode is very close to the electrosorption capacity of composite carbon nanotubes with carbon nanofibres (CNTs-CNFs) electrode, which was 13.35 mg/g [324]. The maximum electrosorption capacity results of 9-CNT/mwGO/RVC and CNT/RVC electrodes are lower than graphene electrode

which was 21.04 mg/g [208]. This graphene electrode mainly consists of mesopores with an average pore diameter of about 7.42 nm which is greatly beneficial to a capacitive deionization system.

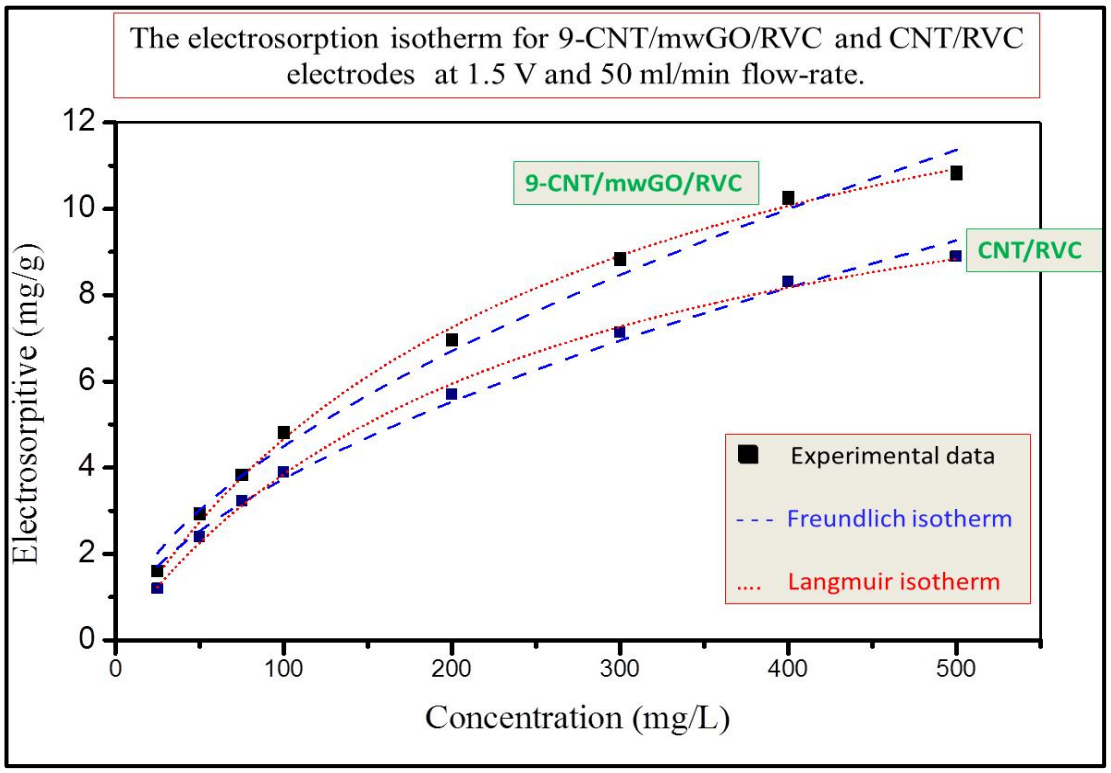

Figure 5.18: The electrosorption isotherms for 9-CNT/mwGO/RVC and CNT/RVC electrodes at 1.5 V and 50 ml/min flow-rate using different initial concentrations of NaCl solutions..

Table 5.5: Determined parameters of regression coefficients R^2, K_L and K_F of Langmuir and Freundlich isotherms for NaCl electrosorption by using the 9-CNT/mwGO/RVC electrode.

Isotherm	**Parameter**	**Value 9-CNT/mwGO/RVC**	**Value* CNT/RVC**
Langmuir	q_m (mg/g)	16.59	13.08
	K_L (L/mg)	0.01	0.01
	R^2	0.995	0.997
Freundlich	K_F (L/mg)	0.32	0.28
	n	1.74	1.74
	R^2	0.981	0.989

* These results were calculated in Chapter 4, Section (4.3.17.).

5.3.8.5 Water production by CDI system

In this chapter, experiments were performed using a 75 mg/L NaCl feed solution. Therefore, water production calculations are here by based on this feed concentration. From the above Section (5.3.8.4.), it can be concluded that, 1 g of 9:CNT/mwGO composite coated on 43.20 cm^3 RVC electrode adsorbed 3.82 mg NaCl during 13 min using an initial concentration of solution of 75 mg/L and the solution concentration after 1 desalination cycle became 71.18 mg/L. Furthermore, 1 g of CNT coated on 43.20 cm^3 RVC electrode adsorbed 3.23 mg NaCl during 18 min using an initial concentration of solution of 75 mg/L and the solution concentration after 1 desalination cycle became 71.77 mg/L. In addition, the amount of salt electrosorbed will change with solution concentration as shown by the relationship between the electrosorption capacity and solution concentration (Figure 5.18). Figure 5.18 also shows that the electrosorption capacity appears to be linearly related to the NaCl concentration below 100 mg/L. This is confirmed by the straight line fit shown in Figure 5.19 (a) which affords Equation (5.3) for the 9:CNT/mwGO/RVC composite electrode and Equation (5.4) for the CNT/RVC composite electrode.

For the 9:CNT/mwGO/RVC composite electrode:

Electrosorption (mg/g) = 0.050 * Concentration **(Eq 5.3)**

For the CNT/RVC composite electrode:

Electrosorption (mg/g) = 0.042 * Concentration **(Eq 5.4)**

From these equations (Eq 5.3. and Eq 5.4.), the concentration change after each desalination cycle will be known and this information can be used to obtain Figure (5.19 (b)). Figure 5.19 (b) shows the concentration change after each desalination cycle to reach less than 1 mg/L using 1 g of CNT/mwGO composite or CNT coated on a 43.20 cm^3 RVC electrode. It is clear that when the CDI system uses the CNT/RVC composite electrode, the total desalination process requires 103 cycles to reduce the concentration of solution from 75 mg/L to less than 1 mg/L. This means that water production, employing this electrode, needs 1854 min (18 min * 85 cycles) to produce 1L of water containing NaCl concentration of less than 1 mg/L. Thus, the desalinated water produced per day is 0.78 L using 1 g of CNT coated on a 43.20 cm^3 RVC electrode, or 17,855 L using $1m^3$ of the same composite electrode. On the other hand, when the CDI system uses the 9-CNT/mwGO/RVC composite electrode, the total desalination process requires 85 cycles to reduce the concentration of solution from 75 mg/L to less than 1 mg/L. This means that water production, employing this electrode, needs 1105 min (13 min * 85 cycles) to produce 1L of desalinated water containing NaCl concentration of less than 1 mg/L. Thus, the water produced per day is 1.30 L using 1 g of 9-CNT/mwGO coated on a 43.20 cm^3 RVC electrode, or 29,958 L using $1m^3$ of the same composite electrode. In conclusion, the full desalination process to produce water of less than 1 mg/L NaCl concentration in the CDI system using the 9-CNT/mwGO/RVC composite electrode produced 67.78% more desalinated water per day compared with the same CDI system using the CNT/RVC composite electrode.

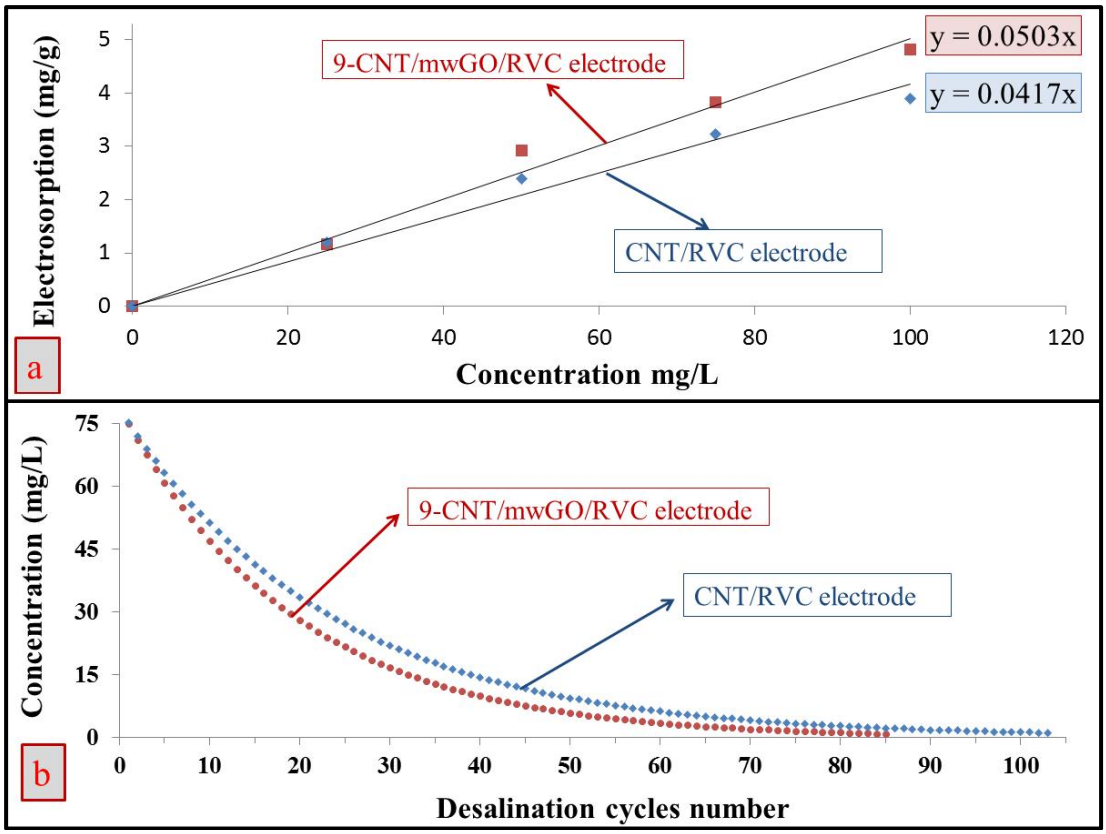

Figure 5.19: (a) Calibration curve of electrosorption vs concentration of NaCl feed solution. (b) Concentration of feed solution vs desalination cycles number for full desalination process to produce water of less than 1 mg/L NaCl concentration.

5.4 Conclusion

In summary, graphene oxide nanosheets were successfully synthesised through a modified Hummer's method and were reduced and exfoliated using microwave irradiation. The ensuing SEM images show significantly altered structure that is highly porous, forming an interconnected network with minimal re-stacking of the graphene. The XRD confirms the exfoliation, by microwave irradiation, of the GO due to the significant suppression of the sharp peak at $2\theta = 10.8°$ and the distance between graphene nanosheets layers in the individual stacks (however the distance between individual stacks is increased, Figure 5.2(a) compared with Figure 5.2 (b)) being decreased to 0.435 nm; while XPS spectra confirm that reduction of the GO is apparent due to the much sharper sp^2 (C=C) at 284.4 eV peak. The D /G band ratio of the Raman spectra decreased from 1.26 to 1.08 signifying that the GO has undergone removal of some of its functional groups. After that, mwGO powder (0.1% w/v) was dispersed in DMF solution by ultrasonic probe, consuming 14 KJ per mg, and the sonication time was optimized by monitoring with Visible spectra. Furthermore, functionalised single-walled carbon nanotubes were dispersed in DMF solution as well. After that the mwGO solution was combined with CNT solution at various ratios to form the CNT/mwGO composite solutions which were used to coat RVC electrodes to fabricate 3D novel electrodes for a CDI system. In these electrodes, the CNT materials were found to be sandwiched between the graphene sheets to build a 3D highly porous architecture that facilitates rapid ion diffusion. These lead to enhanced van der Waals forces and friction. In addition the best electrochemical response in terms of capacitance and kinetic behaviour among all target electrodes was investigated using CVs with a three-electrode system in 1M

NaCl solution. The results lead to a conclusion that the best performing electrode, with a specific capacitance of 179.39 F/g was the composite 9 a-SWCNT: 1 mwGO coated RVC electrode (9-CNT/mwGO/RVC), which represents a 29 % increase in specific capacitance compared with the CNT/RVC electrode. This optimal electrode also had very high cyclic voltammogram (CV) curve stability, maintaining an electrochemical cycling stability of 99% after 200 cycles. Moreover, the time saving of one electrosorption–desorption cycle with the 9-CNT/mwGO/RVC electrode was 27.78 %; compared with the CNT/RVC electrode which required 18 min. In addition, the electrosorption removal of NaCl by the 9-CNT/mwGO/RVC electrode in terms of mass of the electrode (3.82 mg/g) increased 18.27 % compared with that of the CNT/RVC electrode (3.23 mg/g), applied voltage and 50 ml/min flow-rate as the optimum conditions. The full desalination process to produce water of less than 1 mg/L NaCl concentration in the CDI system using the 9-CNT/mwGO/RVC composite electrode increased desalinated water production by 67.78% per day compared with the same CDI system using the CNT/RVC composite electrode. The maximum water produced per day is 29,958 L using $1m^3$ of 9-CNT/mwGO/RVC electrode, and the maximum electrosorption capacity result for the same electrode was 10.84 mg/g at 500 mg/L feed concentration, as compared with a theoretical maximum value of 16.59 mg/g calculated using the Langmuir isotherm model. The results for the 9-CNT/mwGO/RVC composite electrode demonstrate it to be a promising electrode in CDI technology.

6 CONCLUSIONS AND RECOMMENDATION

6.1 Summary and conclusion

The main aim of this thesis, which was to increase potable water production by a capacitive deionization (CDI) system, was achieved via building 3D nanostructured electrodes and improving the design of the flow-through cell. The design of the flow-through cell in a CDI system was modified to accept solution flow directly through the electrodes in a CDI system. This simple change saves the time of one desalination cycle and increases the production around three times. Furthermore, all materials used in the CDI electrodes were based on RVC electrodes as substrata to build novel 3D electrodes because RVC electrodes reduce the resistance of solution flow through the electrode, increase the stability of composite electrode towards high flow-rate pressure, increase the possibility of ions to reach all electrode surfaces in a short time for electrosorption, and shorten the time of ions release from the electrode surface.

PEDOT material on RVC electrode was used for the first time in a CDI system; chosen because of its interesting properties such as high electrical conductivity, surface area, environmental stability, porosity, most stable conducting polymer currently available. PEDOT was used in Chapter 3 and it was successfully deposited by electropolymerization on RVC. The aim of this chapter was achieved as demonstrated by the improved performance of the CDI electrode in terms of unit geometric volume and unit geometric area. The electrosorption capacity in terms of unit geometric volume and unit geometric area of electrodes increase with increase in the amount of PEDOT in the electrode, and the highest electrosorption capacity was 0.37 mg/cm^3 or 0.12 mg/cm^2 or 6.52 mg/g of PEDOT in PEDOT-120min/RVC electrode ((240 mg coated 4.2 cm^3 RVC electrode) at a 75 mg/L NaCl solution

concentration. The electrical voltage of 0.8 V and flow-rate of 80 ml/min were the optimum conditions and key factors which affected the NaCl ions removal performance at the sites of the PEDOT/RVC electrode. This result has better desalting performance than carbon materials and the adsorption/regeneration of PEDOT/RVC electrodes was facile with high efficiency achieved. The water production by $1m^3$ of PEDOT-120min/RVC electrode, from a 75 mg/L NaCl feed solution, was 129,176 L/day of water containing less than 1 mg/L NaCl concentration. In addition, the results in Chapter 3 have shown that the capacitance of PEDOT-120min/RVC electrode compared to a bare RVC electrode had increased by a factor of 2230, and the electrochemical properties were ideal.

The successful use of 3D PEDOT/RVC in a CDI system led to the use of RVC electrodes again in Chapter 4 to build 3D nanoweb functionalized SWCNT (a-SWCNT) electrode structures by filling the RVC pores using a dip coating method. The main aims were to build 3D CNT to decrease CNT bundles (80-100 nm) diameters and to afford a strong structure with void spaces (macropores) formed by neighbouring bundles. These led to an increase in the electrode surface area resulting in an increase in the electrosorption performance in the CDI system. The aims were achieved and SWCNT bundles diameters were between 50 to 80 nm with void spaces. In addition, a unique 3D electrode has been constructed and explored as a novel CDI electrode. The electrical voltage of 1.5 V and flow-rate of 50 ml/min were the optimum conditions, and they were key factors which affected the NaCl ions removal performance at the sites of a-SWCNT. The maximum electrosorption capacity result for the 23.58 %wt a-SWCNT/RVC (50 mg a-SWCNT coated RVC electrode) was 3.23 mg/g of CNT or 0.08 mg/cm^3 for a 75 mg/L NaCl feed

concentration; which had high electrosorption capacity compared with CNT electrode material (2.33 mg/g) in other research. It is worth mentioning that the time required for one adsorption/desorption cycle in the CNT electrode material, which was 100 min in other research, was decreased more than 16 times when the CNT coated RVC electrode was used (6 min). This means that the amount of pure water produced is increased more than 16 times when the CNT coated RVC electrode is used. This Chapter also describes work on an improved flow-through cell for the CDI system achieved by a simple design to accept solution flow through the electrodes and its effect on desalination cycle time was studied. It is clear that for one desalination cycle, 42 minutes was required for the flow-between (FB) electrodes configuration and 18 minutes for the flow-through (FT) electrodes configuration. This encouraged efforts to design a new CDI cell with a flow-through electrode system. The electrosorption capacity of all electrodes in the new cell was increased and the time required for one desalination cycle decreased as well. For example, the electrosorption capacity for 3.63 %wt a-SWCNT was increased from 8.39 mg/g to 10.40 mg/g and the time of one desalination cycle decreased from 30 min to 10 min using flow feed between (FB) electrodes and flow feed through (FT) electrodes, respectively. This means that electrosorption capacity increased 23.96% and the time required for one desalination cycle decreased around three times. In addition, the effect of distance between electrodes was studied using new cell. The ion removal characteristics were affected by various distances between electrodes. As the distance increased, the ion removal amount was not affected in the range of distances from 5mm to 15 mm, but was less when the gap between electrodes was 25 mm. However the adsorption time required increased when the distance was increased in all cases

and the energy output of the CDI system was affected by an increase in the space between electrodes. Furthermore, the electrosorption dynamic and isotherm were studied using new cell. It observed that NaCl adsorption has obeyed pseudo first - order kinetics rather than pseudo second-order kinetics and that NaCl ions were not adsorbed onto the a-SWCNT surface via chemical interaction. It was found that the electrosorption for this electrode obeys both the Langmuir isotherm and the Freundlich isotherm models. This phenomenon suggests that monolayer adsorption was the primary adsorption mechanism during the electrosorption process. The maximum electrosorption capacity result for 23.58 %wt a-SWCNT electrode was 8.89 mg/g at 500 mg/L feed concentration, as compared with a theoretical maximum value of 13.08 mg/g calculated using the Langmuir isotherm model.

The goal of Chapter 5 is to increase the electrosorption capacity of 3D CNT/RVC electrodes from Chapter 4, and reduce the duration of electrosorption–desorption cycles of Chapter 4 by improving the ease of ions adsorption to and ions desorption from the electrode surfaces. This was achieved by preparing composites of microwave irradiated graphene oxide (mwGO) with CNT. The CNT materials were contained sandwiched between the graphene sheets to build a 3D highly porous architecture inside the electrodes and increase the electrodes conductivity as well as afford rapid ions diffusion. All composite materials were coated on RVC by the dip coating method. A maximum of 50 mg loading was used because previous work (Chapter 4) showed that 50 mg was the highest amount of CNT material that can be loaded into the RVC electrode and it afforded the highest capacitance and electrosorption capacity in terms of geometric volume. The results lead to a conclusion that the best performing electrode, with a specific capacitance of 179.39

F/g was the 9-CNT/mwGO/RVC electrode, which represents a 29 % increase in specific capacitance compared with the CNT/RVC electrode. This 9-CNT/mwGO/RVC electrode also had very high CV curve stability, maintaining 99 % current stability after 200 cycles. Moreover, the time saving of one electrosorption–desorption cycle with the 9-CNT/mwGO/RVC electrode was 27.78 %; compared with the CNT/RVC electrode which required 18 min. In addition, the electrosorption removal of NaCl by the 9-CNT/mwGO/RVC electrode in terms of mass of the electrode (3.82 mg/g) increased 18.27 % compared with that of the CNT/RVC electrode (3.23 mg/g), applied voltage and 50 ml/min flow-rate as the optimum conditions. The full desalination process to produce water of less than 1 mg/L NaCl concentration in the CDI system using the 9-CNT/mwGO/RVC composite electrode increased water production per day by 67.78% as compared with the same CDI system using the CNT/RVC composite electrode. The maximum water produced per day is 29,958 L using $1m^3$ of the 9-CNT/mwGO/RVC electrode, and the maximum electrosorption capacity result for the same electrode is 10.84 mg/g at 500 mg/L NaCl feed concentration, as compared with a theoretical maximum value of 16.59 mg/g calculated using the Langmuir isotherm model. The results for the 9-CNT/mwGO/RVC composite electrode demonstrate it to be a promising electrode in CDI technology. Table 6.1 shows comparison of capacity, electrosorption capacity, estimate the maximum electrosorption amount (q_m) and the adsorption rate constant (k_1) of the best performance electrodes developed using geometric size in CDI system in this thesis.

Table 6.1: Comparison of capacity, electrosorption capacity, estimate the maximum electrosorption amount (q_m) and the adsorption rate constant (k_1) of electrodes developed in this thesis.

Chapter	**The best electrode performance using geometric size in CDI system**	**Capacity (F/cm^3)**	**electrosorption capacity (mg/cm^3)**	**electrosorption capacity (mg/cm^3)**	**q_m (mg/g)**	**K_1 (Min^{-1})**
3	PEDOT-120min/RVC	6.18	0.37	0.37	-	-
4	23.5%wt SWCNT/RVC	3.23	0.07	0.07	13.08	0.816
5	9-CNT/mwGO/RVC	4.13	0.10	0.10	16.59	0.525

6.2 Recommendations

At the moment, the need for desalination of brackish water sources is increasing more rapidly than the need for seawater desalination because 70% of the world's available ground water is brackish. The main reason for choosing a capacitive deionization system is that it has an extremely wide potential application field. It was normally used in the scope of research for brackish desalination applications to remove ions from brackish water sources like ground water, secondary municipal, industrial effluent, and river and dam waters. The other potential future applications of a CDI system include boiler feedwater treatment, ultrapure water production, hydrogen fuel cell water treatment, seawater desalination, selective removal of ions dissolved in nuclear waste streams, recovery of trace precious materials for instance gold recovery from water based streams.

The CDI system which was used in this thesis can be enhanced by a modified flow-through cell that decrease the distance between electrodes in the micrometre range (500 to 200 µm) using 3D printing. Electrodes are separated by a spacer (porous membrane) to prevent short circuiting. This could lead to rapid energy transfer through interfaces in the micro-space. Also the time of one electrosorption–desorption cycle can be greatly reduced. This will save the energy consumption and also increase the potable water production.

The 3D PEDOT/RVC and CNT/mwGO /RVC structure electrodes gave amazing results in the CDI system. These electrodes can afford extensive results if these materials, PEDOT, CNT and graphene oxide are made into composites with each other, then used to coat RVC by dip coating method. This composite electrode

can be prepared by three steps. The first step is the intercalation of PEDOT between graphene layers and optimising for the best ratio. The second step is the intercalation of CNT as well, optimising for the best ratio. The last step fabricates this composite material as a 3D electrode using the RVC electrode structure.

6.3 References

1. El-Sadek, A., *Water desalination: An imperative measure for water security in Egypt.* Desalination, 2010. **250**(3): p. 876-884.
2. Karagiannis, I.C. and P.G. Soldatos, *Water desalination cost literature: review and assessment.* Desalination, 2008. **223**(1-3): p. 448-456.
3. El-Dessouky, H., H.I. Shaban and H. Al-Ramadan, *Steady-state analysis of multi-stage flash desalination process.* Desalination, 1995. **103**(3): p. 271-287.
4. Khawaji, A.D., I.K. Kutubkhanah and J.-M. Wie, *Advances in seawater desalination technologies.* Desalination, 2008. **221**(1-3): p. 47-69.
5. Yang, C.-M., W.-H. Choi, B.-K. Na, B.W. Cho and W.I. Cho, *Capacitive deionization of NaCl solution with carbon aerogel-silicagel composite electrodes.* Desalination, 2005. **174**(2): p. 125-133.
6. Anderson, M.A., A.L. Cudero and J. Palma, *Capacitive deionization as an electrochemical means of saving energy and delivering clean water. Comparison to present desalination practices: Will it compete.* Electrochimica Acta, 2010. **55**(12): p. 3845-3856.
7. UNESCO Centre for Membrane Science and Technology. *Water from Electricity: Energy Minimisation*. Emerging trends in desalination: A review. 2008.
8. Wheida, E. and R. Verhoeven, *Desalination as a water supply technique in Libya.* Desalination, 2004. **165**: p. 89-97.
9. Otles, S. and S. Otles, *Desalination Techniques* Environmental, Agricultural and Food Chemistry, 2005. **4**(4): p. 963-969.
10. Semiat, R., *Desalination: Present and Future.* International Water Resources Association, 2000. **25**(1): p. 54-65.
11. Welgemoed, T.J. and C.F. Schutte, *Capacitive Deionization Technology(TM): An alternative desalination solution.* Desalination, 2005. **183**(1-3): p. 327-340.
12. Younos, T. and K.E. Tulou, *Overview of Desalination Techniques.* CONTEMPORARY WATER RESEARCH & EDUCATION, 2005. **2**(132): p. 3-10.
13. Cheremisinoff, N.P., *Membrane Separation Technologies*, in *Handbook of Water and Wastewater Treatment Technologies*2002, Butterworth-Heinemann: Woburn. p. 335-371.
14. Arnal, J.M., B. Garcia-Fayos, G. Verdu and J. Lora, *Ultrafiltration as an alternative membrane technology to obtain safe drinking water from surface water: 10 years of experience on the scope of the AQUAPOT project.* Desalination, 2009. **248**(1-3): p. 34-41.
15. Hafez, A., M. Khedr and H. Gadallah, *Wastewater treatment and water reuse of food processing industries. Part II: Techno-economic study of a membrane separation technique.* Desalination, 2007. **214**(1-3): p. 261-272.
16. Jacob, C., *Seawater desalination: Boron removal by ion exchange technology.* Desalination, 2007. **205**(1-3): p. 47-52.
17. Kahdim, A.S., S. Ismail and A.A. Jassim, *Modeling of reverse osmosis systems.* Desalination, 2003. **158**(1-3): p. 323-329.

18. Hays, J., *Iowa's first electrodialysis reversal water treatment plant.* Desalination, 2000. **132**(1-3): p. 161-165.
19. Ortiz, J.M., J.A. Sotoca, E. Expósito, F. Gallud, V. García-García, V. Montiel and A. Aldaz, *Brackish water desalination by electrodialysis: batch recirculation operation modeling.* Journal of Membrane Science, 2005. **252**(1-2): p. 65-75.
20. Le-Clech, P., V. Chen and T.A.G. Fane, *Fouling in membrane bioreactors used in wastewater treatment.* Journal of Membrane Science, 2006. **284**(1-2): p. 17-53.
21. Rengaraj, S., K.H. Yeon and S.H. Moon, *Removal of chromium from water and wastewater by ion exchange resins.* Journal of Hazardous Materials, 2001. **87**(1-3): p. 273-287.
22. Aybar, H.S., F. Egelioglu and U. Atikol, *An experimental study on an inclined solar water distillation system.* Desalination, 2005. **180**(1-3): p. 285-289.
23. Mazzotti, M., M. Rosso, A. Beltramini and M. Morbidelli, *Dynamic modeling of multistage flash desalination plants.* Desalination, 2000. **127**(3): p. 207-218.
24. Abdel-Jabbar, N.M., H.M. Qiblawey, F.S. Mjalli and H. Ettouney, *Simulation of large capacity MSF brine circulation plants.* Desalination, 2007. **204**(1-3): p. 501-514.
25. Aly, S.E., *A study of a new thermal vapor compression/multi-effect stack (TVC/MES) low temperature distillation system.* Desalination, 1995. **103**(3): p. 257-263.
26. Industrynews, *American Water goes Dutch on desalination technology project.* Filtration & Separation, 2009. **46**(6): p. 4-4.
27. Wang, J., S. Wang and M. Jin, *A study of the electrodeionization process high-purity water production with a RO/EDI system.* Desalination, 2000. **132**(1-3): p. 349-352.
28. Wood, J., J. Gifford, J. Arba and M. Shaw, *Production of ultrapure water by continuous electrodeionization.* Desalination, 2010. **250**(3): p. 973-976.
29. El-Bourawi, M.S., Z. Ding, R. Ma and M. Khayet, *A framework for better understanding membrane distillation separation process.* Journal of Membrane Science, 2006. **285**(1-2): p. 4-29.
30. Zhang, J., N. Dow, M. Duke, E. Ostarcevic, J.-D. Li and S. Gray, *Identification of material and physical features of membrane distillation membranes for high performance desalination.* Journal of Membrane Science, 2010. **349**(1-2): p. 295-303.
31. Beier, N., D. Sego, R. Donahue and K. Biggar, *Laboratory investigation on freeze separation of saline mine waste water.* Cold Regions Science and Technology, 2007. **48**(3): p. 239-247.
32. Garg, S., P. Sharma, S.G. Jayaprakashan and R. Subramanian, *Spray evaporation of liquid foods.* LWT - Food Science and Technology, 2009. **42**(1): p. 119-124.
33. Pan, L., X. Wang, Y. Gao, Y. Zhang, Y. Chen and Z. Sun, *Electrosorption of anions with carbon nanotube and nanofibre composite film electrodes.* Desalination, 2009. **244**(1-3): p. 139-143.

34. Xu, P., J. Drewes, D. Heil and G. Wang, *Treatment of brackish produced water using carbon aerogel-based capacitive deionization technology.* Water Research, 2008. **42**(10-11): p. 2605-2617.
35. Ahn, H.-J., J.-H. Lee, Y. Jeong, J.-H. Lee, C.-S. Chi and H.-J. Oh, *Nanostructured carbon cloth electrode for desalination from aqueous solutions.* Materials Science and Engineering: A, 2007. **449-451**: p. 841-845.
36. Oh, H.-J., J.-H. Lee, H.-J. Ahn, Y. Jeong, Y.-J. Kim and C.-S. Chi, *Nanoporous activated carbon cloth for capacitive deionization of aqueous solution.* Thin Solid Films, 2006. **515**(1): p. 220-225.
37. Park, K.-K., J. Lee, P. Park, S. Yoon, J. Moon, H. Eum and C. Lee, *Development of a carbon sheet electrode for electrosorption desalination.* Desalination, 2007. **206**(1-3): p. 86-91.
38. Ryoo, M., J. Kim and G. Seo, *Role of titania incorporated on activated carbon cloth for capacitive deionization of NaCl solution.* Journal of Colloid and Interface Science, 2003. **264**(2): p. 414-419.
39. Ryoo, M. and G. Seo, *Improvement in capacitive deionization function of activated carbon cloth by titania modification.* Water Research, 2003. **37**(7): p. 1527-1534.
40. Sfeir, M., T. Beetz, F. Wang, L. Huang, H. Huang, M. Huang, J. Hone, S. Obrien, J. Misewich, T. Heinz, L. Wu, Y. Zhu and L. Brus, *Optical Spectroscopy of Individual Single-Walled Carbon Nanotubes of Defined Chiral Structure.* Science, 2006. **312**(5773): p. 554-556.
41. Oren, Y., *Capacitive deionization (CDI) for desalination and water treatment past, present and future (a review).* Desalination, 2008. **228**(1-3): p. 10-29.
42. Porada, S., R. Zhao, A. van der Wal, V. Presser and P.M. Biesheuvel, *Review on the science and technology of water desalination by capacitive deionization.* Progress in Materials Science, 2013. **58**(8): p. 1388-1442.
43. Lee, J.-B., K.-K. Park, H.-M. Eum and C.-W. Lee, *Desalination of a thermal power plant wastewater by membrane capacitive deionization.* Desalination, 2006. **196**(1-3): p. 125-134.
44. Kim, Y., J. Hur, W. Bae and J. Choi, *Desalination of brackish water containing oil compound by capacitive deionization process.* Desalination, 2010. **253**(1-3): p. 119-123.
45. Dai, K., L. Shi, J. Fang, D. Zhang and B. Yu, *NaCl adsorption in multi-walled carbon nanotubes.* Materials Letters, 2005. **59**(16): p. 1989-1992.
46. Biesheuvel, P.M., *Thermodynamic cycle analysis for capacitive deionization.* Journal of Colloid and Interface Science, 2009. **332**(1): p. 258-264.
47. Biesheuvel, P.M. and A. van der Wal, *Membrane capacitive deionization.* Journal of Membrane Science, 2010. **346**(2): p. 256-262.
48. Choi, J.-H., *Fabrication of a carbon electrode using activated carbon powder and application to the capacitive deionization process.* Separation and Purification Technology, 2010. **70**(3): p. 362-366.
49. Dermentzis, K. and K. Ouzounis, *Continuous capacitive deionization-electrodialysis reversal through electrostatic shielding for desalination and deionization of water.* Electrochimica Acta, 2008. **53**(24): p. 7123-7130.

50. Jung, H., S. Hwang, S. Hyun, K. Lee and G.-. Kim, *Capacitive deionization characteristics of nanostructured carbon aerogel electrodes synthesized via ambient drying.* Desalination, 2007. **216**(1-3): p. 377-385.
51. Seo, S., H. Jeon, J.K. Lee, G.-Y. Kim, D. Park, H. Nojima, J. Lee and S.-H. Moon, *Investigation on removal of hardness ions by capacitive deionization (CDI) for water softening applications.* Water Research, 2010. **44**(7): p. 2267-2275.
52. Pekala, R.W., J.C. Farmer, C.T. Alviso, T.D. Tran, S.T. Mayer, J.M. Miller and B. Dunn, *Carbon aerogels for electrochemical applications.* Journal of Non-Crystalline Solids, 1998. **225**(1): p. 74-80.
53. Demirer, O.N., R.M. Naylor, C.A. Rios Perez, E. Wilkes and C. Hidrovo, *Energetic performance optimization of a capacitive deionization system operating with transient cycles and brackish water.* Desalination, 2013. **314**(3): p. 130-138.
54. Kim, B.C., J.M. Ko and G.G. Wallace, *A novel capacitor material based on Nafion-doped polypyrrole.* Journal of Power Sources, 2008. **177**(2): p. 665-668.
55. Zhang, Y., H. Feng, X. Wu, L. Wang, A. Zhang, T. Xia, H. Dong, X. Li and L. Zhang, *Progress of electrochemical capacitor electrode materials: A review.* International Journal of Hydrogen Energy, 2009. **34**(11): p. 4889-4899.
56. Conway, B.E., E. Ayranci and H. Al-Maznai, *Use of quasi-3-dimensional porous electrodes for adsorption and electrocatalytic removal of impurities from waste-waters.* Electrochimica Acta, 2001. **47**(5): p. 705-718.
57. Gabelich, C.J., T.D. Tran and I.H. Suffet, *Electrosorption of inorganic salts from aqueous solution using carbon aerogels.* Environmental Science & Technology, 2002. **36**(13): p. 3010-3019.
58. Wang, X.Z., M.G. Li, Y.W. Chen, R.M. Cheng, S.M. Huang, L.K. Pan and Z. Sun, *Electrosorption of ions from aqueous solutions with carbon nanotubes and nanofibers composite film electrodes - art. no. 053127.* Applied Physics Letters, 2006. **89**(5): p. 53127-53127.
59. Yurum, Y., A. Taralp and T.N. Veziroglu, *Storage of hydrogen in nanostructured carbon materials.* International Journal of Hydrogen Energy, 2009. **34**(9): p. 3784-3798.
60. Czerwinski, A. and M. Zelazowska, *Electrochemical behavior of lead dioxide deposited on reticulated vitreous carbon (RVC).* Journal of Power Sources. **64**(1-2): p. 29-34.
61. Pec, M.K., R. Reyes, E. Sa¡nchez, D. Carballar, A. Delgado, J. Santamar, M. Arruebo and C. Evora, *Reticulated vitreous carbon: a useful material for cell adhesion and tissue invasion.* European cells & materials, 2010. **20**(4): p. 282-294.
62. Friedrich, J.M., C. Ponce-de-León, G.W. Reade and F.C. Walsh, *Reticulated vitreous carbon as an electrode material.* Journal of Electroanalytical Chemistry, 2004. **561**: p. 203-217.
63. Friedrich, J.M., *Reticulated vitreous carbon as an electrode material.* Journal of Electroanalytical Chemistry and Interfacial Electrochemistry, 2004. **561**(1): p. 203-217.

64. Shui, X. and D.D.L. Chung, *High-strength high-surface-area porous carbon made from submicron-diameter carbon filaments.* Carbon, 1996. **34**(6): p. 811-814.
65. Ukaszewski, M., A. Zurowski and A. Czerwi„ski, *Hydrogen in thin Pd-based layers deposited on reticulated vitreous carbon-A new system for electrochemical capacitors.* Journal of Power Sources, 2008. **185**(2): p. 1598-1604.
66. Tangirala, R., C.T.J. Low, Ponce-De-Lean, S. Campbell and F. Walsh, *Copper deposition at segmented, reticulated vitreous carbon cathode in Hull cell.* Transactions of the Institute of Metal Finishing, 2010. **88**(2): p. 84-92.
67. Saleh, M.M., C. Weidlich, K.M. Mangold and K. Jattner, *Absorption/desorption of calcium ions on polypyrrole-loaded reticulated vitreous carbon.* Journal of Applied Electrochemistry, 2006. **36**(2): p. 179-186.
68. Yuan, Y. and S. Kim, *Polypyrrole-coated reticulated vitreous carbon as anode in microbial fuel cell for higher energy output.* Bulletin of the Korean Chemical Society, 2008. **29**(1): p. 168-172.
69. Dalmolin, C., S.R. Biaggio, R.C. Rocha-Filho and N. Bocchi, *Reticulated vitreous carbon/polypyrrole composites as electrodes for lithium batteries: Preparation, electrochemical characterization and charge-discharge performance.* Synthetic Metals, 2010. **160**(2): p. 173-179.
70. Dalmolin, C., S.R. Biaggio, R.C. Rocha-Filho and N. Bocchi, *Preparation, electrochemical characterization and charge-discharge of reticulated vitreous carbon/polyaniline composite electrodes.* Electrochimica Acta, 2009. **55**(1): p. 227-233.
71. Frydrychewicz, A., S.Y. Vassiliev, G.A. Tsirlina and K. Jackowska, *Reticulated vitreous carbon-polyaniline-palladium composite electrodes.* Electrochimica Acta, 2005. **50**(9): p. 1885-1893.
72. Rogulski, Z., W. Lewdorowicz, W. Tokarz and A. Czerwiski, *Applications of Reticulated Vitreous Carbon (RVC) in the electrochemical power sources.* Polish Journal of Chemistry, 2004. **78**(9): p. 1357-1370.
73. Kaplan, R.B., *Open cell tantalum structures for cancellous bone implants and cell and tissue receptors*, in *US Patent 52828611*994.
74. Jenkins, G.M. and C.J. Grigson, *The fabrication of artifacts out of glassy carbon and carbon-fiber-reinforced carbon for biomedical applications.* Journal of Biomedical Materials Research, 1979. **13**(3): p. 371-394.
75. Schmitt Jr, J.L. and P.L. Walker Jr, *Carbon molecular sieve supports for metal catalysts-II. Selective hydrogenation of hydrocarbons over platinum supported on polyfurfuryl alcohol carbon.* Carbon, 1972. **10**(1): p. 87-92.
76. Lestrade, C., P.Y. Guyomar and M. Astruc, *Electrochemical removal of dilute heavy metals with carbon felt porous electrodes.* Environmental Technology Letters, 1981. **2**(9): p. 409-418.
77. Tan, W.X., M.A. Hasnat, N.H.M. Ramalan, W.M. Soh and N. Mohamed, *Influence of flow rates on the electrogenerative Co 2+ recovery at a reticulated vitreous carbon cathode.* Chemical Engineering Journal, 2012. **189-190**(1): p. 182-187.

78. Czerwiski, A., Z. Rogulski, S. Obrecbowski, H. Siwek, I. Paleska, M. Chotkowski and M. A Vicaszewski, *RVC as new carbon material for batteries.* Journal of Applied Electrochemistry, 2009. **39**(5): p. 559-567.
79. Czerwiski, A., S. Obrecbowski and Z. Rogulski, *New high-energy lead-acid battery with reticulated vitreous carbon as a carrier and current collector.* Journal of Power Sources, 2012. **198**: p. 378-382.
80. El-Deab, M.S. and M.M. Saleh, *Electrocatalytic production of hydrogen on reticulated vitreous carbon.* International Journal of Hydrogen Energy, 2003. **28**(11): p. 1199-1206.
81. Chakhovskoi, A.G., C.E. Hunt, G. Forsberg, T. Nilsson and P. Persson, *Reticulated vitreous carbon field emission cathodes for light source applications.* Journal of Vacuum Science and Technology B: Microelectronics and Nanometer Structures, 2003. **21**(1): p. 571-575.
82. Coffey, B., P.V. Madsen, T.O. Poehler and P.C. Searson, *High Charge Density Conducting Polymer/Graphite Fiber Composite Electrodes for Battery Applications.* Journal of The Electrochemical Society, 1995. **142**(2): p. 321-325.
83. Dalmolin, C., S.C. Canobre, S.R. Biaggio, R.C. Rocha-Filho and N. Bocchi, *Electropolymerization of polyaniline on high surface area carbon substrates.* Journal of Electroanalytical Chemistry, 2005. **578**(1): p. 9-15.
84. Iroh, J.O. and G.A. Wood, *Physical and chemical properties of polypyrrole–carbon fiber interphases formed by aqueous electrosynthesis.* Journal of Applied Polymer Science, 1996. **62**(10): p. 1761-1769.
85. CzerwiÅ„ski, A., M. Dmochowska, M. GrdeÅ„, M. Kopczyk, G. WÃ³jcik, G. MÅ‚ynarek, J. KoÅ‚ata and J.M. SkowroÅ„ski, *Electrochemical behavior of nickel deposited on reticulated vitreous carbon.* Journal of Power Sources, 1999. **77**(1): p. 28-33.
86. frysz, C.A., X. Shui and D.D.L. Chung, *Electrochemical behavior of porous carbons.* Carbon, 1997. **35**(7): p. 893-916.
87. Jenkins and Wamura, *Polymeric carbons, carbon fibre, glass and char.* Cambridge University Press, 1976: p. 178.
88. Chiang, C.K., C.R. Fincher, Jr., Y.W. Park, A.J. Heeger, H. Shirakawa, E.J. Louis, S.C. Gau and A.G. MacDiarmid, *Electrical conductivity in doped polyacetylene.* Physical Review Letters, 1977. **39**(17): p. 1098-1101.
89. Shirakawa, H., E.J. Louis, A.G. MacDiarmid, C.K. Chiang and A.J. Heeger, *Synthesis of electrically conducting organic polymers: halogen derivatives of polyacetylene, (CH)x.* Journal of the Chemical Society, Chemical Communications, 1977(16): p. 578-580.
90. Wallace, G.G., G.M. Spinks and P.R. Teasdale, *Conductive electroactive polymers : intelligent materials systems*2002, Boca Raton, FL: CRC Press.
91. MacDiarmid, A.G., *"Synthetic metals": A novel role for organic polymers (Nobel Lecture).* Angewandte Chemie International Edition, 2001. **40**(14): p. 2581-2590.
92. Shirakawa, H., *The discovery of polyacetylene film: The dawning of an era of conducting polymers (Nobel Lecture).* Angewandte Chemie International Edition, 2001. **40**(14): p. 2574-2580.

93. Shirakawa, H., E.J. Louis and A.G. Macdiarmid, *Synthesis of Electrically Conducting Organic Polymers: Halogen Derivatives of Polyacetylene, (CH)x*1977: J.C.S. CHEM. COMM. 578-580.
94. Guimard, N.K., N. Gomez and C.E. Schmidt, *Conducting polymers in biomedical engineering.* Progress in Polymer Science, 2007. **32**(8-9): p. 876-921.
95. Skotheim, T., R.L. Elsenbaumer and J.R. Reynolds, *Handbook of conducting polymers*1998, New York: Marcel Dekker.
96. Bhadra, S., D. Khastgir, N.K. Singha and J.H. Lee, *Progress in preparation, processing and applications of polyaniline.* Progress in Polymer Science (Oxford), 2009. **34**(8): p. 783-810.
97. Gerard, M., A. Chaubey and B.D. Malhotra, *Application of conducting polymers to biosensors.* Biosensors and Bioelectronics, 2002. **17**(5): p. 345-359.
98. De Barros, R.A., C.R. Martins and W.M. de Azevedo, *Writing with conducting polymer.* Synthetic Metals, 2005. **155**(1): p. 35-38.
99. Adhikari, B. and S. Majumdar, *Polymers in sensor applications.* Progress in Polymer Science, 2004. **29**(7): p. 699-766.
100. Wallace, G.G., G.M. Spinks and P.R.Teasdale, *Conductive electroactive polymers : intelligent materials systems*2002, Boca Raton, FL: CRC Press.
101. Kirchmeyer, S. and K. Reuter, *Scientific importance, properties and growing applications of poly(3,4-ethylenedioxythiophene).* Journal of Materials Chemistry, 2005. **15**(21): p. 2077-2088.
102. Chou, C., C. Chou, Y. Kuo and C. Wang, *Preparation of a working electrode with a conducting PEDOT:PSS film and its applications in a dye-sensitized solar cell.* Advanced Powder Technology, 2013. **24**(1): p. 336-343.
103. Song, I.-S., S.-W. Heo, J.-y. Lee and D.-K. Moon, *Study on the ClO4 doped PEDOT-PEG in organic solvent using a hole injection layer for PLEDs.* Journal of Industrial and Engineering Chemistry, 2011. **17**(4): p. 651-656.
104. Mousavi, Z., T. Alaviuhkola, J. Bobacka, R.-M. Latonen, J. Pursiainen and A. Ivaska, *Electrochemical characterization of poly(3,4-ethylenedioxythiophene) (PEDOT) doped with sulfonated thiophenes.* Electrochimica Acta, 2008. **53**(11): p. 3755-3762.
105. Patra, S., K. Barai and N. Munichandraiah, *Scanning electron microscopy studies of PEDOT prepared by various electrochemical routes.* Synthetic Metals, 2008. **158**(10): p. 430-435.
106. Dietrich, M., J. Heinze, G. Heywang and F. Jonas, *Electrochemical and spectroscopic characterization of polyalkylenedioxythiophenes.* Journal of Electroanalytical Chemistry, 1994. **369**(1-2): p. 87-92.
107. Heywang, G. and F. Jonas, *Poly(alkylenedioxythiophene)s—new, very stable conducting polymers.* Advanced Materials, 1992. **4**(2): p. 116-118.
108. Lang, U. and J. Dual, *Mechanical properties of the intrinsically conductive polymer poly(3,4-ethylenedioxythiophene) poly(styrenesulfonate) (PEDOT/PSS).* Key Engineering Materials, 2007. **345-346**: p. 1189-1192.
109. Yue, R. and J. Xu, *Poly(3,4-ethylenedioxythiophene) as promising organic thermoelectric materials: A mini-review.* Synthetic Metals, 2012. **162**(11–12): p. 912-917.

110. Groenendaal, L., F. Jonas, D. Freitag, H. Pielartzik and J.R. Reynolds, *Poly(3,4-ethylenedioxythiophene) and Its Derivatives: Past, Present, and Future.* Advanced Materials, 2000. **12**(7): p. 481-494.
111. Collazos-Castro, J.E., J.L. Polo, G.R. Hernández-Labrado, V. Padial-Cañete and C. García-Rama, *Bioelectrochemical control of neural cell development on conducting polymers.* Biomaterials, 2010. **31**(35): p. 9244-9255.
112. Ryu, K.S., Y.-G. Lee, Y.-S. Hong, Y.J. Park, X. Wu, K.M. Kim, M.G. Kang, N.-G. Park and S.H. Chang, *Poly(ethylenedioxythiophene) (PEDOT) as polymer electrode in redox supercapacitor.* Electrochimica Acta, 2004. **50**(2–3): p. 843-847.
113. King, Z.A., C.M. Shaw, S.A. Spanninga and D.C. Martin, *Structural, chemical and electrochemical characterization of poly(3,4-Ethylenedioxythiophene) (PEDOT) prepared with various counter-ions and heat treatments.* Polymer, 2011. **52**(5): p. 1302-1308.
114. Zhan, L., Z. Song, J. Zhang, J. Tang, H. Zhan, Y. Zhou and C. Zhan, *PEDOT: Cathode active material with high specific capacity in novel electrolyte system.* Electrochimica Acta, 2008. **53**(28): p. 8319-8323.
115. Novak, P., K. Muller, K.S.V. Santhanam and O. Haas, *Electrochemically active polymers for rechargeable batteries.* Chemical Reviews, 1997. **97**(1): p. 207-281.
116. Xu, Y., J. Wang, W. Sun and S. Wang, *Capacitance properties of poly(3,4-ethylenedioxythiophene)/polypyrrole composites.* Journal of Power Sources, 2006. **159**(1): p. 370-373.
117. Howden, R.M., E.J. Flores, V. Bulović and K.K. Gleason, *The application of oxidative chemical vapor deposited (oCVD) PEDOT to textured and non-planar photovoltaic device geometries for enhanced light trapping.* Organic Electronics, 2013. **14**(9): p. 2257-2268.
118. Duraisamy, N., S. Hong and K. Choi, *Deposition and characterization of silver nanowires embedded PEDOT:PSS thin films via electrohydrodynamic atomization.* Chemical Engineering Journal, 2013. **225**: p. 887-894.
119. Chu, C.-Y., J.-T. Tsai and C.-L. Sun, *Synthesis of PEDOT-modified graphene composite materials as flexible electrodes for energy storage and conversion applications.* International Journal of Hydrogen Energy, 2012. **37**(18): p. 13880-13886.
120. Yan, J., C. Sun, F. Tan, X. Hu, P. Chen, S. Qu, S. Zhou and J. Xu, *Electropolymerized poly(3,4-ethylenedioxythiophene):poly(styrene sulfonate) (PEDOT:PSS) film on ITO glass and its application in photovoltaic device.* Solar Energy Materials and Solar Cells, 2010. **94**(2): p. 390-394.
121. Selvakumar, M. and D. Krishna Bhat, *Activated carbon-polyethylenedioxythiophene composite electrodes for symmetrical supercapacitors.* Journal of Applied Polymer Science, 2008. **107**(4): p. 2165-2170.
122. Mastragostino, M., R. Paraventi and A. Zanelli, *Supercapacitors Based on Composite Polymer Electrodes.* Journal of The Electrochemical Society, 2000. **147**(9): p. 3167-3170.
123. Ryu, K.S., Y.G. Lee, Y.S. Hong, Y.J. Park, X. Wu, K.M. Kim, M.G. Kang, N.G. Park and S.H. Chang, *Poly(ethylenedioxythiophene) (PEDOT) as*

polymer electrode in redox supercapacitor. Electrochimica Acta, 2004. **50**(2-3 SPEC. ISS.): p. 843-847.
124. Laforgue, A., *All-textile flexible supercapacitors using electrospun poly(3,4-ethylenedioxythiophene) nanofibers.* Journal of Power Sources, 2011. **196**(1): p. 559-564.
125. Lei, C., P. Wilson and C. Lekakou, *Effect of poly(3,4-ethylenedioxythiophene) (PEDOT) in carbon-based composite electrodes for electrochemical supercapacitors.* Journal of Power Sources, 2011. **196**(18): p. 7823-7827.
126. Kelly, T.L., K. Yano and M.O. Wolf, *Supercapacitive Properties of PEDOT and Carbon Colloidal Microspheres.* ACS Applied Materials & Interfaces, 2009. **1**(11): p. 2536-2543.
127. Babakhani, B. and D.G. Ivey, *Improved capacitive behavior of electrochemically synthesized Mn oxide/PEDOT electrodes utilized as electrochemical capacitors.* Electrochimica Acta, 2010. **55**(12): p. 4014-4024.
128. Paik, S.J., Y. Park and D.I.D. Cho, *Roughened polysilicon for low impedance microelectrodes in neural probes.* Journal of Micromechanics and Microengineering, 2003. **13**(3): p. 373-379.
129. Kim, K.-S. and S.-J. Park, *Influence of dispersion of multi-walled carbon nanotubes on the electrochemical performance of PEDOT–PSS films.* Materials Science and Engineering: B, 2011. **176**(3): p. 204-209.
130. Yamato, H., K.I. Kai, M. Ohwa, T. Asakura, T. Koshiba and W. Wernet, *Synthesis of free-standing poly(3,4-ethylenedioxythiophene) conducting polymer films on a pilot scale.* Synthetic Metals, 1996. **83**(2): p. 125-130.
131. Ghilane, J., P. Martin, M. Janin, H. Randriamahazaka, P. Hapiot and J.-C. Lacroix, *Electrochemical investigation of thin PEDOT film above an insulating substrate using scanning electrochemical microscopy.* Electrochemistry Communications, 2009. **11**(12): p. 2304-2307.
132. Iijima, S., *Helical microtubules of graphitic carbon.* Nature, 1991. **354**(6348): p. 56-58.
133. Bethune, D.S., C.H. Klang, M.S. de Vries, G. Gorman, R. Savoy, J. Vazquez and R. Beyers, *Cobalt-catalysed growth of carbon nanotubes with single-atomic-layer walls.* Nature, 1993. **363**(6430): p. 605-607.
134. Iijima, S. and T. Ichihashi, *Single-shell carbon nanotubes of 1-nm diameter.* Nature, 1993. **363**(6430): p. 603-605.
135. Dyke, C.A. and J.M. Tour, *Covalent functionalization of single-walled carbon nanotubes for materials applications.* The Journal of Physical Chemistry A, 2004. **108**(51): p. 11151-11159.
136. Meyyappan, M., *Carbon nanotubes: science and applications*2005, Boca Raton, FL: CRC Press.
137. Dresselhaus, M.S., G. Dresselhaus and P.C. Eklund, *Science of fullerenes and carbon nanotubes*1996, San Diego: Academic Press.
138. Dillon, A.C., M. Yudasaka and M.S. Dresselhaus, *Employing Raman Spectroscopy to Qualitatively Evaluate the Purity of Carbon Single-Wall Nanotube Materials.* Journal of Nanoscience and Nanotechnology, 2004. **4**(7): p. 691-703.

139. Kang, I., Y.Y. Heung, J.H. Kim, J.W. Lee, R. Gollapudi, S. Subramaniam, S. Narasimhadevara, D. Hurd, G.R. Kirikera, V. Shanov, M.J. Schulz, D. Shi, J. Boerio, S. Mall and M. Ruggles-Wren, *Introduction to carbon nanotube and nanofiber smart materials.* Composites Part B: Engineering, 2006. **37**(6): p. 382-394.
140. Baughman, R.H., A.A. Zakhidov and W.A. de Heer, *Carbon Nanotubes--the Route Toward Applications.* Science, 2002. **297**(5582): p. 787-792.
141. Avouris, P., *Carbon nanotube electronics.* Chemical Physics, 2002. **281**(2-3): p. 429-445.
142. Hong, S. and S. Myung, *Nanotube electronics: A flexible approach to mobility.* Nature Nanotechnology, 2007. **2**(2): p. 207-208.
143. Reilly, R.M., *Carbon nanotubes: Potential benefits and risks of nanotechnology in nuclear medicine.* Journal of Nuclear Medicine, 2007. **48**(7): p. 1039-1042.
144. Thostenson, E.T., Z. Ren and T.-W. Chou, *Advances in the science and technology of carbon nanotubes and their composites: a review.* Composites Science and Technology, 2001. **61**(13): p. 1899-1912.
145. Li, F., H.M. Cheng, S. Bai, G. Su and M.S. Dresselhaus, *Tensile strength of single-walled carbon nanotubes directly measured from their macroscopic ropes.* Applied Physics Letters, 2000. **77**(20): p. 3161-3163.
146. Dervishi, E., L. Zhongrui, X. Yang, V. Saini, A.R. Biris, D. Lupu and A.S. Biris, *Carbon nanotubes: Synthesis, properties, and applications.* Particulate Science & Technology, 2009. **27**(2): p. 107-125.
147. Baddour, C. and C. Briens, *Carbon nanotube synthesis: A review.* International Journal of Chemical Reactor Engineering, 2005. **3**(1): p. 1-20.
148. Wang, X., X.Y. Wang and J. Xiao, *A non-linear analysis of the bending modulus of carbon nanotubes with rippling deformations.* Composite Structures, 2005. **69**(3): p. 315-321.
149. Saito, R., G. Dresselhaus and M.S. Dresselhaus, *Trigonal warping effect of carbon nanotubes.* Physical Review B, 2000. **61**(4): p. 2981-2990.
150. Balandin, A.A., *Thermal properties of graphene and nanostructured carbon materials.* Nature Materials, 2011. **10**(8): p. 569-581.
151. Kwon, Y.-K. and P. Kim, *Unusually High Thermal Conductivity in Carbon Nanotubes*, in *High Thermal Conductivity Materials*, S. Shindé and J. Goela, Editors. 2006, Springer New York. p. 227-265.
152. Kim, P., L. Shi, A. Majumdar and P.L. McEuen, *Thermal transport measurements of individual multiwalled nanotubes.* Physical Review Letters, 2001. **87**(21): p. 215502.
153. Yu, C., L. Shi, Z. Yao, D. Li and A. Majumdar, *Thermal conductance and thermopower of an individual single-wall carbon nanotube.* Nano Letters, 2005. **5**(9): p. 1842-1846.
154. Han, Z. and A. Fina, *Thermal conductivity of carbon nanotubes and their polymer nanocomposites: A review.* Progress in Polymer Science. **36**(7): p. 914-944.
155. Durkop, T., S.A. Getty, E. Cobas and M.S. Fuhrer, *Extraordinary mobility in semiconducting carbon nanotubes.* Nano Letters, 2003. **4**(1): p. 35-39.

156. Yao, Z., C.L. Kane and C. Dekker, *High-field electrical transport in single-wall carbon nanotubes.* Physical Review Letters, 2000. **84**(13): p. 2941-2944.
157. Fan, J., M. Wan, D. Zhu, B. Chang, Z. Pan and S. Xie, *Synthesis and properties of carbon nanotube-polypyrrole composites.* Synthetic Metals, 1999. **102**(1-3): p. 1266-1267.
158. Dai, H., J.H. Hafner, A.G. Rinzler, D.T. Colbert and R.E. Smalley, *Nanotubes as nanoprobes in scanning probe microscopy.* Nature, 1996. **384**(6605): p. 147-150.
159. Dresselhaus, M.S., G. Dresselhaus and P. Avouris, *Carbon nanotubes: synthesis, structure, properties, and applications*2001, London: Springer.
160. Zanello, L.P., B. Zhao, H. Hu and R.C. Haddon, *Bone Cell Proliferation on Carbon Nanotubes.* Nano Letters, 2006. **6**(3): p. 562-567.
161. Williams, D., *Carbon nanotubes in medical technology.* Medical Device Technology, 2007. **18**(2): p. 8-10.
162. Tans, S.J., A.R.M. Verschueren and C. Dekker, *Room-temperature transistor based on a single carbon nanotube.* Nature, 1998. **393**(6680): p. 49-52.
163. Yan, C., L. Zou and R. Short, *Single-walled carbon nanotubes and polyaniline composites for capacitive deionization.* Desalination, 2012. **290**(0): p. 125-129.
164. Kar, S., R.C. Bindal and P.K. Tewari, *Carbon nanotube membranes for desalination and water purification: Challenges and opportunities.* Nano Today, 2012. **7**(5): p. 385-389.
165. Dumee, L., *Carbon-nanotube-based membranes for water desalination by membrane distillation*, in *Institute for Sustainability and Innovation*2011, Victoria University. p. 370.
166. Wang, L., M. Wang, Z.-H. Huang, T. Cui, X. Gui, F. Kang, K. Wang and D. Wu, *Capacitive deionization of NaCl solutions using carbon nanotube sponge electrodes.* Journal of Materials Chemistry, 2011. **21**(45): p. 18295-18299.
167. Zhang, D., T. Yan, L. Shi, Z. Peng, X. Wen and J. Zhang, *Enhanced capacitive deionization performance of graphene/carbon nanotube composites.* Journal of Materials Chemistry, 2012. **22**(29): p. 14696-14704.
168. Geim, A.K. and K.S. Novoselov, *The rise of graphene.* Nat Mater, 2007. **6**(3): p. 183-191.
169. Geim, A.K., *Graphene: Status and Prospects.* Science, 2009. **324**(5934): p. 1530-1534.
170. Wallace, P.R., *The Band Theory of Graphite.* Physical Review, 1947. **71**(9): p. 622-634.
171. Boehm, H.P., A. Clauss, G.O. Fischer and U. Hofmann, *Das Adsorptionsverhalten sehr dünner Kohlenstoff-Folien.* Zeitschrift für anorganische und allgemeine Chemie, 1962. **316**(3-4): p. 119-127.
172. Fasolino, A., J.H. Los and M.I. Katsnelson, *Intrinsic ripples in graphene.* Nat Mater, 2007. **6**(11): p. 858-861.
173. Zhu, Y., S. Murali, W. Cai, X. Li, J.W. Suk, J.R. Potts and R.S. Ruoff, *Graphene and Graphene Oxide: Synthesis, Properties, and Applications.* Advanced Materials, 2010. **22**(35): p. 3906-3924.

174. Novoselov, K.S., A.K. Geim, S.V. Morozov, D. Jiang, Y. Zhang, S.V. Dubonos, I.V. Grigorieva and A.A. Firsov, *Electric Field Effect in Atomically Thin Carbon Films.* Science, 2004. **306**(5696): p. 666-669.
175. Pei, S. and H.-M. Cheng, *The reduction of graphene oxide.* Carbon, 2012. **50**(9): p. 3210-3228.
176. Bae, S., H. Kim, Y. Lee, X. Xu, J.-S. Park, Y. Zheng, J. Balakrishnan, T. Lei, H. Ri Kim, Y.I. Song, Y.-J. Kim, K.S. Kim, B. Ozyilmaz, J.-H. Ahn, B.H. Hong and S. Iijima, *Roll-to-roll production of 30-inch graphene films for transparent electrodes.* Nat Nano, 2010. **5**(8): p. 574-578.
177. Bolotin, K.I., K.J. Sikes, Z. Jiang, M. Klima, G. Fudenberg, J. Hone, P. Kim and H.L. Stormer, *Ultrahigh electron mobility in suspended graphene.* Solid State Communications, 2008. **146**(9-10): p. 351-355.
178. Morozov, S.V., K.S. Novoselov, M.I. Katsnelson, F. Schedin, D.C. Elias, J.A. Jaszczak and A.K. Geim, *Giant intrinsic carrier mobilities in graphene and its bilayer.* Physical Review Letters, 2008. **100**(1).
179. Lee, C., X.D. Wei, J.W. Kysar and J. Hone, *Measurement of the elastic properties and intrinsic strength of monolayer graphene.* Science, 2008. **321**(5887): p. 385-388.
180. Balandin, A.A., S. Ghosh, W.Z. Bao, I. Calizo, D. Teweldebrhan, F. Miao and C.N. Lau, *Superior thermal conductivity of single-layer graphene.* Nano Letters, 2008. **8**(3): p. 902-907.
181. Cai, W.W., Y.W. Zhu, X.S. Li, R.D. Piner and R.S. Ruoff, *Large area few-layer graphene/graphite films as transparent thin conducting electrodes.* Applied Physics Letters, 2009. **95**(12).
182. Li, X.S., Y.W. Zhu, W.W. Cai, M. Borysiak, B.Y. Han, D. Chen, R.D. Piner, L. Colombo and R.S. Ruoff, *Transfer of Large-Area Graphene Films for High-Performance Transparent Conductive Electrodes.* Nano Letters, 2009. **9**(12): p. 4359-4363.
183. Xin, Y., J.G. Liu, Y. Zhou, W. Liu, J. Gao, Y. Xie, Y. Yin and Z. Zou, *Preparation and characterization of Pt supported on graphene with enhanced electrocatalytic activity in fuel cell.* Journal of Power Sources, 2011. **196**(3): p. 1012-1018.
184. Wang, Z., C.P. Puls, N.E. Staley, Y. Zhang, A. Todd, J. Xu, C.A. Howsare, M.J. Hollander, J.A. Robinson and Y. Liu, *Technology ready use of single layer graphene as a transparent electrode for hybrid photovoltaic devices.* Physica E: Low-Dimensional Systems and Nanostructures, 2011. **44**(2): p. 521-524.
185. Luan, V.H., H.N. Tien, L.T. Hoa, N.T.M. Hien, E.-S. Oh, J. Chung, E.J. Kim, W.M. Choi, B.-S. Kong and S.H. Hur, *Synthesis of a highly conductive and large surface area graphene oxide hydrogel and its use in a supercapacitor.* Journal of Materials Chemistry A, 2013. **1**(2): p. 208-211.
186. Hill, E.W., A. Vijayaragahvan and K. Novoselov, *Graphene Sensors.* Sensors Journal, IEEE, 2011. **11**(12): p. 3161-3170.
187. Wu, Y., K.A. Jenkins, A. Valdes-Garcia, D.B. Farmer, Y. Zhu, A.A. Bol, C. Dimitrakopoulos, W. Zhu, F. Xia, P. Avouris and Y.-M. Lin, *State-of-the-Art Graphene High-Frequency Electronics.* Nano Letters, 2012. **12**(6): p. 3062-3067.

188. Eda, G., G. Fanchini and M. Chhowalla, *Large-area ultrathin films of reduced graphene oxide as a transparent and flexible electronic material.* Nat Nano, 2008. **3**(5): p. 270-274.
189. Liu, H., L. Zhang, Y. Guo, C. Cheng, L. Yang, L. Jiang, G. Yu, W. Hu, Y. Liu and D. Zhu, *Reduction of graphene oxide to highly conductive graphene by Lawesson's reagent and its electrical applications.* Journal of Materials Chemistry C, 2013. **1**(18): p. 3104-3109.
190. Hummers, W.S. and R.E. Offeman, *Preparation of Graphitic Oxide.* Journal of the American Chemical Society, 1958. **80**(6): p. 1339-1339.
191. Eda, G., G. Fanchini and M. Chhowalla, *Large-area ultrathin films of reduced graphene oxide as a transparent and flexible electronic material.* Nature Nanotechnology, 2008. **3**(5): p. 270-274.
192. Brodie, B.C., *On the Atomic Weight of Graphite.* Philosophical Transactions of the Royal Society of London, 1859. **149**: p. 249-259.
193. Staudenmaier, L., *Verfahren zur Darstellung der Graphitsäure.* Berichte der deutschen chemischen Gesellschaft, 1898. **31**(2): p. 1481-1487.
194. Compton, O.C. and S.T. Nguyen, *Graphene Oxide, Highly Reduced Graphene Oxide, and Graphene: Versatile Building Blocks for Carbon-Based Materials.* Small, 2010. **6**(6): p. 711-723.
195. Johnson, J.A., C.J. Benmore, S. Stankovich and R.S. Ruoff, *A neutron diffraction study of nano-crystalline graphite oxide.* Carbon, 2009. **47**(9): p. 2239-2243.
196. Luo, Z., Y. Lu, L.A. Somers and A.T.C. Johnson, *High Yield Preparation of Macroscopic Graphene Oxide Membranes.* Journal of the American Chemical Society, 2009. **131**(3): p. 898-899.
197. Marcano, D.C., D.V. Kosynkin, J.M. Berlin, A. Sinitskii, Z. Sun, A. Slesarev, L.B. Alemany, W. Lu and J.M. Tour, *Improved Synthesis of Graphene Oxide.* ACS Nano, 2010. **4**(8): p. 4806-4814.
198. Antiohos, D., K. Pingmuang, M.S. Romano, S. Beirne, T. Romeo, P. Aitchison, A. Minett, G. Wallace, S. Phanichphant and J. Chen, *Manganosite–microwave exfoliated graphene oxide composites for asymmetric supercapacitor device applications.* Electrochimica Acta, 2013. **101**(4): p. 99-108.
199. Novoselov, K.S., *Electric Field Effect in Atomically Thin Carbon Films.* Science (New York, N.Y.), 2004. **306**(5696): p. 666-669.
200. Loh, K.P., Q. Bao, G. Eda and M. Chhowalla, *Graphene oxide as a chemically tunable platform for optical applications.* Nat Chem, 2010. **2**(12): p. 1015-1024.
201. Robinson, J.T., F.K. Perkins, E.S. Snow, Z. Wei and P.E. Sheehan, *Reduced Graphene Oxide Molecular Sensors.* Nano Letters, 2008. **8**(10): p. 3137-3140.
202. Zhou, M., Y. Zhai and S. Dong, *Electrochemical Sensing and Biosensing Platform Based on Chemically Reduced Graphene Oxide.* Analytical Chemistry, 2009. **81**(14): p. 5603-5613.
203. Williams, G., B. Seger and P.V. Kamat, *TiO2-Graphene Nanocomposites. UV-Assisted Photocatalytic Reduction of Graphene Oxide.* ACS Nano, 2008. **2**(7): p. 1487-1491.

204. Si, Y. and E.T. Samulski, *Synthesis of Water Soluble Graphene.* Nano Letters, 2008. **8**(6): p. 1679-1682.
205. Kim, K.S., Y. Zhao, H. Jang, S.Y. Lee, J.M. Kim, K.S. Kim, J.-H. Ahn, P. Kim, J.-Y. Choi and B.H. Hong, *Large-scale pattern growth of graphene films for stretchable transparent electrodes.* Nature, 2009. **457**(7230): p. 706-710.
206. Stoller, M.D., S. Park, Y. Zhu, J. An and R.S. Ruoff, *Graphene-Based Ultracapacitors.* Nano Letters, 2008. **8**(10): p. 3498-3502.
207. Li, X., X. Wang, L. Zhang, S. Lee and H. Dai, *Chemically Derived, Ultrasmooth Graphene Nanoribbon Semiconductors.* Science, 2008. **319**(5867): p. 1229-1232.
208. Li, H., T. Lu, L. Pan, Y. Zhang and Z. Sun, *Electrosorption behavior of graphene in NaCl solutions.* Journal of Materials Chemistry, 2009. **19**(37): p. 6773-6779.
209. Li, H., L. Zou, L. Pan and Z. Sun, *Novel Graphene-Like Electrodes for Capacitive Deionization.* Environmental Science & Technology, 2010. **44**(22): p. 8692-8697.
210. Li, H., L. Pan, C. Nie, Y. Liu and Z. Sun, *Reduced graphene oxide and activated carbon composites for capacitive deionization.* Journal of Materials Chemistry, 2012. **22**(31): p. 15556-15561.
211. Li, H., S. Liang, J. Li and L. He, *The capacitive deionization behaviour of a carbon nanotube and reduced graphene oxide composite.* Journal of Materials Chemistry A, 2013. **1**(21): p. 6335-6341.
212. Wimalasiri, Y. and L. Zou, *Carbon nanotube/graphene composite for enhanced capacitive deionization performance.* Carbon, 2013. **59**: p. 464-471.
213. Hernandez-Perez, T., M. Morales, N. Batina and M. Salmon, *Effect of the Electrosynthesis Method on the Surface Morphology of the Polypyrrole Film: An Atomic Force Microscopy Study.* Journal of the Electrochemical Society, 2001. **148**(5): p. C369-C375.
214. Chen, J., A.M. Rao, S. Lyuksyutov, M.E. Itkis, M.A. Hamon, H. Hu, R.W. Cohn, P.C. Eklund, D.T. Colbert, R.E. Smalley and R.C. Haddon, *Dissolution of Full-Length Single-Walled Carbon Nanotubes.* The Journal of Physical Chemistry B, 2001. **105**(13): p. 2525-2528.
215. Zhang, J., H. Zou, Q. Qing, Y. Yang, Q. Li, Z. Liu, X. Guo and Z. Du, *Effect of Chemical Oxidation on the Structure of Single-Walled Carbon Nanotubes.* The Journal of Physical Chemistry B, 2003. **107**(16): p. 3712-3718.
216. Dillon, A.C., T. Gennett, K.M. Jones, J.L. Alleman, P.A. Parilla and M.J. Heben, *A Simple and Complete Purification of Single-Walled Carbon Nanotube Materials.* Advanced Materials, 1999. **11**(16): p. 1354-1358.
217. Dujardin, E., T.W. Ebbesen, A. Krishnan and M.M.J. Treacy, *Purification of Single-Shell Nanotubes.* Advanced Materials, 1998. **10**(8): p. 611-613.
218. Hussain, S., P. Jha, A. Chouksey, R. Raman, S. Islam, T. Islam and K. Choudhary, *Spectroscopic Investigation of Modified Single Wall Carbon Nanotube (SWCNT).* Journal of Modern Physics, 2011. **2**(6): p. 538-543.

219. Yuca, N., N. Karatepe and F. Yakuphanoglu, *Thermal and electrical properties of carbon nanotubes purified by acid digestion.* World Academy of Science, Engineering and Technology, 2011. **79**(4): p. 611-616.
220. Dumitrescu, I., N.R. Wilson and J.V. Macpherson, *Functionalizing Single-Walled Carbon Nanotube Networks Effect on Electrical and Electrochemical Properties.* The Journal of Physical Chemistry C, 2007. **111**(35): p. 12944-12953.
221. Kuznetsova, A., I. Popova, J.T. Yates, M.J. Bronikowski, C.B. Huffman, J. Liu, R.E. Smalley, H.H. Hwu and J.G. Chen, *Oxygen-Containing Functional Groups on Single-Wall Carbon Nanotubes: NEXAFS and Vibrational Spectroscopic Studies.* Journal of the American Chemical Society, 2001. **123**(43): p. 10699-10704.
222. Mawhinney, D., V. Naumenko, A. Kuznetsova, J. Yates Jr, J. Liu and R. Smalley, *Surface defect site density on single walled carbon nanotubes by titration.* Chemical Physics Letters, 2000. **324**(3): p. 213-216.
223. Tchoul, M.N., W.T. Ford, G. Lolli, D.E. Resasco and S. Arepalli, *Effect of Mild Nitric Acid Oxidation on Dispersability, Size, and Structure of Single-Walled Carbon Nanotubes.* Chemistry of Materials, 2007. **19**(23): p. 5765-5772.
224. Zhang, X., T.V. Sreekumar, T. Liu and S. Kumar, *Properties and Structure of Nitric Acid Oxidized Single Wall Carbon Nanotube Films.* The Journal of Physical Chemistry B, 2004. **108**(42): p. 16435-16440.
225. Zhao, W., C. Song and P.E. Pehrsson, *Water-Soluble and Optically pH-Sensitive Single-Walled Carbon Nanotubes from Surface Modification.* Journal of the American Chemical Society, 2002. **124**(42): p. 12418-12419.
226. Yuca, N., N. Karatepe and F. Yakuphanoglu, *Thermal and Electrical Properties of Carbon Nanotubes Purified by Acid Digestion.* World Academy of Science, Engineering and Technology, 2011. **40**(55): p. 611-616.
227. Hamon, M.A., J. Chen, H. Hu, Y. Chen, M.E. Itkis, A.M. Rao, P.C. Eklund and R.C. Haddon, *Dissolution of single-walled carbon nanotubes.* Advanced Materials, 1999. **11**(10): p. 834-840.
228. Nuriel, S., L. Liu, A.H. Barber and H.D. Wagner, *Direct measurement of multiwall nanotube surface tension.* Chemical Physics Letters, 2005. **404**(4-6): p. 263-266.
229. Sainz, R., W.R. Small, N.A. Young, C. Valles, A.M. Benito, W.K. Maser and M. in het Panhuis, *Synthesis and properties of optically active polyaniline carbon nanotube composites.* Macromolecules, 2006. **39**(21): p. 7324-7332.
230. Balasubramanian, K. and M. Burghard, *Chemically functionalized carbon nanotubes.* Small, 2005. **1**(2): p. 180-192.
231. Rinzler, A.G., J. Liu, H. Dai, P. Nikolaev, C.B. Huffman, F.J. Rodríguez-Macías, P.J. Boul, A.H. Lu, D. Heymann, D.T. Colbert, R.S. Lee, J.E. Fischer, A.M. Rao, P.C. Eklund and R.E. Smalley, *Large-scale purification of single-wall carbon nanotubes: process, product, and characterization.* Applied Physics A: Materials Science & Processing, 1998. **67**(1): p. 29-37.
232. Benedict, B., P.E. Pehrsson and W. Zhao, *Optically sensing additional sonication effects on dispersed HiPco nanotubes in aerated water.* The Journal of Physical Chemistry B, 2005. **109**(16): p. 7778-7780.

233. Lin, Y., S. Taylor, H. Li, S. Fernando, L. Qu, W. Wang, L. Gu, B. Zhou and Y.-P. Sun, *Advances toward bioapplications of carbon nanotubes.* Journal of Materials Chemistry, 2004. **14**(4): p. 527-541.
234. Star, A., J.F. Stoddart, D. Steuerman, M. Diehl, A. Boukai, E.W. Wong, X. Yang, S.-W. Chung, H. Choi and J.R. Heath, *Preparation and properties of polymer-wrapped single-walled carbon nanotubes.* Angewandte Chemie International Edition, 2001. **40**(9): p. 1721-1725.
235. Boge, J., L.J. Sweetman, M. in het Panhuis and S.F. Ralph, *The effect of preparaton conditions and biopolymer dispersants on the properties of SWNT buckypaper.* Journal of Materials Chemistry, 2009. **19**(48): p. 9131-9140.
236. Ferris, C.J. and M. in het Panhuis, *Conducting bio-materials based on gellan gum hydrogels.* Soft Matter, 2009. **5**(18): p. 3430-3437.
237. Granero, A.J., J.M. Razal, G.G. Wallace and M. in het Panhuis, *Spinning carbon nanotube-gel fibers using polyelectrolyte complexation.* Advanced Functional Materials, 2008. **18**(23): p. 3759-3764.
238. Hrapovic, S., K.B. Male, Y. Liu and J.H.T. Luong, *Preparation of polymer–carbon nanotube composite materials and their applications for enzyme entrapment.* Analytical Letters, 2008. **41**(2): p. 278 - 288.
239. Moulton, S.E., A.I. Minett, R. Murphy, K.P. Ryan, D. McCarthy, J.N. Coleman, W.J. Blau and G.G. Wallace, *Biomolecules as selective dispersants for carbon nanotubes.* Carbon, 2005. **43**(9): p. 1879-1884.
240. Razal, J.M., K.J. Gilmore and G.G. Wallace, *Carbon nanotube biofiber formation in a polymer-free coagulation bath.* Advanced Functional Materials, 2008. **18**(1): p. 61-66.
241. Vaisman, L., H.D. Wagner and G. Marom, *The role of surfactants in dispersion of carbon nanotubes.* Advances in Colloid and Interface Science, 2006. **128-130**: p. 37-46.
242. Wang, J., M. Musameh and Y. Lin, *Solubilization of carbon nanotubes by nafion toward the preparation of amperometric biosensors.* Journal of the American Chemical Society, 2003. **125**(9): p. 2408-2409.
243. Coleman, J.N., *Liquid-Phase Exfoliation of Nanotubes and Graphene.* Advanced Functional Materials, 2009. **19**(23): p. 3680-3695.
244. Landi, B.J., H.J. Ruf, J.J. Worman and R.P. Raffaelle, *Effects of Alkyl Amide Solvents on the Dispersion of Single-Wall Carbon Nanotubes.* The Journal of Physical Chemistry B, 2004. **108**(44): p. 17089-17095.
245. Furtado, C.A., U.J. Kim, H.R. Gutierrez, L. Pan, E.C. Dickey and P.C. Eklund, *Debundling and Dissolution of Single-Walled Carbon Nanotubes in Amide Solvents.* Journal of the American Chemical Society, 2004. **126**(19): p. 6095-6105.
246. Brandao, S., D. Andrada, A. Mesquita, A. Santos, H. Gorgulho, R. Paniago, M. Pimenta, C. Fantini and C. Furtado, *The influence of oxygen-containing functional groups on the dispersion of single-walled carbon nanotubes in amide solvents.* Journal of Physics. Condensed Matter : an Institute of Physics journal, 2010. **22**(33): p. 334222.
247. Nicholson, R.S., *Theory and Application of Cyclic Voltammetry for Measurement of Electrode Reaction Kinetics.* Analytical Chemistry, 1965. **37**(11): p. 1351-1355.

248. Kissinger, P.T. and W.R. Heineman, *Cyclic voltammetry.* Journal of Chemical Education, 1983. **60**(9): p. 702-706.
249. Ran, L., C. Seung Il and L. Sang Bok, *Poly(3,4-ethylenedioxythiophene) nanotubes as electrode materials for a high-powered supercapacitor.* NANOTECHNOLOGY, 2008. **19**(21): p. 215710.
250. Simon, P. and Y. Gogotsi, *Materials for electrochemical capacitors.* Nature Materials, 2008. **7**(11): p. 845-54.
251. Attal, S., R. Thiruvengadathan and O. Regev, *Determination of the concentration of single-walled carbon nanotubes in aqueous dispersions using UV-visible absorption spectroscopy.* Analytical Chemistry, 2006. **78**(23): p. 8098-8104.
252. Grossiord, N., O. Regev, J. Loos, J. Meuldijk and C.E. Koning, *Time-dependent study of the exfoliation process of carbon nanotubes in aqueous dispersions by using UV-visible spectroscopy.* Analytical Chemistry, 2005. **77**(16): p. 5135-5139.
253. Smith, G.D. and R.J.H. Clark, *Raman microscopy in archaeological science.* Journal of Archaeological Science, 2004. **31**(8): p. 1137-1160.
254. Tu, Q. and C. Chang, *Diagnostic applications of Raman spectroscopy.* Nanomedicine: Nanotechnology, Biology and Medicine, 2012. **8**(5): p. 545-558.
255. Robinson, I.K. and D.J. Tweet, *Surface x-ray diffraction.* Reports on Progress in Physics, 1992. **55**(5): p. 599-651.
256. Valderrama, C., X. Gamisans, X. de las Heras, A. Farrán and J.L. Cortina, *Sorption kinetics of polycyclic aromatic hydrocarbons removal using granular activated carbon: Intraparticle diffusion coefficients.* Journal of Hazardous Materials, 2008. **157**(2–3): p. 386-396.
257. Demirbasa, E., K. Mehmet, S. Elif and O. Tuncay, *Adsorption kinetics for the removal of chromium (VI) from aqueous solutions on the activated carbons prepared from agricultural wastes.* Journal of Water, 2004. **30**(4): p. 533-539.
258. Malash, G.F. and M.I. El-Khaiary, *Piecewise linear regression: A statistical method for the analysis of experimental adsorption data by the intraparticle-diffusion models.* Chemical Engineering Journal, 2010. **163**(3): p. 256-263.
259. Weber, J. and Moriss, *Kinetics of adsorption on carbon solution.* Sanitary Engineering Division ASCE., 1963. **89**: p. 31-59.
260. Lagergren, S., *About the theory of so-called adsorption of soluble substances.* Svenska Vetens Kapsarsed Handle, 1898. **24**(4): p. 1-39.
261. Erdoğan, B.C. and S. Ülkü, *Ammonium sorption by Gördes clinoptilolite rich mineral specimen.* Applied Clay Science, 2011. **54**(3–4): p. 217-225.
262. Langmuir, I., *The adsorption of gases on plane surfaces of glass, mica and platinum.* Journal of the American Chemical Society, 1918. **40**(9): p. 1361-1403.
263. Kapoor, A., R.T. Yang and C. Wong, *Surface Diffusion.* Catalysis Reviews, 1989. **31**(1-2): p. 129-214.
264. Chen, Z., C. Song, X. Sun, H. Guo and G. Zhu, *Kinetic and isotherm studies on the electrosorption of NaCl from aqueous solutions by activated carbon electrodes.* Desalination, 2011. **267**(2–3): p. 239-243.

265. Wang, G., C. Pan, L. Wang, Q. Dong, C. Yu, Z. Zhao and J. Qiu, *Activated carbon nanofiber webs made by electrospinning for capacitive deionization.* Electrochimica Acta, 2012. **69**(1): p. 65-70.
266. Peng, Z., D. Zhang, L. Shi and T. Yan, *High performance ordered mesoporous carbon/carbon nanotube composite electrodes for capacitive deionization.* Journal of Materials Chemistry, 2012. **22**(14): p. 6603-6612.
267. Villar, I., D.J. Suarez-De La Calle, Z. González, M. Granda, C. Blanco, R. Menéndez and R. Santamaría, *Carbon materials as electrodes for electrosorption of NaCl in aqueous solutions.* Adsorption, 2011. **17**(3): p. 467-471.
268. Li, H., L. Zou, L. Pan and Z. Sun, *Using graphene nano-flakes as electrodes to remove ferric ions by capacitive deionization.* Separation and Purification Technology, 2010. **75**(1): p. 8-14.
269. Zhang, Y., Y. Wang, S. Xu, J. Wang, Z. Wang and S. Wang, *Polypyrrole nanowire modified graphite (PPy/G) electrode used in capacitive deionization.* Synthetic Metals, 2010. **160**(13-14): p. 1392-1396.
270. Liu, Q., Y. Wang, Y. Zhang, S. Xu and J. Wang, *Effect of dopants on the adsorbing performance of polypyrrole/graphite electrodes for capacitive deionization process.* Synthetic Metals, 2012. **162**(7–8): p. 655-661.
271. Wallace, G.G., *Conductive Electroactive Polymers : Intelligent Polymer Systems*, 2008, Taylor & Francis: Hoboken.
272. Frydrychewicz, A., A. Czerwiński and K. Jackowska, *Electrochemistry of multilayer electrodes RVC\Pani\Pd\Pani.* Synthetic Metals, 2001. **121**(1-3): p. 1401-1402.
273. Wen, X., D. Zhang, L. Shi, T. Yan, H. Wang and J. Zhang, *Three-dimensional hierarchical porous carbon with a bimodal pore arrangement for capacitive deionization.* Journal of Materials Chemistry, 2012. **22**(45): p. 23835-23844.
274. Rolison, D.R., *Catalytic Nanoarchitectures--the Importance of Nothing and the Unimportance of Periodicity.* Science (New York, N.Y.), 2003. **299**(5613): p. 1698-1701.
275. Carriazo, D., F. Pico, M.C. Gutierrez, F. Rubio, J.M. Rojo and F. del Monte, *Block-Copolymer assisted synthesis of hierarchical carbon monoliths suitable as supercapacitor electrodes.* Journal of Materials Chemistry, 2010. **20**(4): p. 773-780.
276. Wang, D.W., F. Li, M. Liu, G.Q. Lu and H.-M. Cheng, *3D Aperiodic Hierarchical Porous Graphitic Carbon Material for High-Rate Electrochemical Capacitive Energy Storage.* Angewandte Chemie, 2008. **120**(2): p. 379-382.
277. Xu, F., R. Cai, Q. Zeng, C. Zou, D. Wu, F. Li, X. Lu, Y. Liang and R. Fu, *Fast ion transport and high capacitance of polystyrene-based hierarchical porous carbon electrode material for supercapacitors.* Journal of Materials Chemistry, 2011. **21**(6): p. 1970-1976.
278. Wang, J., *Reticulated vitreous carbon--a new versatile electrode material.* Electrochimica Acta, 1981. **26**(12): p. 1721-1726.

279. Shedge, H.Y., *Specific and non-specific binding of proteins and nucleic acids on chemically modified reticulated vitreous carbon electrodes.* ProQuest Dissertations and Theses, 2009: p. 32.
280. Otero, T.F. and M. Caballero Romero, *Conformational energy from the oxidation kinetics of poly(3,4-ethylenedioxythiophene) films.* Polymer International, 2010. **59**(3): p. 329-336.
281. Seshadri, V., L. Wu and G.A. Sotzing, *Conjugated Polymers via Electrochemical Polymerization of Thieno[3,4-b]thiophene (T34bT) and 3,4-Ethylenedioxythiophene (EDOT).* Langmuir, 2003. **19**(22): p. 9479-9485.
282. Liu, Y.-C. and B.-J. Hwang, *Identification of oxidized polypyrrole on Raman spectrum.* Synthetic Metals, 2000. **113**(1–2): p. 203-207.
283. Tamburri, E., S. Orlanducci, F. Toschi, M.L. Terranova and D. Passeri, *Growth mechanisms, morphology, and electroactivity of PEDOT layers produced by electrochemical routes in aqueous medium.* Synthetic Metals, 2009. **159**(5–6): p. 406-414.
284. Downard, A.J. and D. Pletcher, *The influence of water on the electrodeposition of polypyrrole in acetonitrile.* Journal of Electroanalytical Chemistry, 1986. **206**(1-2): p. 139-145.
285. Heinze, J., A. Rasche, M. Pagels and B. Geschke, *On the origin of the so-called nucleation loop during electropolymerization of conducting polymers.* Journal of Physical Chemistry B, 2007. **111**(5): p. 989-997.
286. Sakmeche, N., S. Aeiyach, J.J. Aaron, M. Jouini, J.C. Lacroix and P.C. Lacaze, *Improvement of the electrosynthesis and physicochemical properties of poly(3,4-ethylenedioxythiophene) using a sodium dodecyl sulfate micellar aqueous medium.* Langmuir, 1999. **15**(7): p. 2566-2574.
287. Sadki, S., P. Schottland, N. Brodie and G. Sabouraud, *The mechanisms of pyrrole electropolymerization.* Chemical Society Reviews, 2000. **29**(5): p. 283-293.
288. Lock, J.P., S.G. Im and K.K. Gleason, *Oxidative Chemical Vapor Deposition of Electrically Conducting Poly(3,4-ethylenedioxythiophene) Films.* Macromolecules, 2006. **39**(16): p. 5326-5329.
289. Im, S.G., E.A. Olivetti and K.K. Gleason, *Systematic control of the electrical conductivity of poly (3,4-ethylenedioxythiophene) via oxidative chemical vapor deposition (oCVD).* Surface and Coatings Technology, 2007. **201**(22–23): p. 9406-9412.
290. Ha, Y.H., N. Nikolov, S.K. Pollack, J. Mastrangelo, B.D. Martin and R. Shashidhar, *Towards a Transparent, Highly Conductive Poly(3,4-ethylenedioxythiophene).* Advanced Functional Materials, 2004. **14**(6): p. 615-622.
291. Randriamahazaka, H., V. Noel and C. Chevrot, *Nucleation and growth of poly(3,4-ethylenedioxythiophene) in acetonitrile on platinum under potentiostatic conditions.* Journal of Electroanalytical Chemistry, 1999. **472**(2): p. 103-111.
292. Chao, F., M. Costa and C. Tian, *Different steps in electrodeposition of poly(3-methylthiophene) films on platinum electrodes studied by ellipsometry, SEM and AFM techniques.* Synthetic Metals, 1993. **53**(2): p. 127-147.

293. Schrebler, R., P. Grez, P. Cury, C. Veas, M. Merino, H. Gomez, R. Cordova and M.A. Del Valle, *Nucleation and growth mechanisms of poly(thiophene) part 1. Effect of electrolyte and monomer concentration in dichloromethane.* Journal of Electroanalytical Chemistry, 1997. **430**(1-2): p. 77-90.
294. Snook, G.A., C. Peng, D.J. Fray and G.Z. Chen, *Achieving high electrode specific capacitance with materials of low mass specific capacitance: Potentiostatically grown thick micro-nanoporous PEDOT films.* Electrochemistry Communications, 2007. **9**(1): p. 83-88.
295. Roncali, J., *Conjugated poly(thiophenes): synthesis, functionalization, and applications.* Chemical Reviews, 1992. **92**(4): p. 711-738.
296. Xu, H., H. Zhang, Y. Huang and Y. Wang, *Porous carbon/silica composite monoliths derived from resorcinol–formaldehyde/TEOS.* Journal of Non-Crystalline Solids, 2010. **356**(20–22): p. 971-976.
297. Shin, H.-J., S.S. Jeon and S.S. Im, *CNT/PEDOT core/shell nanostructures as a counter electrode for dye-sensitized solar cells.* Synthetic Metals, 2011. **161**(13–14): p. 1284-1288.
298. Yuvaraj, H., Y.T. Jeong, W.K. Lee and K.T. Lim, *Synthesis of MWNT/PEDOT Composites for the Application of Organic Light Emitting Diodes.* Molecular Crystals and Liquid Crystals, 2009. **514**: p. 366-374.
299. Goncalves, E.S., M.C. Rezende and N.G. Ferreira, *Dynamics of defects and surface structure formation in reticulated vitreous carbon.* Brazilian Journal of Physics, 2006. **36**(2): p. 264-266.
300. Pesin, L.A., *Review Structure and properties of glass-like carbon.* Journal of Materials Science, 2002. **37**(1): p. 1-28.
301. Garreau, S., G. Louarn, J.P. Buisson, G. Froyer and S. Lefrant, *In Situ Spectroelectrochemical Raman Studies of Poly(3,4-ethylenedioxythiophene) (PEDT).* Macromolecules, 1999. **32**(20): p. 6807-6812.
302. Tamburri, E., S. Sarti, S. Orlanducci, M.L. Terranova and M. Rossi, *Study of PEDOT conductive polymer films by admittance measurements.* Materials Chemistry and Physics, 2011. **125**(3): p. 397-404.
303. Selvaganesh, S.V., J. Mathiyarasu, K.L.N. Phani and V. Yegnaraman, *Chemical Synthesis of PEDOT–Au Nanocomposite.* Nanoscale Research Letters, 2007. **2**(11): p. 546-549.
304. Bard, A., *Electrochemical methods : fundamentals and applications / Allen J. Bard, Larry R. Faulkner*. 2nd ed ed2001, New York: John Wiley.
305. Wang, J., Y. Xu, X. Sun, X. Li and X. Du, *Electrochemical capacitance of the composite of poly (3,4-ethylenedioxythiophene) and functionalized single-walled carbon nanotubes.* Journal of Solid State Electrochemistry, 2008. **12**(7-8): p. 947-952.
306. Sen, P. and A. De, *Electrochemical performances of poly(3,4-ethylenedioxythiophene)–NiFe2O4 nanocomposite as electrode for supercapacitor.* Electrochimica Acta, 2010. **55**(16): p. 4677-4684.
307. Si, W., W. Lei, Z. Han, Y. Zhang, Q. Hao and M. Xia, *Electrochemical sensing of acetaminophen based on poly(3,4-ethylenedioxythiophene)/graphene oxide composites.* Sensors and Actuators, B: Chemical, 2014. **193**(2): p. 823-829.

308. Lota, K., V. Khomenko and E. Frackowiak, *Capacitance properties of poly(3,4-ethylenedioxythiophene)/carbon nanotubes composites.* Journal of Physics and Chemistry of Solids, 2004. **65**(2–3): p. 295-301.
309. Czardybon, A. and M. Lapkowski, *Synthesis and electropolymerisation of 3,4-ethylenedioxythiophene functionalised with alkoxy groups.* Synthetic Metals, 2001. **119**(1–3): p. 161-162.
310. Anothumakkool, B., S.N. Bhange, S.M. Unni and S. Kurungot, *1-Dimensional confinement of porous polyethylenedioxythiophene using carbon nanofibers as a solid template: an efficient charge storage material with improved capacitance retention and cycle stability.* RSC Advances, 2013. **3**(29): p. 11877-11887.
311. Wang, J., Y. Xu, X. Chen and X. Du, *Electrochemical supercapacitor electrode material based on poly(3,4-ethylenedioxythiophene)/polypyrrole composite.* Journal of Power Sources, 2007. **163**(2): p. 1120-1125.
312. Pandey, G.P. and A.C. Rastogi, *Synthesis and characterization of pulsed polymerized poly(3,4-ethylenedioxythiophene) electrodes for high-performance electrochemical capacitors.* Electrochimica Acta, 2013. **87**(3): p. 158-168.
313. Endut, Z., M. Hamdi and W.J. Basirun, *Pseudocapacitive performance of vertical copper oxide nanoflakes.* Thin Solid Films, 2013. **528**(5): p. 213-216.
314. Chen, J.H., W.Z. Li, D.Z. Wang, S.X. Yang, J.G. Wen and Z.F. Ren, *Electrochemical characterization of carbon nanotubes as electrode in electrochemical double-layer capacitors.* Carbon, 2002. **40**(8): p. 1193-1197.
315. Li, L., L. Zou, H. Song and G. Morris, *Ordered mesoporous carbons synthesized by a modified sol–gel process for electrosorptive removal of sodium chloride.* Carbon, 2009. **47**(3): p. 775-781.
316. Lu, Y., T. Li, X. Zhao, M. Li, Y. Cao, H. Yang and Y.Y. Duan, *Electrodeposited polypyrrole/carbon nanotubes composite films electrodes for neural interfaces.* Biomaterials, 2010. **31**(19): p. 5169-5181.
317. Chen, L., C. Yuan, H. Dou, B. Gao, S. Chen and X. Zhang, *Synthesis and electrochemical capacitance of core–shell poly (3,4-ethylenedioxythiophene)/poly (sodium 4-styrenesulfonate)-modified multiwalled carbon nanotube nanocomposites.* Electrochimica Acta, 2009. **54**(8): p. 2335-2341.
318. Kim, Y.-J. and J.-H. Choi, *Improvement of desalination efficiency in capacitive deionization using a carbon electrode coated with an ion-exchange polymer.* Water Research, 2010. **44**(3): p. 990-996.
319. Kim, Y.-J., J. Hur, W. Bae and J.-H. Choi, *Desalination of brackish water containing oil compound by capacitive deionization process.* Desalination, 2010. **253**(1-5): p. 119-123.
320. Wang, Z., B. Dou, L. Zheng, G. Zhang, Z. Liu and Z. Hao, *Effective desalination by capacitive deionization with functional graphene nanocomposite as novel electrode material.* Desalination, 2012. **299**(4): p. 96-102.
321. Nie, C., L. Pan, H. Li, T. Chen, T. Lu and Z. Sun, *Electrophoretic deposition of carbon nanotubes film electrodes for capacitive deionization.* Journal of Electroanalytical Chemistry, 2012. **666**: p. 85-88.

322. Wang, X.Z., M.G. Li, Y.W. Chen, R.M. Cheng, S.M. Huang, L.K. Pan and Z. Sun, *Electrosorption of ions from aqueous solutions with carbon nanotubes and nanofibers composite film electrodes.* Applied Physics Letters, 2006. **89**(5): p. 053127-3.
323. Hou, C.-H., J.-F. Huang, H.-R. Lin and B.-Y. Wang, *Preparation of activated carbon sheet electrode assisted electrosorption process.* Journal of the Taiwan Institute of Chemical Engineers, 2012. **43**(3): p. 473-479.
324. Li, H., L. Pan, Y. Zhang, L. Zou, C. Sun, Y. Zhan and Z. Sun, *Kinetics and thermodynamics study for electrosorption of NaCl onto carbon nanotubes and carbon nanofibers electrodes.* Chemical Physics Letters, 2010. **485**(1–3): p. 161-166.
325. Purdom, P.W., *Environmental Health*. second ed 1980, New York: Academic Press.
326. Marichev, V.A., *Partial charge transfer during anion adsorption: Methodological aspects.* Surface Science Reports, 2005. **56**(8): p. 277-324.
327. Yang, K.L., S. Yiacoumi and C. Tsouris, *Electrosorption capacitance of nanostructured carbon aerogel obtained by cyclic voltammetry.* Journal of Electroanalytical Chemistry, 2003. **540**: p. 159-167.
328. Michael, M.S. and S.R.S. Prabaharan, *High voltage electrochemical double layer capacitors using conductive carbons as additives.* Journal of Power Sources, 2004. **136**(1): p. 250-256.
329. Yang, C.M., W.H. Choi, B.K. Na, B.W. Cho and W.I. Cho, *Capacitive deionization of NaCl solution with carbon aerogel-silicagel composite electrodes.* Desalination, 2005. **174**(2): p. 125-133.
330. Dai, K., L. Shi, D. Zhang and J. Fang, *NaCl adsorption in multi-walled carbon nanotube/active carbon combination electrode.* Chemical Engineering Science, 2006. **61**(2): p. 428-433.
331. Li, L., H. Song and X. Chen, *Ordered mesoporous carbons from the carbonization of sulfuric-acid-treated silica/triblock copolymer/sucrose composites.* Microporous and Mesoporous Materials, 2006. **94**(1-3): p. 9-14.
332. Wang, S., D. Wang, L. Ji, Q. Gong, Y. Zhu and J. Liang, *Equilibrium and kinetic studies on the removal of NaCl from aqueous solutions by electrosorption on carbon nanotube electrodes.* Separation and Purification Technology, 2007. **58**(1): p. 12-16.
333. Zou, L., L. Li, H. Song and G. Morris, *Using mesoporous carbon electrodes for brackish water desalination.* Water Research, 2008. **42**(8-9): p. 2340-2348.
334. Mayes, R.T., C. Tsouris, J.O. Kiggans Jr, S.M. Mahurin, D.W. DePaoli and S. Dai, *Hierarchical ordered mesoporous carbon from phloroglucinol-glyoxal and its application in capacitive deionization of brackish water*. Journal of Materials Chemistry, 2010. **20**(39): p. 8674-8678.
335. Biener, J., M. Stadermann, M. Suss, M.A. Worsley, M.M. Biener, K.A. Rose and T.F. Baumann, *Advanced carbon aerogels for energy applications.* Energy & Environmental Science, 2011. **4**(3): p. 656-667.
336. Chen, Z., C. Song, X. Sun, H. Guo and G. Zhu, *Kinetic and isotherm studies on the electrosorption of NaCl from aqueous solutions by activated carbon electrodes.* Desalination, 2011. **267**(2-3): p. 239-243.

337. Li, H., L. Pan, T. Lu, Y. Zhan, C. Nie and Z. Sun, *A comparative study on electrosorptive behavior of carbon nanotubes and graphene for capacitive deionization.* Journal of Electroanalytical Chemistry, 2011. **653**(1-2): p. 40-44.
338. Jitianu, A., T. Cacciaguerra, R. Benoit, S. Delpeux, F. Béguin and S. Bonnamy, *Synthesis and characterization of carbon nanotubes-TiO2 nanocomposites.* Carbon, 2004. **42**(5-6): p. 1147-1151.
339. Campidelli, S., C. Klumpp, A. Bianco, D.M. Guldi and M. Prato, *Functionalization of CNT: Synthesis and applications in photovoltaics and biology.* Journal of Physical Organic Chemistry, 2006. **19**(8-9): p. 531-539.
340. Itoh, E., I. Suzuki and K. Miyairi, *Field emission from carbon-nanotube-dispersed conducting polymer thin film and its application to photovoltaic devices.* Japanese Journal of Applied Physics Part 1-Regular Papers Brief Communications & Review Papers, 2005. **44**(1B): p. 636-640.
341. Li, L., F. Li, Y. xiao and z. Aigin, *The effect of carbonyl, carboxyl and hydroxyl groups on the capacitance of carbon nanotubes.* New Carbon Materials, 2012. **26**(3): p. 224-228.
342. Ausman, K.D., R. Piner, O. Lourie, R.S. Ruoff and M. Korobov, *Organic Solvent Dispersions of Single-Walled Carbon Nanotubes: Toward Solutions of Pristine Nanotubes.* The Journal of Physical Chemistry B, 2000. **104**(38): p. 8911-8915.
343. Roberts, M., A.F. Huang, P. Johns and J. Owen, *Dip–spin coating of reticulated vitreous carbon with composite materials to act as an electrode for 3D microstructured lithium ion batteries.* Journal of Power Sources, 2013. **224**(2): p. 250-259.
344. Dresselhaus, M.S., G. Dresselhaus, R. Saito and A. Jorio, *Raman spectroscopy of carbon nanotubes.* Physics Reports, 2005. **409**(2): p. 47-99.
345. Mussi, V., C. Biale, S. Visentin, N. Barbero, M. Rocchia and U. Valbusa, *Raman analysis and mapping for the determination of COOH groups on oxidized single walled carbon nanotubes.* Carbon, 2010. **48**(12): p. 3391-3398.
346. Osswald, S., M. Havel and Y. Gogotsi, *Monitoring oxidation of multiwalled carbon nanotubes by Raman spectroscopy.* Journal of Raman Spectroscopy, 2007. **38**(6): p. 728-736.
347. Bandow, S., A.M. Rao, G.U. Sumanasekera, P.C. Eklund, F. Kokai, K. Takahashi and M. Yudasaka, *Evidence for anomalously small charge transfer in doped single-wall carbon nanohorn aggregates with Li, K and Br.* Applied Physics A: Materials Science and Processing, 2000. **71**(5): p. 561-564.
348. Tuinstra, F. and J.L. Koenig, *Raman Spectrum of Graphite.* Journal of Chemical Physics, 1970. **53**(3): p. 1126-1130.
349. Reyhani, A., S.Z. Mortazavi, A.N. Golikand, A.Z. Moshfegh and S. Mirershadi, *The effect of various acids treatment on the purification and electrochemical hydrogen storage of multi-walled carbon nanotubes.* Journal of Power Sources, 2008. **183**(2): p. 539-543.
350. Jorio, A., M. Pimenta, A. Souza Filho, R. Saito and S. Dresselhaus, *Characterizing carbon nanotube samples with resonance Raman scattering.* New Journal of Physics, 2003. **5**(139): p. 1-17.

351. Dresselhaus, M.S., *Raman spectroscopy on isolated single wall carbon nanotubes.* Carbon (New York), 2002. **40**(12): p. 2043-2061.
352. Kim, Y., D. Lee, Y. Oh, J. Choi and S. Baik, *The effects of acid treatment methods on the diameter dependent length separation of single walled carbon nanotubes.* Synthetic Metals, 2006. **156**(16-17): p. 999-1003.
353. Saini, R.K., I.W. Chiang, H. Peng, R.E. Smalley, W.E. Billups, R.H. Hauge and J.L. Margrave, *Covalent Sidewall Functionalization of Single Wall Carbon Nanotubes.* Journal of the American Chemical Society, 2003. **125**(12): p. 3617-3621.
354. Shen, J., A. Liu, Y. Tu, G. Foo, C. Yeo, M. Chan, R. Jiang and Y. Chen, *How carboxylic groups improve the performance of single-walled carbon nanotube electrochemical capacitors?* Energy & Environmental Science, 2011. **4**(10): p. 4220-4229.
355. Niyogi, S., M.A. Hamon, H. Hu, B. Zhao, P. Bhowmik, R. Sen, M.E. Itkis and R.C. Haddon, *Chemistry of Single-Walled Carbon Nanotubes.* Accounts of Chemical Research, 2002. **35**(12): p. 1105-1113.
356. Attal, S., R. Thiruvengadathan and O. Regev, *Determination of the concentration of single-walled carbon nanotubes in aqueous dispersions using UV−Visible absorption spectroscopy.* Analytical Chemistry, 2006. **78**(23): p. 8098-8104.
357. Grossiord, N., O. Regev, J. Loos, J. Meuldijk and C.E. Koning, *Time-dependent study of the exfoliation process of carbon nanotubes in aqueous dispersions by using UV−Visible spectroscopy.* Analytical Chemistry, 2005. **77**(16): p. 5135-5139.
358. Ryabenko, A.G., T.V. Dorofeeva and G.I. Zvereva, *UV-VIS-NIR spectroscopy study of sensitivity of single-wall carbon nanotubes to chemical processing and Van-der-Waals SWNT/SWNT interaction. Verification of the SWNT content measurements by absorption spectroscopy.* Carbon, 2004. **42**(8-9): p. 1523-1535.
359. S. Hussain, J. P, A. Chouksey, R. Raman, S. S Islam, T. Islam, P. Choudhary and Harsh., *Spectroscopic Investigation of Modified Single Wall Carbon Nanotube (SWCNT).* Journal of Modern Physics, 2011. **2**(6): p. 538-543.
360. O'Connell, M.J., S.M. Bachilo, C.B. Huffman, V.C. Moore, M.S. Strano, E.H. Haroz, K.L. Rialon, P.J. Boul, W.H. Noon, C. Kittrell, J. Ma, R.H. Hauge, R.B. Weisman and R.E. Smalley, *Band gap fluorescence from individual single-walled carbon nanotubes.* Science, 2002. **297**(5581): p. 593-596.
361. Aldalbahi, A. and M. in het Panhuis, *Electrical and mechanical characteristics of buckypapers and evaporative cast films prepared using single and multi-walled carbon nanotubes and the biopolymer carrageenan.* Carbon, 2012. **50**(3): p. 1197-1208.
362. Tondi, G., V. Fierro, A. Pizzi and A. Celzard, *Tannin-based carbon foams.* Carbon, 2009. **47**(6): p. 1480-1492.
363. Zhang, M., K.R. Atkinson and R.H. Baughman, *Multifunctional Carbon Nanotube Yarns by Downsizing an Ancient Technology.* Science, 2004. **306**(5700): p. 1358-1361.

364. Zhang, X., Q. Li, Y. Tu, Y. Li, J.Y. Coulter, L. Zheng, Y. Zhao, Q. Jia, D.E. Peterson and Y. Zhu, *Strong Carbon-Nanotube Fibers Spun from Long Carbon-Nanotube Arrays.* Small, 2007. **3**(2): p. 244-248.
365. Zhang, X., Q. Li, T.G. Holesinger, P.N. Arendt, J. Huang, P.D. Kirven, T.G. Clapp, R.F. DePaula, X. Liao, Y. Zhao, L. Zheng, D.E. Peterson and Y. Zhu, *Ultrastrong, Stiff, and Lightweight Carbon-Nanotube Fibers.* Advanced Materials, 2007. **19**(23): p. 4198-4201.
366. Naoi, K. and P. simon, *New Materials and New Configurations for Advanced Electrochemical Capacitors.* Journal of the Electrochemical Society, 2008. **17**(1): p. 34-37.
367. Wang, D., F. Li, M. Liu and H. Cheng, *Improved capacitance of SBA-15 templated mesoporous carbons after modification with nitric acid oxidation.* New Carbon Materials, 2007. **22**(4): p. 307-314.
368. Nian, Y.R. and H.S. Teng, *Nitric acid modification of activated carbon electrodes for improvement of electrochemical capacitance.* Journal of the Electrochemical Society, 2002. **149**(8): p. A1008-A1014.
369. Oda, H., A. Yamashita, S. Minoura, M. Okamoto and T. Morimoto, *Modification of the oxygen-containing functional group on activated carbon fiber in electrodes of an electric double-layer capacitor.* Journal of Power Sources, 2006. **158**(2): p. 1510-1516.
370. Li, L. and F. Li, *The effect of carbonyl, carboxyl and hydroxyl groups on the capacitance of carbon nanotubes.* New Carbon Materials, 2011. **26**(3): p. 224-228.
371. Kim, T., S. Lim, K. Kwon, S.-H. Hong, W. Qiao, C.K. Rhee, S.-H. Yoon and I. Mochida, *Electrochemical Capacitances of Well-Defined Carbon Surfaces.* Langmuir, 2006. **22**(22): p. 9086-9088.
372. Teng, H., Y.J. Chang and C.T. Hsieh, *Performance of electric double-layer capacitors using carbons prepared from phenol-formaldehyde resins by KOH etching.* Carbon, 2001. **39**(13): p. 1981-1987.
373. Mitali, S., D. Soma and D. Monica, *A Study of Effect of Electrolytes on the Capacitive Properties of Mustard Soot Containing Multiwalled Carbon Nanotubes.* Research Journal of Chemical Sciences, 2011. **1**(3): p. 109-113.
374. Guo, Y., J. Qi, Y. Jiang, S. Yang, Z. Wang and H. Xu, *Performance of electrical double layer capacitors with porous carbons derived from rice husk.* Materials Chemistry and Physics, 2003. **80**(3): p. 704-709.
375. Show, Y. and K. Imaizumi, *Electric double layer capacitor with low series resistance fabricated by carbon nanotube addition.* Diamond and Related Materials, 2007. **16**(4-7): p. 1154-1158.
376. Suss, M.E., T.F. Baumann, W.L. Bourcier, C.M. Spadaccini, K.A. Rose, J.G. Santiago and M. Stadermann, *Capacitive desalination with flow-through electrodes.* Energy & Environmental Science, 2012. **5**(11): p. 9511-9519.
377. Mohrous, M., I. Sakr, A. Balabel and K. Ibrahim, *Experimental Investigation of the Operating Parameters Affecting Hydrogen Production Process through Alkaline Water Electrolysis.* Thermal & Environmental Engineering, 2011. **2**(2): p. 113-116.

378. Nagai, N., M. Takeuchi, T. Kimura and T. Oka, *Existence of optimum space between electrodes on hydrogen production by water electrolysis.* International Journal of Hydrogen Energy, 2003. **28**(1): p. 35-41.
379. Andelman, M., *Flow through capacitor basics.* Separation and Purification Technology, 2011. **80**(2): p. 262-269.
380. Li, H. and L. Zou, *Ion-exchange membrane capacitive deionization: A new strategy for brackish water desalination.* Desalination, 2011. **275**(1–3): p. 62-66.
381. Boparai, H.K., M. Joseph and D.M. O'Carroll, *Kinetics and thermodynamics of cadmium ion removal by adsorption onto nano zerovalent iron particles.* Journal of Hazardous Materials, 2011. **186**(1): p. 458-465.
382. Senthil Kumar, P. and R. Gayathri, *Adsorption of Pb2+ ions from aqueous solutions onto Bael tree leaf powder: isotherms, kinetics and thermodynamics.* Journal of Engineering Science and Technology (JESTEC), 2009. **4**(4): p. 381-399.
383. Beidaghi, M. and C. Wang, *Micro-Supercapacitors Based on Interdigital Electrodes of Reduced Graphene Oxide and Carbon Nanotube Composites with Ultrahigh Power Handling Performance.* Advanced Functional Materials, 2012. **22**(21): p. 4501-4510.
384. Wang, Y., Y. Shao, D.W. Matson, J. Li and Y. Lin, *Nitrogen-doped graphene and its application in electrochemical biosensing.* ACS Nano, 2010. **4**(4): p. 1790-1798.
385. Wang, Y., Z. Li, J. Wang, J. Li and Y. Lin, *Graphene and graphene oxide: Biofunctionalization and applications in biotechnology.* Trends in Biotechnology, 2011. **29**(5): p. 205-212.
386. Wang, Y., Y. Li, L. Tang, J. Lu and J. Li, *Application of graphene-modified electrode for selective detection of dopamine.* Electrochemistry Communications, 2009. **11**(4): p. 889-892.
387. Reddy, A.L.M., A. Srivastava, S.R. Gowda, H. Gullapalli, M. Dubey and P.M. Ajayan, *Synthesis of nitrogen-doped graphene films for lithium battery application.* ACS Nano, 2010. **4**(11): p. 6337-6342.
388. Loh, K.P., Q. Bao, G. Eda and M. Chhowalla, *Graphene oxide as a chemically tunable platform for optical applications.* Nature Chemistry, 2010. **2**(12): p. 1015-1024.
389. He, Q., H.G. Sudibya, Z. Yin, S. Wu, H. Li, F. Boey, W. Huang, P. Chen and H. Zhang, *Centimeter-long and large-scale micropatterns of reduced graphene oxide films: Fabrication and sensing applications.* ACS Nano, 2010. **4**(6): p. 3201-3208.
390. Guo, S. and S. Dong, *Graphene nanosheet: Synthesis, molecular engineering, thin film, hybrids, and energy and analytical applications.* Chemical Society Reviews, 2011. **40**(5): p. 2644-2672.
391. Ghosh, S., I. Calizo, D. Teweldebrhan, E.P. Pokatilov, D.L. Nika, A.A. Balandin, W. Bao, F. Miao and C.N. Lau, *Extremely high thermal conductivity of graphene: Prospects for thermal management applications in nanoelectronic circuits.* Applied Physics Letters, 2008. **92**(15).
392. Fan, Z., J. Yan, L. Zhi, Q. Zhang, T. Wei, J. Feng, M. Zhang, W. Qian and F. Wei, *A three-dimensional carbon nanotube/graphene sandwich and its*

application as electrode in supercapacitors. Advanced Materials, 2010. **22**(33): p. 3723-3728.
393. Alwarappan, S., A. Erdem, C. Liu and C.Z. Li, *Probing the electrochemical properties of graphene nanosheets for biosensing applications.* Journal of Physical Chemistry C, 2009. **113**(20): p. 8853-8857.
394. Xia, J., F. Chen, J. Li and N. Tao, *Measurement of the quantum capacitance of graphene.* Nat Nano, 2009. **4**(8): p. 505-509.
395. Zeng, F., Y. Kuang, N. Zhang, Z. Huang, Y. Pan, Z. Hou, H. Zhou, C. Yan and O.G. Schmidt, *Multilayer super-short carbon nanotube/reduced graphene oxide architecture for enhanced supercapacitor properties.* Journal of Power Sources, 2014. **247**(1): p. 396-401.
396. Tryba, B., A.W. Morawski and M. Inagaki, *Preparation of exfoliated graphite by microwave irradiation.* Carbon, 2005. **43**(11): p. 2417-2419.
397. Falcao, E.H.L., R.G. Blair, J.J. Mack, L.M. Viculis, C.W. Kwon, M. Bendikov, R.B. Kaner, B.S. Dunn and F. Wudl, *Microwave exfoliation of a graphite intercalation compound.* Carbon, 2007. **45**(6): p. 1367-1369.
398. Wissler, M., *Graphite and carbon powders for electrochemical applications.* Journal of Power Sources, 2006. **156**(2): p. 142-150.
399. Sorokina, N.E., M.A. Khaskov, V.V. Avdeev and I.V. Nikol'skaya, *Reaction of Graphite with Sulfuric Acid in the Presence of KMnO4.* Russian Journal of General Chemistry, 2005. **75**(2): p. 162-168.
400. Hirata, *Thin-film-like particles having skeleton constructed by carbons and isolated films*, 2003: US patent 6596396.
401. Chen, Y., Y. Zhang, D. Geng, R. Li, H. Hong, J. Chen and X. Sun, *One-pot synthesis of MnO2/graphene/carbon nanotube hybrid by chemical method.* Carbon, 2011. **49**(13): p. 4434-4442.
402. Shen, L., C. Yuan, H. Luo, X. Zhang, S. Yang and X. Lu, *In situ synthesis of high-loading Li4Ti5O12-graphene hybrid nanostructures for high rate lithium ion batteries.* Nanoscale, 2011. **3**(2): p. 572-574.
403. Wojtoniszak, M., X. Chen, R.J. Kalenczuk, A. Wajda, J. Łapczuk, M. Kurzewski, M. Drozdzik, P.K. Chu and E. Borowiak-Palen, *Synthesis, dispersion, and cytocompatibility of graphene oxide and reduced graphene oxide.* Colloids and Surfaces B: Biointerfaces, 2012. **89**(4): p. 79-85.
404. Dreyer, D.R., S. Park, C.W. Bielawski and R.S. Ruoff, *The chemistry of graphene oxide.* Chemical Society Reviews, 2010. **39**(1): p. 228-240.
405. Li, J., Z. Yang, H. Qiu, Y. Dai, Q. Zheng, G.-P. Zheng and J. Yang, *Microwave-assisted simultaneous reduction and titanate treatment of graphene oxide.* Journal of Materials Chemistry A, 2013. **1**(37): p. 11451-11456.
406. Zhang, T., D. Zhang and M. Shen, *A low-cost method for preliminary separation of reduced graphene oxide nanosheets.* Materials Letters, 2009. **63**(23): p. 2051-2054.
407. Mermoux, M., Y. Chabre and A. Rousseau, *FTIR and 13C NMR study of graphite oxide.* Carbon, 1991. **29**(3): p. 469-474.
408. Chandra, S., P. Das, S. Bag, R. Bhar and P. Pramanik, *Mn2O3 decorated graphene nanosheet: An advanced material for the photocatalytic*

degradation of organic dyes. Materials Science and Engineering: B, 2012. **177**(11): p. 855-861.
409. Yang, T., L.-h. Liu, J.-w. Liu, M.-L. Chen and J.-H. Wang, *Cyanobacterium metallothionein decorated graphene oxide nanosheets for highly selective adsorption of ultra-trace cadmium.* Journal of Materials Chemistry, 2012. **22**(41): p. 21909-21916.
410. Liu, Z., L. Jiang, F. Galli, I. Nederlof, R.C.L. Olsthoorn, G.E.M. Lamers, T.H. Oosterkamp and J.P. Abrahams, *A Graphene Oxide¨Streptavidin Complex for Biorecognition – Towards Affinity Purification.* Advanced Functional Materials, 2010. **20**(17): p. 2857-2865.
411. Zhu, Y., S. Murali, M.D. Stoller, A. Velamakanni, R.D. Piner and R.S. Ruoff, *Microwave assisted exfoliation and reduction of graphite oxide for ultracapacitors.* Carbon, 2010. **48**(7): p. 2118-2122.
412. Zhong, C., J.-Z. Wang, D. Wexler and H.-K. Liu, *Microwave autoclave synthesized multi-layer graphene/single-walled carbon nanotube composites for free-standing lithium-ion battery anodes.* Carbon, 2014. **66**(2): p. 637-645.
413. Fan, Z., M. Xie, X. Jin, J. Yan and T. Wei, *Characteristics and electrochemical performances of supercapacitors using double-walled carbon nanotube/δ-MnO 2 hybrid material electrodes.* Journal of Electroanalytical Chemistry, 2011. **659**(2): p. 191-195.
414. Lu, X., H. Dou, B. Gao, C. Yuan, S. Yang, L. Hao, L. Shen and X. Zhang, *A flexible graphene/multiwalled carbon nanotube film as a high performance electrode material for supercapacitors.* Electrochimica Acta, 2011. **56**(14): p. 5115-5121.
415. Yang, S., K. Chang, H. Tien, Y. Lee, S. Li, Y. Wang, J. Wang, C. Ma and C. Hu, *Design and tailoring of a hierarchical graphene-carbon nanotube architecture for supercapacitors.* Journal of Materials Chemistry, 2011. **21**(7): p. 2374-2380.
416. Some, S., P. Bhunia, E. Hwang, K. Lee, Y. Yoon, S. Seo and H. Lee, *Can Commonly Used Hydrazine Produce n-Type Graphene?* Chemistry – A European Journal, 2012. **18**(25): p. 7665-7670.
417. Some, S., Y. Kim, Y. Yoon, H. Yoo, S. Lee, Y. Park and H. Lee, *High-Quality Reduced Graphene Oxide by a Dual-Function Chemical Reduction and Healing Process.* Sci. Rep., 2013. **3**.
418. DasA, PisanaS, ChakrabortyB, PiscanecS, S.K. Saha, U.V. Waghmare, K.S. Novoselov, H.R. Krishnamurthy, A.K. Geim, A.C. Ferrari and A.K. Sood, *Monitoring dopants by Raman scattering in an electrochemically top-gated graphene transistor.* Nat Nano, 2008. **3**(4): p. 210-215.
419. Dresselhaus, M.S., A. Jorio, M. Hofmann, G. Dresselhaus and R. Saito, *Perspectives on Carbon Nanotubes and Graphene Raman Spectroscopy.* Nano Letters, 2010. **10**(3): p. 751-758.
420. Metin, Ö., E. Kayhan, S. Özkar and J.J. Schneider, *Palladium nanoparticles supported on chemically derived graphene: An efficient and reusable catalyst for the dehydrogenation of ammonia borane.* International Journal of Hydrogen Energy, 2012. **37**(10): p. 8161-8169.

421. Casiraghi, C., S. Pisana, K.S. Novoselov, A.K. Geim and A.C. Ferrari, *Raman fingerprint of charged impurities in graphene.* Applied Physics Letters, 2007. **91**(23): p. 233108-3.
422. Wu, Z.-S., W. Ren, L. Xu, F. Li and H.-M. Cheng, *Doped Graphene Sheets As Anode Materials with Superhigh Rate and Large Capacity for Lithium Ion Batteries.* ACS Nano, 2011. **5**(7): p. 5463-5471.
423. Kudin, K.N., B. Ozbas, H.C. Schniepp, R.K. Prud'homme, I.A. Aksay and R. Car, *Raman Spectra of Graphite Oxide and Functionalized Graphene Sheets.* Nano Letters, 2007. **8**(1): p. 36-41.
424. Wu, Z.-S., W. Ren, L. Gao, J. Zhao, Z. Chen, B. Liu, D. Tang, B. Yu, C. Jiang and H.-M. Cheng, *Synthesis of Graphene Sheets with High Electrical Conductivity and Good Thermal Stability by Hydrogen Arc Discharge Exfoliation.* ACS Nano, 2009. **3**(2): p. 411-417.
425. Soin, N., S. Sinha Roy, S. Roy, K.S. Hazra, D.S. Misra, T.H. Lim, C.J. Hetherington and J.A. McLaughlin, *Enhanced and Stable Field Emission from in Situ Nitrogen-Doped Few-Layered Graphene Nanoflakes.* The Journal of Physical Chemistry C, 2011. **115**(13): p. 5366-5372.
426. Yan, J., T. Wei, B. Shao, Z. Fan, W. Qian, M. Zhang and F. Wei, *Preparation of a graphene nanosheet/polyaniline composite with high specific capacitance.* Carbon, 2010. **48**(2): p. 487-493.
427. Feng, H., R. Cheng, X. Zhao, X. Duan and J. Li, *A low-temperature method to produce highly reduced graphene oxide.* Nature Communications, 2013. **4**: p. 1539.
428. Shin, H.-J., K.K. Kim, A. Benayad, S.-M. Yoon, H.K. Park, I.-S. Jung, M.H. Jin, H.-K. Jeong, J.M. Kim, J.-Y. Choi and Y.H. Lee, *Efficient Reduction of Graphite Oxide by Sodium Borohydride and Its Effect on Electrical Conductance.* Advanced Functional Materials, 2009. **19**(12): p. 1987-1992.
429. Song, P., Z. Cao, Y. Cai, L. Zhao, Z. Fang and S. Fu, *Fabrication of exfoliated graphene-based polypropylene nanocomposites with enhanced mechanical and thermal properties.* Polymer, 2011. **52**(18): p. 4001-4010.
430. Jeong, H.-K., Y.P. Lee, R.J.W.E. Lahaye, M.-H. Park, K.H. An, I.J. Kim, C.-W. Yang, C.Y. Park, R.S. Ruoff and Y.H. Lee, *Evidence of Graphitic AB Stacking Order of Graphite Oxides.* Journal of the American Chemical Society, 2008. **130**(4): p. 1362-1366.
431. Wilson, N.R., P.A. Pandey, R. Beanland, R.J. Young, I.A. Kinloch, L. Gong, Z. Liu, K. Suenaga, J.P. Rourke, S.J. York and J. Sloan, *Graphene Oxide: Structural Analysis and Application as a Highly Transparent Support for Electron Microscopy.* ACS Nano, 2009. **3**(9): p. 2547-2556.
432. Hernandez, Y., V. Nicolosi, M. Lotya, F.M. Blighe, Z. Sun, S. De, I.T. McGovern, B. Holland, M. Byrne, Y.K. Gun'ko, J.J. Boland, P. Niraj, G. Duesberg, S. Krishnamurthy, R. Goodhue, J. Hutchison, V. Scardaci, A.C. Ferrari and J.N. Coleman, *High-yield production of graphene by liquid-phase exfoliation of graphite.* Nature Nanotechnology, 2008. **3**(9): p. 563-568.
433. Jalili, R., S.H. Aboutalebi, D. Esrafilzadeh, K. Konstantinov, S.E. Moulton, J.M. Razal and G.G. Wallace, *Organic Solvent-Based Graphene Oxide Liquid Crystals: A Facile Route toward the Next Generation of Self-*

Assembled Layer-by-Layer Multifunctional 3D Architectures. ACS Nano, 2013. **7**(5): p. 3981-3990.
434. Lu, T., L. Pan, H. Li, C. Nie, M. Zhu and Z. Sun, *Reduced graphene oxide–carbon nanotubes composite films by electrophoretic deposition method for supercapacitors.* Journal of Electroanalytical Chemistry, 2011. **661**(1): p. 270-273.
435. Romano, M.S., N. Li, D. Antiohos, J.M. Razal, A. Nattestad, S. Beirne, S. Fang, Y. Chen, R. Jalili, G.G. Wallace, R. Baughman and J. Chen, *Carbon Nanotube – Reduced Graphene Oxide Composites for Thermal Energy Harvesting Applications.* Advanced Materials, 2013. **25**(45): p. 6602-6606.
436. Wang, Y.-S., S.-Y. Yang, S.-M. Li, H.-W. Tien, S.-T. Hsiao, W.-H. Liao, C.-H. Liu, K.-H. Chang, C.-C.M. Ma and C.-C. Hu, *Three-dimensionally porous graphene–carbon nanotube composite-supported PtRu catalysts with an ultrahigh electrocatalytic activity for methanol oxidation.* Electrochimica Acta, 2013. **87**(2): p. 261-269.
437. Ren, X., C. Chen, M. Nagatsu and X. Wang, *Carbon nanotubes as adsorbents in environmental pollution management: A review.* Chemical Engineering Journal, 2011. **170**(2–3): p. 395-410.
438. Han, J.T., J.S. Kim, S.B. Jo, S.H. Kim, J.S. Kim, B. Kang, H.J. Jeong, S.Y. Jeong, G.-W. Lee and K. Cho, *Graphene oxide as a multi-functional p-dopant of transparent single-walled carbon nanotube films for optoelectronic devices.* Nanoscale, 2012. **4**(24): p. 7735-7742.
439. Li, H., L. Pan, T. Lu, Y. Zhan, C. Nie and Z. Sun, *A comparative study on electrosorptive behavior of carbon nanotubes and graphene for capacitive deionization.* Journal of Electroanalytical Chemistry, 2011. **653**(1–2): p. 40-44.